ACCESSING METASTABLE SOLID-SOLUTION NANOPARTICLES FROM SOLUTION-PHASE CONDENSATION REACTIONS: APPLICATIONS IN HIGH-K DIELECTRICS, GEOPOLYMERIZATION, AND X-RAY PHOSPHORS

A Dissertation

by

GREGORY RYAN WAETZIG

Submitted to the Office of Graduate and Professional Studies of
Texas A&M University
in partial fulfillment of the requirements for the degree of

DOCTOR OF PHILOSOPHY

Chair of Committee,	Sarbajit Banerjee
Committee Members,	Abraham Clearfield
	Dong Hee Son
	Jamie Grunlan
Head of Department,	Simon North

May 2018

Major Subject: Chemistry

ABSTRACT

This dissertation focuses on the design, synthesis, and functional applications of ceramic materials prepared with precise compositional, dimensional, and structural control from molecular precursors using a versatile sol—gel condensation process. Three primary thrusts have stemmed from this central idea: (i) mapping the size-dependent phase diagram of HfO_2 and stabilizing the metastable tetragonal phase of HfO_2 at room temperature as a result of dimensional confinement, thereby obtaining a technologically important high-dielectric-constant polymorph that is only accessible above a temperature of 1720°C in the bulk; (ii) developing a method to cross-link plant fibers through creation of siloxane frameworks, resulting in the stabilization of a mechanically resilient load-bearing composite for roadworks in the Alberta Oil Sands; and (iii) stabilizing solid-solution rare earth oxychloride (REOCl) nanocrystals across a broad compositional range to obtain a full palette of X-ray phosphors, allowing for elucidation of activation channels, sensitization mechanisms, and recombination pathways underpinning X-ray-activated optical luminescence.

The dissertation develops a versatile synthetic toolbox for defining oxide and oxyhalide frameworks. The choice of molecular precursors and ligands added during synthesis strongly influence kinetics of particle growth and allow for compositional control as well as tunability of particle dimensions. The metastable materials synthesized in this work have allowed for exploration of the size-dependent phase diagram of HfO_2 and have enabled the development of quaternary and quintary solid-solution phosphors based on the PbFCl-type LaOCl and GdOCl frameworks.

DEDICATION

There have been many people who have given me strength and guidance throughout my life to get me to where I am today. In particular I dedicate this dissertation to my beautiful, intelligent, caring, and loving wife, Shawna, whom I am incredibly indebted to for being alongside me every step of the way through my college and graduate student experiences. Shawna, you have been crucial to my success and I love you immensely for joining me on this wild ride. I also dedicate this dissertation to Dr. William "Bill" Ballard. Grandpa, you were the role-model in my life that I wanted to emulate and first instilled in me the goal of one day obtaining a Ph.D. just like you did many years ago. Thank you for all your help and guidance along the way. Lastly, I dedicate this dissertation to my parents Linda "Sue" Larsen and Gary Waetzig for loving me unconditionally and providing the support to push me toward my goals. Mom and Dad, without you I would not be the man, husband, and scientist I am today. Thank you.

ACKNOWLEDGMENTS

Foremost, I would like to express my sincere gratitude to my advisor Prof. Sarbajit Banerjee for the continuous support of my Ph.D. research. His devotion towards nanoscience, his motivation to push myself and other members of our lab to perform at our best, and his pursuit of immense knowledge has instilled in me a passion for science that I once thought was not possible. Without him I would not be prepared for my career as a scientist and I thank him deeply.

I would also like to thank my committee members, Prof. Abraham Clearfield, Prof. Dong Hee Son, and Prof. Jamie Grunlan, for their guidance and support throughout the course of this research.

Over the years, I have been fortunate enough to collaborate with several outstanding research groups. To this extent, I would like to thank Dr. Lucia Zuin at the Canadian Light Source for her support and assistance during XAS and XEOL experiments. I also want to thank Dr. Beth Hudak and Dr. Beth Guiton at the University of Kentucky for giving us the opportunity to image and understand the transition states of hafnia. Thank you to Cenovus Energy Inc. for the support of our muskeg work.

Thanks also goes to my friends, colleagues, department faculty, and staff for making my time at Texas A&M University a great experience. Finally, thank you to the past and present Banerjee Group members for their support and friendship through my graduate career.

CONTRIBUTORS AND FUNDING SOURCES

Contributors

Contributions in Chapter III came from Dr. Anol Mukhopadhyay and Kai-Wei Liu at Texas A&M University for their help with the mechanical testing measurements of muskeg and to Angelo Kirchon, Zachary Perry, and Prof. Hong-Cai Zhou for their help with BET measurements of muskeg. Also, contributions from Dr. Robert Dennis for obtaining SEM images and EDX of our nanopowders throughout this dissertation are recognized.

Much of the work in this dissertation would also not be possible if it were not for the incredible facilities at Texas A&M University. Specifically, the Materials and Characterization Facility, the Microscopy and Imaging Center, and the Center for Chemical Characterization and Analysis are acknowledged for providing the instruments needed to perform optically stimulated luminescence measurements, obtain transmission electron microscopy images, and determine the atomic concentration of the samples, respectively.

Funding Sources

The work in this dissertation was supported by the National Science Foundation under DMR 1504702, Cenovus Energy Inc., the Canadian Light Source, which is supported by the Natural Sciences and Engineering Research Council of Canada, the National Research Council Canada, the Canadian Institutes of Health Research, the Province of Saskatchewan, Western Economic Diversification Canada, and the University of Saskatchewan. 11-BM beamline measurements were performed at the Advanced Photon Source of the Argonne National Laboratory, which is supported by the U. S. Department of Energy, Office of Science, Office of Basic Energy Sciences, under Contract No. DE-AC02-06CH11357.

TABLE OF CONTENTS

Page

Page

Page

LIST OF FIGURES

Page

Page

Page

LIST OF TABLES

Page

Page

CHAPTER I

INTRODUCTION AND MOTIVATION

In this dissertation, the development and utilization of low-temperature solution-phase condensation routes for the preparation of extended ceramic frameworks from molecular precursors is explored. The kinetics of the condensation reactions are controlled with the help of passivating ligands that allow for dimensional confinement and the incorporation of dopant atoms. Nanoscale dimensional confinement and incorporation of dopant atoms on the cation lattice of oxides and oxychlorides allow for considerable tunability of the phase diagram and properties of the prepared materials. The dissertation will focus on three separate systems as case studies demonstrating the utility and versatility of this synthetic approach. Chapter II explores the stabilization of a metastable tetragonal phase of HfO_2 based on precise control of particle size at <10 nm dimensions, which has been established through control of condensation kinetics. The unprecedented stabilization of this metastable polymorph at room temperature, otherwise stable only above 1720°C in the bulk, represents a dramatic example of size tunability of phase diagrams in ceramic systems and paves the way to the preparation of high-dielectric-constant nanocomposite thin films.[1–6] A critical size of 3.6—3.8 nm is observed as the cross-over point wherein surface energy terms outweigh bulk free energy considerations allowing for stabilization of the tetragonal phase under conditions of constrained equilibrium. Chapter III explores a similar (but hydrolytic) condensation reaction for the preparation of amorphous SiO_2 within templates defined by plant fibers wherein the precipitated ceramic framework allows for construction of a load-bearing composite.[7] Muskeg fibers are interconnected and reinforced through formation of a siloxane network with cellulosic linkages providing an additional cross-linking mode. Such load-bearing composites provide a means of solidifying marshy soils in the

sub-Arctic regions of Canada. Chapters IV—VI explore the stabilization of GdOCl and LaOCl nanocrystals incorporating luminescent lanthanide cations on the cation sublattice. These materials are accessed through the elimination of alkyl halides upon the condensation of metal halides and metal alkoxides; the added ligands constrain crystal growth resulting in the stabilization of nanoparticles with well-defined morphologies.[8,9] The oxychlorides, crystallized in a tetragonal PbFCl lattice, serve as excellent optical and X-ray phosphors owing to their low phonon cut-off energies, anisotropic structures that inhibit cross-relaxation mechanisms, and excellent thermal as well as chemical stability. A broad palette of phosphors spanning the entire visible spectrum has been prepared through incorporation of single and multiple luminescent dopant atoms, Eu^{2+}, Eu^{3+}, and Tb^{3+}, on the cation lattice of GdOCl and LaOCl nanocrystals. Remarkable ligand tunability of the oxidation state of europium dopant atoms has been established; TOPO and oleylamine serve as redox non-innocent ligands resulting in stabilization of oxidized Eu^{3+} and reduced Eu^{2+} luminescent centers, respectively. The broad palette of X-ray phosphors rendered accessible by this synthetic approach have enabled detailed elucidation of activation channels, sensitization mechanisms, and recombination pathways upon X-ray excitation of these materials, which show substantial differences from optical stimulation. A consistent diminution of luminescence intensity is manifested at and near the giant resonance absorption of the host matrix as a result of distinctly divergent recombination channels. Resonant excitation results in recombination through a Coster-Kronig Auger electron ionization process and relaxation of a single electron—hole pair, whereas excitation away from the giant resonance results in thermalization of "hot" electron-hole pairs, resulting in activation and radiative recombination events at the luminescent centers.

I.1 Size-Dependent Phase Diagrams of Transition Metal Oxides: HfO_2 as a Case Study

Scaling materials to nanoscale dimensions provides remarkable opportunities for tuning phase diagrams and stabilizing metastable polymorphs; specifically, surface free energy terms can counteract bulk free energy descriptors and enable stabilization of unusual structural motifs under conditions of constrained equilibrium. Metastable polymorphs can be synthetically accessed either through kinetic trapping, preserving short-range structural motifs imposed by specific reaction conditions,[10,11] or can be thermodynamically stabilized as a result of size-dependent surface free energy considerations.[1,5,6,12] The stabilization of the tetragonal polymorph of HfO_2 is of immense technological importance given the predicted high dielectric constant of this phase,[13,14] but has proven to be much more synthetically challenging in comparison to the stabilization of tetragonal ZrO_2, which is structurally similar and is characterized by an analogous sequence of phase transformations. Indeed, HfO_2 and ZrO_2 are often denoted as "twin metal oxides" given the close parallels in their chemical reactivities and physical properties. The similarities between the two metal oxides derive from the almost identical ionic radii of tetravalent hafnium (0.78 Å) and zirconium-ions (0.79 Å), which is a result of lanthanide contraction.[15] Their similar ionic radii also allows for considerable miscibility of the two cations in substitutional solid-solutions; $Hf_xZr_{1-x}O_2$ solid-solutions can be stabilized across the entire compositional range $0 < x < 1$.[16] However, while the tetragonal phase of ZrO_2 can be readily accessed below a critical size of 30 nm,[4,17,18] stabilization of tetragonal HfO_2 has proven to be a considerably greater synthetic challenge.

The phase diagram for HfO_2 is depicted in **Figure I.1**. At room temperature, bulk HfO_2 crystallizes in a monoclinic ($P2_1/c$ or space group C_{2h}^5) lattice.[19] With increasing temperature (variously pegged at 1670—1720°C for HfO_2), a Martensitic phase transformation from the

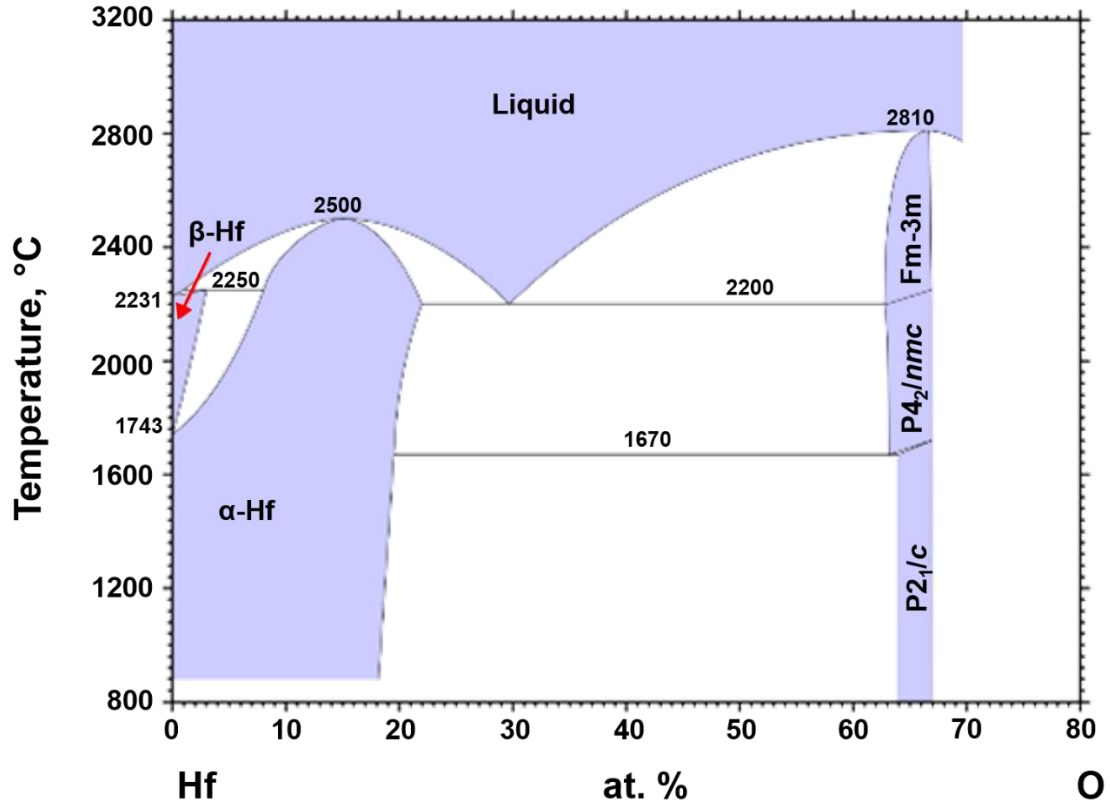

Figure I.1. Hf—O binary phase diagram for 0 – 80 at.% oxygen content. Adapted with permission from Ref. 19. Copyright Springer Materials Release 2016

monoclinic to the tetragonal (*P*4$_2$/*nmc* or space group D_{4h}^{15}) phase is observed. A further increase in temperature to *ca.* 2200^{o}C brings about a diffusionless tetragonal to cubic (*Fm*-3*m* or space group O_h^5) phase transformation; the cubic structure is retained until HfO_2 is congruently melted at 2810^{o}C.[15,20,21] Unit cells for these three thermally accessible phases of HfO_2 are depicted in **Figure I.2**. **Video A.1** (uploaded separately) depicts the sequence of atomic displacements that bring about the phase transformations, as visualized using the AMPLIMODES symmetry mapping program.

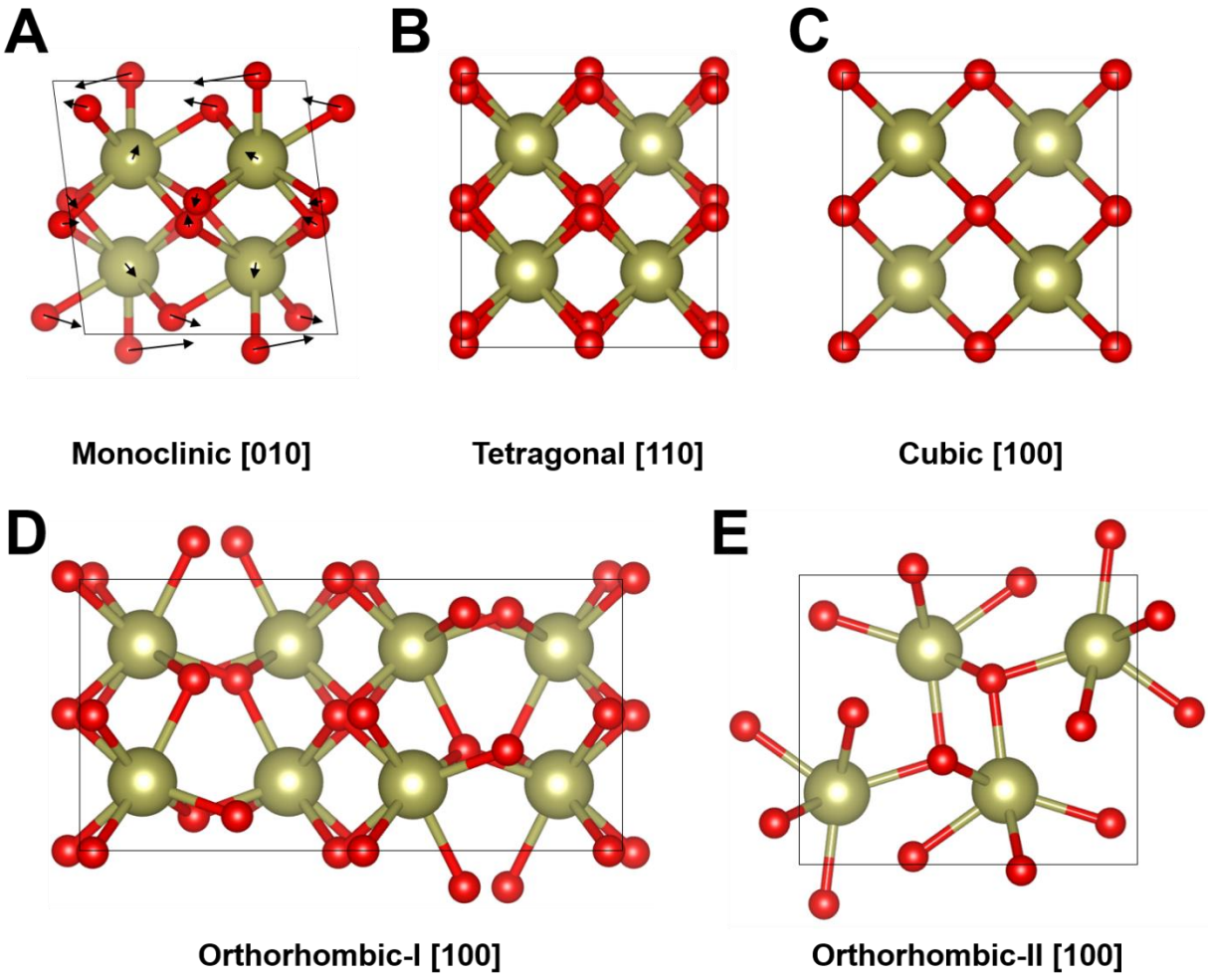

Figure I.2. Unit cells of A) monoclinic, B) tetragonal, C) cubic D) orthorhombic-I, and E) orthorhombic-II phases of HfO_2. The arrows in (A) depict the atomic displacements necessary to transform to the tetragonal phase in (B). Hafnium atoms are represented in gold and the oxygen atoms in red.

The monoclinic crystal structure of HfO_2 is characterized by the tetravalent hafnium-cations being ensconced within a seven-coordinated local geometry defined by oxide ions with cell parameters of a = 5.1505 Å, b = 5.2116 Å, c = 5.3173 Å, and β = 99.230°. The monoclinic to tetragonal phase transition involves a 9° shear of the unit cell and a volume expansion of 2.7% for HfO_2 (compared to *ca*. 4.5%[5] for ZrO_2).[22,23] Both phases further have a number of twin

variants allowing for manifestation of ferroelastic domains that can further self-organize into periodic patterns upon dimensional confinement or strain.[24–26]

In the tetragonal unit cell of HfO_2 (and ZrO_2), the tetravalent metal ions are ensconced within eight-coordinated environments comprising four oxygen atoms in close proximity to the metal atom at a separation of 2.09 Å, and four oxygen atoms further away at a distance of 2.31 Å, defining two distinct tetrahedra around the metal atom. During the symmetry-raising monoclinic—tetragonal phase transition, the oxide ions are displaced along the <001> direction as a result of close O—O contacts, creating a tetragonal distortion with a *c*/*a* ratio of 1.025.[8,27] The transition from monoclinic to tetragonal phases of HfO_2 and the resulting change of symmetry can be more clearly seen in Video A.1.

Almost 50 years ago, Garvie discovered that below a grain size of 30 nm, ZrO_2 can be stabilized in the tetragonal phase at room temperature. This remarkable stabilization originates from the surface energy contribution outweighing the bulk free energy since the tetragonal phase exposes considerably lower energy surface facets.[18,28] With decreasing size and a larger surface-to-volume ratio, the surface energy term acquires greater prominence and results in preferential stabilization of the tetragonal phase. The stabilization of tetragonal HfO_2 has proven to be a much greater synthetic challenge owing to the increased differential in thermodynamic stabilization between the monoclinic and tetragonal phases as depicted in **Table I.1** (the tetragonal phase of ZrO_2 is stabilized at 1170°C, whereas stabilization of tetragonal HfO_2 requires temperatures of 1670—1720°C).[15,29,30] The differential in bulk free energy is estimated to be 196 meV for HfO_2 as compared to 140 meV for ZrO_2. The smaller volume expansion for HfO_2 also brings about a more facile reversion to the monoclinic phase upon cooling, which further renders kinetic trapping of the metastable polymorph more difficult.[24] In Chapter II, we

explore the size-dependent phase diagram of HfO_2 availing the precise synthetic control afforded by a non-hydrolytic sol-gel condensation route to stabilize tetragonal HfO_2 nanocrystals at room

Table I.1. Calculated differentials in bulk and surface energies between the monoclinic and tetragonal phases of HfO_2 and ZrO_2[31] Reprinted with permission from Ref. 24.

Oxide	Tetragonal→Monoclinic Transition Temperature (°C)	Volume Expansion (%)	Difference in Surface Energy Between Monoclinic and Tetragonal Phase (mJ/m^2) $(\Delta U_{surface,monoclinic} - \Delta U_{surface,tetragonal})$	Difference in Bulk Energy Between Monoclinic and Tetragonal Phase (meV) $(\Delta G_{bulk,monoclinic} - \Delta G_{bulk,tetragonal})$
HfO_2	1670—1720 [15,29,30,32]	2.7 [22,23]	-246 [31]	196 [31]
ZrO_2	1170 [15,29]	~4.0 [33]	-225 [31]	140 [31]

temperature. The critical size for stabilization of HfO_2 is determined to be almost one order of magnitude lower than that of ZrO_2.

The eight-coordinate cubic *Fm*-3*m* phase of ZrO_2 has a unit cell parameter of 5.15 Å and has not thus far been stabilized at room temperature without incorporation of dopant atoms. Cubic ZrO_2 (and for that matter HfO_2) can be stabilized at room temperature through aliovalent incorporation of divalent or trivalent dopants such as Ca^{2+}, Y^{3+} and Sc^{3+}. These dopants introduce oxygen vacancies allowing for the Zr atoms to be seven-coordinated, while allowing for crystallization in a higher-symmetry cubic geometry.[34,35] Indeed, cubic ZrO_2 incorporating aliovalent dopants such as Y^{3+}, Sc^{3+}, or Ca^{2+} is known to be an excellent solid-state electrolyte at high temperatures owing to the facile diffusion of oxygen vacancies. Rauwel *et al*. have reported

the stabilization of cubic HfO_2 using sol—gel methods at an average size of 2.6 nm although the prepared materials have not been extensively characterized to rule out the incorporation of extrinsic dopants and to unequivocally establish the crystal structure.[36]

While Figure I.1 depicts a temperature-variant phase stability diagram, an alternative pressure-variant phase diagram can be mapped and indeed shows two non-centrosymmetric oxygen deficient orthorhombic phases of HfO_2 and ZrO_2. An orthorhombic I (O1, space group *Pbca*) is stabilized above 4.3 GPa and an orthorhombic II (O2, space group *Pnma*) phase is stabilized when the pressure exceeds 14.5 GPa (Figure I.1D and E).[37,38] These pressure-induced transformations are also theorized to be diffusionless Martensitic transitions and result from displacive unit cell distortions.[29,39,40]

The rich phase diagrams of HfO_2 and ZrO_2, tunable as a function of temperature, pressure, and oxygen stoichiometry, along with the facile accessibility of several polar variants for the low-symmetry polymorphs, have inspired extensive investigations of the properties of these materials. Two important implications of this rich phase diagram are transformation toughening and shape memory behavior, which hold promise for realizing unprecedented mechanical properties in ceramic materials that tend to otherwise be rather brittle. Since ferroelastic properties have been observed in the monoclinic structure as a result of stabilization of nanotwinned domains, it has been posited that the tetragonal structure may display superelastic properties.[41] Upon application of stress to the tetragonal structure, it undergoes a phase change to the monoclinic structure, followed by domain switching through ferroelastic domain wall movement, thereby allowing for multiple means of energy dissipation before plastic deformation.

In addition, considerable attention has focused on the utilization of the high dielectric constant of HfO_2 polymorphs stemming from their soft phonon modes and high Born effective charge tensors.[14] The phonon dispersion and extent of covalency of metal—oxygen bonds is determined by the crystal structure of HfO_2 and ZrO_2, which thus plays an important role in determining the dielectric constant. In the room-temperature monoclinic phase of HfO_2, the dielectric constant is roughly 18. In contrast, first-principles calculations predict a dielectric constant of 70 for tetragonal HfO_2[14] and 29 for cubic HfO_2.[42] The interest in new dielectric materials arises from the fundamental limitations of SiO_2 dielectrics. While SiO_2 dielectrics are entirely compatible with Si active elements, SiO_2 has a dielectric constant of only *ca*. 3.5.[43] Since C varies with the area (A), thickness (d), and dielectric strength (k) as $C = kA/d$, in order to preserve the same value of capacitance while aggressively scaling areal dimensions of the device, the dielectric constant must be increased or the thickness of the dielectric layer has to be decreased. The latter approach is severely constrained by enhanced leakage currents that result in increased power consumption. Indeed, at very low thicknesses, the mechanism for leakage is quantum tunneling, which is unavoidable even for the highest quality films. Consequently, higher dielectric constant materials have emerged as an urgent imperative and indeed the development of amorphous HfO_2 dielectrics and their integration onto Si marks a key milestone that has enabled the continued scaling of device dimensions.[14,43] The high predicted dielectric constant of the tetragonal phase of HfO_2 holds tantalizing promise for reducing power consumption but rather inconveniently, this phase is a high-temperature phase stable only above 1670^{o}C for HfO_2 and 1170^{o}C for ZrO_2 in the bulk.

I.2 Nucleation of Tetragonal HfO_2 from Twin Boundaries

Despite the rich phase diagrams of HfO_2 and ZrO_2 documented in Figure I.1, the high temperatures have thus far precluded detailed experimental evaluation of the mechanisms underpinning the phase transitions. Most of the available information is derived from theoretical calculations of deformations, bond stretching, and putative displacement pathways that however remain to be experimentally validated (or refuted).[12,44] An alternative mechanism for stabilizing tetragonal HfO_2 well below its equilibrium transition temperature of 1670°C involves modification of the transformation mechanism through nucleation of the phase transition at a coherent twin boundary. In past work, we've observed that (100) coherent twin boundaries (**Figure I.3**) are stabilized across monoclinic 1D HfO_2 nanorods grown by the condensation of $HfCl_4$ and $Hf(O^tBu)_4$; these twin defects are thought to form in order to alleviate strain within the crystallite upon cooling from an incipient tetragonal phase to the monoclinic phase that is stabilized at room temperature.[24] In order to alleviate strain generated upon volume expansion during the phase transformation, deformation and spontaneous organization of twin boundaries is observed along the length of the crystal. Figure I.3 depicts the ferroelastic organization of twinned domains that are seen to form "bar-code" like patterns spanning the entire diameter of a nanorod.

The phase evolution of these nanorods upon heating has been examined using *in-situ* high-angle annular dark field scanning transmission electron microscopy (HAADF STEM) measurements.[39] Remarkably, **Figure I.4** indicates that at a temperature of 600°C, the nucleation of a tetragonal domain is observed at a twin boundary, depressed by over 1000°C from the bulk transition temperature.[24] The sequence of images in Figure I.4 further indicates the propagation of a transformation dislocation across the nanorod, with conservation of a one-to-one lattice

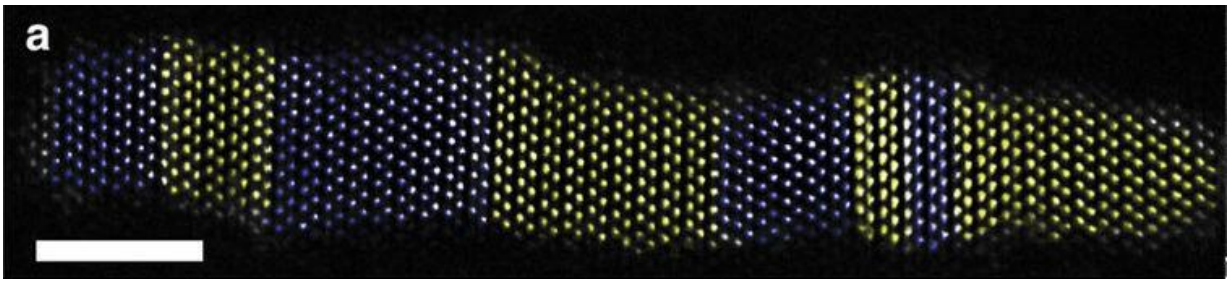

Figure I.3. (a) False-coloured HAADF image of a hafnia nanorod with twin domains imaged in the [110] zone colored yellow and blue. The scale bar represents 2 nm. Reprinted with permission from Ref. 39.

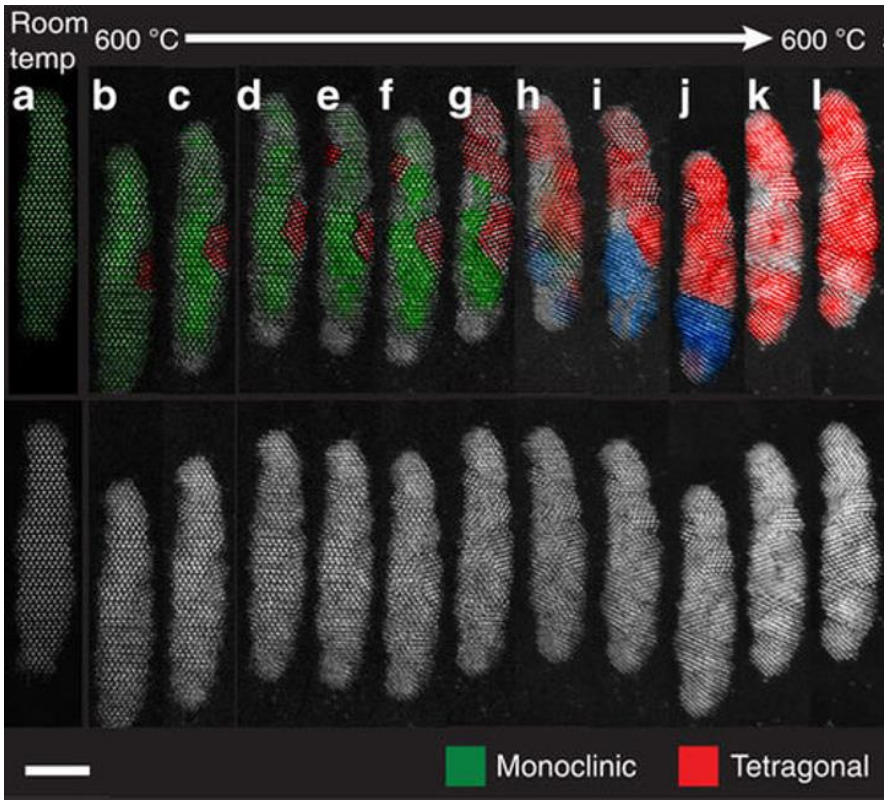

Figure I.4. False-colored HAADF STEM images highlighting the structural phases present in each frame. (a) Before annealing, the nanorod is monoclinic. (b–l) Over a period of about 40 min the nanowire converts completely from single-crystalline twinned monoclinic to polycrystalline tetragonal hafnia with retention of the overall morphology. Adapted with permission from Ref. 39.

correspondence across a phase boundary; the nanorod is entirely transformed to the tetragonal phase after 60 min. The thermodynamic underpinnings of the depressed phase transformation is parsed in different of different energetic contributions in a subsequent section of this chapter.

I.3 Synthetic Strategies for the Stabilization of Metastable Phases

The potential energy landscape can be understood to be a geometric representation of the free energy of a material as a function of configurational degrees of freedom. **Figure I.5** depicts a schematic representation of a multidimensional energy landscape. As a system relaxes towards equilibrium, from a high-energy state, it explores the landscape in search for efficient paths for the dissipation of the available free energy (Figure I.5). The degree to which a material is able to explore its energy landscape depends greatly on the available energy with which the material begins its relaxation towards a metastable equilibrium state. Conventional ceramic and metallurgical processing routes provide an abundance of energy to a material so it is usually able to efficiently explore the path towards equilibrium, without being trapped in metastable states. In contrast, solution-phase synthesis routes as well as templated routes involving heterogeneous nucleation onto epitaxially matched surfaces have the potential to carefully 'deposit' the material in a local minimum that can effectively 'trap' the system into forms exhibiting unusual chemical bonding motifs that can enable novel functionalities otherwise not accessible.

One promising strategy for stabilizing high-temperature polymorphs, such as the tetragonal phase of HfO_2, at room temperature is to explore scaling to nanometer-sized dimensions. Grain size stabilization of tetragonal HfO_2, along the lines of the stabilization of ZrO_2, would allow for the tetragonal HfO_2 phase and its desirable dielectric properties to be

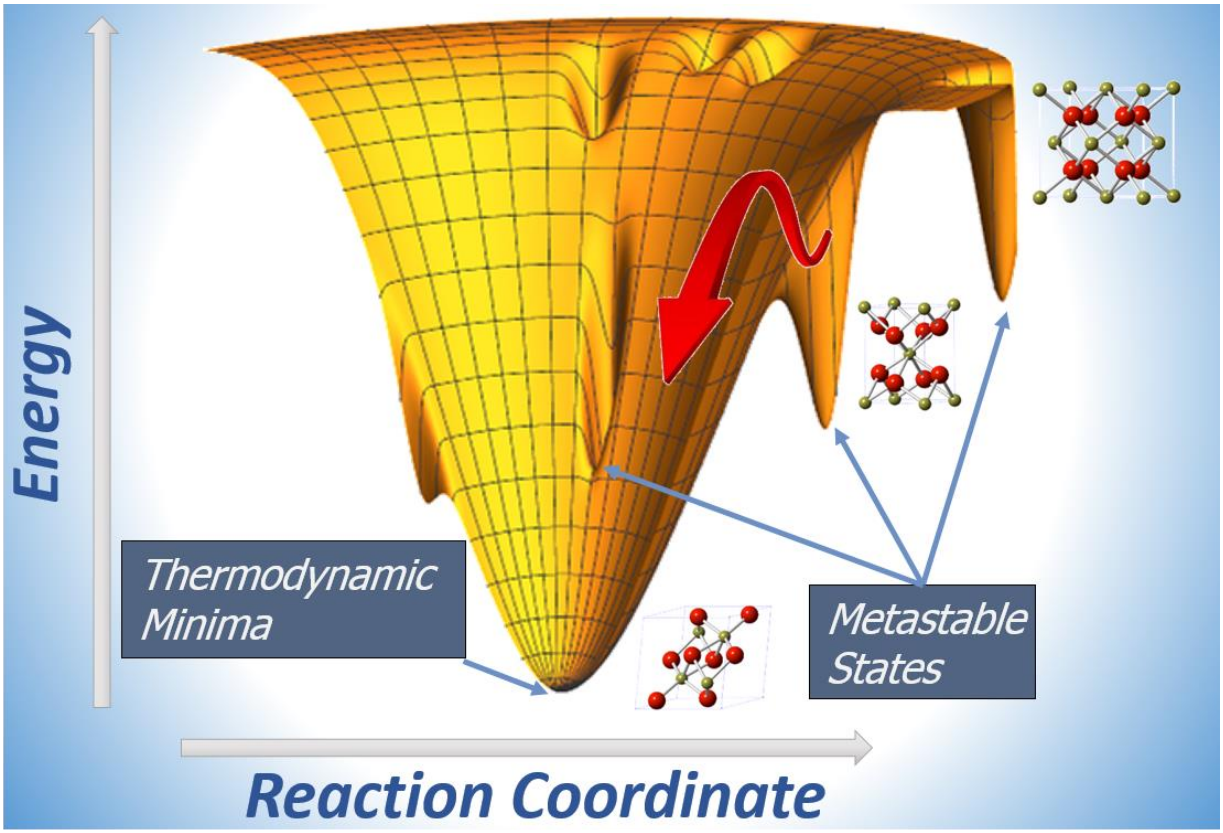

Figure I.5. Kinetically trapped metastable compounds can exhibit radical departures from equilibrium behavior and thereby provide a much more richly varied landscape of structures, properties, and function as compared to those accessible within thermodynamic minima. Several polymorphs of HfO_2 are schematically depicted in the sketch (not drawn to scale).

accessed without need for operating temperatures in excess of 1670°C. Non-hydrolytic sol—gel syntheses represent a useful palette of "soft chemistry" synthetic routes for traversing energy landscapes without excess energy that would result in coarsening of grain size. The addition of ligands that stabilize nuclei and mediate monomer addition allows for preparation of well-defined HfO_2, ZrO_2, as well as the mixed $Hf_xZr_{1-x}O_2$ nanocrystals.[15,16,20] In this approach, oxo linkages are created as a result of the condensation reaction between a metal halide and a metal alkoxide with elimination of an alkyl halide as per:

$$\equiv M—X + \equiv M—O—R \rightarrow \equiv M—O—M\equiv + R—X \qquad (I.1)^{15,16,20,45}$$

The condensation reaction is believed to involve coordination of the metal center of the halide to the oxygen atom of the metal alkoxide, followed by nucleophilic attack of the R-group by the halide, and the elimination of an alkyl halide in an S_N1-type fashion.[8,46,47] Vioux has recently reviewed various non-hydrolytic sol—gel syntheses for the preparation of metal oxides.[45] Typically tri-*n*-octylphosphine oxide (TOPO) is used as the surface-passivating ligand for obtaining nanocrystals that are monodisperse although recent ^{31}P nuclear magnetic resonance studies suggest that the protonated form of TOPO, hydroxyl-tri-*n*-octylphosphonium, $[HO\text{-}PR_3]^+$ is tightly bound to the nanocrystal surfaces along with di-*n*-octylphosphinate and *P,P′*-(di-*n*-octyl) pyrophosphonate.[48] Non-hydrolytic condensation chemistry, combined with the use of phosphonate and phosphonium ligands as the surfactant inhibit hydroxyl formation on the surface, thereby mitigating a deleterious surface trap for electron transport.[49] As a high-boiling point solvent, TOPO allows for relatively high reaction temperatures thereby allowing for stabilization of crystalline phases; the long alkyl chains of TOPO impart solubility in organic solvents and prevent agglomeration unlike metal oxides synthesized via aqueous methods.

The non-hydrolytic sol—gel synthesis route not only yields monodisperse nanocrystals, but also provides a means to control size, shape, stoichiometry, and crystal structure. Recognizing that the condensation reaction proceeds through an S_N1 mechanism, the electronic and steric substituent effects of the alkyl chain of the alkoxide precursor have a significant influence on the reactivity of the precursor in the condensation reaction and can thus substantially impact the kinetics of crystal growth, the eventual morphology, and even the crystal structure of the nanocrystalline products. The rate limiting step in the condensation reaction is thought to be stabilization of the carbocation during the halide attack on the alkoxide;[50] in other words cleavage of the MO—R bond is believed to be the rate-determining step and strongly

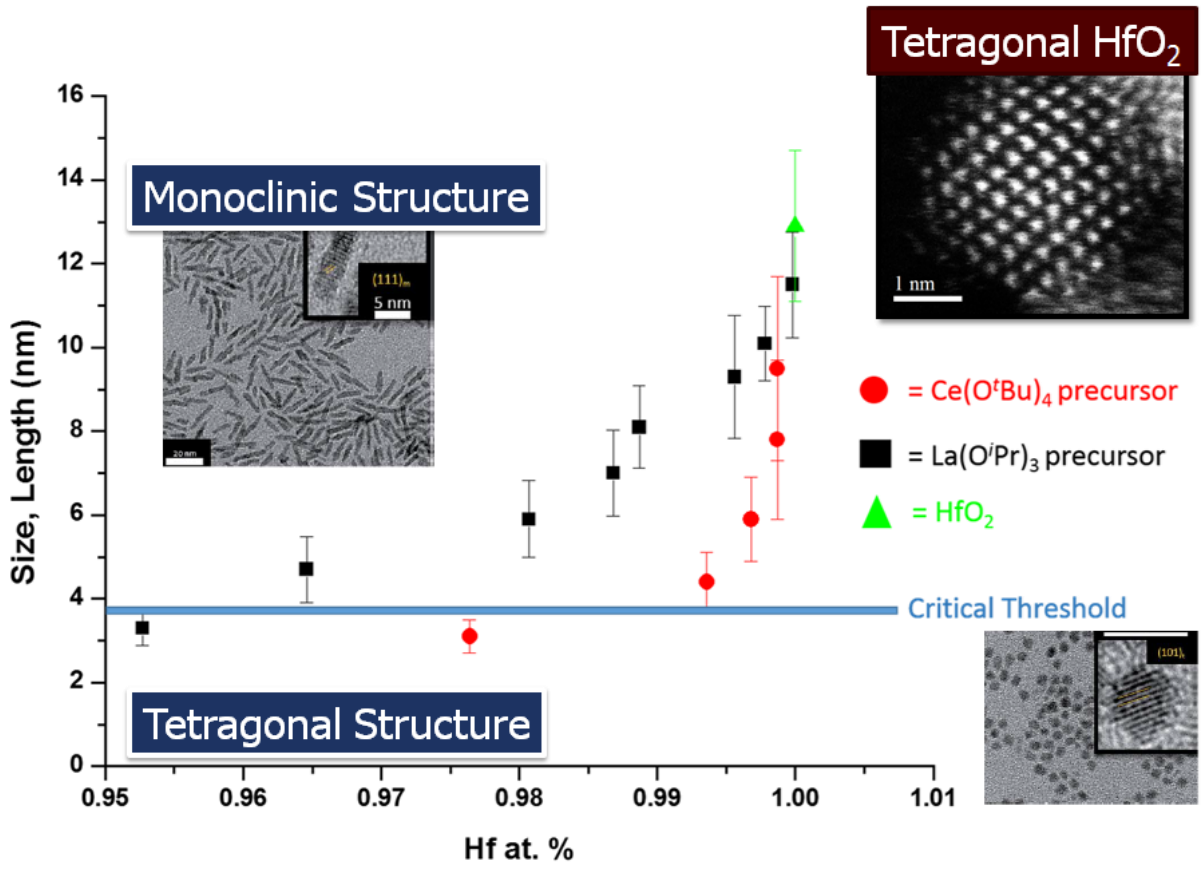

Figure I.6. Size dependence of crystal structure of HfO_2 nanocrystals prepared by a non-hydrolytic condensation approach. The tetragonal phase of HfO_2 is stabilized below a critical size of 3.6—3.8 nm. The top right inset depicts an atomically resolved electron microscopy image of an individual tetragonal HfO_2 particle, whereas the top left and bottom right insets depict HRTEM images of monoclinic and tetragonal HfO_2 nanocrystals, respectively. Adapted with permission from Ref. 3.

influences the kinetics of the reaction. In previous work, we have demonstrated that the dimensions of HfO_2 and ZrO_2 nanocrystals can be tuned based on the length of the alkyl chain of the alkoxide ligand; the length and branching of the chain furthermore controls the relative Hf:Zr incorporation within $Hf_xZr_{1-x}O_2$ nanocrystals.[16,24]

The first step in the condensation reaction between $M(OR)_4$ and MX_4 precursors is believed to involve ligand exchange, resulting in stabilization of haloalkoxides, $M(OR)_{4-x}Cl_x$.[45,51]

$M(OR)_3Cl$ has been proposed to catalyze the transformation of an alkoxo-bridge to an oxo-bridge. However, when two different metal precursors are reacted, the condensation rate is strongly influenced by the reactivity of each precursor, which allows for substantial control over the relative stoichiometry of metals incorporated within solid-solution products of a heterocondensation reaction:[15,29]

$$mMX_n + nM'(OR)_m \rightarrow M_mM'_nO_{nm} + nmRX \quad \text{(I.2)}$$

Chapter II details the incorporation of a less reactive precursor (e.g., $Ce(O^tBu)_4$ or $La(O^iPr)_3$) in conjunction with $HfCl_4$ and $Hf(O^tBu)_4$, which greatly retards the kinetics of the homocondensation reaction. Constraining the growth kinetics yields HfO_2 nanocrystals with ultra-small dimensions, enabling a detailed evaluation of the size dependence of the phase diagram of HfO_2. **Figure I.6** indicates that the critical size for stabilization of tetragonal HfO_2 is *ca*. 3.6 nm, substantially reduced from the 30 nm value generally accepted for ZrO_2.[3] By preventing coarsening of grain size and yielding monodisperse nanocrystals with tunable dimensions, this synthetic approach provides a means to systematically evaluate the balance between surface energy and bulk free energy as a function of particle size.

I.4 Thermodynamic Considerations Determining Phase Stabilization in HfO_2

As noted above, Garvie and co-workers first reported in 1965 that the tetragonal phase of ZrO_2 can be stabilized below a certain critical size (variously estimated to be 15—30 nm) with respect to the monoclinic phase because the surface energies of the former are significantly lower than the latter.[1,18,32,52] As shown in Table I.1 the monoclinic phase of ZrO_2 is 5.5 kJ/mol more stable in terms of bulk enthalpy as compared to the tetragonal phase; however, the surface energy of the tetragonal phase is 225 mJ/m^2 lower than that of the monoclinic phase.[1,31,52] Below a

critical size, the tetragonal phase is thus stabilized at room temperature as a result of increased surface energy contributions. Examples of the stabilization of tetragonal ZrO_2 have been well documented for bulk ceramics and thin films; however, the stabilization of tetragonal HfO_2 has proven to be much more difficult.[23,31,32] As noted above, the primary origin of this challenge is the greater differential of bulk free energies (ΔG); almost 40% greater for HfO_2 as compared to ZrO_2 (Table 1).[23,31,32] A full accounting of the different energy terms involved in the phase transformation is warranted to understand the pronounced size dependence of the phase stability. The change in free energy for a monoclinic—tetragonal transformation can be separated into the following components:[53]

$$\Delta G_{M\rightarrow T} = G_M^c - G_T^c + U_{SE}^M - U_{SE}^T + U_S^M - U_S^T \quad \text{(I.3)}$$

where G^c is the chemical free energy, U_{SE} is the strain energy, U_S is the surface energy, and the superscripts M and T represent the tetragonal and monoclinic phases, respectively.[54] At room temperature the ΔG^c value will be strongly positive, again owing to the 196 meV differential (Table I.1), which favors retention of the thermodynamically stable monoclinic phase. Indeed, even at a temperature of 600°C, the ΔG^c value will be strongly positive in the bulk, favoring retention of the monoclinic phase. Nevertheless, it is clear that $\Delta G_{M\rightarrow T} \leq 0$ at 600°C for the twinned nanorods where a monoclinic→tetragonal transition is observed (Figure I.4); indeed, this implies that the surface and strain energy differentials must be of a sufficient magnitude to overcome the highly positive chemical free energy differential. It is these two parameters that thus underpin suppression of the transition temperature by almost 1000°C.

The first term we will examine is the ΔU_S surface energy term, which can be written for a spherical particle as:

$$\Delta U_S^{M\to T} = \frac{6(\gamma_T - g_s\gamma_M)}{D} \quad \text{(I.4)}$$

where the γ terms represent the interfacial surface energies, *D* is the diameter of the particle and $g_s = A_M/A_T$, which describes the ratio of the interfacial surface areas.[54] Equation I.4 suggests that the smaller the size of the particle, higher the numerical value of the surface energy differential. The numerical values of the γ terms determine the sign of the $\Delta U_S^{M\to T}$ term. Ramprasad and co-workers have shown using first principles density functional theory calculations that the surface energies of the lowest-energy {110} and {001} lattice planes of HfO_2 will dictate the relative phase stabilities at finite dimensions. Calculated values for {110} and {001} planes of monoclinic HfO_2 are 1.38 J m^{-2} and 1.51 J m^{-2}, respectively, whereas the corresponding values for the tetragonal planes are 1.08 J m^{-2} and 1.21 J m^{-2}, respectively, clearly indicating that the $\Delta U_S^{M\to T}$ term will be negative with the diameter serving as an inversely proportional weighting factor.[12] Consequently, the particle size plays a key role in counteracting the strongly positive ΔG^c value and drives the stabilization of the tetragonal phase at room temperature upon scaling to ultra-small dimensions as evidenced in Figure I.6.

The second term that impacts the transition temperature is the ΔU_{SE} strain energy term. This term can be attributed to the twin planes of the nanorods where in Figure I.3 the compensation of the transformation strain across the nanorod is alleviated by the plastic deformation induced by the twin planes during synthesis. The energy stored within the twin planes is dissipated during the transformation from monoclinic to tetragonal symmetry, thus implying $\Delta U_{SE}^{M\to T} < 0$, further working in the opposite direction from the positive ΔG^c differential. Lange and co-workers have deduced a size-dependent expression for twin boundaries as per:[54]

$$\Delta U_{SE}^{M\rightarrow T} = -\frac{6\gamma_{twin}g_{twin}}{D} \quad \text{(I.5)}$$

where γ_{twin} is the twinning energy per unit area and g_{twin} is a dimensionless quantity expressed as $\frac{A_{twin}}{\pi D^2}$, where A_{twin} is the total area of the twin boundaries. As seen in Figure I.4, the twin plane serves as a nucleation point within the nanorod, which corresponds to a high energy region of the energy landscape. A high local density of twin domains within a small particle size thereby renders $\Delta U_{SE}^{M\rightarrow T}$ strongly negative and further contributes to the depression of the transition temperature.

To summarize, kinetically trapping crystals at small sizes can bring about the stabilization of metastable phases wherein the surface energy terms outweigh bulk free energy terms. Both surface energy and strain energy terms are size dependent. In Chapter II the stabilization of ultra-small nanocrystals of tetragonal HfO_2 at room-temperature will be discussed in detail based on dimensional confinement.

I.5 LaOCl as an Optical and X-ray Phosphor: Structure, Synthetic Strategies, Thin Films, and an Introduction to X-ray Excited Optical Luminescence

Lighting accounts for almost 20% of worldwide energy consumption.[55] A concerted global effort is focused on replacement of incandescent and fluorescent lamps with "cold" energy efficient solid-state lighting technologies.[56–58] The fundamental idea underpinning this approach is the extraction of light from wide bandgap semiconductors (e.g., AlGaInP and InGaN) utilizing electroluminescent phenomena[59–61] and stimulation of one or more phosphors to obtain white light emission, thereby bringing about a direct conversion of electrical energy to light. Increasing efficiencies of light extraction from solid-state diodes as well as improvements

in the quantum yields of phosphors render this approach considerably more energy efficient as compared to incandescent and compact fluorescent alternatives. Some estimates suggest that inorganic solid-state lighting constructs readily exceed 70% efficiency in their ability to convert electrical energy to visible luminescence.[57] The landmark discovery of the blue light-emitting diode (LED), which won Nakamura *et al*. the 2014 Nobel Prize in Physics, as well as subsequent advances that have increased the efficiency and reduced the cost of solid-state diodes have made solid-state lighting a viable technology.[62] The availability of thermally robust and color tunable phosphors is imperative for advancement of this technology to enable a high conversion efficiency and allow for precise tuning of the color temperature. The intense push to develop solid-state lighting has led to the exploration of a wide range of phosphors spectrally matched to specific LEDs and has unraveled fundamental descriptors for conversion efficiency such as the Debye temperature (a higher Debye temperature is thought to be reflective of a more rigid framework, thereby diminishing non-radiative recombination pathways).[63–65]

In contrast, the design of phosphors that convert high-energy VUV and X-ray radiation (or for that matter low-energy electrons) to visible light is far less explored. Such phosphors absorb high-energy X-ray photons through creation of hot electron—hole pairs that undergo cascades of thermalization events activating multiple luminescent centers and yielding multiple photons of visible light for each absorbed X-ray photon.[66–68] Efficient amplification, color tunability, and high spectral resolution of X-ray converter materials is imperative to their use in medical imaging, scintillators, and detectors.[69] Efficient phosphors underpin improved differentiation of X-ray contrast at low radiographic doses and are furthermore of utmost importance to detection of γ-radiation for national security applications. The lack of a detailed understanding of activation channels, sensitization mechanisms, and recombination pathways has

impeded the rational design of X-ray phosphors. The development of new classes of luminescent materials, underpinned by rational design principles along the lines of those elucidated for optically stimulated phosphors, has emerged as an urgent imperative to push the limits of resolution and quality of displays. In Chapters IV—VI we explore rare-earth oxychlorides as X-ray phosphors, develop synthetic strategies for dimensional confinement and incorporation of different luminescent centers, and examine X-ray stimulated sensitization phenomena.

Rare earth ions provide a promising palette for optoelectronic technologies owing to their widely tunable emission colors, emanating from their 4f → 4f or 5d → 4f transitions.[70] Rare-earth oxychlorides are a promising host lattice for X-ray phosphors given their thermal robustness and preservation of the tetragonal matlockite PbFCl structure across the early lanthanides, which allows for stabilization of solid-solutions incorporating multiple luminescent centers. In particular, LaOCl has emerged as a prominent host given the large ionic radius of La^{3+}, which readily allows for substitutional incorporation of other lanthanide ions. Much recent interest has focused on the fabrication of field-emission displays, radiation detectors, scintillators, and medical imaging device technologies utilizing variously doped LaOCl as the active element.[66,71–73] However, electron-hole pair formation, carrier diffusion, scattering, and recombination processes induced upon X-ray excitation are almost entirely unexplored in these materials.[67,74,75] Chapters IV – VI of this dissertation will examine GdOCl and LaOCl as host matrices specifically discussing the activation channels, sensitization mechanisms, and recombination pathways stimulated by X-ray excitation of Tb^{3+} in GdOCl (Chapter IV), Eu^{3+} and Eu^{2+} in LaOCl stabilized through ligand-mediated oxidative or reductive chemistry (Chapter V), and multiply doped Tb^{3+}-Eu^{3+} and Tb^{3+}-Eu^{2+} in LaOCl (Chapter VI).

I.6 Crystal Chemistry and Growth Mechanisms of Rare-Earth Oxychlorides

The selection of a host matrix is of utmost importance for the design of a phosphor since the interaction of the photoexcited luminescent centers with the surrounding environment as well

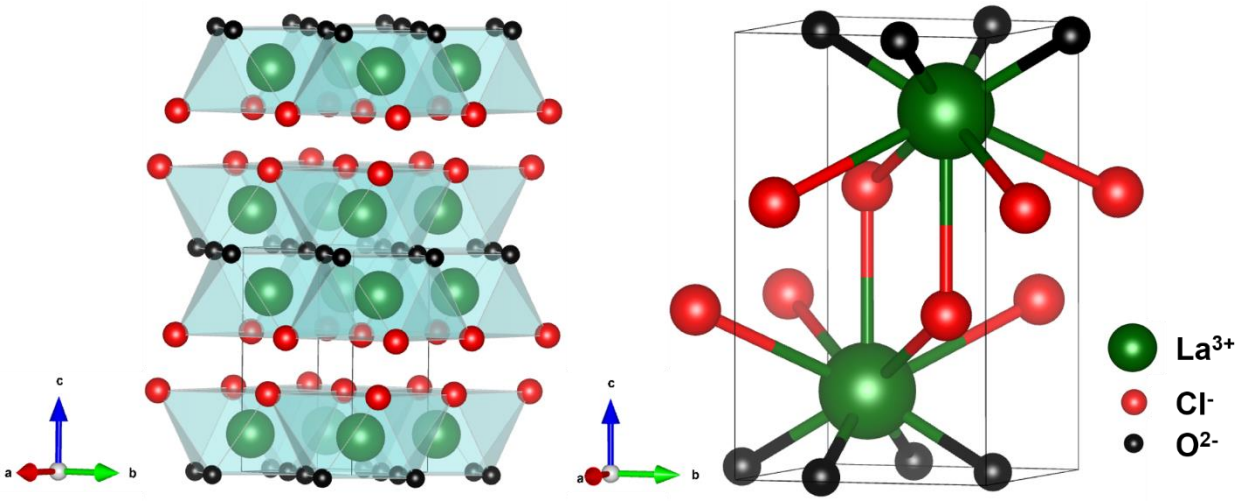

Figure I.7. The extended matlockite tetragonal PbFCl structure adopted by rare-earth oxychlorides (left) and depiction of an individual unit cell (right).

as adjacent chromophores and activators determines the color of the material as well as the efficacy with which it converts the impinging radiation to visible light. REOCl, where RE = La to Ho, crystallizes in the tetragonal matlockite PbFCl structure with a space group of *P*4/*nmm* (*Z* = 2).[47,76] The structure can be described as alternating cationic layers of $(REO)_n^{n+}$ and anionic Cl^- layers arrayed along the crystallographic *c* direction as depicted in **Figure I.7**. Each RE cation has a C_{4v} site symmetry and resides within a mono-capped square antiprism defined by four O^{2-} ions in the underlying layer and five Cl^- ions in the layer above.[8,47] The distal fifth Cl^- ion resides in the next-to-nearest anionic layer and this interaction imparts 3D connectivity to the lattice and is the primary mode through which the infinite $(REO)_n^{n+}$ and anionic Cl^- sheets are

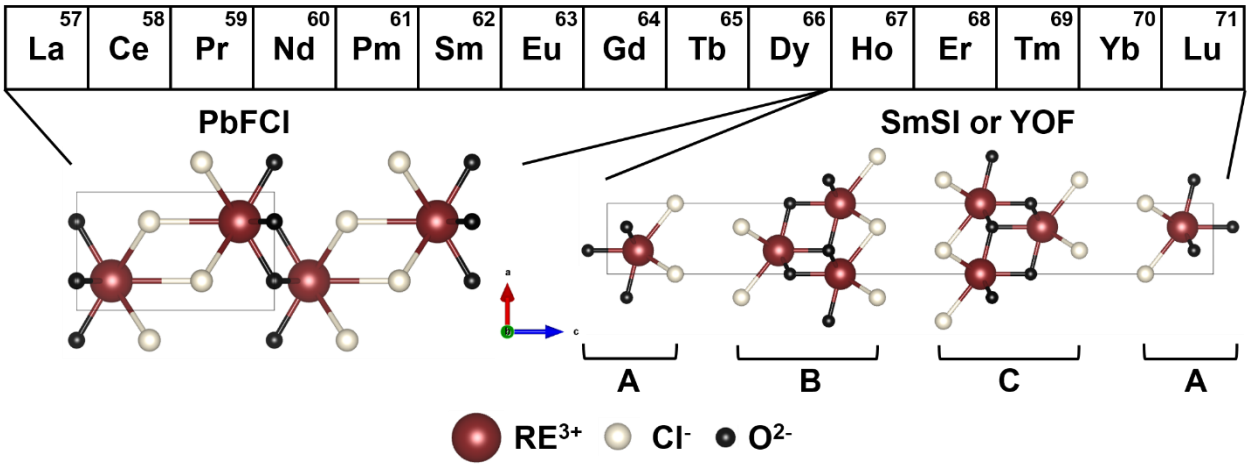

Figure I.8. The lanthanide series indicating the preferred stable polymorphs for REOCl; the PbFCl structure-type is adopted by the early lanthanides from La to Ho, whereas polytypic mixtures SmSI and YOF crystal structures are observed for the later lanthanides.

held together. Notably, for the later lanthanides, beyond Ho, the PbFCl structure can no longer be stabilized and the hexagonal SmSI structure (space group: *R*-3*m*) structure is preferentially adopted.[77,78] This structure comprises alternating slabs of hexagonally packed bilayers of RE^{3+} ions sandwiched between Cl^- layers (also hexagonally packed and aligned along the edges of the van der Waals' gap) with oxygen atoms situated in the tetrahedral holes of the RE layers.[77–79] A second crystalline phase has also been identified for the heavier rare earths, which can exist as a mixture with the SmSI phase. The YOF structure (space group: *R*-3*m*) is comparable to the SmSI phase and differs only in the stacking sequence of the layers. Instead of the ABC sequence of the SmSI structure, YOF adopts an ACB sequence as depicted in **Figure I.8**.[77,78] The distinctive properties of the PbFCl structure make it an attractive host matrix for luminescence applications for three reasons. First, these structures have low phonon cut-off energies, which substantially alleviates phonon-mediated non-radiative recombination channels and facilitates efficacious energy transfer to dopant rare earth luminescent ions.[80–83] Secondly, the anisotropic structure

separates cations into different layers, thereby limiting cross-relaxation mechanisms and enabling high concentrations of luminescent centers to be incorporated without concentration quenching (*ca*. 8—10 at.% of dopant ions can typically be incorporated in LaOCl and GdOCl without concentration quenching).[8,9,47] Finally, these structures are chemically stable and thermally robust, which is a necessary condition for X-ray phosphors that are subjected to high-energy excitation.[84]

Scaling the dimensions of materials down to nanometer-sized dimensions is essential since the resolution of a solid-state phosphor is fundamentally limited by the grain size.[85,86] The non-hydrolytic sol—gel condensation method has been developed in our research group as distinctive means of stabilizing rare-earth oxychloride nanocrystals.[16,24,87] As noted in Section I.3 above, the condensation of metal halides and metal alkoxides yields metal oxides for early transition metals;[15,16,20,24,29] however, several years ago, research in the group established that the condensation of trivalent lanthanide halides and lanthanide alkoxides instead allows for the unprecedented stabilization of lanthanide oxyhalide frameworks.[46,47,87,88]

The following sequence of reactions has been proposed wherein lanthanide chloroalkoxides are initially stabilized as per:

$$LnCl_3 + Ln'(OR)_3 \rightarrow LnCl_{3-x}(OR)_x + Ln'Cl_x(OR)_{3-x} \quad (I.6)$$

A subsequent condensation step yields the oxychloride framework upon elimination of an alkyl halide as per:

$$LnCl_{3-x}(OR)_x + Ln'Cl_x(O\text{-}R)_{3-x} \rightarrow (OR)(Cl)\text{-}Ln\text{-}O\text{-}Ln'\text{-}(Cl)(OR) + RCl \quad (I.7)$$

In order to structure the obtained networks into discrete unagglomerated particles, a stabilizing ligand such as tri-*n*-octylphosphine oxide (TOPO) or oleylamine is used. TOPO is a high-boiling-point molecule that serves as a coordinating ligand and constrains crystal growth to

nanoscale dimensions.[3,39,89] Interestingly, ligand molecules selectively bind to particular crystallographic facets allowing for the orthogonal addition of monomers to other "bare" facets that are more accessible to monomer addition; controlled monomer addition allows for a means of establishing control over the morphologies of the obtained materials.[46,47,88]

A detailed study of the growth mechanisms of GdOCl by Kort *et al*. has established that the morphology of the obtained crystallites depends upon differential binding of various ligands, the extent to which the monomer concentration and the extent of supersaturation is buffered by the ligands, and the rate of monomer addition along dislocations.[46] In the instance of TOPO, crystal growth appears to occur along the <101> direction and yields large, thick, and polydisperse nanodiscs as shown in **Figure I.9**. A spiral pattern is clearly discernible on the surface of these nanodisks suggesting that growth is mediated by the propagation of screw dislocations. In the case of oleylamine, octadecylamine, tri-*n*-octylamine, and didodecylamine the preferred growth direction is <110>, which induces dimensional confinement along the crystallographic *c* direction and yields nanosheet morphologies (Figure I.9). Interestingly these particles also exhibit spiral contours suggesting that the addition of monomers drives the morphology-controlled growth along these imperfections. Comparing the vertical dimensions of these materials shows that relatively platelets grown using relatively weakly bound TOPO are substantially thicker than the nanosheets stabilized by the more strongly basic amine ligands. The amine ligands strongly and selectively bind Gd^{3+} ions of GdOCl in the <001> direction, thereby constricting growth in the vertical dimension, whereas TOPO does not bind as strongly to the Gd^{3+} ions, thus allowing for the nanodisks to grow to thicker dimensions (growth occurs along the <101> direction).[46]

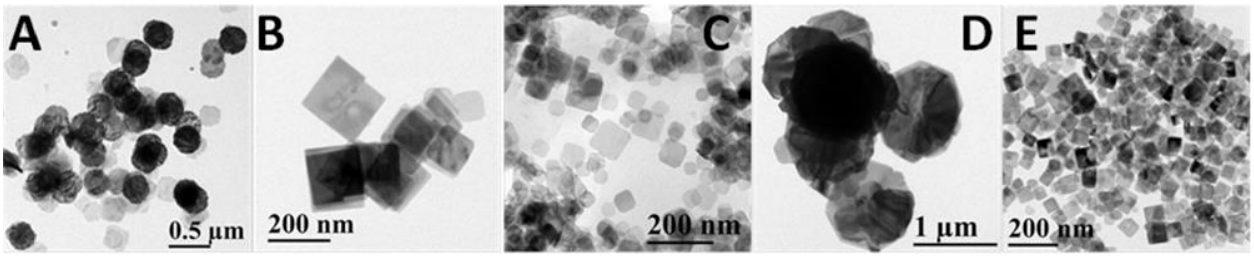

Figure I.9. TEM images of GdOCl nanoplatelets prepared by the reaction of $GdCl_3$ and $Gd(O^iPr)_3$ for 2 h in the following coordinating solvents: A) TOPO; B) oleylamine; C) octadecylamine; D) didodecylamine; and E) tri-*n*-octylamine. Reproduced from Ref. 46 with permission from the American Chemical Society.

As for growth along the lateral dimension of these nanocrystals, the stabilizing ligands (both TOPO and the amines) buffer the precursor concentration thus allowing for control of the growth kinetics. The extent of supersaturation thus contributes to the anisotropy seen in these nanocrystals and allows for tunability of particle size in dislocation-mediated growth as illustrated in Figure I.9.

I.7 Incorporation of REOCl Nanocrystals within Thin Films

For application within high-resolution emissive display screens, scintillator elements, and solid-state lighting, it is imperative to incorporate the nanocrystals within thin films of controllable thickness. Recently, electrophoretic deposition has emerged as a versatile technique to deposit conformal nanoparticle coatings with high packing density. This technique is also highly desirable from a manufacturing perspective given its scalability, production rate, and cost effectiveness. For the preparation of phosphors via electrophoretic deposition, it is particularly desirable to align the basal plane of nanoplatelets along the substrate to prepare flat optically transparent thin films.[90,91]

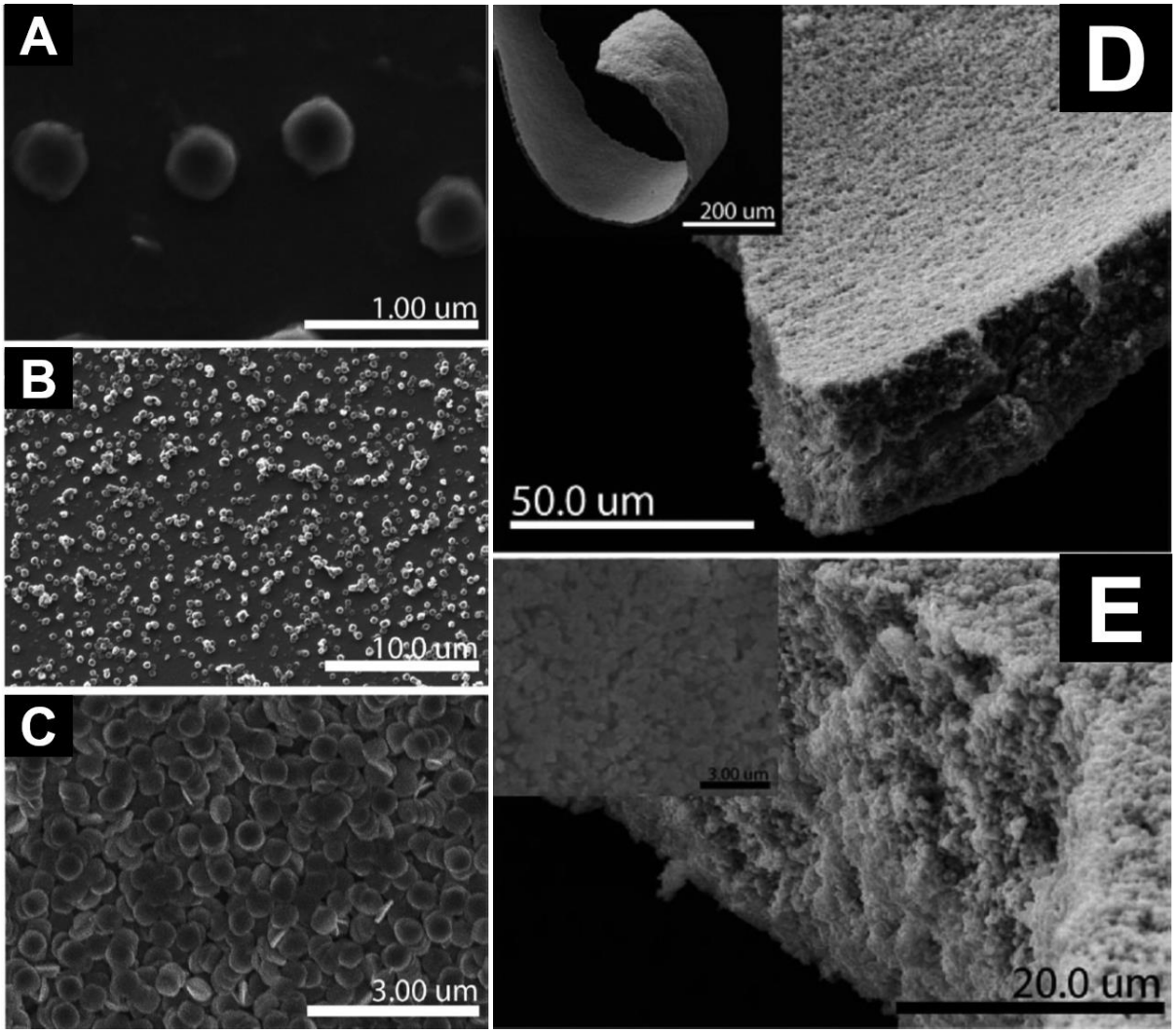

Figure I.10. (A) Electrophoretically deposited GdOCl nanoplatelets obtained under potentiostatic conditions upon application of a constant 25 V voltage between a pair of ITO electrodes for 3 min. Deposition was performed from a 250 mg/L cyclohexane dispersion of the nanoplatelets. (B) Higher surface coverage is obtained upon deposition under potentiostatic conditions for 3 min using a 500 mg/L colloidal dispersion of the nanoplatelets. (C) Multilayer coverage with considerable retention of particle alignment is obtained upon deposition for 3 min from a 1000 mg/L cyclohexane dispersion of the nanoplatelets. (D) SEM image of a fragments of a free-standing GdOCl nanoplatelet construct delaminated from the ITO-coated glass substrate. The thin films were originally deposited potentiostatically at 600 V for 15 min from a 1000 mg/L cyclohexane dispersion. The inset shows the flexion of a free-standing fragment. (E) Cross-sectional SEM image of a free-standing fragment; the inset shows a top-view of the free-standing construct. Adapted from Ref. 88 with permission from the American Chemical Society.

Kort *et al*. have developed a methodology for the oriented electrophoretic deposition of GdOCl nanoplatelets from non-polar solvents.[88] These authors have reported a detailed evaluation of deposition conditions. Upon subjecting a 250 mg/L dispersion of GdOCl nanoplatelets in cyclohexane to a constant voltage of 25 V for 3 min, a thin film with oriented GdOCl nanoplatelets is obtained although the surface coverage is observed to be rather sparse. Increasing the concentration to 1000 mg/L results in a homogenous and densely packed oriented thin film of GdOCl nanoplatelets (as shown in **Figure I.10**). Keeping the 1000 mg/L concentration and increasing the voltage and time to 600 V and 15 min allows for deposition of thin films spanning several micrometers in thickness that can further be delaminated from the indium tin oxide (ITO)-coated glass substrate. Figure I.10 illustrates the flexible nature of these freestanding GdOCl films upon delamination. It can also be seen in the corresponding SEM images that the GdOCl nanoplatelets align parallel to the electrode surface in the basal plane. Therefore, this method for deposition of highly aligned films of varying thicknesses provides a powerful manufacturing tool for oriented deposition of nanostructured phosphors.

I.8 Towards Viable X-ray Phosphors: Installation of Dopant Centers and Elucidation of Mechanisms Underpinning X-ray Stimulated Visible Light Luminescence

Chapter IV of this dissertation examines the elaboration of the non-hydrolytic condensation strategy to prepare solid-solution REOCl nanocrystals incorporating other luminescent rare earth ions. A novel cross-coupling method is developed to incorporate green emitting Tb^{3+} ions within a GdOCl host matrix. A novel solvothermal treatment with XeF_2 of the $Gd_{1-x}Tb_xOCl$ nanocrystals has also been developed to topotactically transform $Gd_{1-x}Tb_xOCl$ to $Gd_{1-x}Tb_xF_3$ nanocrystals in an attempt to stabilize the metastable hexagonal GdF_3 structure.[8] Both

$Gd_{1-x}Tb_xOCl$ and $Gd_{1-x}Tb_xF_3$ nanocrystals have been examined as potential X-ray phosphors based on X-ray excited optical luminescence measurements across the $^8S_{7/2} \rightarrow {}^8P_J$ transition of the Gd^{3+} host lattice. A remarkable modulation of luminescent intensity is detected at the giant resonant absorption corresponding to activation of a non-radiative Auger photoionization process that supplants the thermalization and activation of luminescent centers observed above and below the giant resonance absorption.

Chapter V further establishes control over the oxidation state of europium dopants incorporated within LaOCl lattices based on the use of redox non-innocent stabilizing ligands. The inclusion of divalent europium is further accompanied by stabilization of chloride vacancies in the lattice. Optical and X-ray excitation of divalent and trivalent europium dopants are contrasted, further expanding the palette of available X-ray phosphors.[9]

Having obtained RGB X-ray induced luminescence through incorporation of Eu^{3+}, Tb^{3+}, and Eu^{2+} dopants, the incorporation of multiple luminescent centers and sensitization mechanisms are examined in Chapter VI. Specifically, the coupling of Tb^{3+} with either Eu^{3+} or Eu^{2+} within a LaOCl host matrix, yields color tunability across the visible spectrum. The energy transfer processes and sensitization mechanisms that occur between the doped luminescent ions have been examined via optical and X-ray excited luminescence, which show starkly distinct mechanisms and sensitization efficiencies.

I.9 References

(1) Navrotsky, A. Nanoscale Effects on Thermodynamics and Phase Equilibria in Oxide Systems. *ChemPhysChem* **2011**, *12*, 2207–2215.

(2) Waitz, T.; Tsuchiya, K.; Antretter, T.; Fischer, F. D. Phase Transformations of

Nanocrystalline Martensitic Materials. *MRS Bull.* **2009**, *34*, 814–821.

(3) Waetzig, G. R.; Depner, S. W.; Asayesh-Ardakani, H.; Cultrara, N. D.; Shahbazian-Yassar, R.; Banerjee, S. Stabilizing Metastable Tetragonal HfO_2 Using a Non-Hydrolytic Solution-Phase Route: Ligand Exchange as a Means of Controlling Particle Size. *Chem. Sci.* **2016**, *7*, 4930–4939.

(4) Clearfield, A. Structural Aspects of Zirconium Chemistry. *Rev. Pure Appl. Chem.* **1964**, *14* (3), 91–108.

(5) Grünwald, M.; Lutker, K.; Alivisatos, A. P.; Rabani, E.; Geissler, P. L. Metastability in Pressure-Induced Structural Transformations of CdSe/ZnS Core/shell Nanocrystals. *Nano Lett.* **2013**, *13* (4), 1367–1372.

(6) Tolbert, S. H.; Alivisatos, a P. Size Dependence of a First Order Solid-Solid Phase Transition: The Wurtzite to Rock Salt Transformation in CdSe Nanocrystals. *Science* **1994**, *265* (5170), 373–376.

(7) Waetzig, G. R.; Cho, J.; Lacroix, M.; Banerjee, S. Building on Sub-Arctic Soil: Geopolymerization of Muskeg to a Densified Load-Bearing Composite. *Sci. Rep.* **2017**, *7* (1), 14711.

(8) Waetzig, G. R.; Horrocks, G. A.; Jude, J. W.; Zuin, L.; Banerjee, S. X-Ray Excited Photoluminescence near the Giant Resonance in Solid-Solution $Gd_{1-x}Tb_xOCl$ Nanocrystals and Their Retention upon Solvothermal Topotactic Transformation to $Gd_{1-x}Tb_xF_3$. *Nanoscale* **2016**, *8* (2), 979–986.

(9) Waetzig, G. R.; Horrocks, G. A.; Jude, J. W.; Villalpando, G. V.; Zuin, L.; Banerjee, S. Ligand-Mediated Control of Dopant Oxidation State and X-Ray Excited Optical Luminescence in Eu-Doped LaOCl. *under review.* **2018**.

(10) Liu, H.; Strobridge, F. C.; Borkiewicz, O. J.; Wiaderek, K. M.; Chapman, K. W.; Chupas, P. J.; Grey, C. P. Capturing Metastable Structures during High-Rate Cycling of $LiFePO_4$ Nanoparticle Electrodes. *Science.* **2014**, *344* (6191), 1252817.

(11) Sun, W.; Dacek, S. T.; Ong, S. P.; Hautier, G.; Jain, A.; Richards, W. D.; Gamst, A. C.; Persson, K. A.; Ceder, G. The Thermodynamic Scale of Inorganic Crystalline Metastability. *Sci. Adv.* **2016**, *2* (11), e1600225.

(12) Batra, R.; Huan, T. D.; Ramprasad, R. Stabilization of Metastable Phases in Hafnia Owing to Surface Energy Effects. *Appl. Phys. Lett.* **2016**, *108* (November), 172902.

(13) Luo, X.; Demkov, A. A. Structure, Thermodynamics, and Crystallization of Amorphous Hafnia. *J. Appl. Phys.* **2015**, *118*, 124105.

(14) Zhao, X.; Vanderbilt, D. First-Principles Study of Structural, Vibrational, and Lattice Dielectric Properties of Hafnium Oxide. *Phys. Rev. B* **2002**, *65*, 233106.

(15) Tang, J.; Fabbri, J.; Robinson, R. D.; Zhu, Y.; Herman, I. P.; Steigerwald, M. L.; Brus, L. E. Solid-Solution Nanoparticles: Use of a Nonhydrolytic Sol-Gel Synthesis To Prepare HfO_2 and $Hf_xZr_{1-x}O_2$ Nanocrystals. *Chem. Mater.* **2004**, *16*, 1336–1342.

(16) Depner, S. W.; Kort, K. R.; Banerjee, S. Precursor Control of Crystal Structure and Stoichiometry in Twin Metal Oxide Nanocrystals. *Cryst. Eng. Commun.* **2009**, *11*, 841–846.

(17) Bajaj, S.; Haverty, M. G.; Arróyave, R.; Goddard III FRSC, W. A.; Shankar, S. Phase Stability in Nanoscale Material Systems: Extension from Bulk Phase Diagrams. *Nanoscale* **2015**, *7* (21), 9868–9877.

(18) Garvie, R. C. The Occurrence of Metastable Tetragonal Zirconia as a Crystallite Size Effect. *J. Phys. Chem.* **1965**, *69* (4), 1238–1243.

(19) Hf-O Binary Phase Diagram 0-80 At.% O: Datasheet from "PAULING FILE Multinaries Edition – 2012" in SpringerMaterials (Http://materials.springer.com/isp/phase-diagram/docs/c_0901278).

(20) Joo, J.; Yu, T.; Kim, Y. W.; Park, H. M.; Wu, F.; Zhang, J. Z.; Hyeon, T. Multigram Scale Synthesis and Characterization of Monodisperse Tetragonal Zirconia Nanocrystals. *J. Am. Chem. Soc.* **2003**, *125*, 6553–6557.

(21) Shukla, S.; Seal, S. Mechanisms of Room Temperature Metastable Tetragonal Phase Stabilisation in Zirconia. *Int. Mater. Rev.* **2005**, *50* (1), 45–64.

(22) Trolliard, G.; Mercurio, D.; Perez-Mato, J. M. Martensitic Phase Transition in Pure Zirconia: A Crystal Chemistry Viewpoint. *Zeitschrift fur Krist.* **2011**, *226* (3), 264–290.

(23) Zhou, W.; Ushakov, S. V.; Wang, T.; Ekerdt, J. G.; Demkov, A. A.; Navrotsky, A. Hafnia: Energetics of Thin Films and Nanoparticles. *J. Appl. Phys.* **2010**, *107*, 123514.

(24) Depner, S. W.; Cultrara, N. D.; Farley, K. E.; Qin, Y.; Banerjee, S. Ferroelastic Domain Organization and Precursor Control of Size in Solution-Grown Hafnium Dioxide Nanorods. *ACS Nano* **2014**, *8* (5), 4678–4688.

(25) Müller, J.; Böscke, T. S.; Schröder, U.; Mueller, S.; Bräuhaus, D.; Böttger, U.; Frey, L.; Mikolajick, T. Ferroelectricity in Simple Binary ZrO2and HfO2. *Nano Lett.* **2012**, *12* (8), 4318–4323.

(26) MacLaren, I.; Ras, T.; MacKenzie, M.; Craven, A. J.; McComb, D. W.; De Gendt, S. Texture, Twinning and Metastable "Tetragonal" Phase in Ultrathin Films of HfO_2 on a Si Substrate. *J. Electrochem. Soc.* **2009**, *156* (April), G103–G108.

(27) Boysen, H.; Frey, F.; Vogt, T. Neutron Powder Investigation of the Tetragonal to Monoclinic Phase Transformation in Undoped Zirconia. *Acta Crystallogr. Sect. B* **1991**,

47 (6), 881–886.

(28) Garvie, R. C. Stabilization of the Tetragonal Structure in Zirconia Microcrystals. *J. Phys. Chem.* **1978**, *82* (2), 218–224.

(29) Tang, J.; Zhang, F.; Zoogman, P.; Fabbri, J.; Chan, S.-W.; Zhu, Y.; Brus, L. E.; Steigerwald, M. L. Martensitic Phase Transformation of Isolated HfO_2, ZrO_2, and $Hf_xZr_{1-x}O_2$ ($0 < x < 1$) Nanocrystals. *Adv. Funct. Mater.* **2005**, *15*, 1595–1602.

(30) Wolten, G. M. Diffusionless Phase Transformations in Zirconia and Hafnia. *J. Am. Ceram. Soc.* **1963**, *46* (9), 418–422.

(31) Iskandarova, I. M.; Knizhnik, A. A.; Rykova, E. A.; Bagatur'yants, A. A.; Potapkin, B. V.; Korkin, A. A. First-Principle Investigation of the Hydroxylation of Zirconia and Hafnia Surfaces. *Microelectron. Eng.* **2003**, *69*, 587–593.

(32) Wang, J.; Li, H. P.; Stevens, R. Hafnia and Hafnia-Toughened Ceramics. *J. Mater. Sci.* **1992**, *27* (20), 5397–5430.

(33) Garvie, R. C.; Hannink, R. H.; Pascoe, R. T. Ceramic Steel? *Nature* **1975**, *258* (5537), 703–704.

(34) Nicoloso, N.; Liibert, A.; Leibold, B. Optical Absorption Studies of Tetragonal Yttria-Stabilized Zirconia. *Sensors Actuators B* **1992**, *8*, 253–256.

(35) Virbukas, D.; Laukaitis, G.; Dudonis, J.; Milčius, D. The Properties of Scandium and Cerium Stabilized Zirconium Thin Films Formed by E-Beam Technique. *Solid State Ionics* **2011**, *188* (1), 46–49.

(36) Rauwel, P.; Rauwel, E.; Persson, C.; Sunding, M. F.; Galeckas, A. One Step Synthesis of Pure Cubic and Monoclinic HfO_2 Nanoparticles: Correlating the Structure to the Electronic Properties of the Two Polymorphs. *J. Appl. Phys.* **2012**, *112* (10), 1–9.

(37) Zhou, B.; Shi, H.; Zhang, X. D.; Su, Q.; Jiang, Z. Y. The Simulated Vibrational Spectra of HfO_2 Polymorphs. *J. Phys. D. Appl. Phys.* **2014**, *47* (11), 115502.

(38) Batra, R.; Huan, T. D.; Rossetti, G. A.; Ramprasad, R. Dopants Promoting Ferroelectricity in Hafnia: Insights from a Comprehensive Chemical Space Exploration. *Chem. Mater.* **2017**, *29* (21), 9102–9109.

(39) Hudak, B. M.; Depner, S. W.; Waetzig, G. R.; Talapatra, A.; Arroyave, R.; Banerjee, S.; Guiton, B. S. Real-Time Atomistic Observation of Structural Phase Transformations in Individual Hafnia Nanorods. *Nat. Commun.* **2017**, *8* (May), 15316.

(40) Perevalov, T. V.; Gritsenko, V. A.; Erenburg, S. B.; Badalyan, A. M.; Wong, H.; Kim, C. W. Atomic and Electronic Structure of Amorphous and Crystalline Hafnium Oxide: X-Ray Photoelectron Spectroscopy and Density Functional Calculations. *J. Appl. Phys.* **2007**, *101* (5), 53704.

(41) Humbeeck, J. Van. Shape Memory Alloys: AMaterial and a Technology. *Adv. Eng. Mater.* **2001**, No. 11, 837–850.

(42) Wang, L. G.; Xiong, Y.; Xiao, W.; Cheng, L.; Du, J.; Tu, H.; Van De Walle, A. Computational Investigation of the Phase Stability and the Electronic Properties for Gd-Doped HfO_2. *Appl. Phys. Lett.* **2014**, *104* (20), 201903.

(43) Zhao, X.; Vanderbilt, D. Phonons and Lattice Dielectric Properties of Zirconia. *Phys. Rev. B* **2002**, *65*, 75105.

(44) Guan, S. H.; Zhang, X. J.; Liu, Z. P. Energy Landscape of Zirconia Phase Transitions. *J. Am. Chem. Soc.* **2015**, *137* (25), 8010–8013.

(45) Vioux, A. Nonhydrolytic Sol-Gel Routes to Oxides. *Chem. Mater.* **1997**, *9*, 2292–2299.

(46) Kort, K. R.; Banerjee, S. Ligand-Mediated Control of Dislocation Dynamics and

Resulting Particle Morphology of GdOCl Nanocrystals. *Small* **2015**, *11* (3), 329-334.

(47) Kort, K. R.; Banerjee, S. Shape-Controlled Synthesis of Well-Defined Matlockite LnOCl (Ln: La, Ce, Gd, Dy) Nanocrystals by a Novel Non-Hydrolytic Approach. *Inorg. Chem.* **2011**, *50*, 5539-5544.

(48) De Keukeleere, K.; Coucke, S.; De Canck, E.; Van Der Voort, P.; Delpech, F.; Coppel, Y.; Hens, Z.; Van Driessche, I.; Owen, J. S.; De Roo, J. Stabilization of Colloidal Ti, Zr, and Hf Oxide Nanocrystals by Protonated Tri-N-Octylphosphine Oxide (TOPO) and Its Decomposition Products. *Chem. Mater.* **2017**, *29* (23), 10233–10242.

(49) Moser, J.; Punchihewa, S.; Infelta, P. P.; Grätzel, M. Surface Complexation of Colloidal Semiconductors Strongly Enhances Interfacial Electron-Transfer Rates. *Langmuir* **1991**, *7* (12), 3012–3018.

(50) Trentler, T. J.; Denler, T. E.; Bertone, J. F.; Agrawal, A.; Colvin, V. L. Synthesis of TiO_2 Nanocrystals by Nonhydrolytic Solution-Based Reactions. *J. Am. Chem. Soc.* **1999**, *121* (7), 1613–1614.

(51) Mutin, P. H.; Vioux, A. Recent Advances in the Synthesis of Inorganic Materials via Non-Hydrolytic Condensation and Related Lowtemperature Routes. *J. Mater. Chem. A* **2013**, *1*, 11504–11512.

(52) Pitcher, M. W.; Ushakov, S. V.; Navrotsky, A.; Woodfield, B. F.; Li, G.; Boerio-goates, J.; Tissue, B. M. Energy Crossovers in Nanocrystalline Zirconia. *J. Am. Ceram. Soc.* **2005**, *88* (1), 160–167.

(53) Chevalier, J.; Gremillard, L.; Virkar, A. V.; Clarke, D. R. The Tetragonal-Monoclinic Transformation in Zirconia: Lessons Learned and Future Trends. *J. Am. Ceram. Soc.* **2009**, *92* (9), 1901–1920.

(54) Lange, F. F. Transformation Toughening. *J. Mater. Sci.* **1982**, *17*, 225–234.

(55) De Almeida, A.; Santos, B.; Paolo, B.; Quicheron, M. Solid State Lighting Review - Potential and Challenges in Europe. *Renew. Sustain. Energy Rev.* **2014**, *34*, 30–48.

(56) Krames, M. R.; Shchekin, O. B.; Mueller-Mach, R.; Mueller, G. O.; Zhou, L.; Harbers, G.; Craford, M. G. Status and Future of High-Power Light-Emitting Diodes for Solid-State Lighting. *J. Disp. Technol.* **2007**, *3* (2), 160–175.

(57) Phillips, J. M.; Coltrin, M. E.; Crawford, M. H.; Fischer, A. J.; Krames, M. R.; Mueller-Mach, R.; Mueller, G. O.; Ohno, Y.; Rohwer, L. E. S.; Simmons, J. A.; Tsao, J. Y. Research Challenges to Ultra-Efficient Inorganic Solid-State Lighting. *Laser Photonics Rev.* **2007**, *1* (4), 307–333.

(58) Thejokalyani, N.; Dhoble, S. J. Novel Approaches for Energy Efficient Solid State Lighting by RGB Organic Light Emitting Diodes - A Review. *Renew. Sustain. Energy Rev.* **2014**, *32*, 448–467.

(59) Li, D.; Cheng, R.; Zhou, H.; Wang, C.; Yin, A.; Chen, Y.; Weiss, N. O.; Huang, Y.; Duan, X. Electric-Field-Induced Strong Enhancement of Electroluminescence in Multilayer Molybdenum Disulfide. *Nat. Commun.* **2015**, *6* (May), 7509.

(60) Zhang, L.; Yang, X.; Jiang, Q.; Wang, P.; Yin, Z.; Zhang, X.; Tan, H.; Yang, Y. M.; Wei, M.; Sutherland, B. R.; Sargent, E. H.; You, J. Ultra-Bright and Highly Efficient Inorganic Based Perovskite Light-Emitting Diodes. *Nat. Commun.* **2017**, *8*, 15640.

(61) Marquardt, C. W.; Grunder, S.; Błaszczyk, A.; Dehm, S.; Hennrich, F.; Löhneysen, H. V.; Mayor, M.; Krupke, R. Electroluminescence from a Single Nanotube-Molecule-Nanotube Junction. *Nat. Nanotechnol.* **2010**, *5* (12), 863–867.

(62) Nakamura, S.; Mukai, T.; Senoh, M. Candela-Class High-Brightness InGaN/AlGaN

Double-Heterostructure Blue-Light-Emitting Diodes. *Appl. Phys. Lett.* **1994**, *64* (13), 1687–1689.

(63) Hermus, M.; Phan, P. C.; Duke, A. C.; Brgoch, J. Tunable Optical Properties and Increased Thermal Quenching in the Blue-Emitting Phosphor Series: $Ba_2(Y_{1-x}Lu_x)_5B_5O_{17}:Ce^{3+}$(x = 0-1). *Chem. Mater.* **2017**, *29* (12), 5267–5275.

(64) George, N. C.; Brgoch, J.; Pell, A. J.; Cozzan, C.; Jaffe, A.; Dantelle, G.; Llobet, A.; Pintacuda, G.; Seshadri, R.; Chmelka, B. F. Correlating Local Compositions and Structures with the Macroscopic Optical Properties of Ce^{3+}-Doped $CaSc_2O_4$, an Efficient Green-Emitting Phosphor. *Chem. Mater.* **2017**, *29* (8), 3538–3546.

(65) Pokhrel, M.; Alcoutlabi, M.; Mao, Y. Optical and X-Ray Induced Luminescence from Eu^{3+} Doped La_2ZrO_7 Nanoparticles. *J. Alloys Compd.* **2017**, *693*, 719–729.

(66) Büchele, P.; Richter, M.; Tedde, S. F.; Matt, G. J.; Ankah, G. N.; Fischer, R.; Biele, M.; Metzger, W.; Lilliu, S.; Bikondoa, O.; Macdonald, J. E.; Brabec, C. J.; Kraus, T.; Lemmer, U.; Schmidt, O. X-Ray Imaging with Scintillator-Sensitized Hybrid Organic Photodetectors. *Nat. Photonics* **2015**, *9* (12), 843–848.

(67) Issler, S. L.; Torardi, C. C. Solid State Chemistry and Luminescence of X-Ray Phosphors. *J. Alloys Compd.* **1995**, *229* (1), 54–65.

(68) Amemiya, Y.; Miyahara, J. Imaging Plate Illuminates Many Fields. *Nature* **1988**, *336* (6194), 89–90.

(69) Jüstel, T.; Nikol, H.; Ronda, C. New Developments in the Field of Luminescent Materials for Lighting and Displays. *Angew. Chemie - Int. Ed.* **1998**, *37* (22), 3084–3103.

(70) Blasse, G.; Grabmaier, B. C. *Luminescent Materials*; Springer-Verlag Berlin Heidelberg, **1994**.

(71) Shrestha, S.; Fischer, R.; Matt, G. J.; Feldner, P.; Michel, T.; Osvet, A.; Levchuk, I.; Merle, B.; Golkar, S.; Chen, H.; Tedde, S. F.; Schmidt, O.; Hock, R.; Rührig, M.; Göken, M.; Heiss, W.; Anton, G.; Brabec, C. J. High-Performance Direct Conversion X-Ray Detectors Based on Sintered Hybrid Lead Triiodide Perovskite Wafers. *Nat. Photonics* **2017**, *11* (7), 436–440.

(72) Wei, H.; Fang, Y.; Mulligan, P.; Chuirazzi, W.; Fang, H. H.; Wang, C.; Ecker, B. R.; Gao, Y.; Loi, M. A.; Cao, L.; Huang, J. Sensitive X-Ray Detectors Made of Methylammonium Lead Tribromide Perovskite Single Crystals. *Nat. Photonics* **2016**, *10* (5), 333–339.

(73) Rabatin, J. X-Ray Image Converters Utilizing Lanthanum and Gadolinium Oxyhalide Luminous Materials Activated with Thulium, **1974**.

(74) Kim, D.; Jang, J.; Ahn, S. Il; Kim, S.-H.; Park, J.-C. Novel Blue-Emitting Eu^{2+}-Activated LaOCl:Eu Materials. *J. Mater. Chem. C* **2014**, *2* (15), 2799.

(75) Kawano, N.; Koshimizu, M.; Okada, G.; Fujimoto, Y.; Kawaguchi, N.; Yanagida, T.; Asai, K. Scintillating Organic-Inorganic Layered Perovskite-Type Compounds and the Gamma-Ray Detection Capabilities. *Sci. Rep.* **2017**, *7* (1), 14754.

(76) Holsa, J.; Sailynoja, E.; Lamminmaki, R.-J.; Deren, P.; Strek, W.; Porcher, P. Crystal Field Energy Level Scheme of Er^{3+} in GdOCl. *J. Chem. Soc. Faraday Trans.* **1997**, *93* (13), 2241–2246.

(77) Garcia, E.; Corbett, J. D.; Ford, J. E.; Vary, W. J. Low-Temperature Routes to New Structures for Yttrium, Holmium, Erbium, and Thulium Oxychlorides. *Inorg. Chem.* **1985**, *24*, 494–498.

(78) Odink, D. A.; Song, K.; Kauzlarich, S. M. Intercalation of Pyridine into the Layered SmSI Structure of YbOCl. *Chem. Mater.* **1992**, *4*, 906–911.

(79) Song, K.; Kauzlarich, S. M. New Intercalation Compounds of Layered Lanthanide Oxychlorides LnOCl (Ln = Ho, Er, Tm, and Yb) with Pyridine and Substituted Pyridines. *Chem. Mater.* **1994**, *6*, 386–394.

(80) Rambabu, U.; Annapurna, K.; Balaji, T.; Buddhudu, S. Fluorescence Spectra of Er^{3+}-REOCl (Re = La, Gd, Y) Powder Phosphors. *Mater. Lett.* **1995**, *23*, 143–146.

(81) Hölsä, J.; Lamminmäki, R. J.; Lastusaari, M.; Porcher, P. Simulation of the Gd^{3+} Energy Level Scheme in GdOCl. In *Journal of Alloys and Compounds*; **2001**, *323-324*, 811-815.

(82) Konishi, T.; Shimizu, M.; Kameyama, Y.; Soga, K. Fabrication of Upconversion Emissive LaOCl Phosphors Doped with Rare-Earth Ions for Bioimaging Probes. In *Journal of Materials Science: Materials in Electronics*; **2007**, *18*, S183-S186.

(83) Kong, Q.; Wang, J.; Dong, X.; Yu, W.; Liu, G. Synthesis and Luminescence Properties of Terbium-Doped Lanthanum Oxychloride Nanostructures. *J. Nanosci. Nanotechnol.* **2015**, *15*, 4304–4315.

(84) Imanaka, N.; Okamoto, K.; Adachi, G. Y. Water-Insoluble Lanthanum Oxychloride-Based Solid Electrolytes with Ultra-High Chloride Ion Conductivity. *Angew. Chemie - Int. Ed.* **2002**, *41*, 3890-3892.

(85) Li, G.; Hou, Z.; Peng, C.; Wang, W.; Cheng, Z.; Li, C.; Lian, H.; Lin, J. Electrospinning Derived One-Dimensional LaOCl: Ln^{3+} (Ln = Eu/Sm, Tb, Tm) Nanofibers, Nanotubes and Microbelts with Multicolor-Tunable Emission Properties. *Adv. Funct. Mater.* **2010**, *20* (20), 3446–3456.

(86) Talbot, J. B. Electrophoretic Deposition of Phosphors for Information Displays and Solid State Lighting. In *Electrophoretic Deposition of Nanomaterials*; Dickerson, J. H., Boccaccini, A. R., Eds.; Springer New York: New York, NY, **2012**; pp 267–294.

(87) Depner, S. W.; Kort, K. R.; Jaye, C.; Fischer, D. A.; Banerjee, S. Nonhydrolytic Synthesis and Electronic Structure of Ligand-Capped $CeO_{2-\delta}$ and CeOCl Nanocrystals. *J. Phys. Chem. C* **2009**, *113*, 14126–14134.

(88) Kort, K. R.; Banerjee, S. Oriented Electrophoretic Deposition of GdOCl Nanoplatelets. *J. Phys. Chem. B* **2013**, *117*, 1585–1591.

(89) Steigerwald, M. L.; Alivisatos, A. P.; Gibson, J. M.; Harris, T. D.; Kortan, R.; Muller, A. J.; Thayer, A. M.; Duncan, T. M.; Douglass, D. C.; Brus, L. E. Surface Derivatization and Isolation of Semiconductor Cluster Molecules. *J. Am. Chem. Soc.* **1988**, *110* (10), 3046–3050.

(90) Ovtar, S.; Lisjak, D.; Drofenik, M. Preparation of Oriented Barium Hexaferrite Films by Electrophoretic Deposition. *J. Am. Ceram. Soc.* **2011**, *94* (10), 3373–3379.

(91) Sugimoto, W.; Terabayashi, O.; Murakami, Y.; Takasu, Y. Electrophoretic Deposition of Negatively Charged Tetratitanate Nanosheets and Transformation into Preferentially Oriented TiO_2(B) Film. *J. Mater. Chem.* **2002**, *12* (12), 3814–3818.

CHAPTER II

STABLIZING METASTABLE TETRAGONAL HFO_2 USING A NON-HYDROLYTIC SOLUTION-PHASE ROUTE: LIGAND EXCHANGE AS A MEANS OF CONTROLLING PARTICLE SIZE*

II.1 Overview

There has been intense interest in stabilizing the tetragonal phase of HfO_2 since it is predicted to outperform the thermodynamically stable lower-symmetry monoclinic phase for almost every application where HfO_2 has found use by dint of his higher dielectric constant, bandgap, and hardness. However, the monoclinic phase is much more thermodynamically stable and the tetragonal phase of HfO_2 is generally accessible only at temperatures above 1720°C. Classical models comparing the competing influences of bulk free energy and specific surface energy predict that the tetragonal phase of HfO_2 ought to be stable at ultra-small dimensions below 4 nm; however, these size regimes have been difficult to access in the absence of synthetic methods that yield well-defined and monodisperse nanocrystals with precise control over size. In this chapter, we have developed a modified non-hydrolytic condensation method to precisely control the size of HfO_2 nanocrystals with low concentrations of dopants by suppressing the kinetics of particle growth by cross-condensation with less-reactive precursors. This synthetic method enables us to stabilize tetragonal HfO_2 while evaluating ideas for critical size at which surface energy considerations surpass the bulk free energy stabilization. The phase assignment has been verified by atomic resolution high angle annular dark field images acquired for

---

* Reproduced with permission from "Stabilizing metastable tetragonal HfO_2 using a non-hydrolytic solution-phase route: ligand exchange as a means of controlling particle size." G.R. Waetzig, S. W. Depner, H. Asayesh-Ardakani, N. D. Cultrara, R. Shahbazian-Yassar, S. Banerjee, *Chemical Science*, **2016**, *7*, 4930-4939. Reproduced by permission of Royal Society of Chemistry. <http://pubs.rsc.org/en/content/articlelanding/2016/sc/c6sc01601d#!divAbstract>

individual nanocrystals.

II.2 Introduction

A particularly powerful aspect of nanoscience that enables much new functionality derives from the greatly altered phase equilibria obtained upon confining materials to nanoscale dimensions.[1–4] The increased contributions from surface free energy terms can outweigh bulk free energy considerations and enable the stabilization of crystalline phases under ambient conditions that can otherwise only be stabilized at high temperatures and pressures. As a few notable examples of such metastable phases and their interesting properties: a metallic 1T phase is stabilized upon exfoliating the bulk semiconducting 2H-phases of MoS_2 and WS_2 to few-layered sheets[5,6] and shows greatly improved activity as a catalyst for hydrogen evolution; a γ-MoC phase is stabilized in preference to β-Mo_2C for nanostructures of molybdenum carbide and also exhibits promising reactivity for hydrogen evolution;[7] the tetragonal phase of ZrO_2 is stabilized in preference to the monoclinic phase for particles below a critical size of *ca*. 30 nm and is used for the transformation toughening of ceramics;[8,9] and a metastable Li_xFePO_4 phase is stabilized upon electrochemically delithiating $LiFePO_4$ nanoparticles at high rates within a Li-ion battery and mitigates the need to go through a much slower nucleation and growth process that would result in phase segregation of $LiFePO_4$ and $FePO_4$.[10,11] Stabilizing metastable structures requires careful control of particle size and the kinetics of crystallization processes. Low-temperature solution-phase routes for defining structural frameworks are particularly well-suited for preparing kinetically trapped metastable structures since the energetics of these reactions are often too low to allow for coarsening of grain size or overcoming shallow valleys in the potential energy landscape.[12–15] In this chapter, we demonstrate a cross-coupling ligand exchange method

for controlling the particle size in the non-hydrolytic sol–gel condensation growth of HfO_2 nanocrystals. Precise control of the size of HfO_2 nanocrystals enables unequivocal determination of the critical size required to stabilize the tetragonal phase and provides access to well-defined crystals of this technologically important metastable structure that is otherwise stable only above *ca*. 1720°C.[16]

Tetragonal ZrO_2 has been widely accessible for several decades, even without incorporation of dopant atoms, since the critical size at which the surface free energy terms overcome bulk free energy considerations is relatively large, variously estimated to be *ca*. 15–30 nm.[8,9,17–19] In contrast, stabilization of the tetragonal phase of HfO_2 is much more challenging since: (a) the bulk free energy stabilization of the monoclinic phase over the tetragonal phase is almost 40% greater for HfO_2 as compared to ZrO_2; and (b) the volume expansion accompanying the tetragonal to monoclinic phase transition is much smaller for HfO_2 (*ca*. 2.7%) as compared to ZrO_2 (4.0%).[20,21] Estimates of the critical size required to stabilize the tetragonal phase of HfO_2 vary widely from about 2 to 10 nm but it is clear that this value is substantially smaller than the critical size for ZrO_2.[16,20,22] Several methods for the preparation of nanometer-sized particles of HfO_2 report the stabilization of at least some fraction of tetragonal HfO2; for instance, signatures of the tetragonal phase have been identified in particles obtained by the thermal decomposition of pure $Hf(OH)_4$,[16] the oxidation of metallic Hf nanocrystals,[23] and a ligand-mediated reaction at the interface of water and oil phases.[24] However, the polydispersity and relatively poor crystallinity of the particles obtained by these methods implies that the obtained samples almost always contain only minor proportions of tetragonal phases and a clear delineation of a size-dependent phase diagram has thus far not been possible. Several instances of stabilizing

tetragonal domains have also been reported for thin films of HfO_2 prepared by methods such as atomic layer deposition in a low-oxygen environment,[25] ultra-thin films deposited onto clean Si (100) surfaces by atomic layer deposition,[26] and ion-beam-assisted deposition in an oxygen deficient ambient.[27] Again, the films usually contain mixtures of multiple crystalline and amorphous phases and exhibit considerable heterogeneity in terms of the dimensions of individual domains.

The stabilization of tetragonal HfO_2 is not just an academic curiosity. Indeed, the tetragonal (space group $P4_2/nmc$) phase of HfO_2 is anticipated to outperform the thermodynamically stable lower-symmetry monoclinic phase (space group $P2_1/c$) for almost every application where HfO_2 has found use. Perhaps the most important application of HfO_2 is in gate dielectric stacks as a high-κ dielectric because of its resistance to silicidation and silicate formation and its much greater dielectric constant as compared to SiO_2.[20,28–30] First-principles calculations predict a dielectric constant of 18 for monoclinic HfO_2, which is far surpassed by the value of almost 70 predicted for tetragonal HfO_2.[31] The bandgap of the tetragonal phase is also predicted to be larger (*ca*. 6.11 eV) as compared to the monoclinic phase (5.78 eV).[32] Finally, the tetragonal phase is denser and has been experimentally found to have a higher Knoop hardness.[27] In comparison to aqueous methods, non-hydrolytic methods, often based on formation of oxo-bridges by elimination of small molecules, provide considerable control of the kinetics of condensation.[14,15,33] Such control is imperative to precisely control particle size and morphology when growing nanoparticles. In an early work, the condensation of hafnium alkoxides in benzyl alcohol with the elimination of alkyl ethers yielded monoclinic, but not tetragonal, HfO_2 nanocrystals.[34] Solvothermal processing of various hafnium alkoxides yielded varying morphologies of HfO_2 nanocrystals, again crystallized in the monoclinic phase.[35] Hyeon and co-

workers adapted the alkyl halide elimination route first proposed by Vioux for the growth of nanocrystals and were able to achieve the multigram synthesis of ZrO_2 nanocrystals as per:[17,36]

$$\equiv M - X + \equiv M - O - R \rightarrow \equiv M - O - M \equiv + R - X \quad \text{(II.1)}$$

Brus and co-workers extended this method to prepare HfO_2 and solid-solution $Hf_xZr_{1-x}O_2$ nanocrystals and established considerable control over the relative Hf : Zr concentrations.[19] In previous work, we have demonstrated that the R group of the alkoxide ligand allows for substantial tunability of the size of HfO_2 and ZrO_2 nanocrystals as well as the relative Hf : Zr ratios of $Hf_xZr_{1-x}O_2$ nanocrystals.[37,38] These studies as well as past work by Vioux have established that upon reacting $M(OR)_4$ and MX_4 species, substantial ligand exchange takes place to stabilize haloalkoxides such as $M(OR)_3Cl$, $M(OR)_2Cl_2$, and $M(OR)Cl_3$.[14,36] The first of these three species has been proposed as a catalyst that brings about transformation of an alkoxo-bridge to an oxo-bridge as per the reaction depicted in **Figure II.1.**

When two different metal precursors are reacted, the composition of the product depends on the relative condensation rates and reactivities. For metals exhibiting comparable reactivity, such as Hf and Zr, the heterocondensation reaction yields solid-solution nanocrystals and can be written as follows:[18,19]

$$m\mathrm{MX}_n + n\mathrm{M'(OR)}_m \rightarrow \mathrm{M}_m\mathrm{M'}_n\mathrm{O}_{nm} + nm\mathrm{RX} \quad \text{(II.2)}$$

However, if the rates of homo- and hetero-condensation are vastly different, the products of the faster reaction are obtained preferentially. In this chapter, we find that adding a much less reactive precursor, either $Ce(O^tBu)_4$ or $La(O^iPr)_3$, greatly modifies the concentration of the active monomer depicted in Figure II.1 and thereby retards the kinetics of the homocondensation reaction, yielding considerable control over the size of HfO_2 nanocrystals with only minimal incorporation of La and Ce. This unprecedented control of nanocrystal size allows us to explore

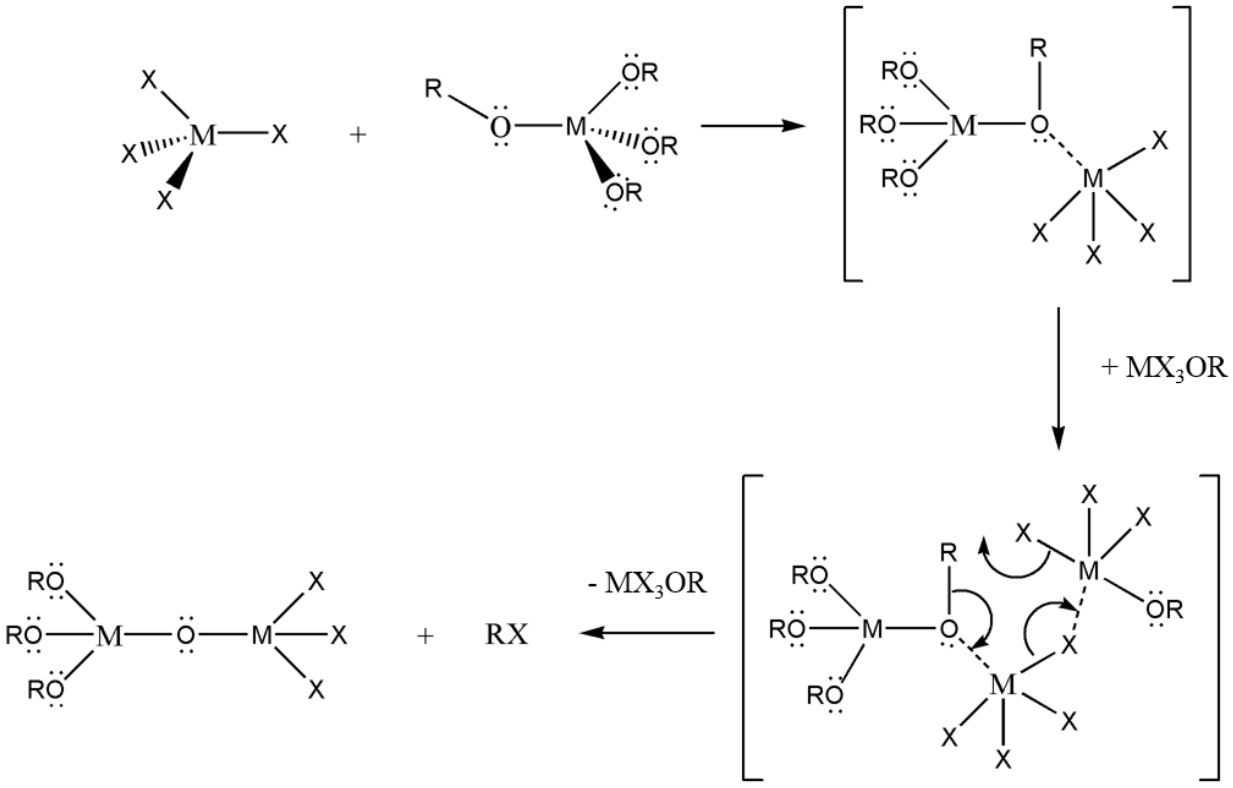

Figure II.1. Non-hydrolytic condensation of metal halide and metal alkoxide to form an alkoxo-bridge intermediate. A "catalyst", MX_3OR, initiates conversion of the alkoxo-bridge to an oxo-bridge then subsequently eliminates an alkyl halide to form the desired metal oxide-product.

ultra-small dimensions and determine the critical size for stabilizing the tetragonal phase of HfO_2.

II.3 Experimental Details

II.3.1 Synthesis

Hafnium(IV) chloride, cerium(III) chloride, lanthanum(III) chloride, lanthanum(III) iso-propoxide, and tri-*n*-octylphosphineoxide (TOPO) were purchased from Strem and used without any further purification. Hafnium(IV) *tert*-butoxide was purchased from Alfa Aesar and used as received. Cerium(IV) *tert*-butoxide was purchased from Gelest and used without further

purification. To synthesize the metal oxide nanocrystals, a metal halide and metal alkoxide are mixed in equimolar amounts with *ca*. 10 g of TOPO in a three-neck round bottom flask under an Ar ambient within a glovebox. The total concentration of metal precursors is maintained at 4 mmol in all of the reactions. In all of the reactions, 2 mmol of $HfCl_4$ is used as the chloride precursor, whereas the alkoxide precursor is *x* mmol of $La(O^iPr)_3$ or $Ce(O^tBu)_4$ and 4 - *x* mmol of $Hf(O^tBu)_4$. CeO_2 nanocrystals were obtained by the reaction of equimolar amounts of $CeCl_3$ and $Ce(O^tBu)_4$ as reported in our previous work.[39] Reducing the amount of the chloride precursor below equimolar amounts solely yields amorphous products as discussed in further detail below.

Briefly, the reaction mixture is heated under an argon ambient on a Schlenk line to *ca*. 60°C, until the TOPO is melted at which point stirring is initiated. Subsequently, the reaction mixture is heated to 340°C and kept at this temperature for 2 h. Next, the reaction mixture is cooled to *ca*. 60°C and solvent/ non-solvent washing is performed alternating acetone and hexanes to remove excess TOPO.

II.3.2 Characterization

A Rigaku Ultima IV diffractometer with a graphite monochromator and a Bruker-AXS D8 Advanced Bragg–Brentano X-ray powder diffractometer, both using Cu Kα radiation (λ = 1.5418 Å), were used for characterization of the samples by powder X-ray diffraction. The crystallinity and size distribution of the nanocrystals was evaluated by high-resolution transmission electron microscopy (HRTEM) using JEOL-2010 and FEI Tecnai G2 F20 ST electron microscopes at an operating voltage of 200 kV. Samples for HRTEM analysis were dispersed in hexanes, drop-cast onto 400-mesh carbon-coated copper grids, and allowed to dry in air. The stoichiometry of the nanocrystals was determined by X-ray fluorescence (XRF) measurements, conducted by Oneida Research Services, Inc. in Whitesboro, NY, by inductively

coupled plasma-mass spectrometry (ICP-MS) using a Perkin Elmer DRCII instrument, and by energy dispersive X-ray spectroscopy (EDX) on a JEOL JSM- 7500F field emission scanning electron microscope (FE-SEM) operated at an accelerating voltage of 20 kV. Samples for ICP-MS analysis were prepared by acid digestion in an aqueous solution of 67% metals grade HNO_3. Further characterization was performed using atomic resolution high-angle annular dark-field (HAADF) imaging. A probe-corrected JEOL JEM-ARM200CF instrument equipped with a cold field-emission gun operated at 200 kV was used with a convergence angle of 22 mrad. The HAADF inner detector angle was 90 mrad.

II.4 Results

Figure II.2 displays XRD patterns for nanocrystals obtained by the reaction of $HfCl_4$ with varying proportions of $Hf(O^tBu)_4$ and $Ce(O^tBu)_4$. **Table II.1** lists the actual Hf and Ce atomic concentrations obtained for the different precursor ratios as well as the primary phase identified from analysis of powder XRD patterns. Energy dispersive X-ray spectroscopy (EDX) was also performed on the $Hf_{1-x}Ce_xO2$ nanocrystals and provides good agreement with the hafnium and cerium concentrations derived by elemental analysis (Figure A.1 and Table A.1). Decreasing the concentration of $HfCl_4$ below 2 mmol results in the formation of entirely amorphous aggregates and thus Hf : Ce concentrations with excess cerium in the reaction mixture are not further discussed. Lower alkoxide concentrations further yield amorphous products. HfO_2 nanocrystals prepared by the reaction of $Hf(O^tBu)_4$ and $HfCl_4$ are clearly monoclinic ($P2_1/c$) as delineated by the appearance of sharp (200) and (220) reflections (Joint Committee on Powder Diffraction Standards (JCPDS) 78-0050) indexed in Figure II-2A.[37,38] In

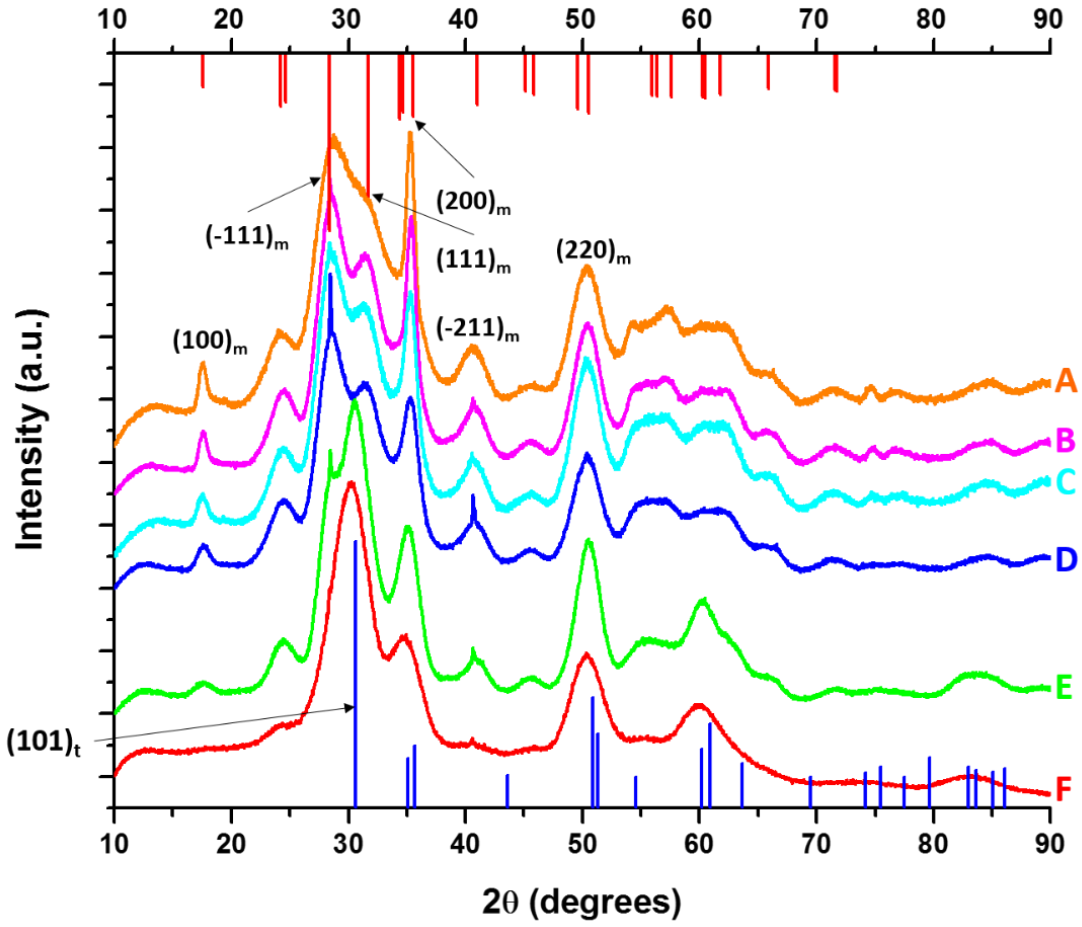

Figure II.2. X-ray diffraction patterns of end-member pure HfO_2 (A) compared to $Hf_{1-x}Ce_xO2$ nanocrystals prepared by the reaction of $HfCl_4$ with varying proportions of $Hf(O^tBu)_4$ and $Ce(O^tBu)_4$. The patterns correspond to detected (and precursor) relative Hf concentrations. The precursors are listed in Table 1. (A) 100% (100%), (B) 99.87% (90%), (C) 99.87% (80%), (D) 99.68% (70%), (E) 99.36% (60%) and (F) 97.64% (50%). Vertical bars indicate positions and relative intensities of reflections expected from JCPDS patterns. Reflections of monoclinic HfO_2 are indicated in red (JCPDS # 78-0050) and tetragonal HfO_2 in blue (XRD pattern simulated as described in the text)

contrast, CeO_2 nanocrystals crystallize in a cubic fluorite structure (Fm-3m) with reflections that can be indexed to JCPDS# 34-0394 (Figure A.2). As the concentration of Hf is decreased, or in other words, the relative ratio of $Ce(O^tBu)_4$ to $Hf(O^tBu)_4$ is increased, the reflections are broadened indicating a pronounced diminution in size even though elemental analysis data

Table II.1. Relative amounts of precursors used in the synthesis of HfO_2 nanocrystals, the atomic percentage of Hf as a function of the total metal content, the detected relative Hf and Ce concentrations, the length of the nanorods determined from statistical analysis of TEM data (the width is invariant at *ca*. 2.5 nm), and the predominant phase determined by powder X-ray diffraction.

$HfCl_4$ [mmols]	$Hf(O\text{-}^tBut)_4$ [mmols]	$Ce(O\text{-}^tBut)_4$ [mmols]	Precursor Hf Concentration [Relative at.%]	Detected Hf Concentration [Relative at.%]	Detected Ce Concentration [Relative at.%]	Length of nanocrystals [nm]	Phase of nanocrystals
2.0	2	0	100	100.00	0	12.9 ± 1.8	Monoclinic
2.0	1.6	0.4	90	99.87	0.13	9.5 ± 2.2	Monoclinic
2.0	1.2	0.8	80	99.87	0.13	7.8 ± 1.9	Monoclinic
2.0	0.8	1.2	70	99.68	0.32	5.9 ± 1.0	Monoclinic
2.0	0.4	1.6	60	99.36	0.64	4.4 ± 0.7	Monoclinic/Tetragonal
2.0	0	2	50	97.64	2.36	3.1 ± 0.4	Tetragonal
0	0	4	0	0	100	1.5 ± 0.5	Cubic

presented in Table II.1 suggests very little Ce incorporation. In contrast to the rest of the series, reaction between 2 mmol of $HfCl_4$ and 2 mmol of $Ce(O^tBu)_4$ preponderantly yields the tetragonal phase of HfO_2 characterized by a pronounced (101) reflection centered at $2\theta = 30.3°$ (Figure II.2F). The simulated pattern of tetragonal HfO_2 has been generated using coordinates for a relaxed structure of this phase calculated by Perevalov and co-workers and is depicted in blue in Figure II.2 (a complete structure solution is thus far absent for this phase).[40] Table A.2 lists the atomic coordinates, lattice constants, and angles of the monoclinic and tetragonal phases of HfO_2 with the latter set of data being derived from the calculation noted above. Careful examination of Figure II.2E, the XRD pattern for the sample prepared with 1.6 mmol of $Ce(O^tBu)_4$, indicates the appearance of a reflection at $2\theta = 31°$ that can be attributed to the (101) reflection of the tetragonal phase and suggests that this set of precursors yields a mixture of tetragonal and monoclinic phases. A reflection at $2\theta =$ *ca*. 41° in Figure II.2E suggests trace amounts of the monoclinic phase although the tetragonal phase is clearly vastly preponderant.

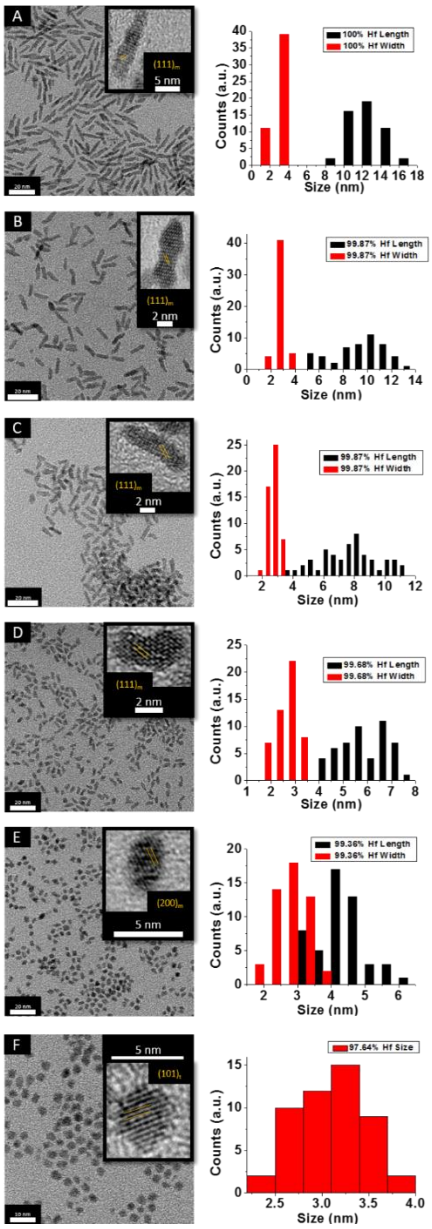

Figure II.3. Low-magnification transmission electron microscopy images of HfO_2 (A) nanocrystals compared to nanocrystals prepared by the reaction of $HfCl_4$ with varying proportions of $Hf(O^tBu)_4$ and $Ce(O^tBu)_4$. The precursors and calculated dimensions are listed in Table 1. The detected (and precursor) relative Hf concentrations of (A) 100% (100%), (B) 99.87% (90%), (C) 99.87% (80%), (D) 99.68% (70%), (E) 99.36% (60%), and (F) 97.64% (50%). Insets show HRTEM images. The lattice-resolved images indicate separations between the (111) and (200) lattice planes of the monoclinic phase in the insets to (A) to (E). The separation between the (101) lattice planes of the tetragonal phase is indicated in the inset to (F). The accompanying size distribution histograms are shown to the right of each sample illustrating that the length of the nanorods decreases with increasing concentration of $Ce(O^tBu)_4$ in the synthesis, whereas the width remains relatively constant.

Figure II.3 indicates HRTEM images and size distribution histograms for these nanocrystals. Table II.1 lists the dimensions determined by statistical analysis of at least 50 nanocrystals. With increasing concentration of $Ce(O^tBu)_4$ in the reaction mixture, the morphology of the obtained nanostructures evolves from elongated nanorods to quasi-spherical particles. The nanorods preferentially grow along the [100] direction of monoclinic HfO_2.[38] As also suggested by the powder XRD data of Figure II.2, the lengths of the $Hf_{1-x}Ce_xO_2$ nanorods are monotonically diminished with reduced concentration of $Hf(O^tBu)_4$ with respect to $Ce(O^tBu)_4$. The average length is decreased from 12.9 ± 1.8 nm for monoclinic nanocrystals grown using only $Hf(O^tBu)_4$ to 3.1 ± 0.4 nm for tetragonal nanocrystals grown using $Ce(O^tBu)_4$ as the only alkoxide precursor. The widths of the $Hf_{1-x}Ce_xO_2$ nanocrystals are not substantially altered and remain around 2.5 ± 0.4 nm. The lattice-resolved HRTEM image in Figure II.3F clearly indicates a lattice separation of 0.292 nm corresponding to the predicted separation between the (101) planes of tetragonal HfO_2 (Table A.2),[40] corroborating the stabilization of this metastable phase under these conditions.

To verify the phase assignment of $Hf_{1-x}Ce_xO_2$ as being tetragonal, atomic-resolution HAADF scanning transmission electron microscopy (STEM) imaging has been performed using an aberration corrected microscope. **Figure II.4** indicates HAADF STEM images and fast Fourier transforms (FFT) acquired for two different nanocrystals along the [010] and [111] zone axes. The simulated diffraction patterns for these zone axis assignments using coordinates of the tetragonal structure are an excellent match to the experimental data (as indicated by the reconstructed solid spheres depiction), providing unequivocal corroboration of the tetragonal crystal structure. Figure A.3A and B indicate the planes of atoms in the tetragonal unit cell that

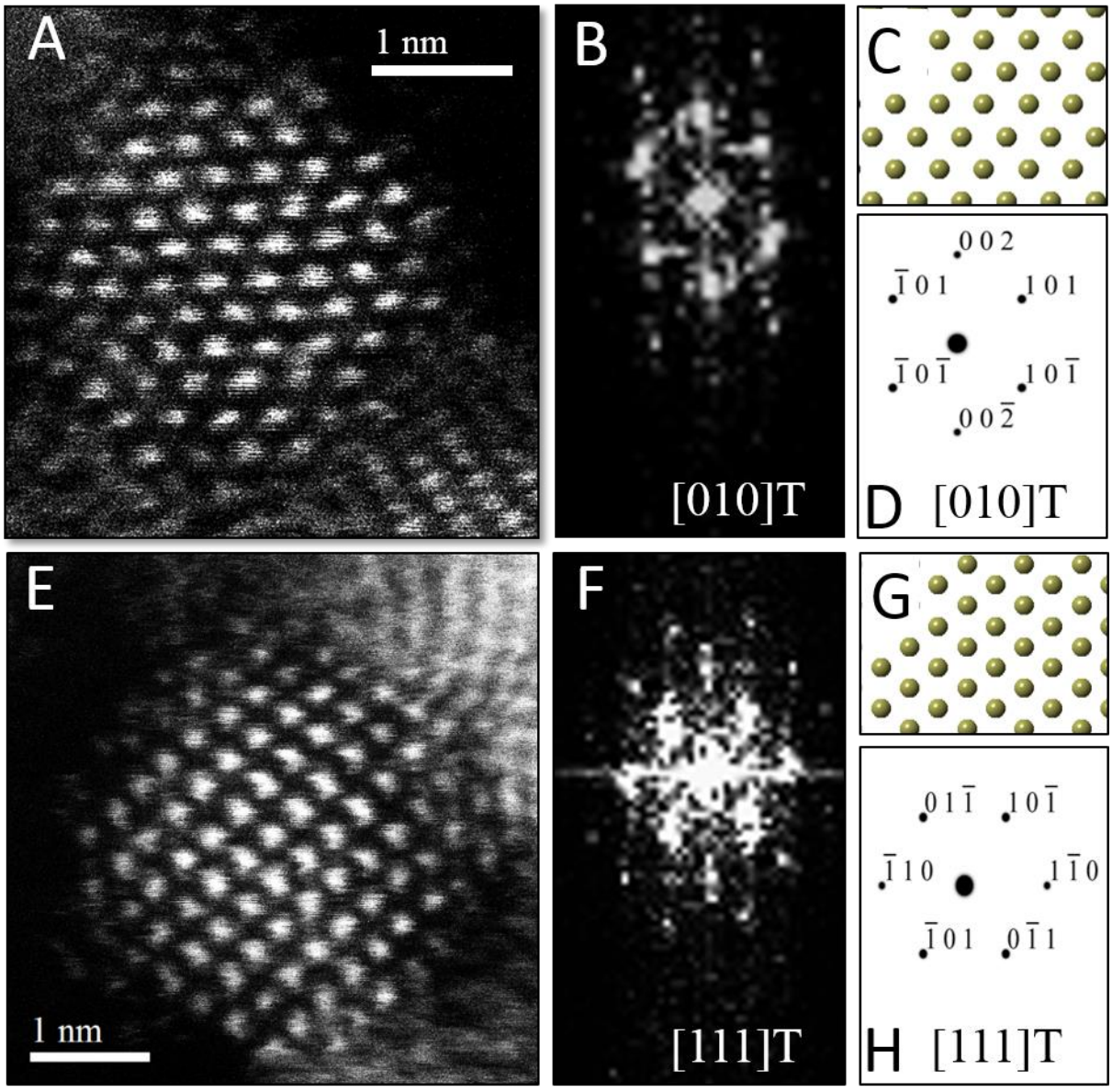

Figure II.4. Scanning transmission electron microscopy analysis of $Hf_{1-x}Ce_xO_2$ tetragonal nanocrystals. (A) Atomic-resolution HAADF image and (B) FFT of (A) acquired along the [010] zone axis of the tetragonal structure. (C) Solid sphere model of the tetragonal structure corresponding to the [010] zone axis and (D) simulated diffraction pattern based on (C), both confirming the tetragonal crystal structure of (A). (E) Atomic-resolution HAADF image and (F) FFT of (E) acquired along the [111] zone axis of the tetragonal structure of another nanocrystal. (G) Solid sphere model of the tetragonal structure corresponding to the [111] zone axis and (H) simulated diffraction pattern based on (G).

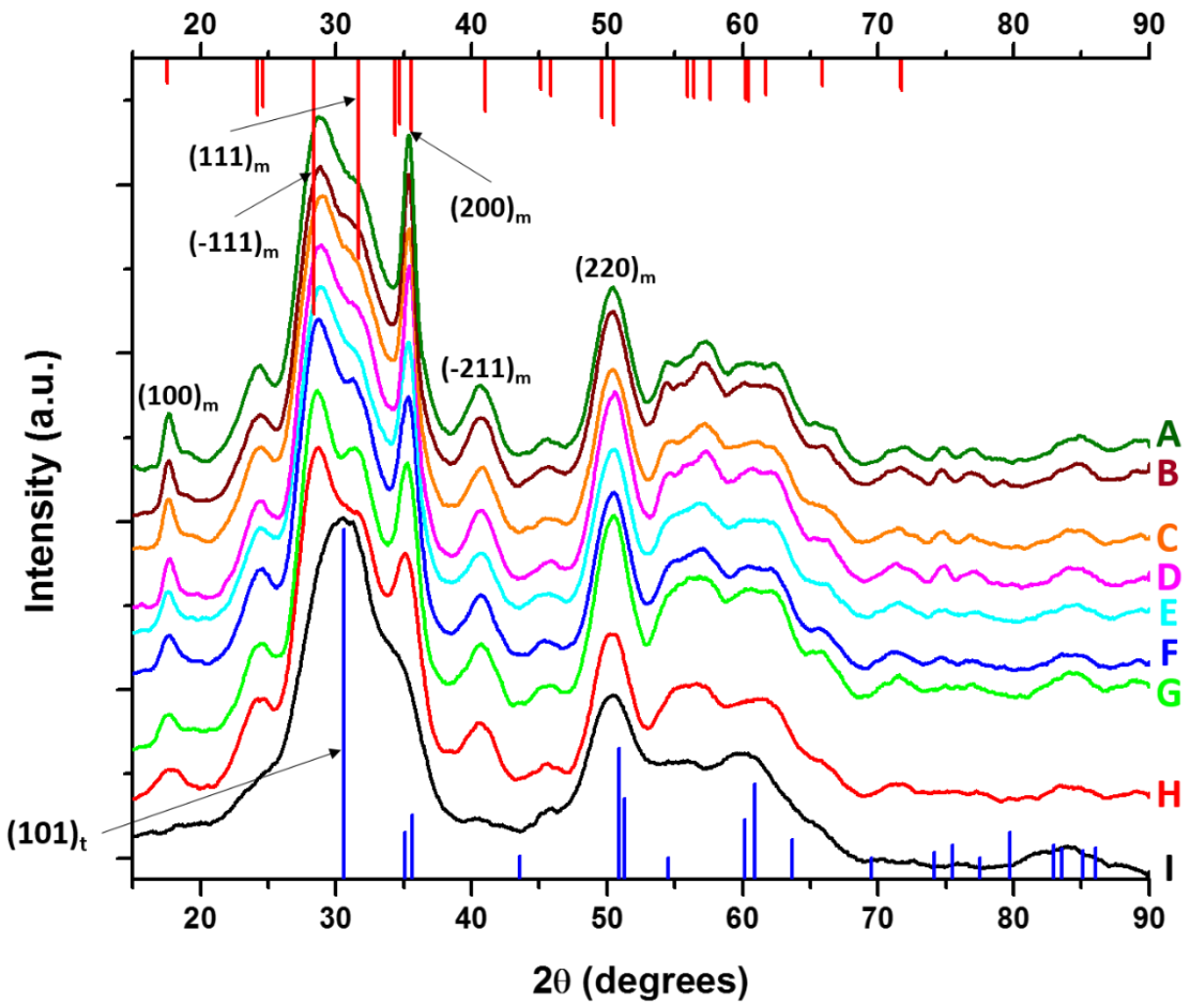

Figure II.5. X-ray diffraction patterns of pure HfO_2 (A) compared to $Hf_{1-x}La_xO_2$ nanocrystals prepared by the reaction of $HfCl_4$ with varying proportions of $Hf(O^tBu)_4$ and $La(O^iPr)_3$. The patterns correspond to detected (and precursor) relative Hf concentrations. The precursors are listed in Table 2. (A) 100% (100%), (B) 99.98% (97.5%), (C) 99.78% (93.75%), (D) 99.56% (87.5%), (E) 98.87% (75%), (F) 98.68% (62.5%), (G) 98.07% (56.25%), (H) 96.46% (52.5%), and (I) 95.27% (50%). Vertical bars indicate positions and relative intensities of reflections expected from JCPDS patterns. Reflections of monoclinic HfO_2 are indicated in red (JCPDS # 78-0050) and tetragonal HfO_2 in blue (XRD pattern simulated as described in the text).

Table II.2. Relative amounts of precursors used in the synthesis of HfO_2 nanocrystals, the atomic percentage of Hf as a function of the total metal content, the detected relative Hf and La concentrations, the length of the nanorods determined from statistical analysis of TEM data (the width is invariant at *ca*. 2.5 nm), and the predominant phase determined by powder X-ray diffraction.

$HfCl_4$ [mmols]	$Hf(O\text{-}^tBut)_4$ [mmols]	$La(O\text{-}^iPro)_3$ [mmols]	Precursor Hf Concentration [Relative at.%]	Detected Hf Concentration [Relative at.%]	Detected La Concentration [Relative at.%]	Length of nanocrystals [nm]	Phase of nanocrystals
2.0	2.0	0.0	100	100.00	0.00	12.9 ± 1.8	Monoclinic
2.0	1.9	0.1	97.5	99.98	0.01	11.5 ± 1.26	Monoclinic
2.0	1.75	0.25	93.75	99.78	0.22	10.1 ± 0.89	Monoclinic
2.0	1.5	0.5	87.5	99.56	0.44	9.3 ± 1.46	Monoclinic
2.0	1	1	75	98.87	1.13	8.1 ± 0.98	Monoclinic
2.0	0.5	1.5	62.5	98.68	1.32	7.0 ± 1.02	Monoclinic
2.0	0.25	1.75	56.25	98.07	1.93	5.9 ± 0.92	Monoclinic
2.0	0.1	1.9	52.5	96.46	3.54	4.7 ± 0.79	Monoclinic
2.0	0.0	2.0	50	95.27	4.73	3.3 ± 0.42	Tetragonal

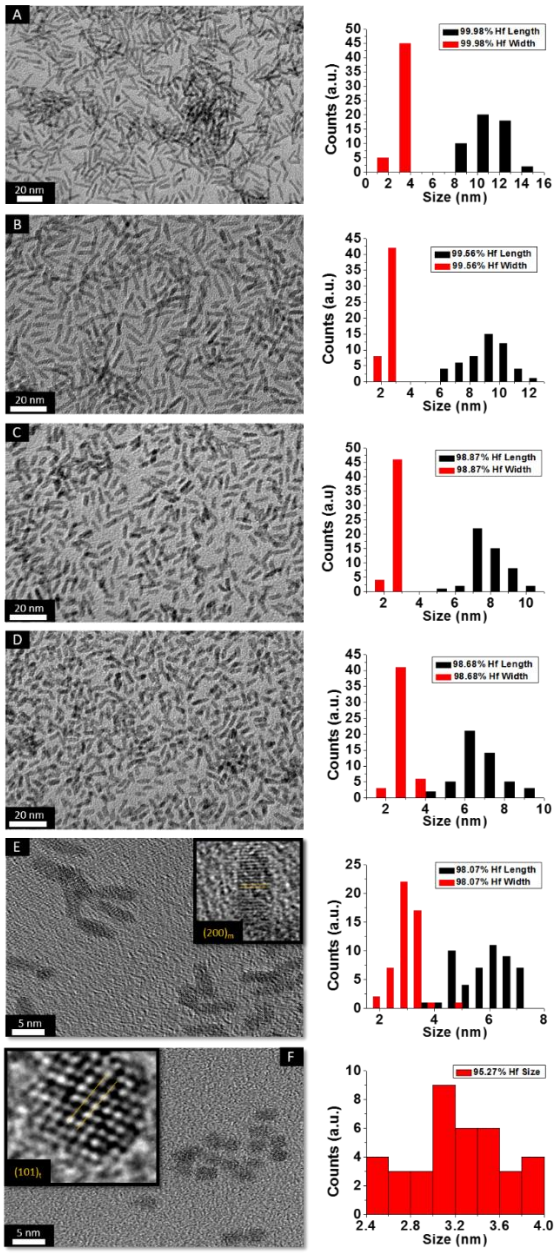

Figure II.6. Low-magnification transmission electron microscopy images of nanocrystals prepared by the reaction of $HfCl_4$ with varying proportions of $Hf(O^tBu)_4$ and $La(O^iPr)_3$. The precursors and calculated dimensions are listed in Table II.2. The detected (and precursor) relative Hf concentrations of (A) 99.98% (97.5%), (B) 99.56% (87.5%), (C) 98.87% (75%), (D) 98.68% (62.5%), (E) 98.07% (56.25%), and (F) 95.27% (50%). Insets show HRTEM images. The lattice-resolved images indicate separations between the (200) lattice planes of the monoclinic phase in the inset of (E) and the (101) lattice planes of the tetragonal phase in the inset of (F). The accompanying size distribution histograms are shown to the right of each sample illustrating that the length of the nanorods decreases with increasing concentration of $La(O^iPr)_3$ in the synthesis, whereas the width remains relatively constant.

are indexed in the simulated diffraction patterns (Figure II.4D & H) for each image acquired along a specific zone axis.

Figure II.5 displays powder XRD patterns acquired for nanocrystals obtained by the reaction of $HfCl_4$ with varying proportions of $Hf(O^tBu)_4$ and $La(O^iPr)_3$. **Table II.2** lists the actual Hf and La atomic concentrations obtained for the different precursor ratios as well as the primary phase identified from analysis of powder XRD patterns. EDX was also performed on $Hf_{1-x}La_xO_2$ nanocrystals and the determined hafnium and lanthanum concentrations are in good agreement with the elemental analysis results (Figure A.4 and Table A.3). Again, upon decreasing the Hf : La ratios such that there is a lower concentration of hafnium precursors as compared to lanthanum precursors, only amorphous aggregates are obtained, and thus we focus our discussion on reaction mixtures with lower concentrations of $La(O^iPr)_3$ as listed in Table II.2. Lower alkoxide concentrations also yield amorphous aggregates. Notably, the homocondensation of $LaCl_3$ and $La(O^iPr)_3$ yields LaOCl nanocrystals crystallized in the matlockite PbFCl-type phase.[41–43]

Analogous to the above discussion for $Ce(O^tBu)_4$, with increasing concentration of $La(O^iPr)_3$ in the reaction mixture, the (100) and (200) reflections indexed to the monoclinic phase of pure HfO_2 are broadened and diminished in intensity suggesting a pronounced diminution in size. Again, although the powder XRD patterns are substantially altered, the elemental analysis results listed in Table II.2 indicate very little incorporation of La in HfO_2. For the sample prepared by the reaction of $HfCl_4$ and $La(O^iPr)_3$, the (100) monoclinic reflection is no longer observed and the (101) tetragonal reflection becomes the most prominent feature in the powder XRD pattern suggesting stabilization of the tetragonal phase of HfO_2 with modest La doping.

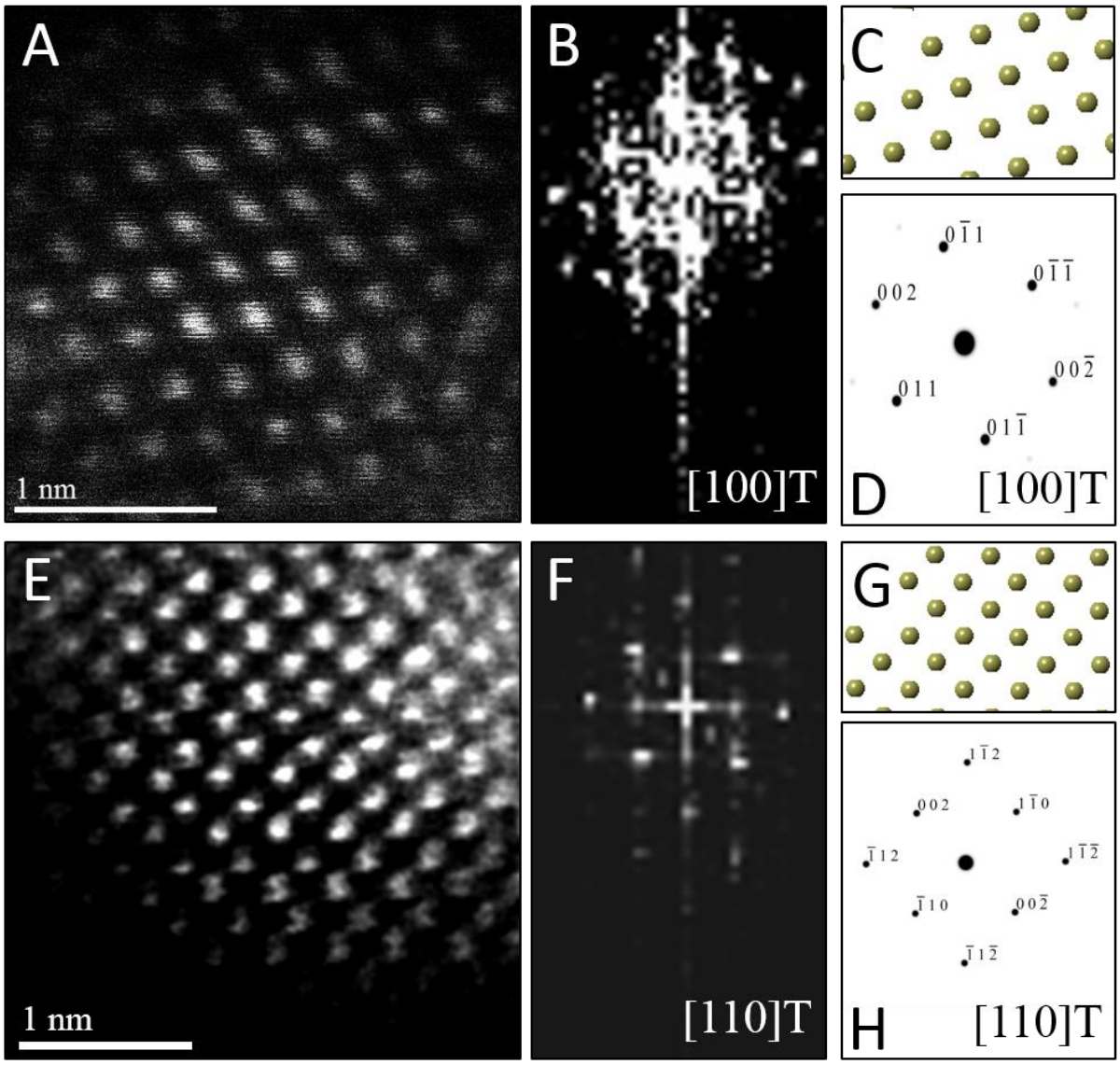

Figure II.7. Scanning transmission electron microscopy analysis of individual $Hf_{1-x}La_xO_2$ tetragonal nanocrystals. (A) Atomic-resolution HAADF image and (B) FFT of (A) acquired along the [100] zone axis of the tetragonal structure. (C) Solid sphere model of the tetragonal structure corresponding to the [100] zone axis and (D) simulated diffraction pattern based on (C), both confirming the crystal structure orientation of (A). (E) Atomic-resolution HAADF image and (F) FFT of (E) acquired along the [110] zone axis of the tetragonal structure of another nanocrystal. (G) Solid sphere model of the tetragonal structure corresponding to the [110] zone axis and (H) simulated diffraction pattern based on (G).

HRTEM images and size distribution histograms of this set of nanocrystals are shown in **Figure II.6** and the relevant dimensions and standard deviations deduced from statistical analysis are listed in Table II.2. With increasing concentration of $La(O^iPr)_3$, the $Hf_{1-x}La_xO_2$ nanocrystals again evolve from elongated nanorods to quasi-spherical nanocrystals. The width of the $Hf_{1-x}La_xO_2$ nanocrystals is relatively unchanged at *ca*. 2.5 ± 0.4 nm for the entire set of samples. However, the length of the nanorods is diminished from 12.9 ± 1.8 nm for monoclinic nanocrystals grown using only $Hf(O^tBu)_4$ to 3.3 ± 0.4 nm for $Hf_{1-x}La_xO_2$ tetragonal nanocrystals grown using $La(O^iPr)_3$ as the only alkoxide precursor.

To confirm the phase assignment of $Hf_{1-x}La_xO_2$ nanocrystals as being tetragonal, atomic-resolution HAADF STEM images and fast Fourier transforms (FFT) of the HAADF images were acquired and are depicted in **Figure II.7**. Images were acquired for different nanocrystals along [100] and [110] zone axes. The simulated diffraction patterns are an excellent match to the Fourier transforms in each case and the reconstructed tetragonal lattice (depicted as solid spheres) is entirely superimposable on the STEM image. Figure A.5A and B indicate the planes of atoms in the tetragonal unit cell that are indexed in the simulated diffraction patterns (Figure II.7D & H). The STEM data further provides unambiguous conformation of the tetragonal crystal structure.

The preceding discussion illustrates that the addition of $Ce(O^tBu)_4$ and $La(O^iPr)_3$ leads to a substantial and monotonic diminution of nanocrystal size even though elemental analysis results indicate that relatively low concentrations of Ce and La are actually incorporated within the lattice. At the smallest dimensions, the tetragonal phase of HfO_2 is stabilized over the monoclinic phase. These results lead to two fundamental questions regarding the mechanistic

basis for the size control achieved by addition of La and Ce precursors and the origin of the altered phase stability.

II.5 Discussion

To understand the origin of the size control achieved by the addition of $Ce(O^tBu)_4$ and $La(O^iPr)_3$, it is important to consider the overall equation depicted in Equation (II.1), which results in formation of an oxo-bridge with the elimination of an alkyl halide, as well as the catalytic scheme proposed by Vioux shown in Figure II.1.[44,45] Indeed, it is thought that the initial step in a heterocondensation reaction between two metal precursors M and M' involves ligand exchange and can be written as:

$$MCl_n + M'(OR)_n \rightarrow MCl_{n-x}(OR)_x + M'Cl_x(OR)_{n-x} \quad \text{(II.3)}$$

Evidence for such ligand-exchange comes from direct observations of chloroalkoxides by Vioux[14,36] as well as the following observations derived from nanocrystal synthesis: (a) reactions of $HfCl_4$ and $Zr(OR)_4$ and $ZrCl_4$ and $Hf(OR)_4$ yield exactly the same compositions of solid-solution $Hf_xZr_{1-x}O_2$ nanocrystals suggesting that ligand scrambling precedes condensation;[37] (b) the reaction of trivalent lanthanide chlorides and lanthanide alkoxides yields lanthanide oxyhalide nanocrystals with well-defined oxyhalide bridges.[41–43] The rates of condensation of the chloroalkoxide species produced as per Equation (II.3) are greatly dependent on the specific metal; precursors with similar reactivities yield solid-solution nanocrystals with a random distribution of two metals, whereas if one species reacts much faster than the second, very little of the second species incorporates within the lattice and the oxide of the first metal is obtained as the primary product.[36] Reasonably well-matched precursor pairs such as Hf/Zr and La/Ce yield solid-solution nanocrystals of $Hf_xZr_{1-x}O_2$ and $La_xCe_{1-x}O_2$, respectively, albeit with compositions

that reflect the relative reactivities of the two metal precursors as modified by the alkoxide ligands.[18,37,39] However, upon reacting Hf precursors with Ce and La precursors, the homocondensation of the former proceeds much faster than heterocondensation. Indeed, HfO_2 with very low dopant concentrations is obtained as the exclusive product upon the reaction of $HfCl_4$ with mixtures of $Hf(O^tBu)_4$ and $Ce(O^tBu)_4/La(O^iPr)_3$. The relatively low incorporation of Ce and La within the doped HfO_2 lattice, very much lower than the precursor concentrations, corroborates the idea of the lower reactivity of these precursors. Figure II.2, II.3, II.5, and II.6 nevertheless indicate that the addition of $Ce(O^tBu)_4$ and $La(O^iPr)_3$ allows for substantial tunability of the size of the obtained doped HfO_2 nanocrystals. In Figure II.1, the initial step involves the formation of an alkoxo-bridge as a result of a Lewis acid–Lewis base interaction between the oxygen atom of the alkoxide and the metal center of a halide. Subsequently, the MX_3OR species (derived from ligand exchange as per Equation (II.3)) mediates conversion of the alkoxo-bridge to an oxo-bridge with elimination of an alkyl halide. Indeed, Vioux has shown that the presence of MX_3OR species is imperative for condensation and that $MX_2(OR)_2$ and $MX(OR)_3$ species are much less reactive.[36] In other words, the Lewis acid–base complex depicted in Figure II.1 is the "monomer", whereas the MX_3OR species formed by ligand exchange serves as the catalyst. The retention of equimolar amounts of halide and alkoxide precursors ensures that the amount of catalyst is kept essentially the same for all of the reactions listed in Table II.1 and Table II.2 as a result of the ligand exchange reaction depicted in Equation (II.3) although it must be qualified that the equilibrium constants for formation of the catalyst will be altered for the different alkoxides. Indeed, since formation of an oxo-bridge, and not diffusion of monomers, is thought to be the rate-determining step, in the absence of a sufficient amount of the catalyst, such as at low alkoxide concentrations, only amorphous aggregates are

obtained. However, since the Lewis acid–base adducts constituted from $HfCl_4$ and $Ce(O^tBu)_4/La(O^iPr)_3$ are much less reactive as compared to those prepared from $HfCl_4$ and $Hf(O^tBu)_4$, the addition of cerium and lanthanum precursors essentially reduces the concentration of the active monomer. In other words, the reaction rate is diminished as a result of the lower reactivity of mixed metal Lewis acid–base adducts towards formation of oxo-bridges. As further corroboration for this idea, Table II.1 and Figure II.1 indicate that the homocondensation of hafnium precursors yields pure HfO_2 nanocrystals that are 12.9 ± 1.8 nm. In contrast, the homocondensation of cerium precursors yields CeO_2 nanocrystals that are 1.5 ± 0.5 nm indicating much slower kinetics of growth (Table II.1 and Figure A.2). Cross-reactions between La and Ce alkoxides indicate even lower reactivities for the La precursors with only *ca*. 20 at% incorporation of La within solid-solution $La_xCe_{1-x}O_2$ nanocrystals when starting with equimolar concentrations.[39] The reduced concentration of the active monomer brings about a systematic and pronounced diminution in the size of the doped HfO_2 nanocrystals by inhibiting their growth. In other words, the cross-condensation reaction enables modulation of the concentration of the active monomer, thereby enabling precise control over crystal size.

As a next point, we discuss the origins of the stabilization of the tetragonal phase of HfO_2. Indeed, the product of the direct reaction of $HfCl_4$ and $Hf(O^iPr)_4$ when ramped at a rate of 15°C to 500°C during thermal analysis is monoclinic HfO_2, the thermodynamically stable phase, along with an oxygen-deficient orthorhombic HfO_2 phase. The inclusion of TOPO still yields monoclinic HfO_2, albeit with a smaller size. These results illustrate that direct reaction of the precursors cannot yield the metastable, kinetically trapped phase. The incorporation of the La and Ce alkoxides is imperative to slow the kinetics of crystal growth. **Figure II.8** indicates the

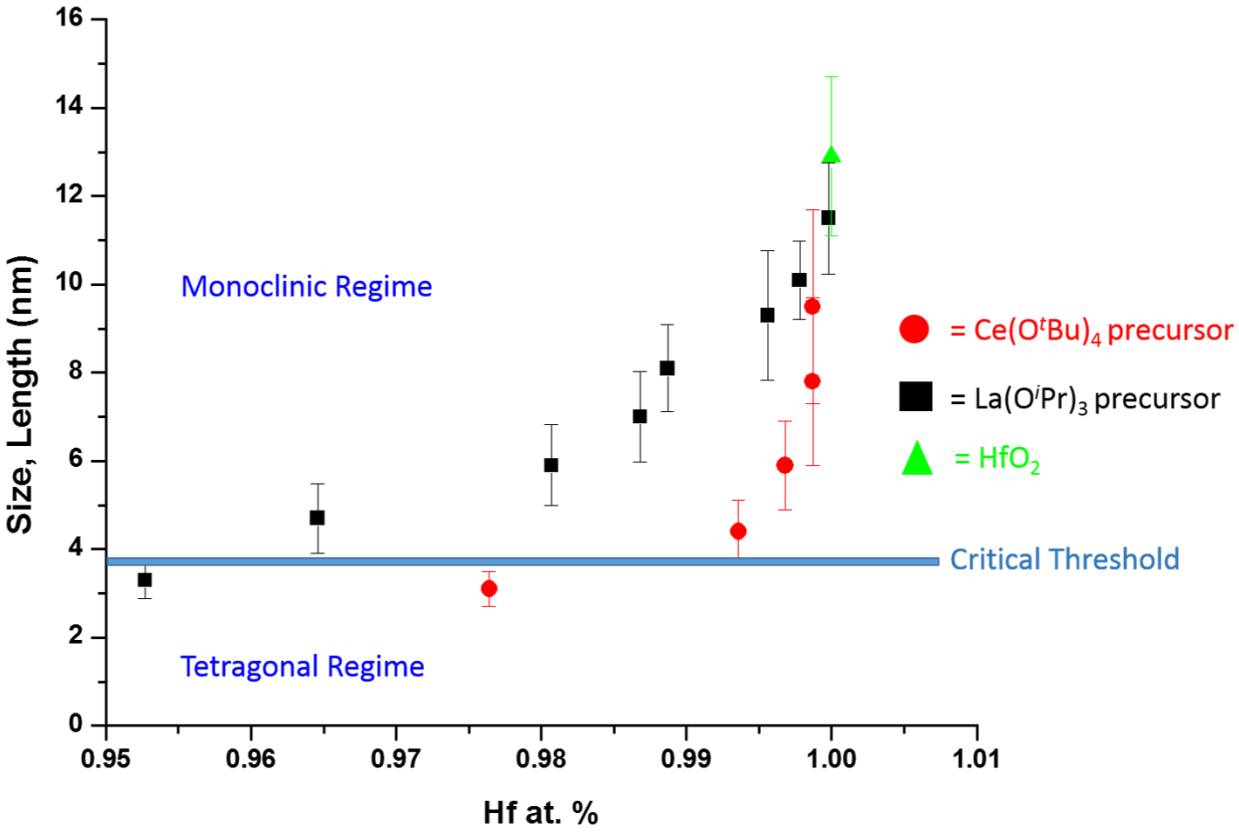

Figure II.8. A plot of nanocrystal size versus the relative atomic percentage of Hf detected by elemental analysis (Table II.1 and Table II.2). The line denoted as the critical threshold separates the monoclinic and tetragonal phases of pure HfO_2.

evolution of size as a function of the measured Hf concentration in the doped nanocrystals and depicts that only below a critical threshold of *ca*. 3.6–3.8 nm is the tetragonal phase stabilized.

Since Table II.1 and Table II.2 indicate that some amount of La and Ce are incorporated within the doped nanocrystals, it is worth considering whether the stabilization of the tetragonal phase results from (a) the size of the La/Ce cations that are displacively doped being different from that of Hf-cations (a strain effect), (b) the creation of oxygen vacancies, or (c) crystal size. Based on the larger size of La^{3+} cations (110 pm for seven-coordinated and 116 pm for eight-coordinated sites) as compared to Ce^{3+} (107 pm for seven-coordinated and 114.3 pm for eight-

coordinated) or Ce^{4+} (97 pm for eight-coordinated),[46,47] if the effects of cation size were to be of paramount importance, one would expect that incorporation of La would more readily bring about stabilization of the tetragonal phase and one would further expect to see substantial tensile strain. However, Table II.1 and Table II.2 indicate that the amount of detected Ce and La are 2.36 at% and 4.73 at%, respectively, for stabilization of the tetragonal phase and thus size of the cations is likely not the primary driving force for stabilization of the tetragonal phase. Furthermore, the reconstructed HAADF images (Figure II.4 and Figure II.7) do not reveal any measurable strain for the tetragonal structure. In other words, if size were the primary factor, relatively lower amounts of La incorporation would be expected to bring about stabilization of the tetragonal phase (Table II.2 indicates that the $Hf_{1-x}La_xO_2$ nanocrystals remain monoclinic even upon incorporation of 3.54 at% of La).

The second scenario pertains to the potential role of oxygen vacancies. The substitutional incorporation of trivalent lanthanum cations in the HfO_2 lattice will result in creation of half an oxygen vacancy to maintain electrostatic neutrality. The Ce^{4+}/Ce^{3+} redox couple is readily accessible but since we start with tetravalent cerium precursors, the vacancy concentration generated upon cerium-incorporation is likely to be lower than upon lanthanum incorporation. Again, if oxygen vacancies were to provide the driving force for stabilization of the tetragonal phase, one would expect that lanthanum-incorporation should more readily bring about stabilization of the tetragonal phase as compared to cerium incorporation. Again, Table II.1 and Table II.2 indicate that $Hf_{1-x}La_xO_2$ nanocrystals with 3.54 at% La are monoclinic, whereas $Hf_{1-x}Ce_xO_2$ nanocrystals with only 2.36 at% Ce are tetragonal. The preceding discussion and Figure II.8 thus implies that it is the size of the nanocrystals that is the primary driving force for stabilization of the tetragonal phase. The stabilization of this phase is derived from the surface

energy of the tetragonal phase being lower than that of the monoclinic phase (the difference between the two phases is 246 $mJ \cdot m^{-2}$).[21] Below the critical size regime, the surface-to-volume ratio of pure HfO_2 nanocrystals becomes such that the surface energy term exceeds the bulk energy component of the free energy term (the difference between the two phases is 196 meV for pure HfO_2),[21] thereby enabling preferentially stabilization of the tetragonal phase at room temperature.[1,2,8,9]

In 1972, Bailey and co-workers developed an expression for calculating the critical size for stabilizing a metastable state based on a classical thermodynamic treatment of the phase transformation and the competing bulk and surface energy terms. In this formulation, the critical size, *d* can be expressed as[48]

$$d = \frac{6}{[(G_T - G_M) + (V_T - V_M)]} \left(\frac{\gamma_M}{\rho_M} - \frac{\gamma_T}{\rho_T}\right) \quad \text{(II.4)}$$

where the subscripts M and T correspond to the relevant values for the monoclinic and tetragonal phases, G is the volume free energy change across the phase transformation, V is the strain energy, γ is the specific surface energy, and ρ represents the density. Hunter *et al*. used this expression to predict a critical size for stabilization of tetragonal HfO_2 of d = 3.6 nm.[16] In the absence of well-defined, monodisperse, and phase-pure nanocrystals, a comprehensive evaluation of this formalism has not been possible thus far. Another notable complication for HfO_2 nanocrystals prepared by aqueous methods is the almost 20– 30% diminution of surface energy as a result of surface hydroxylation, which in this case further dilutes the influence of the surface energy contribution.[20] Figure II.8 indicates a critical size of 3.6–3.8 nm for stabilization of the tetragonal phase of HfO_2, which is in remarkably good agreement with predictions from this thermodynamic model. The origin of the stability of the tetragonal phase at these dimensions

can thus be attributed to the substantially lower surface energies of this phase, which renders this phase energetically stable under conditions of constrained equilibrium.

II.6 Conclusions

Stabilization of the tetragonal phase of HfO_2 has been far more challenging as compared to ZrO_2 given the smaller volume expansion accompanying the tetragonal → monoclinic transformation and the relatively greater stabilization enjoyed by the monoclinic phase. Classical thermodynamic models predict that the tetragonal phase should be stable at dimensions smaller than *ca*. 3.6 nm but the validity of these predictions have been thus far impossible to determine in the absence of synthetic approaches that can access such ultra-small dimensions with precise control of particle size. In this chapter, we have developed a non-hydrolytic condensation route wherein the concentration of the active monomer is precisely modulated by replacing $Hf(O^tBu)_4$ with less reactive $Ce(O^tBu)_4$ or $La(O^iPr)_3$ precursors. The latter alkoxides exhibit much slower kinetics of condensation and thus are incorporated within the doped HfO_2 lattice only to small extents but play a significant role in modifying the growth kinetics by suppressing the concentration of the active monomer. This approach enables precise control of size in ultra-small dimensions and allows for systematic evaluation of the size-dependence of phase stabilities in this system. The much desired metastable tetragonal phase is stabilized at dimensions less than 3.6–3.8 nm, which is in good accord with predictions of thermodynamic models that take into account the competing influences of bulk free energy and specific surface energy.

II.7 References

(1) Navrotsky, A. Nanoscale Effects on Thermodynamics and Phase Equilibria in Oxide Systems. *ChemPhysChem* **2011**, *12*, 2207–2215.

(2) Waitz, T.; Tsuchiya, K.; Antretter, T.; Fischer, F. D. Phase Transformations of Nanocrystalline Martensitic Materials. *MRS Bull.* **2009**, *34*, 814–821.

(3) Grünwald, M.; Lutker, K.; Alivisatos, A. P.; Rabani, E.; Geissler, P. L. Metastability in Pressure-Induced Structural Transformations of CdSe/ZnS Core/shell Nanocrystals. *Nano Lett.* **2013**, *13*, 1367–1372.

(4) Tolbert, S. H.; Alivisatos, A. P. Size Dependence of a First Order Solid-Solid Phase Transition: The Wurtzite to Rock Salt Transformation in CdSe Nanocrystals. *Science.* **1994**, *265*, 373–376.

(5) Lukowski, M. A.; Daniel, A. S.; Meng, F.; Forticaux, A.; Li, L.; Jin, S. Enhanced Hydrogen Evolution Catalysis from Chemically Exfoliated Metallic MoS_2 Nanosheets. *J. Am. Chem. Soc.* **2013**, *135*, 10274–10277.

(6) Ambrosi, A.; Sofner, Z.; Pumera, M. 2H - 1T Phase Transition and Hydrogen Evolution Activity of MoS_2, $MoSe_2$, WS_2 and WSe_2 Strongly Depends on the MX_2 Composition. *Chem. Commun.* **2015**, *51*, 8450–8453.

(7) Wan, C.; Regmi, Y. N.; Leonard, B. M. Multiple Phases of Molybdenum Carbide as Electrocatalysts for the Hydrogen Evolution Reaction. *Angew. Chemie - Int. Ed.* **2014**, *53*, 6407–6410.

(8) Garvie, R. C. The Occurrence of Metastable Tetragonal Zirconia as a Crystallite Size Effect. *J. Phys. Chem.* **1965**, *69* (4), 1238–1243.

(9) Chevalier, J.; Gremillard, L.; Virkar, A. V.; Clarke, D. R. The Tetragonal-Monoclinic

Transformation in Zirconia: Lessons Learned and Future Trends. *J. Am. Ceram. Soc.* **2009**, *92* (9), 1901–1920.

(10) Liu, H.; Strobridge, F. C.; Borkiewicz, O. J.; Wiaderek, K. M.; Chapman, K. W.; Chupas, P. J.; Grey, C. P. Capturing Metastable Structures during High-Rate Cycling of $LiFePO_4$ Nanoparticle Electrodes. *Science.* **2014**, *344* (6191), 1252817.

(11) Malik, R.; Zhou, F.; Ceder, G. Kinetics of Non-Equilibrium Lithium Incorporation in $LiFePO_4$. *Nat. Mater.* **2011**, *10*, 587–590.

(12) Gopalakrishnan, J. Chimie Douce Approaches to the Synthesis of Metastable Oxide Materials. *Chem. Mater.* **1995**, *7*, 1265–1275.

(13) Hodges, J. M.; Kletetschka, K.; Fenton, J. L.; Read, C. G.; Schaak, R. E. Sequential Anion and Cation Exchange Reactions for Complete Material Transformations of Nanoparticles with Morphological Retention. *Angew. Chemie - Int. Ed.* **2015**, *54*, 8669–8672.

(14) Mutin, P. H.; Vioux, A. Recent Advances in the Synthesis of Inorganic Materials via Non-Hydrolytic Condensation and Related Lowtemperature Routes. *J. Mater. Chem. A* **2013**, *1*, 11504–11512.

(15) Mutin, P. H.; Vioux, A. Nonhydrolytic Processing of Oxide-Based Materials: Simple Routes to Control Homogeneity, Morphology, and Nanostructure. *Chem. Mater.* **2009**, *21*, 582–596.

(16) Hunter, O.; Scheidecker, R. W.; Tojo, S. Characterization of Metastable Tetragonal Hafnia. *Ceramurg. Int.* **1979**, *5* (4), 137–142.

(17) Joo, J.; Yu, T.; Kim, Y. W.; Park, H. M.; Wu, F.; Zhang, J. Z.; Hyeon, T. Multigram Scale Synthesis and Characterization of Monodisperse Tetragonal Zirconia Nanocrystals. *J. Am. Chem. Soc.* **2003**, *125*, 6553–6557.

(18) Tang, J.; Zhang, F.; Zoogman, P.; Fabbri, J.; Chan, S.-W.; Zhu, Y.; Brus, L. E.; Steigerwald, M. L. Martensitic Phase Transformation of Isolated HfO_2, ZrO_2, and $Hf_xZr_{1-x}O_2$ ($0< x <1$) Nanocrystals. *Adv. Funct. Mater.* **2005**, *15*, 1595–1602.

(19) Tang, J.; Fabbri, J.; Robinson, R. D.; Zhu, Y.; Herman, I. P.; Steigerwald, M. L.; Brus, L. E. Solid-Solution Nanoparticles: Use of a Nonhydrolytic Sol-Gel Synthesis To Prepare HfO2 and $Hf_xZr_{1-x}O_2$ Nanocrystals. *Chem. Mater.* **2004**, *16*, 1336–1342.

(20) Zhou, W.; Ushakov, S. V.; Wang, T.; Ekerdt, J. G.; Demkov, A. A.; Navrotsky, A. Hafnia: Energetics of Thin Films and Nanoparticles. *J. Appl. Phys.* **2010**, *107*, 123514.

(21) Iskandarova, I. M.; Knizhnik, A. A.; Rykova, E. A.; Bagatur'yants, A. A.; Potapkin, B. V.; Korkin, A. A. First-Principle Investigation of the Hydroxylation of Zirconia and Hafnia Surfaces. *Microelectron. Eng.* **2003**, *69*, 587–593.

(22) Ushakov, S. V.; Navrotsky, A.; Yang, Y.; Stemmer, S.; Kukli, K.; Ritala, M.; Leskelä, M. A.; Fejes, P.; Demkov, A.; Wang, C.; Nguyen, B. Y.; Triyoso, D.; Tobin, P. Crystallization in Hafnia- and Zirconia-Based Systems. *Phys. Status Solidi Basic Res.* **2004**, *241*, 2268–2278.

(23) Matovic, B.; Pantic, J.; Lukovic, J.; Cebela, M.; Dmitrovic, S.; Mirkovic, M.; Prekajski, M. A Novel Reduction-Oxidation Synthetic Route for Hafnia. *Ceram. Int.* **2016**, *42*, 615–620.

(24) Qi, J.; Zhou, X. Formation of Tetragonal and Monoclinic-HfO_2 Nanoparticles in the Oil/water Interface. *Colloids Surfaces A Physicochem. Eng. Asp.* **2015**, *487*, 26–34.

(25) Cho, D.-Y.; Jung, H. S.; Yu, I.-H.; Yoon, J. H.; Kim, H. K.; Lee, S. Y.; Jeon, S. H.; Han, S.; Kim, J. H.; Park, T. J.; Park, B.-G.; Hwang, C. S. Stabilization of Tetragonal HfO_2 under Low Active Oxygen Source Environment in Atomic Layer Deposition. *Chem.*

Mater. **2012**, *24*, 3534–3543.

(26) MacLaren, I.; Ras, T.; MacKenzie, M.; Craven, A. J.; McComb, D. W.; Gendt, S. De. Texture, Twinning, and Metastable "Tetragonal" Phase in Ultrathin Films of HfO_2 on a Si Substrate. *J. Electrochem. Soc.* **2009**, *156*, G103–G108.

(27) Manory, R. R.; Mori, T.; Shimizu, I.; Miyake, S.; Kimmel, G. Growth and Structure Control of HfO_{2-x} Films with Cubic and Tetragonal Structures Obtained by Ion Beam Assisted Deposition. *J. Vac. Sci. Technol. A* **2002**, *20*, 549–554.

(28) Wilk, G. D.; Wallace, R. M.; Anthony, J. M. High-K Gate Dielectrics: Current Status and Materials Properties Considerations. *J. Appl. Phys.* **2001**, *89*, 5243–5275.

(29) O'Hara, A.; Bersuker, G.; Demkov, A. A. Assessing Hafnium on Hafnia as an Oxygen Getter. *J. Appl. Phys.* **2014**, *115*, 183703.

(30) Luo, X.; Demkov, A. A. Structure, Thermodynamics, and Crystallization of Amorphous Hafnia. *J. Appl. Phys.* **2015**, *118*, 124105.

(31) Zhao, X.; Vanderbilt, D. First-Principles Study of Structural, Vibrational, and Lattice Dielectric Properties of Hafnium Oxide. *Phys. Rev. B* **2002**, *65* (23), 75105.

(32) Jiang, H.; Gomez-Abal, R. I.; Rinke, P.; Scheffler, M. Electronic Band Structure of Zirconia and Hafnia Polymorphs from the GW Perspective. *Phys. Rev. B - Condens. Matter Mater. Phys.* **2010**, *81*, 85119.

(33) Deshmukh, R.; Niederberger, M. Non-Hydrolytic Sol-Gel Methods. In *The Sol-Gel Handbook - Synthesis, Characterization, and Applications: Synthesis, Characterization and Applications, 3-Volume Set*; Levy, D., Zayat, M., Eds.; Wiley-VCH Verlag GmbH & Co. KGaA: Weinheim, Germany, **2015**; pp 29–69.

(34) Pinna, N.; Garnweitner, G.; Antonietti, M.; Niederberger, M. Non-Aqueous Synthesis of

High-Purity Metal Oxide Nanopowders Using an Ether Elimination Process. *Adv. Mater.* **2004**, *16*, 2196–2200.

(35) Boyle, T. J.; Steele, L. A. M.; Burton, P. D.; Hoppe, S. M.; Lockhart, C.; Rodriguez, M. A. Synthesis and Structural Characterization of a Family of Modified Hafnium Tert - Butoxide for Use as Precursors to Hafnia Nanoparticles. *Inorg. Chem.* **2012**, *51*, 12075–12092.

(36) Vioux, A. Nonhydrolytic Sol-Gel Routes to Oxides. *Chem. Mater.* **1997**, *9*, 2292–2299.

(37) Depner, S. W.; Kort, K. R.; Banerjee, S. Precursor Control of Crystal Structure and Stoichiometry in Twin Metal Oxide Nanocrystals. *Cryst. Eng. Commun.* **2009**, *11*, 841–846.

(38) Depner, S. W.; Cultrara, N. D.; Farley, K. E.; Qin, Y.; Banerjee, S. Ferroelastic Domain Organization and Precursor Control of Size in Solution-Grown Hafnium Dioxide Nanorods. *ACS Nano* **2014**, *8* (5), 4678–4688.

(39) Depner, S. W.; Kort, K. R.; Jaye, C.; Fischer, D. A.; Banerjee, S. Nonhydrolytic Synthesis and Electronic Structure of Ligand-Capped $CeO_{2-\delta}$ and CeOCl Nanocrystals. *J. Phys. Chem. C* **2009**, *113*, 14126–14134.

(40) Perevalov, T. V.; Gritsenko, V. A.; Erenburg, S. B.; Badalyan, A. M.; Wong, H.; Kim, C. W. Atomic and Electronic Structure of Amorphous and Crystalline Hafnium Oxide: X-Ray Photoelectron Spectroscopy and Density Functional Calculations. *J. Appl. Phys.* **2007**, *101* (5), 53704-1–8.

(41) Kort, K. R.; Banerjee, S. Shape-Controlled Synthesis of Well-Defined Matlockite LnOCl (Ln: La, Ce, Gd, Dy) Nanocrystals by a Novel Non-Hydrolytic Approach. *Inorg. Chem.* **2011**, *50*, 5539–5544.

(42) Kort, K. R.; Banerjee, S. Ligand-Mediated Control of Dislocation Dynamics and Resulting Particle Morphology of GdOCl Nanocrystals. *Small* **2015**, *11* (3), 329–334.

(43) Waetzig, G. R.; Horrocks, G. A.; Jude, J. W.; Zuin, L.; Banerjee, S. X-Ray Excited Photoluminescence near the Giant Resonance in Solid-Solution $Gd_{1-x}Tb_xOCl$ Nanocrystals and Their Retention upon Solvothermal Topotactic Transformation to $Gd_{1-x}Tb_xF_3$. *Nanoscale* **2016**, *8*, 979–986.

(44) Bourget, L.; Corriu, R. J. P.; Leclercq, D.; Mutin, P. H.; Vioux, A. Non-Hydrolytic Sol-Gel Routes to Silica. *J. Non. Cryst. Solids* **1998**, *242*, 81–91.

(45) Arnal, P.; Corriu, R. J. P.; Leclercq, D.; Mutin, P. H.; Vioux, A. A Solution Chemistry Study of Nonhydrolytic Sol-Gel Routes to Titania. *Chem. Mater.* **1997**, *9*, 694–698.

(46) Shannon, R. D. Revised Effective Ionic Radii and Systematic Studies of Interatomic Distances in Halides and Chalcogenides. *Acta Crystallogr. Sect. A* **1976**, *A32*, 751–767.

(47) Dronskoski, R. Classical Approaches. In *Computational Chemistry of Solid State Materials*; Wiley-VCH Verlag GmbH & Co. KGaA, **2006**; pp 13–14.

(48) Bailey, J. E.; Lewis, D.; Librant, Z. M.; Porter, L. J. Phase Transformations in Milled Zirconia. *Trans. J. Brit. Ceram. Soc.* **1972**, *71* (1), 25–30.

CHAPTER III

BUILDING ON SUB-ARCTIC SOIL: GEOPOLYMERIZATION OF MUSKEG TO A DENSIFIED LOAD-BEARING COMPOSITE*

III.1 Overview

The marshy water-saturated soil typical of the sub-Arctic represents a considerable impediment to the construction of roads, thereby greatly hindering human habitation and geological excavation. Muskeg, the native water-laden topsoil characteristic of the North American sub-Arctic, represents a particularly vexing challenge for road construction. Muskeg must either be entirely excavated, or for direct construction on muskeg, a mix of partial excavation and gradual compaction with the strategic placement of filling materials must be performed. In this chapter, we demonstrate a novel and entirely reversible geopolymerization method for reinforcing muskeg with wood fibers derived from native vegetation with the addition of inorganic silicate precursors and without the addition of extraneous metal precursors. A continuous siloxane network is formed that links together the muskeg, wood fibers, and added silicates yielding a load-bearing and low-subsidence composite. The geopolymerization approach developed here, based on catalyzed formation of a siloxane network with further incorporation of cellulose, allows for an increase of density as well as compressive strength while reducing the compressibility of the composite.

---

* Reproduced with permission from "Building on Sub-Arctic Soil: Geopolymerization of Muskeg to a Densified Load-Bearing Composite." G.R. Waetzig, J. Cho, M. Lacroix, and S. Banerjee, *Scientific Reports*, **2017**, *7*, 14711. Reproduced by permission of Nature Publishing Group. <https://www.nature.com/articles/s41598-017-15115-z>

III.2 Introduction

Access to fossil fuel deposits in the Canadian oil sands and in the sub-Arctic is greatly hindered by the difficulties of constructing roads or drilling pads on vast areas of muskeg, the native organic marshy topsoil saturated with water.[1–5] The ready subsidence of muskeg limits earthworks operations to the Arctic winter when the ground is frozen to solid ice or alternatively creates considerable safety and technical challenges when operations are conducted in warmer temperatures. Muskeg comprises mosses, sedges, grasses, and remnants of plant matter decomposed to various extents. In order to facilitate construction, the muskeg must either be entirely excavated and replaced with a compacted engineered fill, or for direct construction on muskeg, a mix of partial excavation and gradual compaction with the strategic placement of filling materials must be performed to ensure an acceptable degree of settlement.[4,6–8] The former approach is prohibitively expensive and labor-intensive, whereas the latter approach may require many months of settlement. The muskeg layers are generally frozen *ca*. 0.3 m below the ground surface during winter. Techniques have been developed to increase the ice depth to provide safe access to remote areas, but thicker ice layers limit settlement control, which is key to avoiding muskeg failure. Layers can be reinforced with biaxial geogrids or geosynthetics but these necessitate expensive capital investments and are still subject to inhomogeneous settling.[4,6,8] In contrast, the subgrade presents a stiff soil that is more amenable to construction. Upon conditioning, the native low-to-medium plastic clay and clay till can also be excavated and used to backfill excavated regions or placed atop the muskeg layer. However, this again is labor intensive and requires considerable excavation; ensuring fills remain unfrozen during compaction also adds an additional level of complexity making winter earthworks a considerable

challenge. Consequently, finding routes to build directly on muskeg has emerged as an urgent imperative for ensuring the viability of sub-Arctic fossil fuel deposits.

Geopolymerization involves the construction of silicate and aluminosilcate solid matrices, typically for purposes such as the sequestration of toxic sludge,[9,10] and provides a potential route for solidification of muskeg. Geopolymers can be cast to specific dimensions, formed into load-bearing structural elements, or deployed within concrete roadways. An attractive potential solution to the challenges of building on muskeg involves the infiltration of liquid precursors within the muskeg layer followed by cross-linking to constitute a solid densified load-bearing matrix. However, such solidification and hardening of the muskeg matrix has thus far not been achievable given the *ca*. 900% moisture content of muskeg and environmental requirements that limit the incorporation of aluminum and transition-metal frameworks given the relatively low natural abundance of these elements in native muskeg. In this chapter, we demonstrate the transformation of muskeg to a solid composite based on the formation of inorganic silicate frameworks that are further reinforced by incorporation of locally sourced cellulosic material derived from mulch. An unprecedented densified load-bearing composite matrix is obtained with no extraneous metal contamination, suggesting an entirely new approach for all-weather earthworks in marshy sub-Arctic environments and substantially mitigating the need for excavation and importation of engineered geofills. The structural framework thus constituted can furthermore be readily dissolved, allowing for restoration of the natural habitat.

III.3 Methods

III.3.1 Materials

The muskeg soils employed in this study were sourced from Cenovus Energy Inc.'s Foster Creek site in Alberta, Canada. Mulch, which is naturally occurring wood-fiber, was sourced from the same site. Tetraethylorthosilicate (TEOS; Strem chemicals) and Na_2SiO_3 (Spectrum chemical MFG Corp.), hydrochloric acid (HCl 36.5–38.0%; Macron), ammonia solution (NH4OH 28–30%; EMD Millipore), and hydroxyethylcellulose (NatrosolTM 250H4Br PA; Ashland) were procured and used without further purification.

III.3.2 Preparation of Densified Muskeg

A silicate matrix was constituted by infiltrating liquid-phase molecular or salt precursors within the muskeg followed by catalytic condensation.[11–13] Two different types of silica precursors, TEOS and Na_2SiO_3, were examined for the densification of muskeg soil. Initially, 10 g of wet muskeg soils were placed within a glass container. Next, fibrous frameworks (mulch), hydroxyethylcellulose, silicate precursors (either TEOS or Na_2SiO_3), and a condensation catalyst (either NH_4OH or HCl) were added in varying amounts. The stoichiometric ratios of muskeg, mulch, silicate precursors, hydroxyethylcellulose, and catalyst were varied as depicted in **Table III.1** After mechanical blending of the mixtures, they were allowed to dry under ambient conditions, which typically required a period of 5–7 days. The modified muskeg samples thus obtained were used for further characterization.

III.3.3 Dissolution of Silicate Framework

The muskeg was arranged in a manner similar to topsoil conditions by placing 20 g of modified muskeg atop 20 g of unmodified muskeg within an open glass column, which was further plugged with glass wool at the collection end of the column. In order to simulate Alberta

Agriculture and Forestry reclamation procedures within a laboratory environment, 3 cm of ground gypsum was then packed on top of the modified muskeg.[14] Subsequently, 250 mL of deionized water (Barnstead Nanopure system; ρ = 18.2 MΩ cm^{-1}), 10^{-1} M NaOH, and 10^{-4} M NaOH were then used separately as three different pH modifiers to induce the hydrolysis of the siloxane linkages. The liquid was then collected and sent to AECOM Canada Ltd. for elemental analysis of free metals by Inductively Coupled Plasma – Mass Spectrometry (ICP-MS).

III.3.4 Characterization

The pH value of muskeg soils was characterized by using a digital pH meter (HQ411d Benchtop pH/mV Meter) equipped with a glass electrode probe. A standard procedure for calibrating pH meters was implemented by plotting the measured potential as a function of pH. The morphological characteristics of the muskeg specimens before and after modification were evaluated using a Leica EZ4 stereomicroscope equipped with KL 1500 LCD and a FEI Quanta 600 field emission scanning electron microscope (FE-SEM) equipped with a conventional Everhart-Thornley detector, back-scattered electron detector, and IR-CCD chamber camera. An accelerating voltage of 10–20 kV was used to image the muskeg. The chemical composition of muskeg was evaluated by energy-dispersive X-ray spectroscopy (EDS) using an Oxford Instruments silicon drift detector. Fourier transform infrared (FT-IR) spectra were obtained using a Bruker VERTEX 70 instrument in the range of 4000–500 cm^{-1} with a spectral resolution of 4 cm^{-1}.

III.3.5 Calculation of Density

The density of modified muskeg soils was calculated by placing 30 g of modified muskeg within a calibrated measuring cylinder and dividing the obtained final mass of the modified

muskeg by the volume of the cylinder occupied. The density measurements were made in triplicate.

III.3.6 Compressibility Testing

The compressibility of the modified muskeg samples was evaluated by placing calibrated weights atop free-standing muskeg pucks with dimensions of 6.0 cm in diameter and 1.2–3.0 cm in height placed on a laboratory bench. The change in the height of the muskeg was measured in each instance using a 30 cm ruler at a measurement resolution of 1 mm. The height displacement (change in %) was calculated by dividing the height difference between initial and final by initial height.

$$\text{Height Displacement (\%)} = \frac{H_i - H_f}{H_i} \text{ x } 100\% \quad \text{(III.1)}$$

where *Hi* is initial height and *Hf* is final height.

III.3.7 Coefficient of Consolidation Testing

Consolidation tests were performed based on ASTM D2435. A Humboldt Conmatic Consolidation frame with a Minilogger and digital indicator were used to perform the consolidation tests. A vertical load of 345 kPa was applied for 8 h until the specimens reached the maximum load and were then unloaded. Coefficient of secondary consolidation data was then collected with the help of the Humboldt Materials Testing Software. The time fitting method was used in order to determine the coefficient of secondary consolidation for the various free-standing pucks as per:[15]

$$C_a = \frac{\Delta H/H_i}{\Delta \log(t)} \quad \text{(III.2)}$$

where *H*i is the initial height of the specimen, Δ*H* is the change in height over one log cycle, and *t* is the time in minutes.

III.3.8 Testing of Compressive Strength

The compressive strength of the muskeg specimens were measured on an Instron 5982 Mechanical Testing Device using a servo-controlled 100 kN load capacity at a displacement rate of 5 mm per minute. The dimensions of the muskeg specimens measured 6.1 cm in diameter and 4.8 cm in height.

III.3.9 Porosity Measurements

Porosity measurements were performed using a Micromeritics ASAP 2420 Accelerated Surface Area and Porosimetry System at 77 K using ultra high purity (UHP) nitrogen. Samples were degassed at 433 K for 12 h under dynamic vacuum prior to dosing with nitrogen. Surface areas and pore volumes were calculated using the Microactive software from Micromeritics based on the Brunauer, Emmett, and Teller model (BET).

III.4 Results and Discussion

III.4.1 Formation of Reinforcing Silicate Framework within Muskeg

Strengthening and reinforcing muskeg soils through aqueous solidification chemistry[16] holds great promise for facilitating direct construction on muskeg by forming a load-bearing cross-linked covalently bonded matrix. **Figure III.1** illustrates the modification and strengthening of muskeg based on infiltration of silica precursors that are catalytically cross-linked to constitute an amorphous siloxane framework. The network is reinforced with naturally occurring wood fibers; hydroxyethylcellulose is further added to promote additional cross-linking by dint of its hydroxyl groups. Free-standing pucks of muskeg with dimensions ranging up to 19.0 cm in diameter and 7.0 cm in height are prepared at 25°C by mixing wet muskeg soil with naturally occurring wood-fiber mulch and hydroxyethylcellulose, followed by addition of the silicate

Table III.1. Densification of Modified Muskeg Composites as a Function of Composition. Measured density of muskeg samples modified using a fixed amount of 10 g of wet muskeg with different concentrations of added mulch and hydroxyethylcellulose. Na_2SiO_3 is used as the precursor and the hydrolysis and condensation reaction is base catalyzed in each instance listed here.

Amount of Na_2SiO_3 (mL)	Amount of Mulch (g)	Amount of Catalyst (mL)	Amount of Additives (g)	Density (g/cm^3)
Unmodified				0.20±0.01 g/cm^3
30 mL	0 g	10 mL	2 g	0.95±0.08 g/cm^3
30 mL	0 g	10 mL	4 g	0.73±0.07 g/cm^3
20 mL	5 g	10 mL	2 g	0.56±0.05 g/cm^3
30 mL	5 g	10 mL	2 g	1.02±0.09 g/cm^3
30 mL	5 g	10 mL	4 g	1.05±0.08 g/cm^3
20 mL	10 g	10 mL	1 g	0.62±0.05 g/cm^3
20 mL	10 g	5 mL	2 g	0.66±0.06 g/cm^3
10 mL	10 g	10 mL	2 g	0.55±0.05 g/cm^3
20 mL	10 g	15 mL	2 g	0.69±0.06 g/cm^3
20 mL	10 g	10 mL	2 g	0.61±0.06 g/cm^3
30 mL	10 g	10 mL	2 g	0.72±0.07 g/cm^3
20 mL	10 g	10 mL	3 g	0.70±0.07 g/cm^3
20 mL	15 g	10 mL	2 g	0.65±0.06 g/cm^3
30 mL	15 g	10 mL	2 g	0.76±0.06 g/cm^3
30 mL	15 g	10 mL	4 g	0.73±0.06 g/cm^3

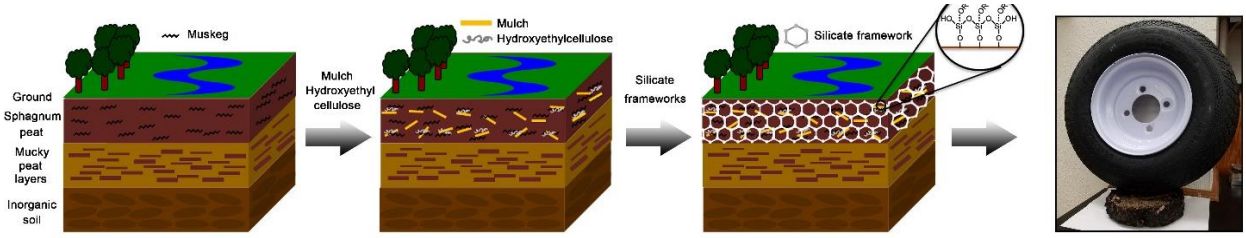

Figure III.1. Illustration of geopolymerization approach developed to solidify muskeg to a load-bearing silicate composite. Schematic depiction of strengthening and solidification of muskeg based on infiltration of aqueous precursors for formation of a siloxane network further reinforced by the addition of mulch fibers and hydroxyethylcellulose.

precursor and initiation of acid- or base-catalyzed condensation. Elimination of free water and solidification occurs within 3–5 days.[17–19] Comparable muskeg specimens have also been prepared at a constant temperature of −25 °C in order to mimic the sub-Arctic environment. Lower temperatures retard the kinetics of framework formation but solidified frameworks are obtained within 7–10 days. The wood fibers are derived from mulch that has the same geographical origin as the muskeg; the hydroxyethylcellulose further provides a means to covalently bond the wood fibers to the incipient silica framework. The use of these naturally sourced materials to facilitate solidification instead of commonly used metal-based geopolymer additives minimizes the environmental impact of the proposed densification process.[20,21] Indeed, the network can be readily dissolved by base treatment suggesting a facile means of restoring the soil to its native condition after use (*vide infra*). The formation of the siloxane framework within the muskeg matrix and the subsequent additional cross-linking induced by reaction with hydroxyethylcellulose results in expulsion of excess water and yields dry cross-linked free-standing samples.

The degree of cross-linking of the silicate frameworks is strongly affected by the nature of the silica precursors, the reaction pH, and the catalyst used. Indeed, the reaction of silicate

precursors with cellulose nanocrystal templates has been previously reported by MacLachlan and co-workers in a different context.[22–24] These researchers have constructed chiral silica matrices by the templated cross-linking of sol—gel precursors in architectures defined by chiral cellulosic templates followed by calcination to remove the soft template; the specific chirality and texturation of the deposited silica depend sensitively on the pH, water content, and evaporation rate.[24] Analogously, these parameters are found to strongly influence the reaction of silica precursors within the composite soil matrices depicted in Figure III.1 and thereby strongly influence the extent of strengthening (or densification) of the muskeg soils.[25–27] In particular, the hydrolysis and condensation reaction kinetics are strongly pH-dependent, and this parameter determines the overall densification achieved. Two distinct silica precursors, Na_2SiO_3 and tetraethylorthosilicate (TEOS), have been examined under acidic and basic conditions (Table A.4). Figure A.6 contrasts the composite materials obtained for the two precursors under acidic and basic conditions. Na_2SiO_3 clearly yields more homogeneous samples with a uniform hue indicative of uniform infiltration, whereas white powdery regions are discernible upon use of TEOS as the precursor suggesting some phase segregation. Density measurements have further been used as a metric to contrast the extent of silica incorporation and densification. Table 1 lists the density values measured for composites prepared using Na_2SiO_3 as the precursor with varying amounts of mulch and hydroxyethylcellulose additives. Unmodified muskeg has a density of 0.2 g·cm−3, which is strongly enhanced upon infiltration of the silica precursors and formation of the siloxane framework reinforced with various amounts of mulch and hydroxyethylcellulose (0.6–1.05 $g \cdot cm^{-3}$; Table III.1). In contrast, the density values of comparable composites prepared using TEOS as the precursor are in the range of ca. 0.2–0.5 $g \cdot cm^{-3}$. For instance, when 10 mL of the silica precursor is used with 2 g of

hydroxyethylcellulose and without the addition of supporting fillers, the Na_2SiO_3 precursor yields a density of 0.78 $g \cdot cm^{-3}$, whereas TEOS yields a density of 0.43 $g \cdot cm^{-3}$. The increased

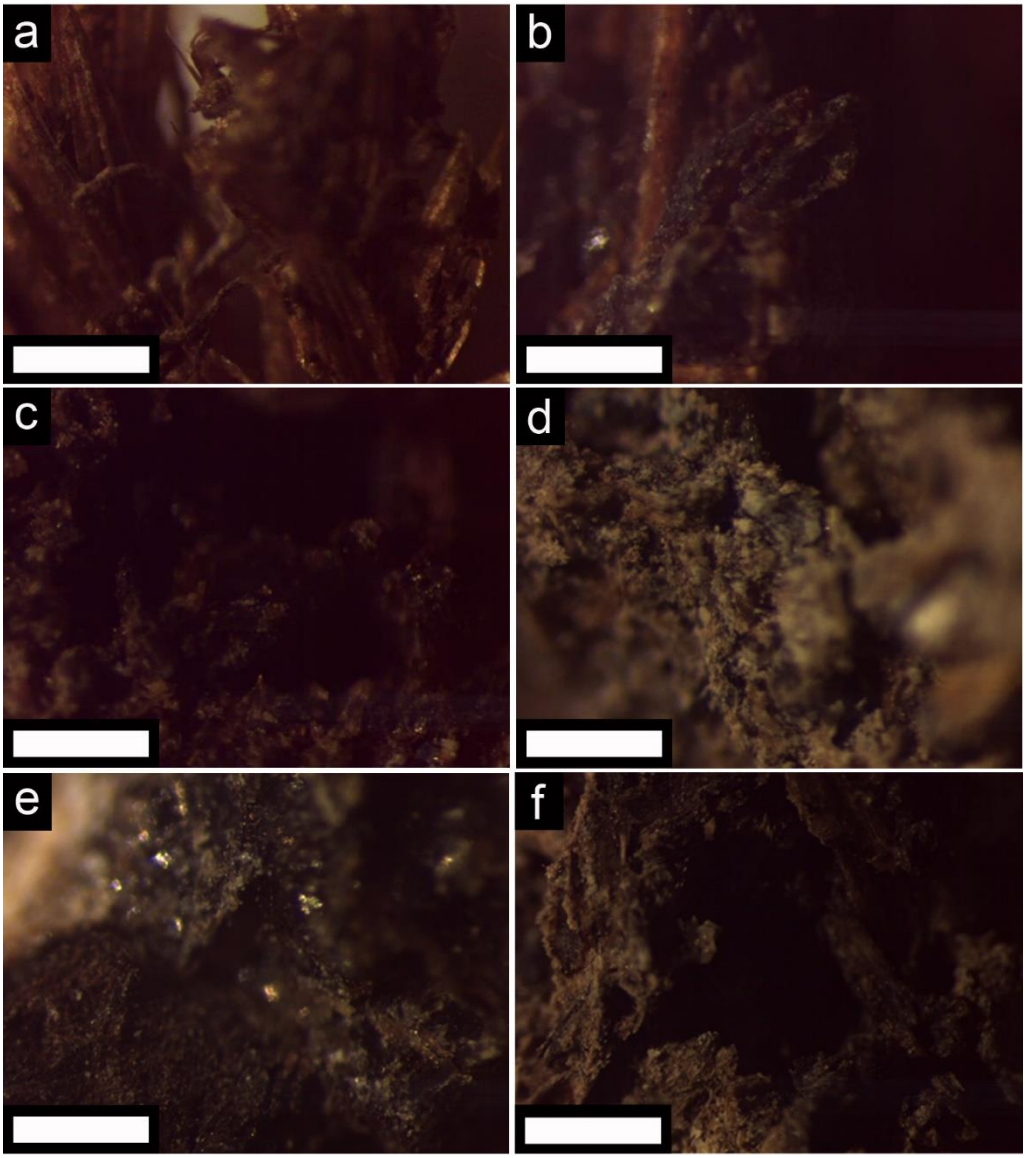

Figure III.2. Optical Microscopy Imaging of Muskeg and Reinforced Composites. Stereomicroscopy images of (a) unmodified and (b–f) modified muskeg with different concentrations of added Na_2SiO_3 and mulch: (b) 20 mL and 10 g; (c) 20 mL and 5 g; (d) 20 mL and 15 g; (e) 30 mL and 5 g; and (f) 30 mL and 15 g. The amount of NH_4OH and hydroxyethylcellulose were held constant for each modified muskeg specimen at 10 mL and 2 g, respectively. Scale bar = 1 mm.

densification observed with the silicate precursor is attributed to the accelerated kinetics of hydrolysis/condensation reactions with this precursor as previously noted in the literature.[28,29] Sai *et al*. have examined the kinetics of the gelation process of TEOS and Na_2SiO_3 and have found that at room temperature the latter precursor is completely reacted within 2 s, whereas the TEOS precursor requires several minutes to a few hours.[29,30] In TEOS, the four ethoxide groups attached to the Si center have to be initially hydrolyzed by water or hydroxide (under acidic or basic conditions, respectively) to generate orthosilicic acid $Si(OH)_4$ for further condensation reactions as per:

$$Si(OR)_4\ (l) + H_2O\ (l) \rightarrow Si(OH)_4\ (aq.) + 4ROH\ (aq.) \quad \text{(III.3)}$$

$$Si(OH)_4\ (aq.) + Si(OH)_4\ (aq.) \xrightarrow{NH_4OH} (OH)_3Si—O—Si(OH)_3\ (s) + H_2O\ (l) \quad \text{(III.4)}$$

In contrast, Na2SiO3 yields ionized corner-sharing oligomeric tetrahedral networks $[SiO_3]_n^{2-}$ in water, as per:

$$n \cdot Na_2SiO_3\ (s) \rightarrow 2n \cdot Na^+\ (aq.) + [SiO_3]_n^{2-}\ (aq.) \quad \text{(III.5)}$$

The ready availability of oligomeric $[SiO_3]_n^{2-}$ (where *n* is the degree of oligomerization) facilitates rapid formation of the siloxane backbone within the muskeg matrix, favors cross-linking with hydroxyl moieties on mulch and hydroxyethylcellulose (facilitating the incorporation of these additives within the monolithic composite), and yields an overall higher degree of condensation of silicate frameworks in comparison to TEOS where monomeric $Si(OH)_4$ need to be individually connected as per Equation III.4. In terms of equilibrium considerations, given the high water content in the muskeg matrix, the formation of a siloxane network as per Equation III.4 is hindered due to the competing back reaction. Given the

significantly improved results with Na_2SiO_3, only this precursor is further examined for subsequent evaluation of reaction conditions.

Muskeg itself is a mildly acidic soil comprising dead plants, peat soils, and excess water.[1–3] The color, gross morphological features, and structure of dried muskeg layers have been evaluated by stereomicroscopy as indicated in **Figure III.2**. Muskeg drained of water by straining comprises dark brown fibrous matter, predominantly disintegrated cellulosic materials.[2] Upon infiltration of Na_2SiO_3, hydrolysis, and condensation, the composite remains homogeneous but a shiny more reflective hue reflecting the formation of siloxane layers is discernible across the entire matrix.

The influence of pH on the hydrolysis/condensation reactions and chemical stability of modified muskeg has further been evaluated26. The muskeg soils themselves are slightly acidic with a pH of 6.82. The pH value is decreased to 2.13 when using TEOS and HCl catalyst whereas an increase in pH to 8.40 occurred when using TEOS and NH_4OH catalyst. The pH values for Na_2SiO_3 as the precursor are 0.37 when using HCl as the catalyst and 10.94 when using NH_4OH as the catalyst (Table A.4). The fundamental mechanism of the dissociative reaction (hydrolysis) of Na_2SiO_3 precursors is the nucleophilic attack of water (under acidic conditions) or hydroxide anions (under basic conditions) on the silicon centers. Under acidic conditions, protonated silicic acid is more susceptible to the nucleophilic attack of water molecules owing to the inductive effect, whereas under basic conditions, nucleophilic substitution is favored based on a direct nucleophilic attack of hydroxide ions.[31] However, when exposed to either strongly acidic or basic conditions, the reverse condensation reaction (depolymerization) is facilitated since water molecules created as a result of the gelation process can, in the presence of a catalyst, nucleophilically attack and cleave the Si-O-Si bonds (reverse

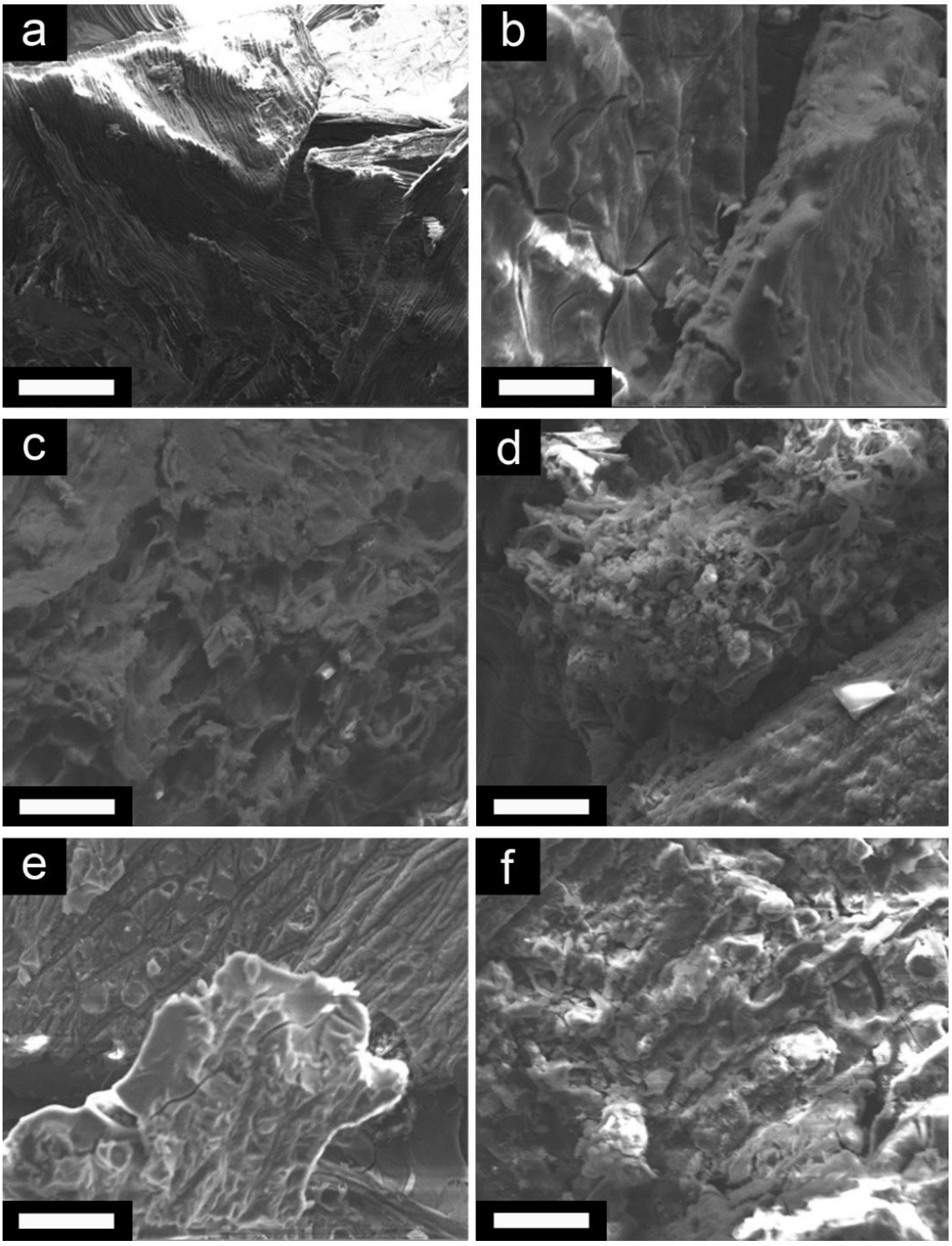

Figure III.3. Electron Microscopy Characterization of Reinforced Muskeg. SEM images of (a) unmodified muskeg and (b–f) modified muskeg with different added ratios of sodium silicate and mulch: (b) 20 mL and 10 g; (c) 20 mL and 5 g; (d) 20 mL and 15 g; (e) 30 mL and 5 g; and (f) 30 mL and 15 g. The hydroxyethylcellulose and NH4OH content was held constant for each modified muskeg specimen at 2 g and 10 mL, respectively. Scale bar = 50 μm.

reaction of Equation III.4). Consequently, upon using HCl as a catalyst, the low pH conditions (pH < 2.5) result in fragmentation of the composite frameworks within less than 24 h. Indeed, monolithic free-standing specimens could not be stabilized for either of the precursors, Na_2SiO_3 or TEOS, under highly acidic conditions (Figure A.6).[11,32] It is likely that the low pH also damages the cellulosic fibers derived from the wood mulch that form a network within the composite matrix compromising their ability to hold together the framework. In contrast, modified muskeg prepared under basic conditions (pH < 11) using NH4OH as the catalyst are weight bearing and form homogenous densified specimens as depicted by the digital photographs in the insets to **Figure III.3**.

III.4.2 Characterization of Reinforced Muskeg

The morphological characteristics of modified muskeg prepared using Na_2SiO_3 as the precursor and NH_4OH as the catalyst have been investigated by scanning electron microscopy (SEM) (Figure III.3). As observed in stereomicroscopy images (Figure III.2), unmodified muskeg exhibits a fibrous cellular structure. The constituent fibers are aligned and assembled within aggregates upon dehydration (Figure III.2a). However, upon infiltration and condensation of Na_2SiO_3, this fibrous morphology is no longer observed and instead amorphous silica deposition is observed completely enveloping the muskeg layers within continuous films (Figure III.2b and c) that appear to conformally coat the fibrous aggregates; the films are characterized by micro-cracks originating from removal of water (Figure III.2b).[33] Figure A.7 shows the presence of sub-micron-sized aggregates of silica particles at the surfaces of the modified muskeg. While there is some interesting literature precedence on the ability of semi-crystalline cellulosic materials to induce some degree of crystallinity in templated continuous polymeric matrices,[34,35] Figure A.8 indicates that the templated silica is entirely amorphous upon deposition

onto the mulch fibers. With increasing relative content of added Na_2SiO_3, a higher density of silica particles are observed at the surfaces (Figure III.3e and f) corresponding to homogeneous nucleation of silica in addition to the conformal heterogeneously nucleated siloxane network coating the muskeg. The chemical composition of muskeg samples before and after assembly of the siloxane framework has been further analyzed by energy dispersive X-ray spectroscopy (EDS, Figure A.9). The unmodified muskeg contains carbon (*ca*. 69.3 at.%), oxygen (*ca*. 29.7 at.%), and some aluminum (1.1 at.%, of mineral origin). The infiltration and condensation of silica precursors results in the appearance of sodium (4.1–8.1 at.%) and silicon (4.8–8.1 at.%), depending on the amount of Na_2SiO_3 used. EDS mapping suggests a homogeneous distribution of Si, C, and O across the modified muskeg composites for 5 and 10 g of added mulch suggesting uniform infiltration of the silica precursor, conformal coverage, and homogeneous distribution of the components of the modified muskeg composite (Figure A.10).

The nature of the silica matrix has been examined by Fourier transform infrared (FTIR) spectroscopy of the modified muskeg composites as depicted in **Figure III.4**. The as-prepared wet muskeg mainly shows strong characteristic vibrations of water, which is unsurprising given the high moisture content. Specifically, the symmetric stretching (3657 cm^{-1}), asymmetric stretching (3756 cm^{-1}), and bending (1595 cm^{-1}) modes of water are discernible.[36,37] After drying of the muskeg under ambient conditions, infrared-active modes characteristic of organic matter are observed as assigned in Figure III.4.[38] The modes at 3600–3700 cm^{-1} and 1595 cm^{-1} are significantly diminished in relative intensity upon elimination of water. After modification of the initial muskeg soils with Na_2SiO_3, mulch, and hydroxyethylcellulose, the band at 3300–3700 cm^{-1} is substantially diminished, attesting to the extrusion of trapped water from the modified

composite matrices. In contrast, new IR bands are observed at 1000–1500 cm^{-1}. In order to facilitate the assignment of these bands, a control experiment has been performed wherein amorphous SiO_2 has been prepared by reacting Na_2SiO_3 with NH_4OH. The FTIR spectrum of the amorphous SiO_2 sample thus prepared is also plotted with the specific mode assignments noted in Figure III.4. The observation of these modes for the modified muskeg unequivocally corroborate the stabilization of a siloxane framework.

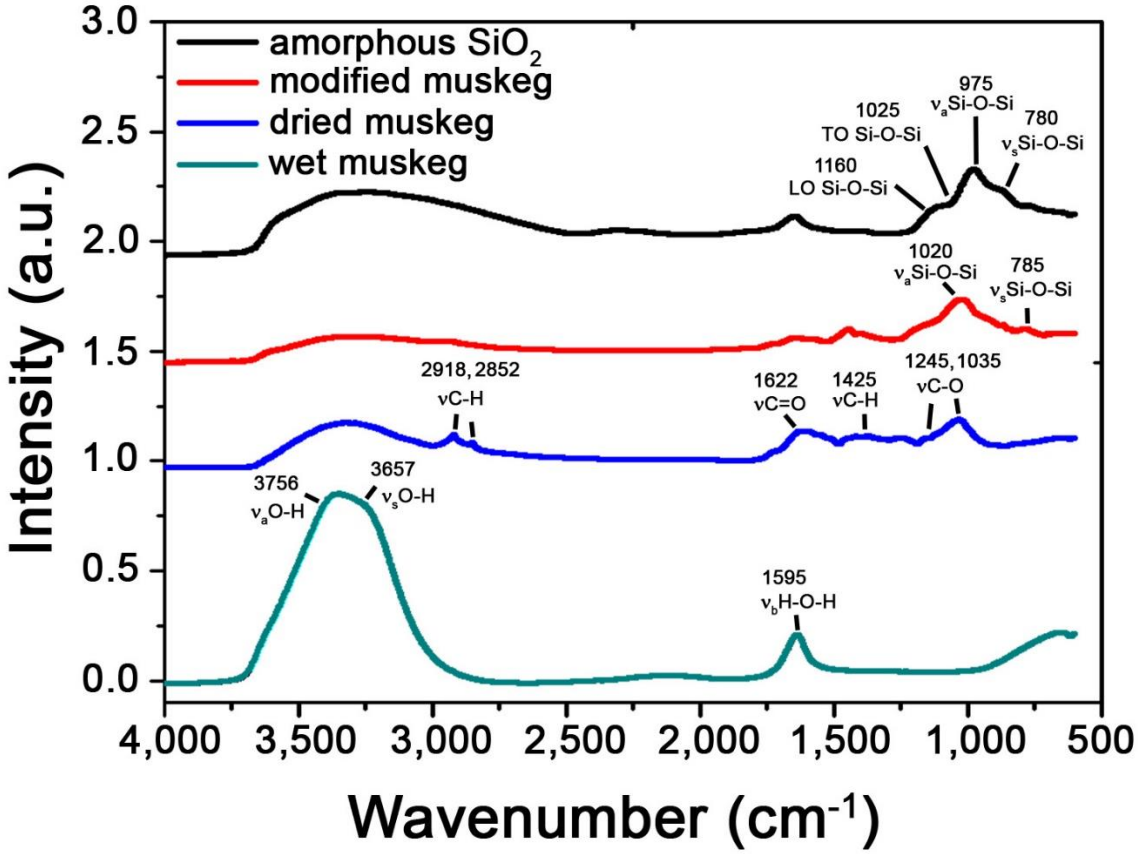

Figure III.4. Infrared Spectroscopy of Muskeg and Modified Composites. FTIR spectra of wet, dried, and modified muskeg, and an amorphous SiO_2 control sample prepared by reacting only Na_2SiO_3 with NH_4OH. The stabilization of a siloxane –Si-O-Si- framework and the substantial reduction of water content is clearly established.

III.4.3 Modified Muskeg as a Load-Bearing Composite

The density of modified muskeg prepared using Na_2SiO_3 has been mapped as a function of the amount of added silicate precursor and mulch (**Figure III.5**a) since these two parameters most strongly influence the density values. Table III.1 indicates that the amounts of added hydroxyethylcellulose and NH_4OH appear to have less of an influence on the measured density; varying the amount of NH_4OH from 5–15 mL while keeping the amount of Na_2SiO_3 and mulch

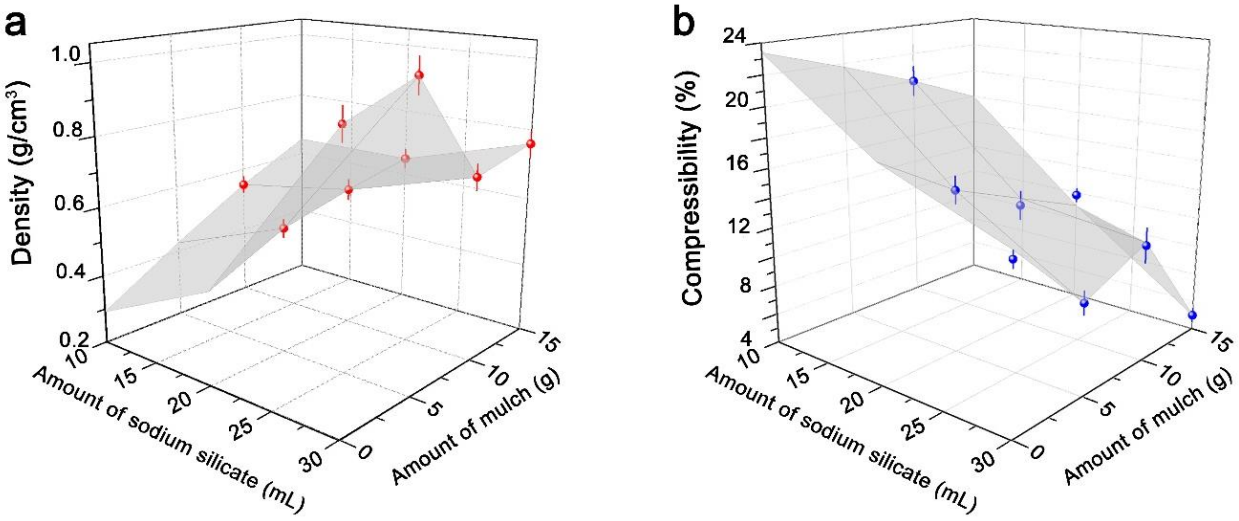

Figure III.5. 3D Mapping of Density and Compressibility of Modified Muskeg Composites as a Function of Added Precursors. (a) Density and (b) compressibility of modified muskeg as a function of the amount of added Na_2SiO_3 and mulch. The error bars depicted are calculated standard deviations for measurements made in triplicate.

constant at 20 mL and 10 g respectively, yields relatively closely spaced density values in the range of 0.62–0.70 g·cm−3. In contrast, the density of modified muskeg increases monotonically as a function of the amount of Na_2SiO_3 used from 0.55 g·cm^{-3} (10 mL), to 0.61 g·cm^{-3} (20 mL), and eventually to 0.72 g·cm^{-3} (30 mL) when the mulch content is held constant at 10 g (Table

III.1). Within this regime of compositional space, the addition of oligomeric silicate precursors gives rise to a denser siloxane matrix. These conditions also correspond to a homogeneous well-dispersed matrix, as discernible in Figure III.3b. The density of modified samples can be drastically increased up to 1.02 $g \cdot cm^{-3}$ by deploying 30 mL of Na_2SiO_3 and 5 g of mulch for the reinforcement of muskeg soils, which represents a dramatic improvement from the value of 0.20 $g \cdot cm^{-3}$ measured for unmodified muskeg. Given the relatively lower density of mulch (ca. 0.2 $g \cdot cm^{-3}$), inclusion of significantly greater amounts decreases the density. For a fixed amount of Na_2SiO_3 held constant at 30 mL, the addition of 15 g of mulch yields a density value of 0.76 $g \cdot cm^{-3}$,whereas the addition of 5 g of mulch leads to a density of 1.02 $g \cdot cm^{-3}$ (Table III.1). Nitrogen adsorption/desorption data is plotted in Figure A. 11 (between $P/P0$ values of 0.05 and 3); Type III isotherms are measured for both modified and unmodified muskeg samples with minimal interaction between nitrogen adsorbate molecules and the soil. The uptake of nitrogen is substantially reduced for the modified muskeg sample. A Brunauer—Emmett—Teller (BET) treatment of data suggests the specimen prepared using 30 mL Na_2SiO_3 and 15 g mulch has a surface area that is approximately halved from 3.41 $m^2 \cdot g^{-1}$ to 1.72 $m^2 \cdot g^{-1}$, further corroborating the measured densification (Figure A.11).

The mulch fibers are entangled to form a reinforcing network across the modified muskeg composite, whereas amorphous SiO_2 is brittle, and thus mechanical properties, particularly compressibility, is not necessarily correlated with density. The increased strength of modified muskeg has been evaluated by measuring the compressibility as a function of applied weight. **Video A.2** (uploaded separately) illustrates that the cross-linked modified muskeg monoliths have a substantially modified appearance, mechanical resilience, and compressibility

as compared to native muskeg. Figure A.12 depicts the placement of weights atop the modified muskeg; weights of up to 4 kg corresponding to pressures of *ca*. 20 kPa are applied and the

Table III.2. Compressibility of Modified Muskeg Composites. Measured compressibility for different modified muskeg compositions upon placement of solid weights as depicted in Figure A.12. Figure A.12 shows representative examples for the acquisition of data shown here.

Sample Composition	**Initial Displacement**	**5 kPa (1 kg)**	**10 kPa (2 kg)**	**20 kPa (4 kg)**
Unmodified muskeg	0%	73.0±8.1%	82.0±10.5%	82.0±10.5%
Na_2SiO_3 (30 mL)/Mulch (0 g) /NH_4OH (10 mL) /Hydroxyethylcellulose (2 g)	0%	0%	7.1±1.5%	14.5±3.1%
Na_2SiO_3 (30 mL)/Mulch (0 g) /NH_4OH (10 mL) /Hydroxyethylcellulose (4 g)	0%	0%	10.0±2.9%	20.0±3.5%
Na_2SiO_3 (20 mL)/Mulch (5 g) /NH_4OH (10 mL) /Hydroxyethylcellulose (2 g)	0%	0%	8.0±1.0%	15.0±1.8%
Na_2SiO_3 (30 mL)/Mulch (5 g) /NH_4OH (10 mL) /Hydroxyethylcellulose (2 g)	0%	0%	5.0±0.7%	10.0±1.5%
Na_2SiO_3 (30 mL)/Mulch (5 g) /NH_4OH (10 mL) /Hydroxyethylcellulose (4 g)	0%	0%	6.3±1.1%	12.5±2.3%
Na_2SiO_3 (10 mL)/Mulch (10 g) /NH_4OH (10 mL) /Hydroxyethylcellulose (2 g)	0%	0%	6.7±0.7%	20.0±2.1%

Table III.2. Continued

Sample Composition	Initial Displacement	5 kPa (1 kg)	10 kPa (2 kg)	20 kPa (4 kg)
Na_2SiO_3 (20 mL)/Mulch (10 g) /NH_4OH (10 mL) /Hydroxyethylcellulose (2 g)	0%	0%	6.3±0.6%	12.5±1.2%
Na_2SiO_3 (30 mL)/Mulch (10 g) /NH_4OH (10 mL) /Hydroxyethylcellulose (2 g)	0%	0%	5.9±1.1%	11.8±2.3%
Na_2SiO_3 (20 mL)/Mulch (10 g) /NH_4OH (5 mL) /Hydroxyethylcellulose (2 g)	0%	0%	8.3±1.0%	16.7±2.2%
Na_2SiO_3 (20 mL)/Mulch (10 g) /NH_4OH (15 mL) /Hydroxyethylcellulose (2 g)	0%	0%	6.3±0.5%	12.5±1.0%
Na_2SiO_3 (20 mL)/Mulch (10 g) /NH_4OH (10 mL) /Hydroxyethylcellulose (1 g)	0%	8.0±0.7%	15.4±1.8%	23.1±2.9%
Na_2SiO_3 (20 mL)/Mulch (10 g) /NH_4OH (10 mL) /Hydroxyethylcellulose (3 g)	0%	0%	7.7±0.9%	15.4±1.8%

Table III.2. Continued

Sample Composition	Initial Displacement	5 kPa (1 kg)	10 kPa (2 kg)	20 kPa (4 kg)
Na_2SiO_3 (20 mL)/Mulch (15 g) /NH_4OH (10 mL) /Hydroxyethylcellulose (2 g)	0%	0%	5.9±0.5%	11.8±1.0%
Na_2SiO_3 (30 mL)/Mulch (15 g) /NH_4OH (10 mL) /Hydroxyethylcellulose (2 g)	0%	0%	2.5±0.2%	5.0±0.4%
Na_2SiO_3 (30 mL)/Mulch (15 g) /NH_4OH (10 mL) /Hydroxyethylcellulose (4 g)	0%	0%	4.5±0.3%	4.5±0.3%

height displacement is measured and plotted in Figure III.5b as a function of the amount of Na_2SiO_3 and mulch. The percentage compressibility as a function of added pressure is listed in **Table III.2**.

Unmodified muskeg is strongly compressed with increasing weight as a result of the extrusion of water; Figure A.12 and Table III.2 depict a remarkable 82% decrease in the height of a muskeg specimen subjected to a 20 kPa pressure applied by placement of a solid weight. Figure III.5 indicates that the compressibility of modified muskeg monoliths is dramatically reduced with increasing addition of Na_2SiO_3 and mulch, consistent with the stabilization of more extensively cross-linked and densified frameworks. A combination of 30 mL of Na_2SiO_3 and 15

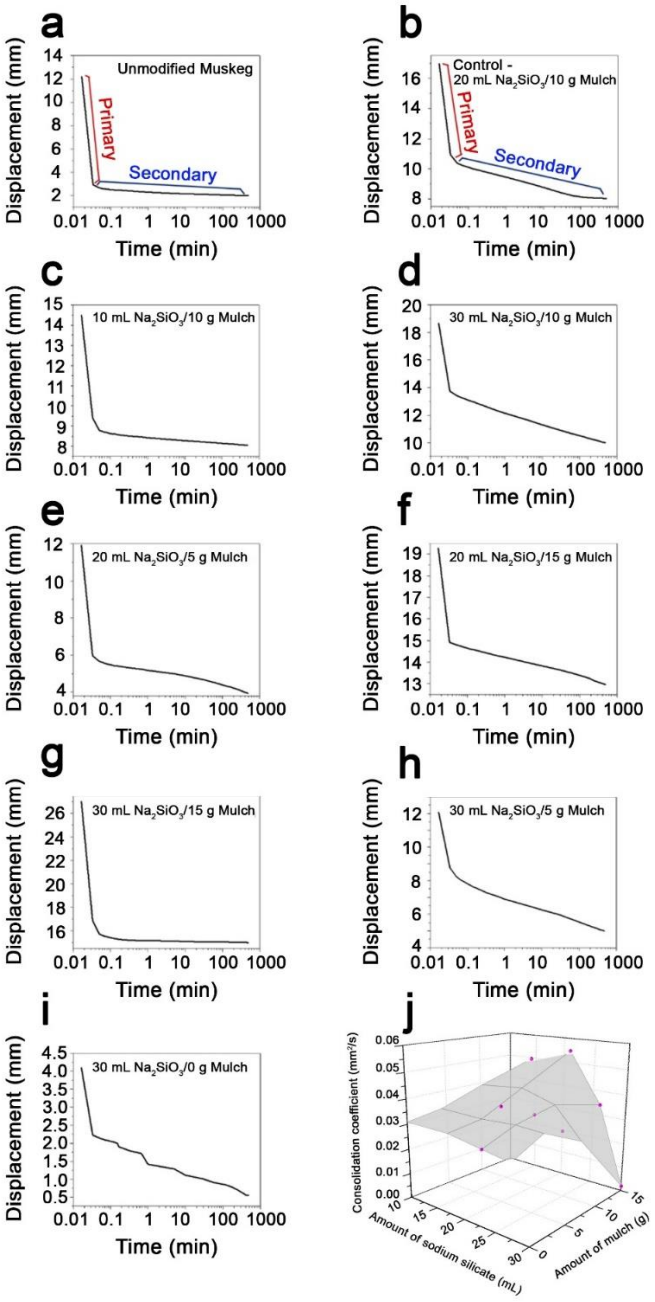

Figure III.6. Consolidation Testing of Modified Muskeg Composites. Unmodified muskeg (a) and modified samples (b-i) containing varying amounts of Na_2SiO_3 (in mL) and mulch (in units of grams). The amount of NH_4OH and hydroxyethylcellulose were held constant for each modified muskeg specimen at 10 mL and 2 g, respectively. The regions outlined in plots (a) and (b) indicate the primary (red) and secondary (blue) consolidation regimes. (j) 3D plot of coefficient of consolidation as a function of the amount of added Na_2SiO_3 and mulch. The measurement errors for the consolidation coefficient have been calculated through error propagation rules for elementary operations and functions.

Table III.3. Consolidation Testing of Modified Muskeg Composites. Measured height displacements and calculated coefficients of consolidation for modified muskeg composites for varying amounts of Na_2SiO_3 and mulch. All samples contained 10 mL of NH_4OH and 2 g of hydroxyethylcellulose.

Sample composition	H_i **(mm)**	H_F **(mm)**	***H%***	D_i **(mm)**	D_F **(mm)**	ΔD **(mm)**	C_a **(mm^2/min)**
Unmodified muskeg	12.2 ±0.02	2.0 ±0.01	83.6± 0.06%	9.268± 0.025	10.202 ±0.025	0.934 ±0.035	0.0085 ±0.0002
Na_2SiO_3 (10 mL)/Mulch (10 g)	14.5 ±0.04	8.0 ±0.02	44.8± 0.25%	5.094± 0.025	6.446 ±0.025	1.352 ±0.035	0.0095 ±0.0002
Na_2SiO_3 (20 mL)/Mulch (10 g)	19.3 ±0.03	9.0 ±0.02	53.4± 0.20%	8.364± 0.025	11.272 ±0.025	2.908 ±0.035	0.0310 ±0.0001
Na_2SiO_3 (30 mL)/Mulch (10 g)	19.5 ±0.04	10.0 ±0.02	48.7± 0.31%	5.758± 0.025	9.490 ±0.025	3.732 ±0.035	0.0398 ±0.0002
Na_2SiO_3 (20 mL)/Mulch (5 g)	13.0 ±0.03	4.0 ±0.01	69.2± 0.16%	7.032± 0.025	9.050 ±0.025	2.018 ±0.035	0.0381 ±0.0002
Na_2SiO_3 (20 mL)/Mulch (10 g)	19.3 ±0.04	9.0 ±0.02	53.4± 0.16%	8.364± 0.025	11.272 ±0.025	2.908 ±0.035	0.0310 ±0.0001
Na_2SiO_3 (20 mL)/Mulch (15 g)	23.2 ±0.05	13.0 ±0.03	43.9± 0.16%	8.280± 0.025	10.238 ±0.025	1.958 ±0.035	0.0194 ±0.0001
Na_2SiO_3 (30 mL)/Mulch (0 g)	4.1 ±0.01	0.5 ±0.00	87.8± 0.05%	1.876± 0.025	3.544 ±0.025	1.668 ±0.035	0.0610 ±0.0007
Na_2SiO_3 (30 mL)/Mulch (5 g)	12.0 ±0.02	5.1 ±0.01	57.5± 0.33%	3.306± 0.025	7.070 ±0.025	3.764 ±0.035	0.0613 ±0.0003

Table III.3. Continued

Sample composition	H_i (mm)	H_F (mm)	H%	D_i (mm)	D_F (mm)	ΔD (mm)	C_a (mm^2/min)
Na_2SiO_3 (30 mL)/Mulch (10 g)	19.5 ±0.04	10.0 ±0.02	48.7± 0.31%	5.758± 0.025	9.490 ±0.025	3.732 ±0.035	0.0398 ±0.0002
Na_2SiO_3 (30 mL)/Mulch (15 g)	27.0 ±0.05	15.0 ±0.03	44.4± 0.19%	10.142 ±0.025	12.004 ±0.025	1.862 ±0.035	0.0018 ±0.0001

g of mulch limits the compressibility to only 4%, more than an order of magnitude improvement over unmodified muskeg. The 3D maps of density and compressibility plotted in Figure III.5 identify a useful compositional space wherein both parameters can be substantially enhanced as compared to unmodified muskeg.

Figure III.6 and **Table III.3** present results of consolidation testing of muskeg as a function of the amounts of added Na_2SiO_3 and mulch. The amounts of hydroxyethylcellulose and NH_4OH have been held constant at 2 g and 10 mL, respectively, based on optimal conditions identified from Table III.1 and Table III.2. The consolidation tests performed here mimic the conditions of placement of a heavy load, either a road or a concrete slab, atop the modified muskeg. Because of the application of a heavy load (345 kPa over an 8 h time period), the initial compression normally observed upon preloading is absent and primary consolidation occurs rapidly within the first few seconds. During this stage, the excess pore water is extruded and the resulting void space is rapidly eliminated, as observed by a sharp drop in displacement.[15,39,40] Subsequently, the samples enter a secondary consolidation regime; the measured displacement in

both regimes is plotted as a function of time on a logarithmic scale (Figure III.6). The initial and final heights, height percentage change, initial and final displacement, and change in displacement for each specimen examined in Figure III.6 are listed in Table III.3. The time fitting method outlined by Lamb and Whitman has further been used to determine the coefficient of secondary consolidation for each sample.[41]

Unmodified muskeg shows a dramatic 83.6% change in height, almost entirely in the initial few seconds, corresponding principally to primary consolidation (Figure III.6a). The coefficient of secondary consolidation measured for unmodified muskeg is low at 0.0085, but considering the sample was almost completely compressed in the primary consolidation regime by the extrusion of the finite amount of water contained in this sample, this value does not provide a meaningful baseline for improvement upon modification. In stark contrast, the modified muskeg samples show substantially reduced overall consolidation (reflecting a 20–50% decrease of consolidation as a result of incorporating the siloxane framework and mulch). The modified sample containing 20 mL Na_2SiO_3 and 15 g mulch (Figure III.6f) shows the lowest percentage height change, limited to 43.9% after a period of 8 h; much of the consolidation is seen to occur in the secondary consolidation regime. Indeed, Figure III.6 indicates that increased Na_2SiO_3 content strongly modifies the consolidation behavior; as a result of the extrusion of water, primary consolidation is greatly reduced and secondary consolidation becomes the predominant mode with behavior reminiscent of clays yielding a predictable subsidence profile. Upon increasing the amount of the Na_2SiO_3 precursor from 10 to 20 to 30 mL while keeping the amount of mulch constant at 10 g, Table III.3 indicates that the overall change coefficient of secondary consolidation is monotonically increased from 0.0095 to 0.0310, and finally to 0.0398

$mm^2 \cdot min^{-1}$. Given the brittle nature of SiO_2, these results suggest that the relative mulch content strongly influences the extent of consolidation. The use of higher silicate precursor concentrations increases the density of the composite but yields a brittle material that is consolidated relatively rapidly and to a greater extent under the applied load. Holding the Na_2SiO_3 amount constant at 20 mL and successively increasing the mulch content from 5 to 10 to 15 g results in a monotonic decrease of the percentage change in height from 69.2% to 53.4%, and finally to 43.9%; analogously, the coefficient of secondary consolidation is decreased from 0.0381 to 0.0310, and finally to 0.0194 $mm^2 \cdot min^{-1}$ (Table III.3). Figure III.6j plots the variation of the coefficient of secondary consolidation as a function of the Na_2SiO_3 and mulch content. These results as well as the dataset where Na_2SiO_3 content is kept constant at 30 mL and the mulch content is varied both underscore the critical need to have a sufficient content of reinforcing mulch fibers without which the intrinsic brittle nature of amorphous silica ceramics, which are subject to fracture under compression is manifested. The percolative network of mulch fibers thus provides a mechanism for load transfer that is not otherwise accessible to the siloxane framework alone. The specimen containing 30 mL Na_2SiO_3 and 15 g mulch yields an attractive secondary consolidation coefficient value of 0.0018 $mm^2 \cdot min^{-1}$ and an overall change in height limited to *ca*. 44.4%.

Compressive testing has further been performed for the modified muskeg samples. While wet unmodified muskeg cannot be cast into an appropriate test structure, typical compressive strengths for fibrous sphagnum peat are in the range of 3.5–11 kPa.[40] **Figure III.7** indicates that a modified muskeg sample with 30 mL Na_2SiO_3 and 5 g mulch yields a compressive strength of 17.7 MPa; increasing the mulch content to 15 g increases the compressive strength to 33.8 MPa

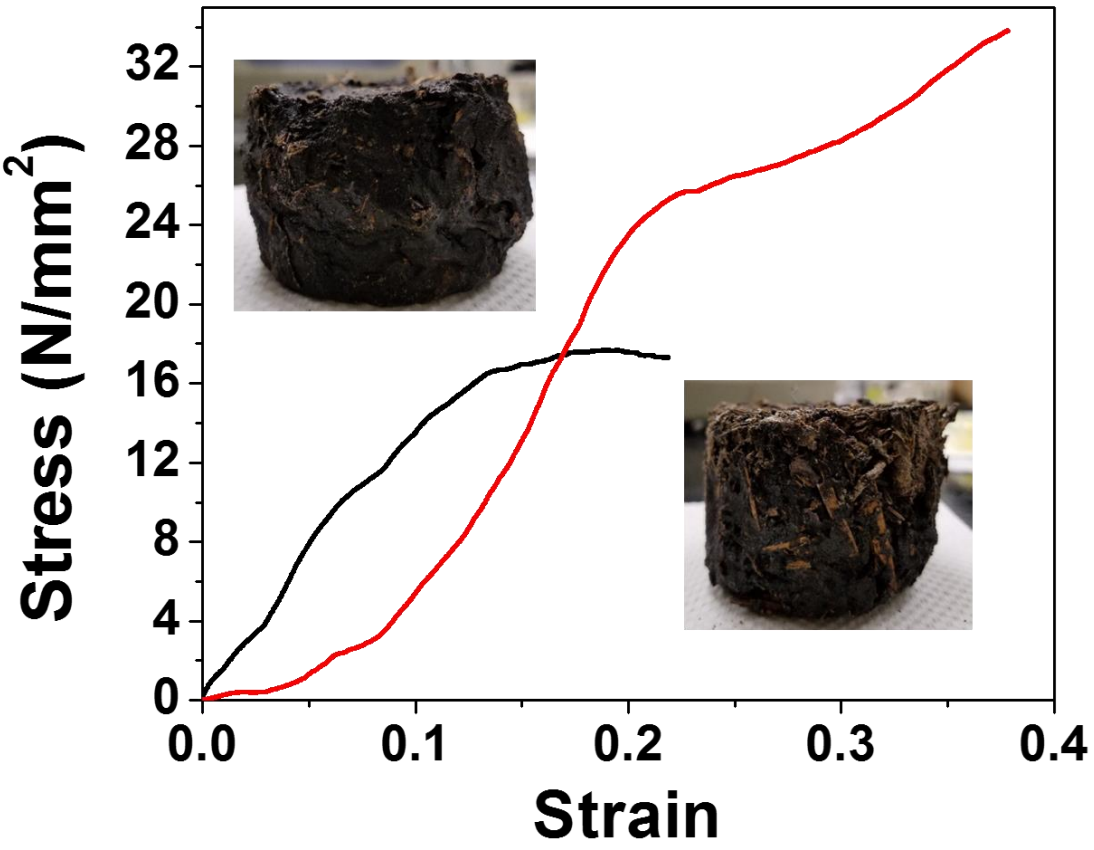

Figure III.7. Compressive Testing of Muskeg Composites. Stress *versus* strain curves measured for modified muskeg samples containing 5 g of mulch (black) and 15 g of mulch (red) while keeping the remaining additives constant at 30 mL Na_2SiO_3, 10 mL NH_4OH, and 2 g hydroxyethylcellulose. The insets depict photographs of the individual samples tested here.

despite a reduction in density (Table III.1). The observed enhancement in compressive strength further attests to the role of mulch in forming an interpenetrating network that is furthermore covalently bonded to the muskeg as a result of the formation of the siloxane framework (Figure III.1).

Recoverability of modified muskeg soil is paramount for reclamation and for environmental protection purposes. It is worth noting that several organosilanetriols has been

designed recently that show improved biocompatibility, and can be further degraded through photocatalytic processes upon exposure to UV light.[42] Reclamation of the modified muskeg has been achieved through a digestion process with gypsum inducing the reverse condensation process (reverse reaction of Equation (III.4)) wherein dissolution of the silicate framework occurs upon treatment with a strong base (NaOH) and the sodium-ions are exchanged for calcium-ions from the gypsum. Elemental analysis shows the residual free sodium to be within the allowable limit of 200 $mg \cdot L^{-1}$ (specified by environmental regulatory agencies in Alberta) in the resulting mulch and muskeg. Future work will examine the inclusion of biodegradable matrices such as poly(ethylene glycol) in conjunction with photocatalytically degradable organosilanetriols.[42]

III.5 Conclusions

Strengthening muskeg has been a formidable challenge with tremendous global implications for the fossil fuel industry given its increasing reliance on extraction of fossil fuel deposits from unconventional sub-Arctic deposits. The seeming intractability of muskeg arises from its high compressibility, high water content, and hollow cellular structure as well as the need to attain solidification in a reversible manner that preserves sub-Arctic habitats. In this work, we report a facile synthetic route for reinforcing muskeg with native mulch fibers with the help of inorganic silicate precursors that facilitate *in situ* formation of a siloxane network upon infiltration of liquid precursors between the pores of muskeg fibers. The approach developed here, based on catalyzed formation of a siloxane network with added cellulose providing a

second cross-linking mode, allows for an increase of density as well as compressive strength while reducing the compressibility of the obtained load-bearing and low-subsidence composites.

III.6 References

(1) Kroetsch, D. J.; Geng, X.; Chang, S. X.; Saurette, D. D. Organic Soils of Canada: Part 1. Wetland Organic Soils. *Can. J. Soil Sci.* **2011**, *91* (5), 807–822.

(2) Lee, J. S.; Seo, S. Y.; Lee, C. Geotechnical and Geophysical Characteristics of Muskeg Samples from Alberta, Canada. *Eng. Geol.* **2015**, *195*, 135141.

(3) Massah, J.; Noorolahi, S. Characterization of the Mechanical Properties of Muskeg Site in Pakdasht Area. *Agric. Eng.* **2010**, *13*.

(4) Phukan, A. Design Methods for Muskeg Area Roads https://ntl.bts.gov/lib/11000/11500/11560/641_ak.pdf (**1982**).

(5) Radforth, N. *Muskeg as an Engineering Problem*; **1969**.

(6) Jarret, P. Evaluation of Geogrids for Construction of Roadways over Muskeg. In *Polymer Grid Reinforcement*; Thomas Telford Publishing, **1984**.

(7) Macfarlane, I. C. *Muskeg Engineering Handbook*; University of Toronto Press, **1969**.

(8) Wong, J. Y.; Garber, M.; Radforth, J. R.; Dowell, J. T. Characterization of the Mechanical Properties of Muskeg with Special Reference to Vehicle Mobility. *J. Terramechanics* **1979**, *16* (4), 163–180.

(9) Dimas, D.; Giannopoulou, I.; Panias, D. Polymerization in Sodium Silicate Solutions: A Fundamental Process in Geopolymerization Technology. *J. Mater. Sci.* **2009**, *44* (14), 3719–3730.

(10) Khale, D.; Chaudhary, R. Mechanism of Geopolymerization and Factors Influencing Its

Development: A Review. *J. Mater. Sci.* **2007**, *42* (3), 729–746.

(11) Brady, P. V.; Walther, J. V. Controls on Silicate Dissolution Rates in Neutral and Basic pH Solutions at 25°C. *Geochim. Cosmochim. Acta* **1989**, *53* (11), 2823–2830.

(12) O'Loughlin, T. E.; Martens, S.; Ren, S. R.; McKay, P.; Banerjee, S. Orthogonal Wettability of Hierarchically Textured Metal Meshes as a Means of Separating Water/Oil Emulsions. *Adv. Eng. Mater.* **2017**, *19* (5), 1–8.

(13) Pelcher, K. E.; Crawley, M. R.; Banerjee, S. Silica-Shell Encapsulation and Adhesion of VO_2 Nanowires to Glass Substrates: Integrating Solution-Derived VO_2 Nanowires within Thermally Responsive Coatings. *Mater. Res. Express* **2014**, *1* (3), 35014.

(14) McKenzie, R. H.; Woods, S. A. *Management of Sodic Soils in Alberta*; **2010**.

(15) Robinson, R. G.; Allam, M. M. Effect of Clay Mineralogy on Coefficient of Consolidation. *Clays Clay Miner.* **1998**, *46* (5), 596–600.

(16) Coradin, T.; Livage, J. Aqueous Silicates in Biological Sol – Gel Applications : New Perspectives for Old Precursors. **2007**, *40* (9), 819–826.

(17) Brinker, C. J.; Scherer, G. W. *Sol-Gel Science: The Physics and Chemistry of Sol-Gel Processing*; Academic Press, **2013**.

(18) Ellerby, L. M.; Nishida, C. R.; Nishida, F.; Yamanaka, S. A.; Dunn, B.; Valentine, J. S.; Zink, J. I. Encapsulation of Proteins in Transparent Porous Silicate-Glasses Prepared by the Sol-Gel Method. *Science.* **1992**, *255* (5048), 1113–1115.

(19) Klien, L. C. Sol-Gel Processing of Silicates. *Annu. Rev. Mater. Res.* **1985**, *15*, 227–248.

(20) Gruda, N. The Effect of Wood Fiber Mulch on Water Retention, Soil Temperature and Growth of Vegetable Plants. *J. Sustain. Agric.* **2008**, *32* (4), 629–643.

(21) El-Haddad, M. N. Hydroxyethylcellulose Used as an Eco-Friendly Inhibitor for 1018 c-

Steel Corrosion in 3.5% NaCl Solution. *Carbohydr. Polym.* **2014**, *112*, 595–602.

(22) Shopsowitz, K. E.; Qi, H.; Hamad, W. Y.; MacLachlan, M. J. Free-Standing Mesoporous Silica Films with Tunable Chiral Nematic Structures. *Nature* **2010**, *468* (7322), 422–426.

(23) Shopsowitz, K. E.; Hamad, W. Y.; MacLachlan, M. J. Flexible and Iridescent Chiral Nematic Mesoporous Organosilica Films. *J. Am. Chem. Soc.* **2012**, *134* (2), 867–870.

(24) Kelly, J. A.; Giese, M.; Shopsowitz, K. E.; Hamad, W. Y.; MacLachlan, M. J. The Development of Chiral Nematic Mesoporous Materials. *Acc. Chem. Res.* **2014**, *47* (4), 1088–1096.

(25) Liu, J.; Yang, Q.; Zhao, X. S.; Zhang, L. Pore Size Control of Mesoporous Silicas from Mixtures of Sodium Silicate and TEOS. *Microporous Mesoporous Mater.* **2007**, *106* (1–3), 62–67.

(26) Phair JW, and V. D. J. . Effect of Silicate Activator pH on the Leaching and Material Characteristics of Waste-Based Inorganic Polymers. *Miner. Eng.* **2001**, *14(3)* (3), 289–304.

(27) Pope, E. J. A.; Mackenzie, J. D. Sol-Gel Processing of Silica. II. The Role of the Catalyst. *J. Non. Cryst. Solids* **1986**, *87* (1–2), 185–198.

(28) Gill, I.; Ballesteros, A. Encapsulation of Biologicals within Silicate, Siloxane, and Hybrid Sol- Gel Polymers: An Efficient and Generic Approach. *J. Am. Chem. Soc.* **1998**, *120* (34), 8587–8598.

(29) Sai, H.; Xing, L.; Xiang, J.; Cui, L.; Jiao, J.; Zhao, C.; Li, Z.; Li, F.; Zhang, T. Flexible Aerogels with Interpenetrating Network Structure of Bacterial Cellulose–Silica Composite from Sodium Silicate Precursor via Freeze Drying Process. *RSC Adv.* **2014**, *4* (57), 30453.

(30) Aelion, R.; Loebel, A.; Eirich, F. Hydrolysis of Ethyl Silicate. *J. Am. Chem. Soc.* **1950**, *72*

(12), 5705–5712.

(31) Corriu, R. J. P.; Leclercq, D. Recent Developments of Molecular Chemistry for Sol–Gel Processes. *Angew. Chemie Int. Ed. English* **1996**, *35* (1314), 1420–1436.

(32) Elshafie, S.; Whittleston, G. Evaluating the Efficiency of Basalt and Glass Fibres on Resisting the Alkaline , Acid , and Thermal Environments. *Am. J. Mater. Sci.* **2016**, *6* (1), 19–34.

(33) Jia, S.; Banerjee, S.; Lee, D.; Bevk, J.; Kysar, J. W.; Herman, I. P. Fracture in Electrophoretically Deposited CdSe Nanocrystal Films. *J. Appl. Phys.* **2009**, *105* (10).

(34) Lee, W. J.; Clancy, A. J.; Kontturi, E.; Bismarck, A.; Shaffer, M. S. P. Strong and Stiff: High-Performance Cellulose Nanocrystal/poly(vinyl Alcohol) Composite Fibers. *ACS Appl. Mater. Interfaces* **2016**, *8* (46), 31500–31504.

(35) Camarero-Espinosa, S.; Boday, D. J.; Weder, C.; Foster, E. J. Cellulose Nanocrystal Driven Crystallization of Poly(D,L-Lactide) and Improvement of the Thermomechanical Properties. *J. Appl. Polym. Sci.* **2015**, *132* (10), 1–11.

(36) Aguiar, H.; Serra, J.; González, P.; León, B. Structural Study of Sol-Gel Silicate Glasses by IR and Raman Spectroscopies. *J. Non. Cryst. Solids* **2009**, *355* (8), 475–480.

(37) Musić, S.; Filipović-Vinceković, N.; Sekovanić, L. Precipitation of Amorphous SiO_2 Particules and Their Properties. *Brazilian J. Chem. Eng.* **2011**, *28* (1), 89–94.

(38) Nawi, M. A.; Ibrahim, M. Z. Synthesis, Characterization and Coagulating Mechanism of Peat Coagulant. *Indo. J. Environ. Chem. Toxicol.* **2005**, *4*, 1–5.

(39) Baumgartl, T.; Köck, B. Modeling Volume Change and Mechanical Properties with Hydraulic Models. *Soil Sci. Soc. Am. J.* **2004**, *68* (1), 57.

(40) Kruse, G. A. M.; den Haan, E. J. Characterisation and Engineering Properties of Dutch

Peats. In *Characterisation and Engineering Properties of Natural Soils, Two Volume Set*; Taylor & Francis, **2006**.

(41) Lambe, T. W.; Whitman, R. V. *Soil Mechanics*; John Wiley & Sons, **1969**.

(42) Pietschnig, R.; Spirk, S. The Chemistry of Organo Silanetriols. *Coord. Chem. Rev.* **2016**,

CHAPTER IV

X-RAY EXCITED PHOTOLUMINESCENCE NEAR THE GIANT RESONANCE IN SOLID-SOLUTION $GD_{1-X}TB_XOCL$ NANOCRYSTALS AND THEIR RETENTION UPON SOLVOTHERMAL TOPOTACTIC TRANSFORMATION TO $GD_{1-X}TB_XF_3$*

IV.1 Overview

Design rules for X-ray phosphors are much less established as compared to their optically stimulated counterparts owing to the absence of a detailed understanding of sensitization mechanisms, activation pathways and recombination channels upon high-energy excitation. Here, we demonstrate a pronounced modulation of the X-ray excited photoluminescence of Tb^{3+} centers upon excitation in proximity to the giant resonance of the host Gd^{3+} ions in solid-solution $Gd_{1-x}Tb_xOCl$ nanocrystals prepared by a non-hydrolytic cross-coupling method. The strong suppression of X-ray excited optical luminescence at the giant resonance suggests a change in mechanism from multiple electron—hole pair generation to single thermal electron—hole pair formation and Auger decay processes. The solid-solution $Gd_{1-x}Tb_xOCl$ nanocrystals are further topotactically transformed with retention of a nine-coordinated cation environment to solid-solution $Gd_{1-x}Tb_xF3$ nanocrystals upon solvothermal treatment with XeF_2. The metastable hexagonal phase of GdF_3 can be stabilized at room temperature through this topotactic approach and is transformed subsequently to the orthorhombic phase. The fluoride nanocrystals indicate an analogous but blue-shifted modulation of the X-ray excited optical luminescence of the Tb^{3+} centers upon X-ray excitation near the giant resonance of the host Gd^{3+} ions.

* Reproduced with permission from "X-ray Excited Photoluminescence Near the Giant Resonance in Solid-Solution $Gd_{1-x}Tb_xOCl$ Nanocrystals and their Retention Upon Solvothermal Topotactic Transformation to $Gd_{1-x}Tb_xF_3$." G.R. Waetzig, G. A. Horrocks, J.W. Jude, L. Zuin, and S. Banerjee, *Nanoscale,* **2016**, *8*, 979-986. Reproduced by permission of Royal Society of Chemistry. <http://pubs.rsc.org/en/content/articlelanding/2016/nr/c5nr07819a#!divAbstract>

IV.2 Introduction

As a result of their strongly localized and electron correlated character, the 4*f* states of lanthanide cations constitute narrow quasi-atomic bands in the solid state.[1–3] The characteristic emission spectra for luminescent lanthanide cations are thus primarily a function of the dipole and multipole allowed transitions and the electronic configuration of the specific cation since the various states of $4f^n$ configurations are split by less than 0.2 eV under the influence of an external electrostatic field. Nevertheless, the specificities of the activation pathways and recombination channels are strongly influenced by the nature of the anion, the lattice type and crystallinity of the host matrix, the presence of additional co-dopants, and the separation between the luminescent centers.[4–6] These parameters provide valuable structural tools for tuning the luminescent properties (color, brightness, and lifetime) of phosphors and scintillators constructed using trivalent rare-earth cations as the active components, and thus have widespread applicability to the construction of flat panel displays, field-emission displays, radiation detectors, light-emitting diodes, and bioimaging probes.[4,6–8] The excitation of lanthanide luminescence by VUV radiation, X-rays, and electrons is mechanistically quite distinct from direct optical excitation and involves the generation of core-holes, diffusion of electron—hole pairs, and thermalization within the host matrix.[9–12] While direct optical excitation of luminescent lanthanide activators is well understood and the $4f^n$ energy level diagrams are readily accessible from both measurement and theory,[12] energy transfer processes upon VUV, X-ray, or electronic excitation are much less explored even though the fundamental understanding of such processes is critical to the design of radiation detectors, scintillators, and

cathodoluminescent devices. In this chapter, we report the pronounced modulation of the optical luminescence of Tb^{3+} cations close to the giant resonance of the host GdOCl matrix.

GdOCl crystallizes in the tetragonal matlockite PbFCl structure (**Figure IV.1,** inset) with a space group of P4/*nmm* wherein alternating cationic layers of $(GdO)_n^{n+}$ are separated by anionic chloride layers arrayed along the crystallographic *c* direction.[13–15] Each Gd cation resides within a C_{4v} monocapped square anti-prism where it is coordinated by four oxygen atoms in an underlying plane and five chloride ions in the layer above with the fifth chloride ion being derived from the next-to-nearest anionic layer. While this structure is not truly 2D in the same vein as the SmSI structure adopted by the latter lanthanides (Ho and beyond),[15,16] the distinct separation of the chloride layers and the high ionic conductivity of these materials render them intriguing targets for anionic topotactic transformations.[17,18] In particular, the short diffusion lengths accessible at nanometer-sized dimensions facilitate chemical transformations that have no analogies in the bulk and indeed such distinctive reactivity derived upon scaling materials to finite sizes is of great relevance to the manifestation of new physical phenomena in nanomaterials and the stabilization of novel (oftentimes metastable) crystal structures.[19–23] Given the typically much greater diffusivities of cations, anionic transformations are much less explored.[24,25] In this chapter we present a solvothermal topochemical route for the conversion of GdOCl to GdF3 upon reaction with XeF_2. The modulation of X-ray stimulated photoluminescence of Tb^{3+} observed near the giant resonance of Gd^{3+} is retained upon topotactic transformation.

The PbFCl structure type has some particularly desirable characteristics that render lanthanide oxychlorides attractive as host matrices for luminescent lanthanide cations. The low phonon cut-off energies of rare-earth oxychlorides allow for efficacious energy transfer to dopant

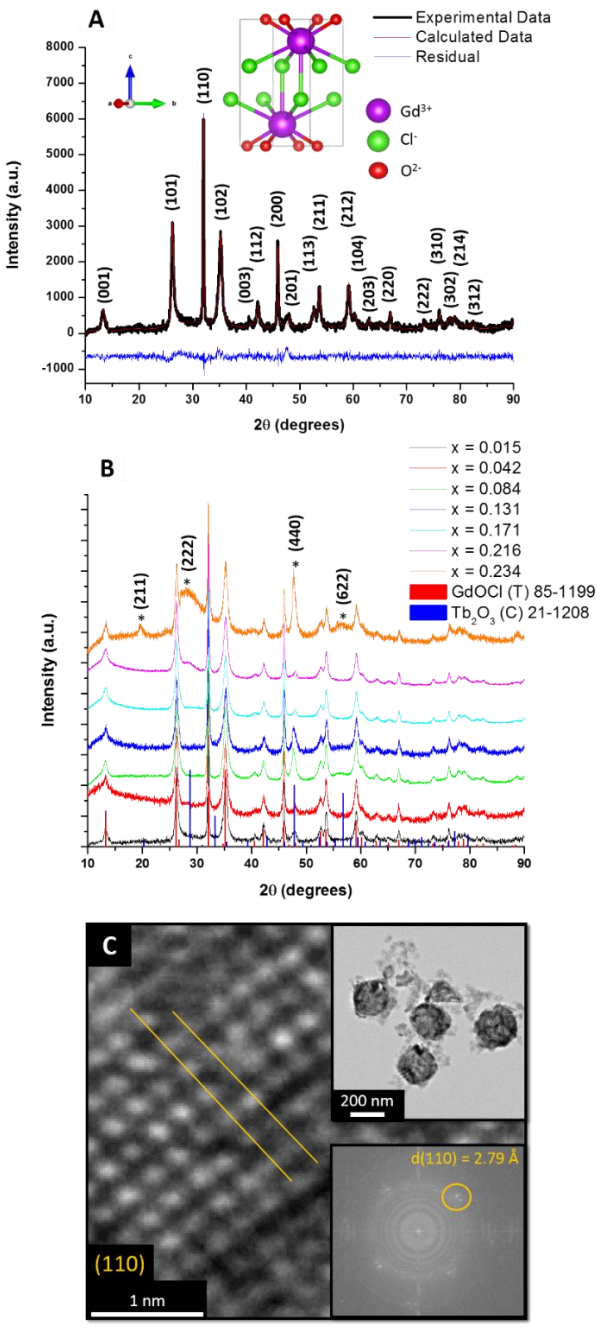

Figure IV.1. (A) Refinement of the powder XRD pattern obtained for $Gd_{0.985}Tb_{0.015}OCl$. The calculated pattern (red) matches the observed reflections (black). The refined unit cell parameters are listed in Table 1. The residuals are depicted in blue. The inset indicates the refined crystal structure. (B) Powder XRD patterns of $Gd_{1-x}Tb_xOCl$ ($0.01 \leq x \leq 0.24$). The asterisked reflections at $2\theta = 20$ and 28° indicate the emergence of reflections corresponding to Tb_2O_3. (C) HRTEM image of $Gd_{0.985}Tb_{0.015}OCl$ nanocrystals; the separation between the (110) lattice planes is clearly visible. The insets depict the quasi-spherical morphology of the obtained materials as well as the FFT pattern indicating the d-spacing for the (110) lattice plane.

luminescent ions, whereas the anisotropic layered structures optimally separate cations, thereby limiting the cross-relaxation mechanisms.[6,26–30] These structures further exhibit high chemical and thermal stabilities and form solid solutions of lanthanides across an expansive range of compositions.

In our previous work, we have demonstrated a solution phase cross-coupling route for the preparation of rare-earth oxychloride nanocrystals with well-defined shapes based on the condensation of metal alkoxides and metal halides.[8,31–33] This synthetic route allows for the facile substitutional incorporation of luminescent lanthanide cations within the oxychloride lattice. Solid-solution $Gd_{1-x}Tb_xOCl$ nanocrystals are prepared in this chapter as model systems to demonstrate an unprecedented modulation of Tb^{3+} luminescence near the giant resonance of the host matrix and to further examine the topotactic transformation under solvothermal conditions.

IV.3 Experimental

IV.3.1 Synthesis

$TbCl_3$, $GdCl_3$, $Gd(O^iPr)_3$, XeF_2, and TOPO were purchased from Strem Chemicals and used as received. The synthesis of GdOCl nanostructures has been described in the previous work and is modified here to incorporate a broad range of Tb^{3+} species.[8,32,33] In the synthesis of GdOCl nanostructures, 2 mmol of anhydrous $GdCl_3$, 2 mmol of $Gd(O^iPr)_3$, and 25 mmol of TOPO were weighed into a three-neck roundbottom flask within an argon-filled glovebox. In order to prepare ternary solid-solution nanocrystals, the desired molar equivalents of Tb^{3+} ions were included within the reaction mixture by substituting an appropriate amount of $GdCl_3$ for TbCl3. The reaction mixture was heated with stirring to a temperature of 340°C under standard

Schlenk conditions. After 2 h of heating, the reaction mixture was cooled to *ca*. 70°C and the as-prepared nanocrystals were flocculated by the addition of acetone. The nanocrystals were then recovered by centrifugation for 25 min at 12 000 rpm. The nanocrystals were further dispersed in hexanes and centrifuged for 5 min at 1500 rpm. The nanocrystals were finally recovered by centrifugation of are-suspended mixture at 12 000 rpm for 25 min.

Topotactic transformation of GdOCl to GdF_3 was performed solvothermally within a Parr acid digestion vessel. In a typical synthetic procedure, 0.25 mmol of $Gd_{1-x}Tb_xOCl$ nanocrystals were mixed with 0.75 mmol of XeF_2, and 2 mL of degassed acetonitrile and placed within a polytetrafluoroethylene (PTFE) cup, which in turn was placed within a sealed autoclave within an argon-filled glovebox. The autoclave was then heated to 210°C for 72 h. The resulting powder was filtered and washed with copious amounts of acetone.

IV.3.2 Characterization

Phase purity was established and the unit cell parameters were refined using laboratory powder X-ray diffraction (XRD) data acquired using a Bruker-AXS D8 Advance Bragg-Brentano X-ray powder diffractometer with Cu Kα radiation (λ = 1.5418 Å). Rietveld refinements were performed using the GSAS/EXPGUI software. The particle morphology was evaluated by transmission electron microscopy (TEM) using a FEI Tecnai G2 F20 ST instrument operated at an accelerating voltage of 200 kV. The samples were prepared for TEM by dispersing the nanocrystals in 2-propanol and depositing onto 400-mesh carboncoated Cu grids. The stoichiometry of the ternary solidsolution nanocrystals was determined by inductively coupled plasma-mass spectrometry (ICP-MS) using a Perkin Elmer DRCII instrument. The samples were prepared by acid digestion in an aqueous solution of concentrated HNO3. X-ray excited optical luminescence (XEOL) and Gd/Tb $N_{4,5}$ X-ray absorption near edge structure

(XANES) spectra were acquired at the Variable Line Spacing-Plane Grating Monochromator (VLS-PGM) beamline ($E/\Delta E > 10\,000$ in the relevant energy range) of the Canadian Light Source.[34] The XAS system at the VLS-PGM beamline allows for the simultaneous collection of the total fluorescence yield (FLY), total electron yield (TEY), and X-ray excited optical luminescence (XEOL). The XANES spectra were acquired using the beamline's high-energy grating, and scanning the energy range from 130–170 eV with a spectral resolution of 0.1 eV at a pressure of 1×10^{-8} Torr, with the FLY signal recorded by using a microchannel plate detector, whereas the total electron yield is measured as the drain current produced during sample ionization.[35] All spectra have been normalized to the intensity of the photon beam as measured by the drain current produced by a nickel mesh situated (transmission 90%) upstream of the sample. The optical luminescence data were collected using an Ocean Optics QE65000 monochromator with a fiber-optic feed-through over a working range of 200–900 nm. The nanocrystal powders were deposited on a carbon tape in air and studied at room temperature. Optically stimulated photoluminescence and absorption measurements were acquired using a Horiba PTI QuantaMaster 40 spectrofluorometer and a Hitachi U4100 UV-Vis-NIR spectrophotometer, respectively. Photoluminescence measurements were analyzed over a range of 450–700 nm at an excitation wavelength of 277 nm. For absorption and optically stimulated photoluminescence measurements, a 1.5×10^{-3} M colloidal dispersion of the nanocrystals was prepared in hexanes.

IV.4 Results and Discussion

IV.4.1 Solid-Solutions and Optically Stimulated Photoluminescence

In our previous work, we have established that the formation of oxychloride nanocrystals upon the reaction of alkoxide and chloride precursors proceeds through an initial ligand

exchange to stabilize a lanthanide chloroalkoxide (*e.g.*, $LnCl_2(O^iPr)$) followed by condensation of these species to constitute the LnOCl framework with the elimination of alkyl halides.[14,15] Figure IV.1A shows the refined powder XRD pattern of GdOCl nanocrystals; the refined structure is depicted in the inset. **Table IV.1** lists the unit cell parameters derived from a Rietveld fit to the data. The calculated unit cell parameters a, b = 3.9451 Å, and c = 6.6546 Å are consistent with data reported previously in the literature for GdOCl (PDF 85-1199). Figure IV.1B indicates the XRD patterns acquired for GdOCl nanocrystals with increasing incorporation of Tb. The indicated Tb compositions have been derived from ICP-MS measurements and closely match the precursor ratios (Table A.5, shows the correspondence between the intended and actual dopant concentrations).

Substitutional doping of nanocrystals can be exceedingly difficult owing to the inherent self-purification effects wherein the dopant atoms segregate to the surface and are eliminated. However, the ionic radii of Gd^{3+} (1.017 Å) and Tb^{3+} (1.095 Å) differ by only 1.1% and we observe complete miscibility of Tb^{3+} in the GdOCl lattice up to a concentration of 21.6 at% with only slight lattice contraction in this regime. However, at a concentration of *ca*. 23.4 at% of Tb, we note the appearance of an oxide phase crystallized in the Tb_2O_3 structure (PDF 21-1208) as indicated by the asterisked reflections in Figure IV.1B. Figure IV.1C indicates low-magnification and HRTEM images of GdOCl nanocrystals with 1.5 at% incorporation of Tb; the nanocrystals present a quasi-spherical appearance with an approximate size of 225 nm.

Figure A.13 shows the optical absorption measured for GdOCl nanocrystals dispersed in hexanes with 1.5 at% Tb incorporation, which is characterized by a broad absorption in the range between 250 and 310 nm corresponding to the $4f^8 5d^0 \rightarrow 4f^7 5d^1$ excitation of the Tb^{3+} ions.[1] **Figure IV.2A** shows the emission spectra obtained at $\lambda_{ex.}$ = 277 nm, corresponding to the

Table IV.1 Refined unit cell parameters and atom positions of GdOCl and GdF_3

GdOCl					
atom	*x*	*y*	*z*	occupancy	U_{iso}
Gd	0.25	0.25	0.17085	0.98	0.01178
Cl	0.25	0.25	0.63137	1.0	0.02852
O	0.75	0.25	0	1.0	0.00683
Tb	0.25	0.25	0.17085	0.02	0.01178
Space Group = P4/nmm, a, b = 3.94514(10), c = 6.6546(9), α, β, γ = 90, χ2 = 2.246, Rw = 3.51%					
GdF_3 (Hexagonal)					
atom	*x*	*y*	*z*	occupancy	U_{iso}
Gd	0.337	0	0.25	0.98	0.01195
F(1)	0.36217	0.32857	0.08902	1.0	0.0072
F(2)	0.33333	0.66667	0.17748	1.0	0.01017
F(3)	0	0	0.25	1.0	-0.04509
Tb	0.337	0	0.25	0.02	0.01195
Space Group = P-3c1, a, b = 6.88214(11), c = 7.05857(26), α, β = 90, γ = 120, χ2 = 1.421, Rw = 2.38%					
GdF_3 (Orthorhombic)					
atom	*x*	*y*	*z*	occupancy	U_{iso}
Gd	0.36037	0.25	0.43888	0.98	0.01018
F(1)	0.19481	0.04525	0.06589	1.0	-0.00623
F(2)	0.0222	0.25	0.63776	1.0	0.0356
Tb	0.36037	0.25	0.43888	0.02	0.01018
Space Group = *Pnma, a* = 6.6548(17), b = 7.0467(16), *c* = 4.4104(13), α, β, γ = 90, χ^2 = 1.421, Rw = 2.38%					

absorption maximum observed in Figure A.13. The emission spectra are characterized by sharp bands derived from $^5D_4 \rightarrow {}^7F_J$ (J = 6–0) relaxations of the photoexcited Tb^{3+} ion in the GdOCl lattice.[9,19–21] The $^5D_4 \rightarrow {}^7F_5$ emission at 544 nm is the most intense band resulting in a characteristic green luminescence of the nanocrystals illustrated in Figure IV.2A. A much weaker set of bands in the 450–475 nm (blue) range can be attributed to $^5D_3 \rightarrow {}^7F_J$ relaxations and are strongly quenched above 13 at% incorporation of Tb as a result of cross-relaxation as the energy separation between $^5D_4$ and $^5D_3$ approaches the separation between $^7F_0$ and $^7F_6$.[4,36] Figure IV.2B depicts the variation of the normalized luminescence intensity of the $^5D_4 \rightarrow {}^7F_5$ emission as a function of the measured concentration of the incorporated Tb (as determined by ICP-MS measurements). The highest emission intensity is observed for x = 0.084 in $Gd_{1-x}Tb_xOCl$ and then it progressively decreases with the increasing concentration of Tb as a result of

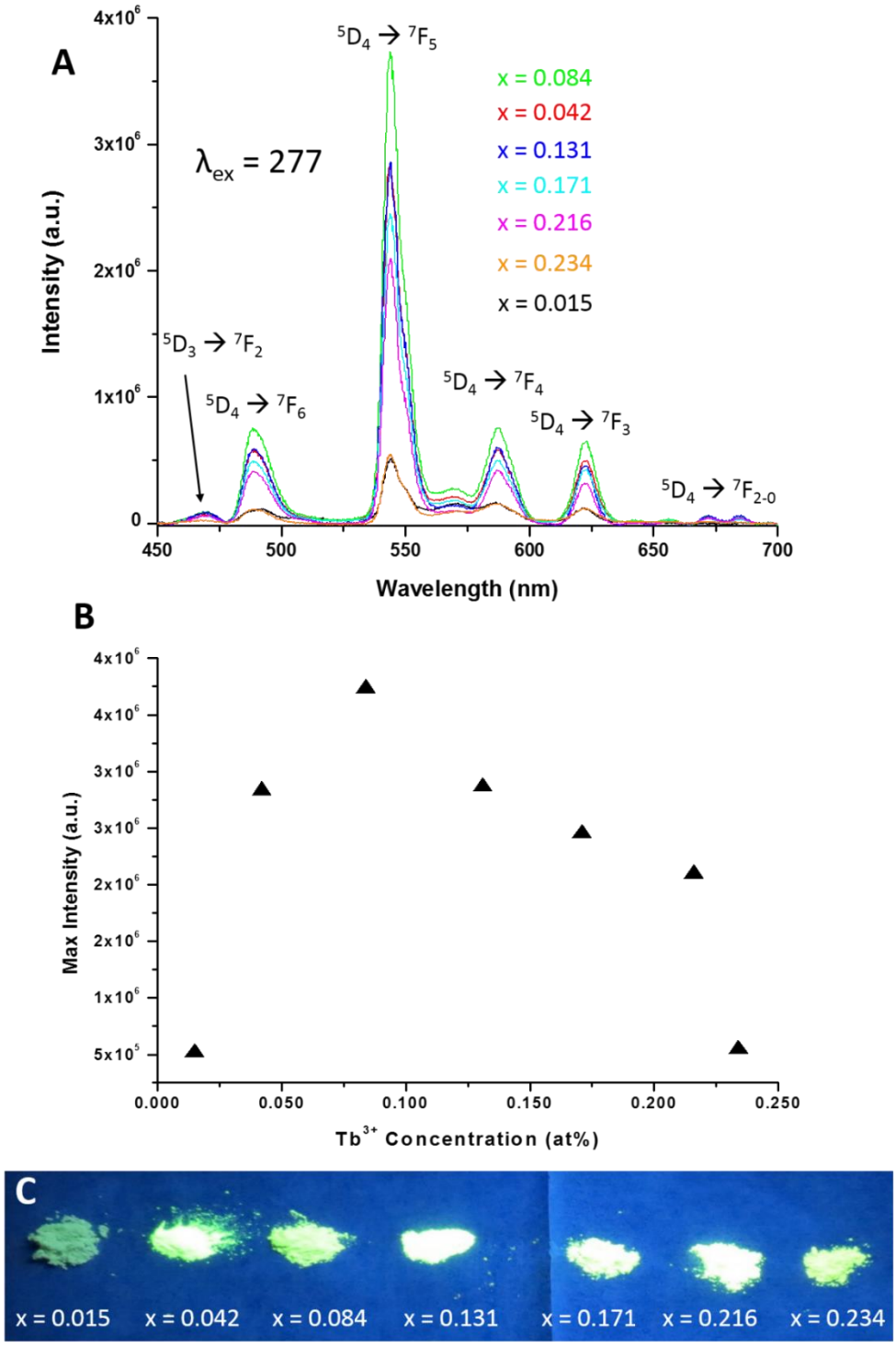

Figure IV.2. (A) Optically stimulated emission spectra of $Gd_{1-x}Tb_xOCl$ ($0.01 \leq x \leq 0.24$). (B) Dependence of the normalized intensity of the $^5D_4 \rightarrow {}^7F_5$ emission on the Tb^{3+} concentration in $Gd_{1-x}Tb_xOCl$ ($0.01 \leq x \leq 0.24$) phosphors. (C) Digital photograph of Tb-incorporated GdOCl powders with increasing Tb content upon illumination with a 254 nm UV light source.

concentration quenching, which is consistent with the previous observations for luminescent fibers and powder phosphors.[4,37] The decrease in the emission intensity can be attributed to the self-quenching phenomena arising from reabsorption of emitted photons, the activation of non-radiative cross-relaxation mechanisms, and multipolar interactions.[29,37]

IV.4.2 Topotactic Transformation

As noted above, topotactic transformations have emerged as important additions to the toolbox of a nanochemist oftentimes without comparable parallels in the bulk; yet, perhaps the most common type of topotactic transformation involves ion exchange of cations.[19–23] Anion exchange has been much less explored although some interesting examples of sulfidation and oxidation reactions have become available recently in the literature.[17,24,38–42] Given the high ionic conductivity of lanthanide oxyhalides, we have examined the reactivity of these nanoparticles towards XeF_2 under solvothermal conditions.[17,18] XeF_2 serves here as an active fluorinating agent with its reactivity derived from the facile cleavability of the Xe–F bond (bond dissociation energy of 133.9 kJ mol^{-1}); the inertness of the evolved Xe gas allows for a topotactic transformation to occur without deleteriously impacting the cation sublattice.[17,18] **Figure IV.3A** and B indicate the nanocrystals obtained upon fluorinating the Tb-incorporated GdOCl nanocrystals indicated in Figure IV.1C. The size distribution is centered at *ca*. 220 nm, which is within the experimental error of the size distribution obtained for the GdOCl nanocrystals but the nanoparticles indicate a more rounded appearance as compared to the faceted precursor morphologies. Figure IV.3C plots the refined powder XRD pattern indicating complete conversion to GdF_3. A mixture of the hexagonal and orthorhombic phases is obtained. The hexagonal phase is a metastable phase at room temperature owing to the small size of the Gd^{3+} cation and is known to convert to the orthorhombic phase, which is the thermodynamic sink in

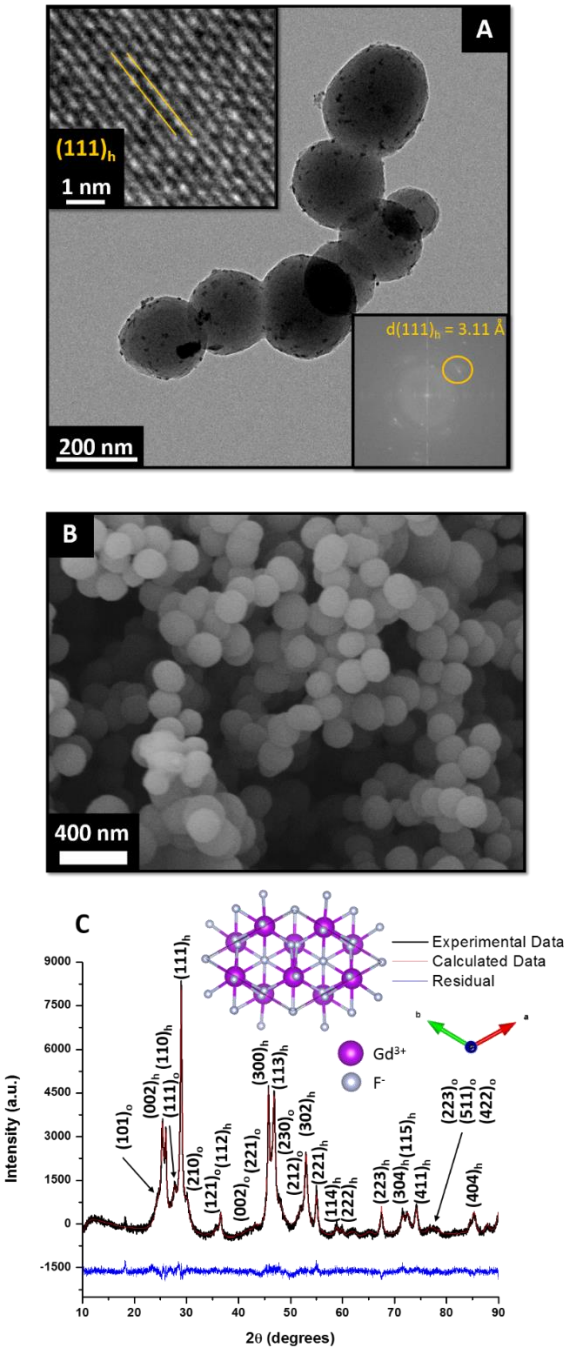

Figure IV.3. (A) HRTEM image of $Gd_{0.985}Tb_{0.015}F_3$ nanocrystals with the insets indicating the separation between the (111) lattice plane of hexagonal GdF_3 with the associated *d*-spacing in the FFT inset. (B) SEM image of $Gd_{0.985}Tb_{0.015}F_3$ nanocrystals obtained upon topotactic transformation. (C) Refinement of XRD pattern after the topotactic transformation. The calculated pattern (red) matches the observed reflections (black) for a mixture of hexagonal and orthorhombic GdF_3. The residuals are depicted in blue. The hexagonal to orthorhombic ratio is 59 : 41. The inset shows the refined hexagonal structure of $Gd_{0.985}Tb_{0.015}F_3$.

this system.[43–45] The lattice parameters derived from a refinement of the unit cell parameters are listed in Table IV.1 and the refined structure of the hexagonal and is corroborated by the absence of OCl^- or F^- species in the recovered supernatant. Note that this reaction is not just enthalpically favored by the facile cleavability of the Xe–F bonds but also has a strong entropic driving force. Reducing the amount of XeF_2 yields a biphasic mixture of the fluoride and the starting material but no oxyfluoride or mixed halide species have been detected under a broad range of reaction conditions. The electron microscopy images of the fluoride nanocrystals suggest that a spherical shape is adopted to minimize the energy but the transformation does not facilitate sintering. The ICP-MS measurements indicate that the Tb : Gd ratio remains unaltered upon fluorination suggesting that the anionic layers are displaced without phase segregation on the cation sublattice. However, the optically stimulated photoluminescence is strongly quenched upon fluorination.

IV.4.3 X-ray Excited Optical Luminescence at the Giant Resonance

In contrast to optical excitation wherein an electron within the luminescent chromophore is directly excited from the $4f^n \rightarrow 4f^{n-1}5d^1$ levels, excitation with X-rays or electrons results in photon absorption from the valence band or higher core levels of the matrix, generating "hot" electron–hole pairs.[10,11] These hot electron—hole pairs have been proposed to thermalize to yield several "thermal" electron—hole pairs that activate the luminescent centers. The excitation channels and recombination pathways thus sensitively depend on energy transfer processes within the matrix, which thus far remains entirely unexplored for rare-earth oxychloride phosphors despite the strong interest in the deployment of these materials as radiation detectors, scintillators, and cathodoluminescent screens.

Figure IV.4A indicates the X-ray absorption near edge structure (XANES) spectra acquired in total luminescence and fluorescence yield modes for $Gd_{1-x}Tb_xOCl$ and $Gd_{1-x}Tb_xF_3$ with $x = 0.015$ while scanning in the range between 135–165 eV, which spans the Gd N_4-edge, acquired in the total luminescence yield ($Gd_{1-x}Tb_xOCl$), and fluorescence yield ($Gd_{1-x}Tb_xOCl$ and $Gd_{1-x}Tb_xF_3$). Figure IV.4B shows the optical luminescence spectra acquired upon excitation at 149 eV (before the giant resonance, *vide infra*). The observed features in the XANES spectra correspond to inner-shell excitations of Gd^{3+} cations from $4d^{10}$, $5p^6$, $4f^7 \rightarrow 4d^9$, $5p^6$, $4f^8$ with the creation of a hole in the 4*d* level. The Gd^{3+}-ion has a half-filled octet ground state ($^8S_{7/2}$) and the fluorescence yield XANES spectra for both the oxychloride and fluoride samples show transitions to octet $^8D_{7/2}$ states at 138.9 eV and a sextet $^6D_{7/2}$ state at 142.4 eV with the latter being allowed owing to spin–orbit coupling within this system.[9,21] The low-energy features of the d^9f^8 multiplet are characterized by sharp features in the fluorescence yield spectra. In stark contrast, a pronounced enhancement of the absorption cross-section is observed for the $^8S_{7/2} \rightarrow {}^8P_J$ (J = 5/2, 7/2, and 9/2) absorption, which further has a greatly broadened lineshape indicating a much shorter lifetime. This broadness of this "giant resonance" spectral feature centered at *ca*. 149.2 eV reflects the strong electron correlation of the f-electrons with energies of 10–20 eV above the ionization threshold required to excite a 4*d* electron into a 4*f* state.[11,42] Owing to the low concentration of Tb^{3+}, no characteristic giant resonance is discernible for the incorporated species.

The X-ray excited optical luminescence spectra depicted in Figure IV.4B are characterized by the $^5D_4 \rightarrow {}^7F_J$ (green) and $^5D_3 \rightarrow {}^7F_J$ (blue) relaxations as assigned previously (Figure IV.2). However, the total luminescence yield spectrum shows an anomalous variation as a function of incident energy. This phenomenon is further illustrated in the 3D contour map

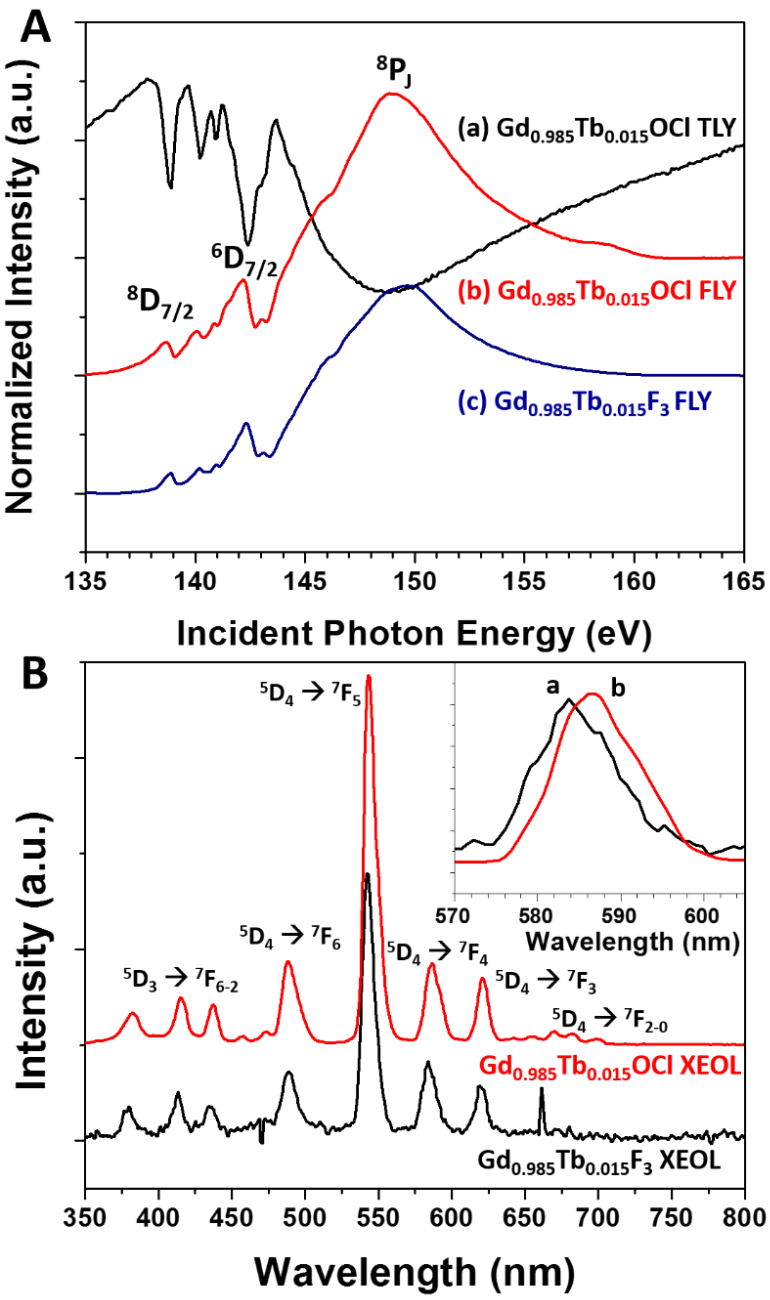

Figure IV.4. (A) Total Luminescence Yield (TLY) XANES spectra acquired at the Gd N_4-edge for $Gd_{0.985}Tb_{0.015}OCl$ (a) recorded in the range between 135–165 eV; (b), (c) recorded fluorescence yield (FLY) spectra of $Gd_{0.985}Tb_{0.015}OCl$ and $Gd_{0.985}Tb_{0.015}F_3$. The absorption features represent the transitions of Gd from the ground state to the multiple excited states. (B) X-ray excited optical luminescence of $Gd_{0.985}Tb_{0.015}OCl$, and $Gd_{0.985}Tb_{0.015}F_3$ upon excitation at 149.0 eV. The inset indicates the blue-shift of the $^5D_4 \rightarrow {}^7F_4$ emission feature for (a) $Gd_{0.985}Tb_{0.015}F_3$ with respect to (b) $Gd_{0.985}Tb_{0.015}OCl$.

plotted in **Figure IV.5B**, which demonstrates the strong modulation of the intensity of the photoluminescence emission in proximity to the giant resonance. Remarkably, the total luminescence yield spectrum is a mirror image of the fluorescence yield spectrum and is characterized by pronounced minima corresponding to the maxima in the fluorescence yield spectrum (Figure IV.4A). The absorption features are further observed to be amplified in the total luminescence yield spectrum. The measured luminescence is observed to be most strongly diminished in the intensity at the giant resonance. Note that the excitation channels here correspond to absorption of photons by the Gd^{3+} cations in the $Gd_{1-x}Tb_xOCl$ matrix with the creation of a 4*d* hole, whereas the measured luminescence in Figure IV.4B and Figure IV.5A is derived from the relaxation of the incorporated Tb^{3+} ions indicating thermalization and activation of the luminescent Tb^{3+} by electron—hole pairs generated on the Gd^{3+} sublattice.

The dips in the total luminescence yield spectra and the pronounced diminution of the luminescence intensity observed at the giant resonance provide valuable insight into the energy transfer process. This remarkable phenomenon can be attributed to three concomitant primary

and secondary processes:[9–11] (1) a pronounced alteration of the internal quantum yield occurs at the giant resonance; the intensity of the optical photoluminescence spectrum is the highest just before the giant resonance and corresponds to the absorption of photons by the Gd^{3+} sublattice accompanied by the creation of "hot" electron–hole pairs that initiate a cascade of thermalization events yielding multiple electron—hole pairs that in turn activate the Tb^{3+} chromophore. In contrast, at the giant resonance, a singular thermal electron—hole pair is generated from the 4*d*–4*f* resonant excitation;[10] (2) owing to the presence of the 4*d* hole, the excited state has a strong proclivity to decay by non-radiative emission of an Auger electron corresponding to a super Coster–Kronig transition, which thus provides an enhanced non-

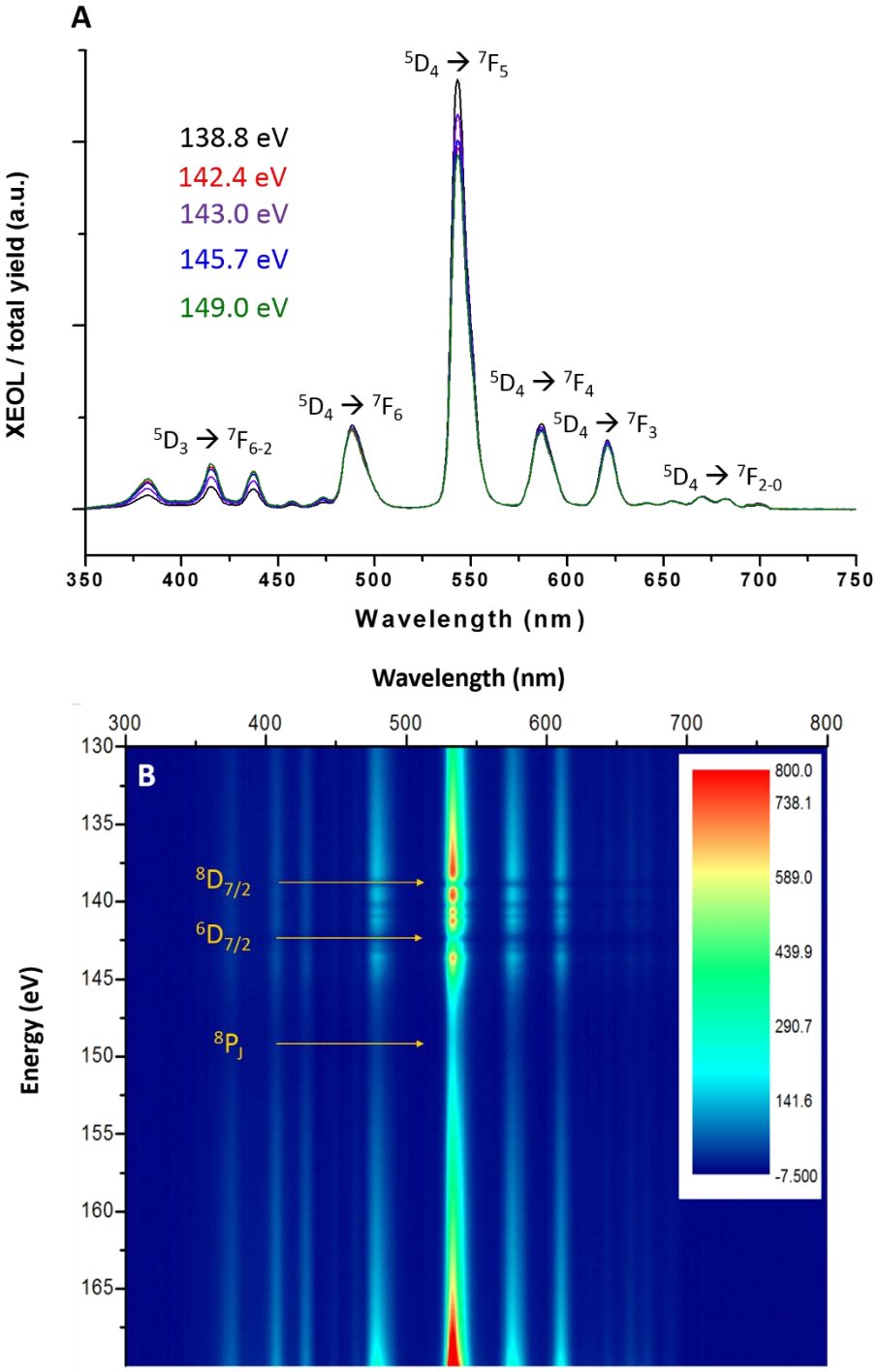

Figure IV.5. (A) Normalized XEOL of $Gd_{0.985}Tb_{0.015}OCl$ as a function of excitation energy as noted in the legend. The spectra indicate the modulation of the relative intensities of the green and blue emissions as a function of excitation energy. (B) 3D plot depicting the evolution of the XEOL of $Gd_{0.985}Tb_{0.015}OCl$ as a function of the excitation energy upon excitation across the Gd N_4-edge.

radiative decay channel;[9,11] (3) the strong enhancement of the absorption cross-section at the giant resonance indicates that the contribution from a surface recombination of the created electron–hole pairs becomes more important.[9–11] In other words, a greater proportion of the thermalized electron—hole pairs can be lost or destroyed at the surface before they activate the luminescent centers, thereby decreasing the measured luminescence. These measurements thus provide detailed insight into the role of thermalization and diffusion in the excitation of luminescent rare-earth chromophores, which is entirely unexplored for this class of materials.

As another notable observation, Figure IV.5 plots the variations in the intensity of the different luminescence peaks as a function of the excitation energy. The $^5D_4 \rightarrow {}^7F_J$ and $^5D_3 \rightarrow {}^7F_J$ transitions show an inverse correlation while traversing the excitation energy range between 135–155 eV. The latter blue bands increase in the relative intensity with an increase of the excitation energy up to the giant resonance but are then decreased. In contrast, the former $^5D_4 \rightarrow {}^7F_J$ green luminescence bands are enhanced with respect to the blue relaxation channels at the giant resonance. This modulation of the relative intensity between transitions emanating from the $^5D_4$ and $^5D_3$ states can be explained based on the relative populations of the levels as facilitated by the $^5D_3$–$^5D_4$ cross-relaxation.[21,26] With the increasing excitation energy, the $^5D_3$ state is more populated upon activation from thermalized electron—hole pairs resulting in the increasing intensity trend observed up to the giant resonance. However, at the giant resonance, cross-relaxation appears to be much more readily facilitated resulting in a diminution of the intensity of the blue bands.[24]

Figure IV.4B also shows the X-ray excited optical luminescence spectrum obtained upon the topotactic transformation of $Gd_{1-x}Tb_xOCl$ to $Gd_{1-x}Tb_xF_3$ ($x = 0.015$ in both cases). The luminescence intensity is strongly diminished as noted above for optically stimulated

luminescence (by a factor of 20) but is still discernible suggesting the operation of similar core–hole formation, diffusion of electron—hole pairs, and thermalization phenomena in the fluoride lattice. Remarkably, the inset to Figure IV.4B shows a 2.5 nm shift of the emission maxima, which is consistent across all of the $^5D_4 \rightarrow {}^7F_J$ bands. This change is likely a result of modulation of the crystal field splitting when the oxide and chloride ligands are replaced by the fluoride within the nine-coordinated local geometry.

IV.5 Conclusions

In conclusion, we use solid-solution $Gd_{1-x}Tb_xOCl$ nanocrystals prepared by a non-hydrolytic sol–gel route as model systems to examine the X-ray-induced generation of multiple electron—hole pairs; the intensity of the X-ray stimulated optical luminescence emanating from relaxations on luminescent Tb^{3+} centers is greatly modulated upon excitation near the giant resonance of Gd^{3+} of the GdOCl matrix. The X-ray-stimulated emission arises from the formation of a 4*d* hole and originates from an excitation pathway that is quite distinct from optical excitation (which results in the formation of a 4*f* hole). The overall photoluminescence intensity and relative contributions of blue and green bands are strongly modified near the giant resonance of the host phosphor. The signature of a transition from the excitation of "hot" electron–hole pairs to thermal electron–hole pairs is observed at the giant resonance. Remarkably, the optical luminescence is a mirror image of the X-ray absorption cross-section.

We further demonstrate the topotactic transformation of $Gd_{1-x}Tb_xOCl$ nanocrystals crystallized in the matlockite PbFCl structure to $Gd_{1-x}Tb_xF3$ crystallized in a hexagonal structure type upon solvothermal treatment with XeF_2. This reaction occurs without disrupting the

miscibility of the Gd and Tb species on the cation sublattice. The X-ray excited optical luminescence is observed to be blue-shifted as a result of the change in crystal field splitting.

IV.6 References

(1) Wang, F.; Liu, X. Recent Advances in the Chemistry of Lathanide-Doped Upconversion Nanocrystals. *Chem. Soc. Rev.* **2009**, *38*, 976–989.

(2) Wang, G.; Peng, Q.; Li, Y. Lanthanide-Doped Nanocrystals, Synthesis, Optical-Magnetic Properties, and Applications. *Acc. Chem. Res.* **2010**, *44* (5), 322–332.

(3) Tissue, B. M. Synthesis and Luminescence of Lanthanide Ions in Nanoscale Insulating Hosts. *Chem. Mater.* **1998**, *10*, 2837–2845.

(4) Kim, S. W.; Jyoko, K.; Masui, T.; Imanaka, N. Green-Emitting (La,M,Tb)OCl (M = Mg, Ca, and Sr) Phosphors. *Opt. Mater. (Amst).* **2012**, *35*, 280–284.

(5) Kim, D.; Jang, J.; Ahn, S. Il; Kim, S.-H.; Park, J.-C. Novel Blue-Emitting Eu^{2+}-Activated LaOCl:Eu Materials. *J. Mater. Chem. C* **2014**, *2* (15), 2799–2805.

(6) Li, G.; Li, C.; Zhang, C.; Cheng, Z.; Quan, Z.; Peng, C.; Lin, J. Tm^{3+} And/or Dy^{3+} Doped LaOCl Nanocrystalline Phosphors for Field Emission Displays. *J. Mater. Chem.* **2009**, *19* (47), 8936–8943.

(7) Wojtowicz, A. J. Rare-Earth-Activated Wide Bandgap Materials for Scintillators. *Nucl. Instruments Methods Phys. Res. A* **2002**, *486*, 201–207.

(8) Kort, K. R.; Banerjee, S. Shape-Controlled Synthesis of Well-Defined Matlockite LnOCl (Ln: La, Ce, Gd, Dy) Nanocrystals by a Novel Non-Hydrolytic Approach. *Inorg. Chem.* **2011**, *50*, 5539–5544.

(9) Moewes, A.; Winarski, R. P.; Ederer, D. L.; Grush, M. M.; Callcott, T. A. Study of 4*f*

Inner Shell Excitations in Gd and Tb Using Resonant Inelastic Soft X-Ray Scattering. *J. Electron Spectrscopy Relat. Phenom.* **1999**, *101–103*, 617–622.

(10) Klaassen, D. B. M.; van Leuken, C. M. G.; Maessen, K. M. H. Giant Resonances in Luminescence Soft X-Ray Excitation Spectra of Phosphors. *Phys. Rev. B* **1987**, *36* (8), 4407–4412.

(11) Heigl, F.; Jürgensen, A.; Zhou, X. T.; Hu, Y. F.; Zuin, L.; Sham, T. K. Communication: X-Ray Excited Optical Luminescence from TbCl3 at the Giant Resonance of Terbium. *J. Chem. Phys.* **2013**, *138* (6), 061104.

(12) Peijzel, P. S.; Meijerink, A.; Wegh, R. T.; Reid, M. F.; Burdick, G. W. A Complete 4f^n Energy Level Diagram for All Trivalent Lanthanide Ions. *J. Solid State Chem.* **2005**, *178*, 448–453.

(13) Hölsä, J.; Säilynoja, E.; Lamminmäki, R.-J.; Deren, P.; Strek, W.; Porcher, P. Crystal Field Energy Level Scheme of Er^{3+} in GdOCl. *J. Chem. Soc. Faraday Trans.* **1997**, *93* (13), 2241–2246.

(14) Garcia, E.; Corbett, J. D.; Ford, J. E.; Vary, W. J. Low-Temperature Routes to New Structures for Yttrium, Holmium, Erbium, and Thulium Oxychlorides. *Inorg. Chem.* **1985**, *24*, 494–498.

(15) Odink, D. A.; Song, K.; Kauzlarich, S. M. Intercalation of Pyridine into the Layered SmSI Structure of YbOCl. *Chem. Mater.* **1992**, *4*, 906–911.

(16) Song, K.; Kauzlarich, S. M. New Intercalation Compounds of Layered Lanthanide Oxychlorides LnOCl (Ln = Ho, Er, Tm, and Yb) with Pyridine and Substituted Pyridines. *Chem. Mater.* **1994**, *6*, 386–394.

(17) Imanaka, N.; Okamoto, K.; Adachi, G. Y. Water-Insoluble Lanthanum Oxychloride-Based

Solid Electrolytes with Ultra-High Chloride Ion Conductivity. *Angew. Chemie - Int. Ed.* **2002**, *41*, 3890–3892.

(18) Imanaka, N.; Kato, Y. A New Type of Bromide Anion Conducting Solid. *Chem. Commun.* **2003**, No. 11, 1270–1271.

(19) Schaak, R. E.; Mallouk, T. E. Perovskites by Design: A Toolbox of Solid-State Reactions. *Chem. Rev.* **2002**, *14*, 1455–1471.

(20) Son, D. H.; Hughes, S. M.; Yin, Y.; Alivisatos, A. P. Cation Exchange Reactions in Ionic Nanocrystals. *Science.* **2004**, *306*, 1009–1012.

(21) Norris, D. J.; Efros, A. L.; Erwin, S. C. Doped Nanocrystals. *Science.* **2008**, *319*, 1776–1779.

(22) Sanjaya Ranmohotti, K. G.; Josepha, E.; Choi, J.; Zhang, J.; Wiley, J. B. Topochemical Manipulation of Perovskites: Low-Temperature Reaction Strategies for Directing Structure and Properties. *Adv. Mater.* **2011**, *23*, 442–460.

(23) Marley, P. M.; Abtew, T. A.; Farley, K. E.; Horrocks, G. A.; Dennis, R. V.; Zhang, P.; Banerjee, S. Emptying and Filling a Tunnel Bronze. *Chem. Sci.* **2015**, *6*, 1712–1718.

(24) Wu, L. M.; Sharma, R.; Seo, D. K. Metathetical Conversion of Nd_2O_3 Nanoparticles into NdS_2 Polysulfide Nanoparticles at Low Temperatures Using Boron Sulfides. *Inorg. Chem.* **2003**, *42*, 5798–5800.

(25) Wu, L. M.; Seo, D. K. New Solid-Gas Metathetical Synthesis of Binary Metal Polysulfides and Sulfides at Intermediate Temperatures: Utilization of Boron Sulfides. *J. Am. Chem. Soc.* **2004**, *126*, 4676–4681.

(26) Rambabu, U.; Annapurna, K.; Balaji, T.; Buddhudu, S. Fluorescence Spectra of Er^{3+} - REOCl (Re = La, Gd, Y) Powder Phosphors. *Mater. Lett.* **1995**, *23*, 143–146.

(27) Hölsä, J.; Lamminmäki, R. J.; Lastusaari, M.; Porcher, P. Simulation of the Gd^{3+} Energy Level Scheme in GdOCl. *J. Alloys Compd.* **2001**, *323–324*, 811–815.

(28) Konishi, T.; Shimizu, M.; Kameyama, Y.; Soga, K. Fabrication of Upconversion Emissive LaOCl Phosphors Doped with Rare-Earth Ions for Bioimaging Probes. *J. Mater. Sci. Mater. Electron.* **2007**, *18*, S183–S186.

(29) Kong, Q.; Wang, J.; Dong, X.; Yu, W.; Liu, G. Synthesis and Luminescence Properties of Terbium-Doped Lanthanum Oxychloride Nanostructures. *J. Nanosci. Nanotechnol.* **2015**, *15*, 4304–4315.

(30) Mondejar, S. P.; Kovtun, A.; Epple, M. Lanthanide-Doped Calcium Phosphate Nanoparticles with High Internal Crystallinity and with a Shell of DNA as Fluorescent Probes in Cell Experiments. *J. Mater. Chem.* **2007**, *17*, 4153–4159.

(31) Depner, S. W.; Kort, K. R.; Jaye, C.; Fischer, D. A.; Banerjee, S. Nonhydrolytic Synthesis and Electronic Structure of Ligand-Capped $CeO_{2-\delta}$ and CeOCl Nanocrystals. *J. Phys. Chem. C* **2009**, *113*, 14126–14134.

(32) Kort, K. R.; Banerjee, S. Oriented Electrophoretic Deposition of GdOCl Nanoplatelets. *J. Phys. Chem. B* **2013**, *117*, 1585–1591.

(33) Kort, K. R.; Banerjee, S. Ligand-Mediated Control of Dislocation Dynamics and Resulting Particle Morphology of GdOCl Nanocrystals. *Small* **2015**, *11* (3), 329–334.

(34) Hu, Y. F.; Zuin, L.; Wright, G.; Igarashi, R.; McKibben, M.; Wilson, T.; Chen, S. Y.; Johnson, T.; Maxwell, D.; Yates, B. W.; Sham, T. K.; Reininger, R. Commissioning and Performance of the Variable Line Spacing Plane Grating Monochromator Beamline at the Canadien Light Source. *Rev. Sci. Intruments* **2007**, *78*, 83109.

(35) Kasrai, M.; Yin, Z.; Bancroft, G. M.; Tan, K. H. X-Ray Fluorescence Measurments of X-

Ray Absorption near Edge Strcuture at the Si, P, and S L Edges. *J. Vac. Sci. Technol. A* **1993**, *11* (5), 2694–2699.

(36) Liu, X.; Pang, R.; Li, Q.; Lin, J. Host-Sensitized Luminescence of Dy^{3+}, Pr^{3+}, Tb^{3+} in Polycrystalline $CaIn_2O_4$ for Field Emission Displays. *J. Solid State Chem.* **2007**, *180*, 1421–1430.

(37) Uitert, L. G. Van. Characterization of Energy Transfer Interactions between Rare Earth Ions. *J. Electrochem. Soc.* **1967**, *114*, 1048–1053.

(38) Muthuswamy, E.; Brock, S. L. Oxidation Does Not (Always) Kill Reactivity of Transition Metals: Solution-Phase Conversion of Nanoscale Transition Metal Oxides to Phosphides and Sulfides. *J. Am. Chem. Soc.* **2010**, *132*, 15849–15851.

(39) Liang, J.; Ma, R.; Ebina, Y.; Geng, F.; Sasaki, T. New Family of Lanthanide-Based Inorganic-Organic Hybrid Frameworks, $Ln_2(OH)_4(O_3S(CH_2)_nSO_3)\cdot 2H_2O$ (Ln = La, Ce, Pr, Nd, Sm, n = 3, 4) and Their Derivatives. *Inorg. Chem.* **2013**, *52*, 1755–1761.

(40) Hu, L.; Ma, R.; Ozawa, T. C.; Geng, F.; Iyi, N.; Sasaki, T. Oriented Films of Layered Rare-Earth Hydroxide Crystallites Self-Assembled at the Hexane,water Interface. *Chem. Commun.* **2008**, *0*, 4897–1899.

(41) Hu, L.; Renzhi, M.; Ozawa, T. C.; Sasaki, T. Oriented Monolayer Film of Gd_2O_3:0.05 Eu Crystallites: Quasi-Topotactic Transformation of the Hydroxide Film and Drastic Enhancement of Photoluminescence Properties. *Angew. Chemie - Int. Ed.* **2009**, *48*, 3846–3849.

(42) Hu, L.; Ma, R.; Ozawa, T. C.; Sasaki, T. Sysnthesis of a Solid Solution Series of Layered $Eu_xGd_{1-x}(OH)_{2.5}Cl_{0.5}\cdot 0.9H_2O$ and Its Transformation into $(Eu_xGd_{1-x})_2O_3$ with Enhanced Photoluminescence Properties. *Inorg. Chem.* **2010**, *49*, 2960–2968.

(43) Zhao, Q.; Shao, B.; Lu, W.; Jia, Y.; Lv, W.; Jiao, M.; You, H. Doping Alkaline-Earth, a Strategy of Stabilizing Hexagonal GdF_3 at Room Temperature. *Dalt. Trans.* **2013**, *42*, 15482.

(44) Dong, C.; Raudsepp, M.; Van Veggel, F. Kinetically Determined Crystal Structures of Undoped and La^{3+}-Doped LnF_3. *J. Phys. Chem. C* **2009**, *113*, 472–478.

(45) Zhang, X.; Hayakawa, T.; Nogami, M.; Ishikawa, Y. Selective Synthesis and Luminescence Properties of Nanocrystalline GdF_3:Eu^{3+} with Hexagonal and Orthorhombic Structures. *J. Nanomater.* **2010**, 651326.

CHAPTER V

LIGAND-MEDIATED CONTROL OF DOPANT OXIDATION STATE AND X-RAY EXCITED OPTICAL LUMINESCENCE IN EU-DOPED LAOCL

V.1 Overview

The development of an expanded palette of X-ray phosphors is a critical imperative for applications in medical imaging, radiation detection, and scientific instrumentation. The rational design of X-ray phosphors has been stymied by the absence of fundamental understanding of activation channels, sensitization mechanisms, and recombination pathways induced upon high-energy excitation of luminescent centers. In this article, we describe the preparation of Eu-doped LaOCl based on the condensation of molecular precursors. The synthetic route allows for control of the oxidation state of the incorporated Eu-atoms based on ligand-induced oxidation or reduction of the Eu-precursors. Nanocrystals exhibiting blue and red X-ray excited optical luminescence are developed by tuning the oxidation state of europium ions incorporated within the LaOCl nanocrystal matrix. Pronounced modulation of the intensity of the optical luminescence is evidenced at and near the giant resonance absorption of the host matrix as a result of distinctly divergent recombination channels. Resonant excitation results in recombination via Auger electron ionization and relaxation of a single electron—hole pair, whereas excitation away from the giant resonance results in thermalization of "hot" electron-hole pairs, while launching cascades of energy transfer, excitation, and radiative recombination events at the Eu-luminescent centers. Mechanistic elucidation and the development of a generalizable synthetic route starting from molecular precursors paves the way to an expanded palette of X-ray phosphors.

V.2 Introduction

Materials that absorb and effectively convert high-energy incident radiation to scores of photons in the visible region of the electromagnetic spectrum underpin numerous technological applications in medical imaging, radiation detection, and scientific instrumentation.[1–5] The effective design of radiation detectors, scintillators, and imaging devices relies on the precise amplification of incident X-ray photons to visible photons. In such materials, the absorption of an X-ray photon initiates a cascade of electron—hole pair formation, carrier diffusion, scattering, and recombination processes that differ substantially from processes initiated by the direct optical excitation of chromophores in optical phosphors.[1,6,7] Fundamental understanding of the activation channels, sensitization mechanisms, and recombination pathways induced upon high-energy excitation of luminescent centers remains rather rudimentary. Consequently, the available palette of viable X-ray phosphors remains substantially limited in scope as compared to optical phosphors where detailed design principles have been elucidated.[8–12] In this chapter, we demonstrate a facile synthetic route to blue and red X-ray phosphors resulting from the ligand-mediated non-hydrolytic sol—gel synthesis of solid-solution Eu-incorporated LaOCl nanocrystals from metal chloride and metal alkoxide precursors. The oxidation state of dopant Eu cations, and thus their luminescent properties, are tuned based on selection of an oxidative (trioctylphosphine oxide (TOPO)) or reductive (oleylamine) ligand. Pronounced modulation of Eu^{3+}- and Eu^{2+}-derived optical luminescence is observed near the giant resonance of the LaOCl matrix and is attributed to the fundamentally distinctive origins of recombination processes near and at the giant resonance.

Rare-earth oxychlorides (REOCl, where RE = La – Dy) crystallize in the tetragonal matlockite PbFCl-type structure and are thermally robust and chemically stable phosphor

hosts.[13–19] The REOCl structure comprises sheets of a $[REO]^+$ cation layer alternating with sheets of a $[Cl]^-$ anion layer with the anionic layers serving to effectively separate cationic sites, thereby limiting cross-relaxation mechanisms.[15,20,21] Luminescent activator cations such as Pr^{3+}, Nd^{3+}, Sm^{3+}, Eu^{3+}, Tb^{3+}, and Yb^{3+} can be readily incorporated within La sites. Europium doped into inorganic phosphors exhibits intense tunable luminescence dependent on the oxidation state; trivalent europium ions (Eu^{3+}) are characterized by narrow atomic-like spectral lines in the red region of the electromagnetic spectrum derived from $^5D_0 \rightarrow {}^7F_J$ ($J = 1 – 4$) electronic transitions, whereas divalent europium ions (Eu^{2+}) are characterized by a broad emission corresponding to a $4f^6 5d^1 \rightarrow 4f^7$ transition in the UV/blue region of the electromagnetic spectrum.[17,22–24] The stabilization of Eu^{2+} within a trivalent environment represents a considerable synthetic challenge. To the best of our knowledge there exists only a single example of stabilizing Eu^{2+} in the crystal lattice of PbFCl-type structure wherein Kim *et al*. obtained a blue-emitting material based on a high-temperature (1000°C) solid-state reaction between rare-earth oxides and ammonium chloride.[6] However, the synthetic route results in considerable heterogeneity of particle morphology, cannot readily be elaborated to enable the stabilization of Eu^{3+}, and furthermore requires high temperatures. In Chapter IV and previous work, we demonstrated a low-temperature solution-phase cross-coupling route for the preparation of rare-earth oxychloride nanocrystals with well-defined shapes based on the condensation of metal alkoxides and metal halides in the presence of various coordinating solvents.[15,19–21,25] This synthetic route allows for the facile substitutional incorporation of luminescent lanthanide cations within the oxychloride lattice. As such, it provides a rich system for exploration of fundamental mechanisms of optical luminescence induced upon absorption of high-energy radiation. In Chapter IV, we also examined the X-ray excited optical luminescence (XEOL) of Tb^{3+} cations doped within GdOCl

nanocrystals upon excitation near the giant resonance of Gd^{3+}.[19] In this chapter, we demonstrate that based on the choice of the stabilizing ligand used for solution-phase cross-condensation, the oxidation state of incorporated dopants can be controlled, allowing for tunable inclusion of Eu^{2+} and Eu^{3+} dopants within the LaOCl lattice. Divalent and trivalent europium cations are furthermore seen to exhibit pronounced differences in their XEOL response upon $4d \rightarrow 4f$ excitation of the La^{3+} host lattice.

V.3 Experimental

V.3.1 Synthesis of Eu-Incorporated LaOCl Nanocrystals

$EuCl_3$, $LaCl_3$, $La(O^iPr)_3$, and trioctyl phosphine oxide (TOPO, 90%) were purchased from Strem Chemicals and used as received. $EuCl_2$ and oleylamine (98%) were purchased from Sigma-Aldrich and used as received. The synthesis of LaOCl nanostructures has been described in previous work and was modified here to incorporate a broad range of Eu^{3+} and Eu^{2+} species in order to stabilize $Eu_xLa_{1-x}OCl$ solid-solution nanocrystals.[15,19–21,25] Briefly, equimolar amounts of halide and alkoxide precursors, for instance, 2 mmol of anhydrous $LaCl_3$ and 2 mmol of $La(O^iPr)$ were reacted within 25 mmol of a coordinating solvent, either TOPO or oleylamine. In order to prepare solid-solution nanocrystals, the desired molar equivalent of Eu^{3+} or Eu^{2+} ions were included within the reaction mixture by substituting an appropriate amount of $LaCl_3$ for $EuCl_3$ or $EuCl_2$. All precursors were weighed into a three-neck round bottom-flask within an Ar-filled glovebox then heated and stirred to a temperature of 340°C using standard Schlenk conditions under an Ar atmosphere. After heating for 2 h, the reaction mixture was then cooled to *ca*. 70 °C followed by addition of acetone or hexanes to flocculate the as-prepared nanocrystals capped with TOPO or oleylamine, respectively. The nanocrystals were then recovered by centrifugation

for 20 min at 12,000 rpm. The nanocrystals were further dispersed in hexanes and centrifuged for 5 min at 1,500 rpm, and ultimately recovered by centrifugation of a re-suspended mixture at 12,000 rpm for 20 min.

V.3.2 Structural Characterization

Powder X-ray diffraction (XRD) was used for examination of phase purity and structure determination. XRD measurements were performed using a Bruker-AXS D8 Advance Bragg-Brentano X-ray powder diffractometer with Cu Kα radiation (λ = 1.5418 Å). Diffraction data for LaOCl nanocrystals was acquired at beamline 11-BM of the Advanced Photon Source and refined using TOPAS 5.0 software. The particle morphology was evaluated by transmission electron microscopy (TEM) using a FEI Technai G2 F20 ST instrument operated at an accelerating voltage of 200 kV. The nanocrystals were prepared for TEM by dispersion in 2-propanol and deposited onto 400-mesh carbon coated Cu grids. The stoichiometry of the ternary solid-solution nanocrystals was determined by inductively coupled plasma-mass spectrometry (ICP-MS) using a Perkin Elmer DRCII instrument. The samples were prepared for ICP-MS analysis by acid digestion in an aqueous solution of concentrated HNO_3.

V.3.3 Optical Measurements

Optically stimulated photoluminescence and absorption measurements were acquired using a Horiba PTI QuantaMaster 40 spectrofluorometer in emission and excitation modes, respectively. For absorption and optically stimulated photoluminescence measurements, the nanocrystals were spread onto a solid sample holder and held in place by a thin layer of AP 101 vacuum grease. XEOL spectra were acquired concurrently with acquisition of La/Eu $N_{4,5}$ X-ray absorption near edge structure (XANES) spectra at the Variable Line Spacing-Plane Grating Monochromator (VLS-PGM) beamline ($E/\Delta E$ > 10,000) of the Canadian Light Source in

Saskatoon, SK.[26] The total fluorescence yield (FLY) and XEOL data were acquired concurrently. XANES spectra were acquired using VLS-PGM's high-energy grating by scanning the energy range from 90–170 eV with a delta step of 0.1 eV. The pressure within the sample chamber was lower than 1×10^{-8} Torr. The FLY signal was recorded using a microchannel plate detector.[27] All spectra were normalized to the intensity of the photon beam as measured by the drain current monitored at a nickel mesh (with a transmission of 90% in the relevant energy range) situated upstream of the sample. The optical luminescence data were collected using an Ocean Optics QE65000 monochromator with a fiber-optic feed-through over a wavelength range of 350–750 nm. The nanocrystal powders were adhered to carbon tape prior to mounting within the sample chamber. All measurements have been performed at room temperature.

V.4 Results and Discussion

As outlined in Chapter IV the cross-condensation of lanthanide halide and lanthanide alkoxide precursors initially yields a lanthanide chloroalkoxide precursor as a result of ligand exchange; the lanthanide chloroalkoxides are further condensed with elimination of alkyl halides to obtain the REOCl framework.[15,19,28] Subsequent condensation reactions propagate the growth of the REOCl framework with dimensional constraints imposed by the binding of stabilizing ligands such as TOPO or oleylamine to the particle surfaces. The ligands are thought to buffer the supersaturation of the monomers and prevent agglomeration of REOCl nuclei, thereby defining faceted nanocrystal morphologies.[25] **Figure V.1** shows a synchrotron powder XRD pattern acquired for (undoped) LaOCl nanocrystals prepared by this approach using TOPO as a ligand. Anisotropic broadening of (001) and (101) reflections is observed due to the preferential growth direction of the LaOCl nanoplatelets. A Pawley fit of the lattice parameters to the

tetragonal (space group: P4/*nmm*) LaOCl crystal structure has been performed and the refined structure is shown in the inset. **Table V.1** lists the refined lattice parameters, R-factors, and goodness-of-fit values. A lattice-resolved HRTEM image of the nanoplatelets viewed down the basal planes displays the separation between the (110) lattice planes and indicates the highly crystalline nature of the prepared material, which grows preferentially along the <101> direction.[25] The capping ligand used in hot colloidal synthesis strongly influences the nucleation and growth of nanocrystals by buffering the supersaturation of the monomer, promoting selective growth along certain directions based on preferential binding to specific crystallographic facets, and modulating the diffusion and addition of monomeric species.[25,29–34] Ligands can therefore be used to sensitively tune nanocrystal dimensions, growth direction, and exposed surface facets. The XRD patterns and TEM images in **Figure V.2** and **Figure V.3**, respectively, demonstrate the contrast between using TOPO and oleylamine as capping ligands for the growth of solid-solution $Eu_xLa_{1-x}OCl$ nanocrystals. $EuCl_3$ is used as the precursor in both cases. For both ligands, the obtained nanocrystals are stabilized in the PbFCl crystal structure; however the morphologies and growth directions are substantially divergent. **Figure V.4** exhibits optically stimulated luminescence spectra and digital photographs acquired for $Eu_xLa_{1-x}OCl$ nanocrystals grown using TOPO and oleylamine using $EuCl_3$ as the dopant precursor. The materials prepared using TOPO as the passivating ligand show the characteristic red luminescence of trivalent europium, whereas the materials prepared using oleylamine as the coordinating ligand show the characteristic blue luminescence of divalent europium suggesting that the nature of the ligand strongly influences the dopant oxidation state (*vide infra*) and the ligands herein serve as redox non-innocent species in addition to their more conventional role of confining nanocrystal growth.

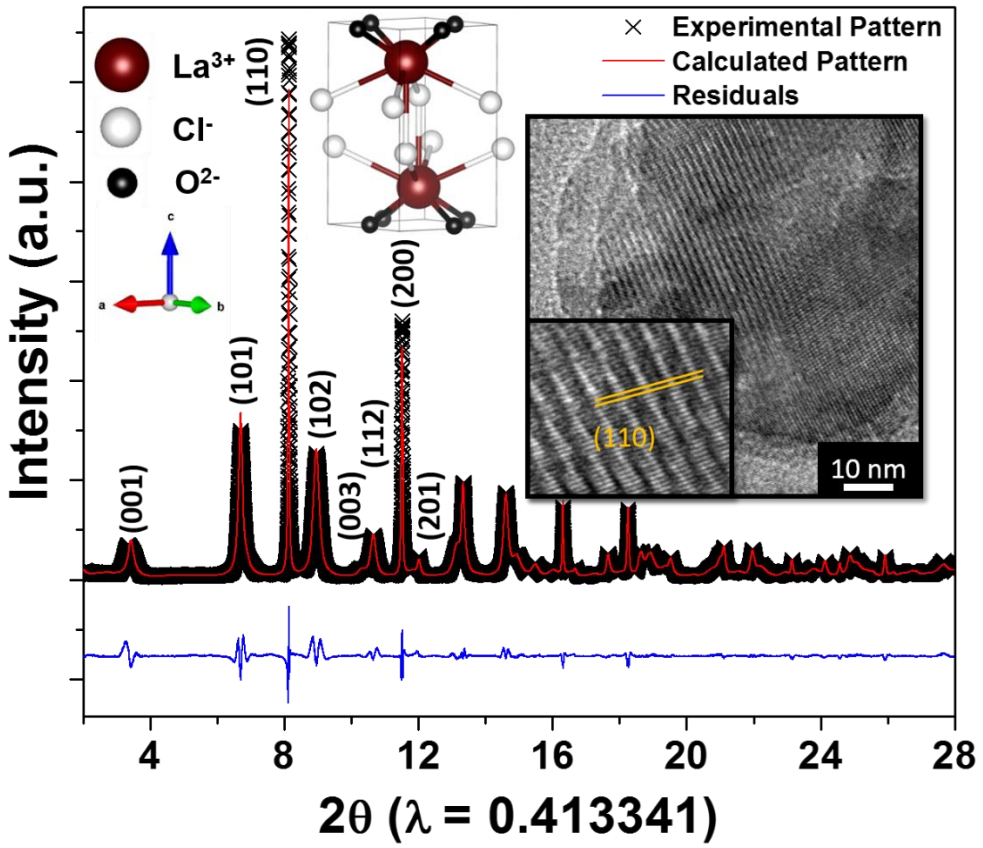

Figure V.1. Synchrotron powder XRD pattern (λ = 0.413341 Å) of LaOCl nanoplatelets prepared using TOPO as the stabilizing ligand acquired at 298 K. The measured data is plotted in black, whereas the red plot denotes the calculated diffraction pattern corresponding to the Pawley fit to tetragonal LaOCl lattice parameters. Table 1 provides the refined lattice parameters, R-factors, and goodness-of-fit (GOF) values. The blue line plots the residuals. The top inset depicts the crystal structure refined from the Pawley fit. The top right inset depicts a lattice-resolution image of an individual LaOCl nanoplatelet.

Table V.1. Refined lattice parameters, R-factors for Pawley fit of lattice parameters, and goodness-of-fit values for refinement shown in Figure V.1.

Space Group: *P4/nmm* *Z* = 2; *a*, *b* = 4.11998 (53) Å; *c* = 4.11998(53) Å; α, β, γ = 90°				
R_{exp}	R_{wp}	R_p	*GOF*	*R-Bragg*
3.78	13.29	10.88	3.51	1.807

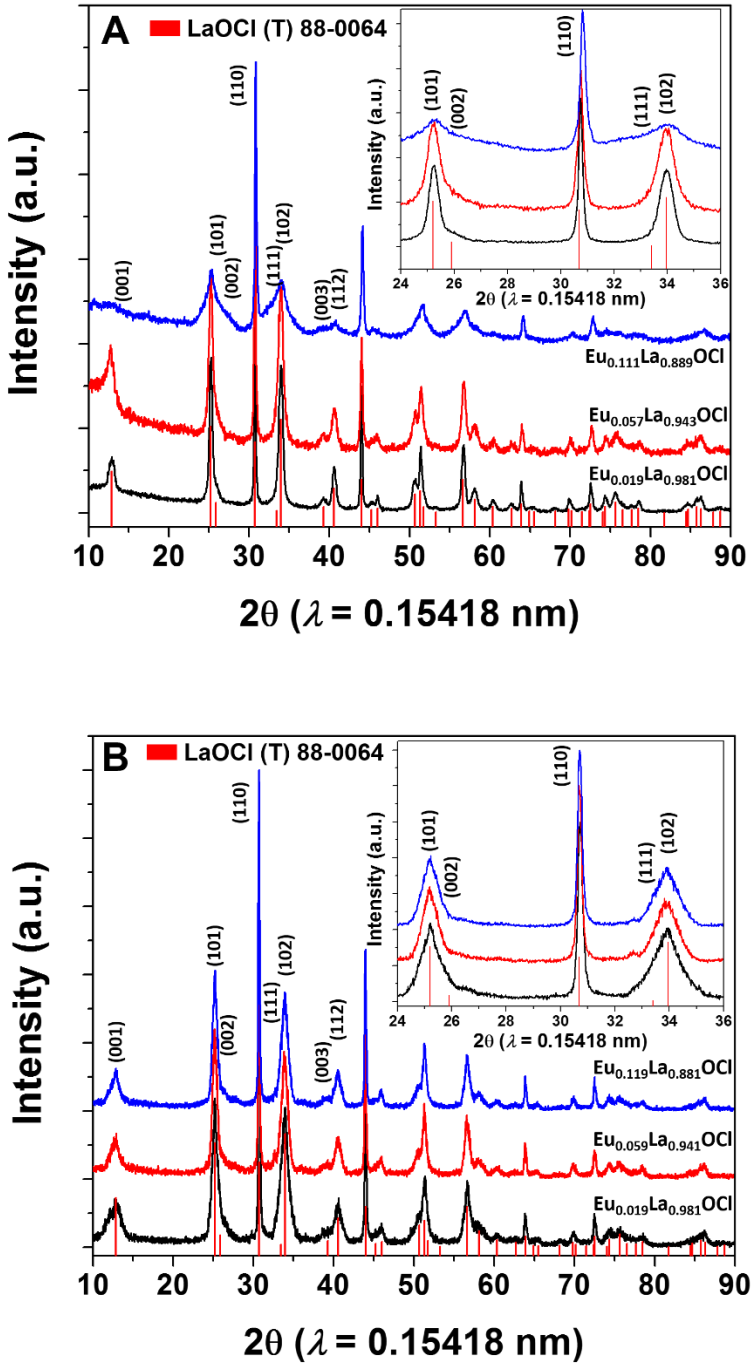

Figure V.2. Powder XRD patterns acquired for solid-solution $Eu_xLa_{1-x}OCl$ nanocrystals where (A) x = 0.019, 0.057, and 0.111 grown using TOPO as a ligand and (B) x = 0.019, 0.059, and 0.119 grown using oleylamine as a ligand. The insets for both (A) and (B) are magnified views of the 2θ range from 24° to 36°. The vertical red bars denote positions and relative intensities expected from JCPDS # 88-0064 for tetragonal LaOCl (Space Group: P4/*nmm*).

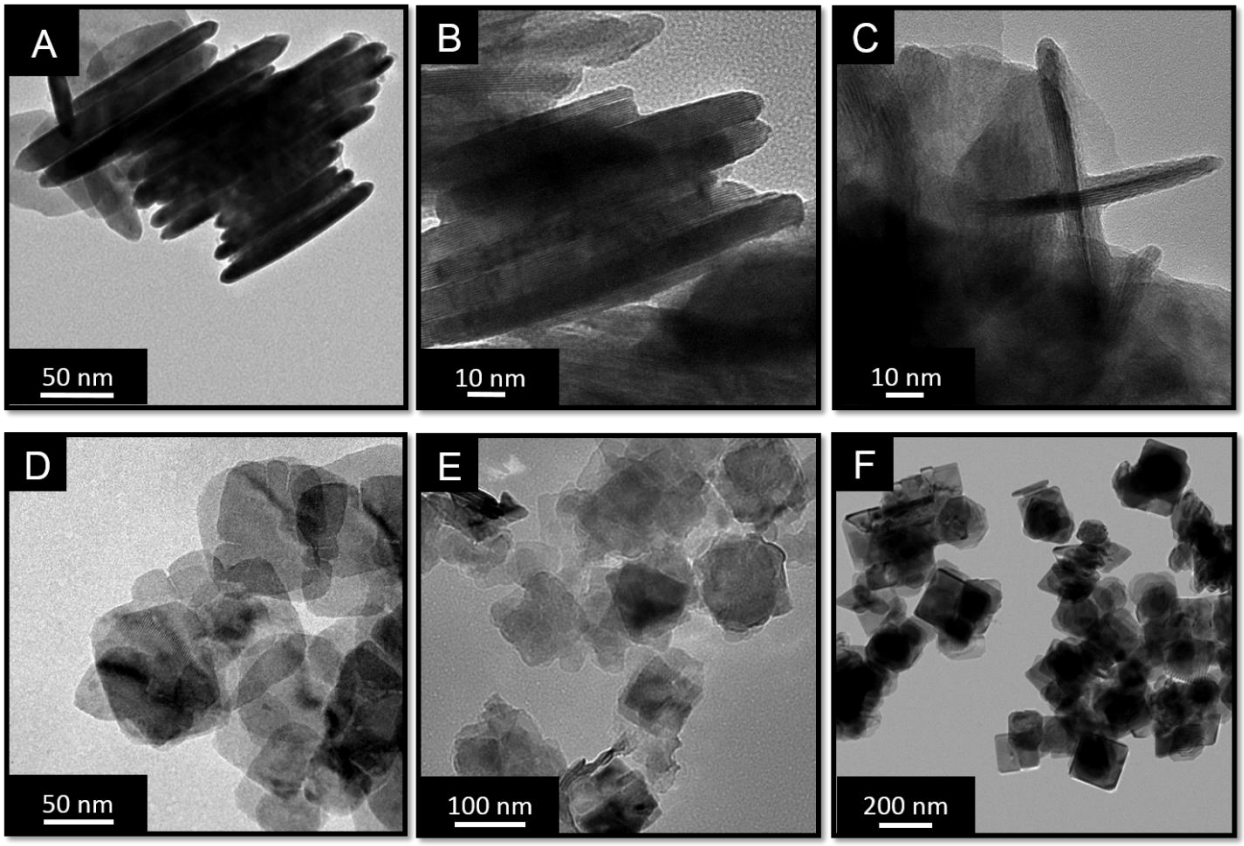

Figure V.3. Low-magnification transmission electron microscopy images of $Eu_xLa_{1-x}OCl$ nanocrystals grown using TOPO as a ligand where (A) $x = 0.019$; (B) $x = 0.057$; and (C) $x = 0.111$. The crystallites exhibit a platelet-like morphology but a discernible thinning of the platelets is observed with increasing Eu concentration. Low-magnification transmission electron microscopy images of $Eu_xLa_{1-x}OCl$ nanocrystals grown using oleylamine as a ligand where (D) $x = 0.019$; (E) $x = 0.059$; and (F) $x = 0.119$. The crystallites adopt a sheet-like morphology.

Considering the XRD patterns acquired for TOPO-capped nanocrystals in Figure V.2A, the (110) reflection is shifted to higher 2θ values with increasing Eu incorporation, reflecting a contraction of the lattice, which can be rationalized based on the smaller ionic radii of the dopant atom (nine-coordinate La^{3+} has an ionic radius of 121.6 pm, whereas nine-coordinate Eu^{3+} is 112.0 pm).[35] Interestingly, significant anisotropic broadening is observed for the (101) and (102) reflections (at 2θ values of 25° and 34°, respectively) with increasing substitutional incorporation

of trivalent europium on La lattice sites (inset to Figure V.2A); the relative intensity of $I_{(110)}/I_{(102)}$ is further strongly increased with increasing incorporation of europium. The pronounced anisotropic broadening and diminution of the (101) and (102) reflections suggest growth confinement along the crystallographic *c* direction (note also the diminution and broadening of the (001) and (003) reflections). The TEM images shown in Figure V.3A—C allow for an evaluation of the thicknesses of the nanoplatelets; thicknesses of 11.1 ± 1.5 nm, 7.5 ± 1.1 nm, and 4.6 ± 0.8 nm are deduced for $Eu_{0.019}La_{0.981}OCl$, $Eu_{0.057}La_{0.943}OCl$, and $Eu_{0.111}La_{0.889}OCl$ nanoplatelets, respectively, indicating thinning of the platelets with increasing Eu concentration. The compressive strain induced as a result of substitutional Eu^{3+} incorporation on the cation sublattice appears to inhibit growth along the *c* direction. The LaOCl structure has a monocapped square-antiprism local coordination environment wherein cations are coordinated by four oxygen atoms and four chlorine atoms in adjacent layers and by a more distant chlorine atom in the next $[Cl]^-$ layer (Figure V.1, inset).

The consequences of substitutional incorporation of a smaller cation will be most pronounced along the *c* direction with regards to the interaction with the chlorine atom in the next layer and is posited to be the origin of the anisotropic growth confinement observed in this case. With oleylamine as the capping ligand, Figure V.2B again indicates sharp (101) reflections and broader (101) and (102) reflections, suggestive of a nanoplatelet or nanosheet morphology.[25] However, in the case of this ligand increasing concentration of divalent europium does not substantially broaden or shift the lattice reflections. The corresponding TEM images in Figure V.3D—F confirm a sheet-like morphology with average edge dimensions of 85 ± 6 nm, 104 ± 9 nm, and 170 ± 25 nm for $Eu_{0.019}La_{0.98}1OCl$, $Eu_{0.059}La_{0.941}OCl$, and $Eu_{0.119}La_{0.881}OCl$,

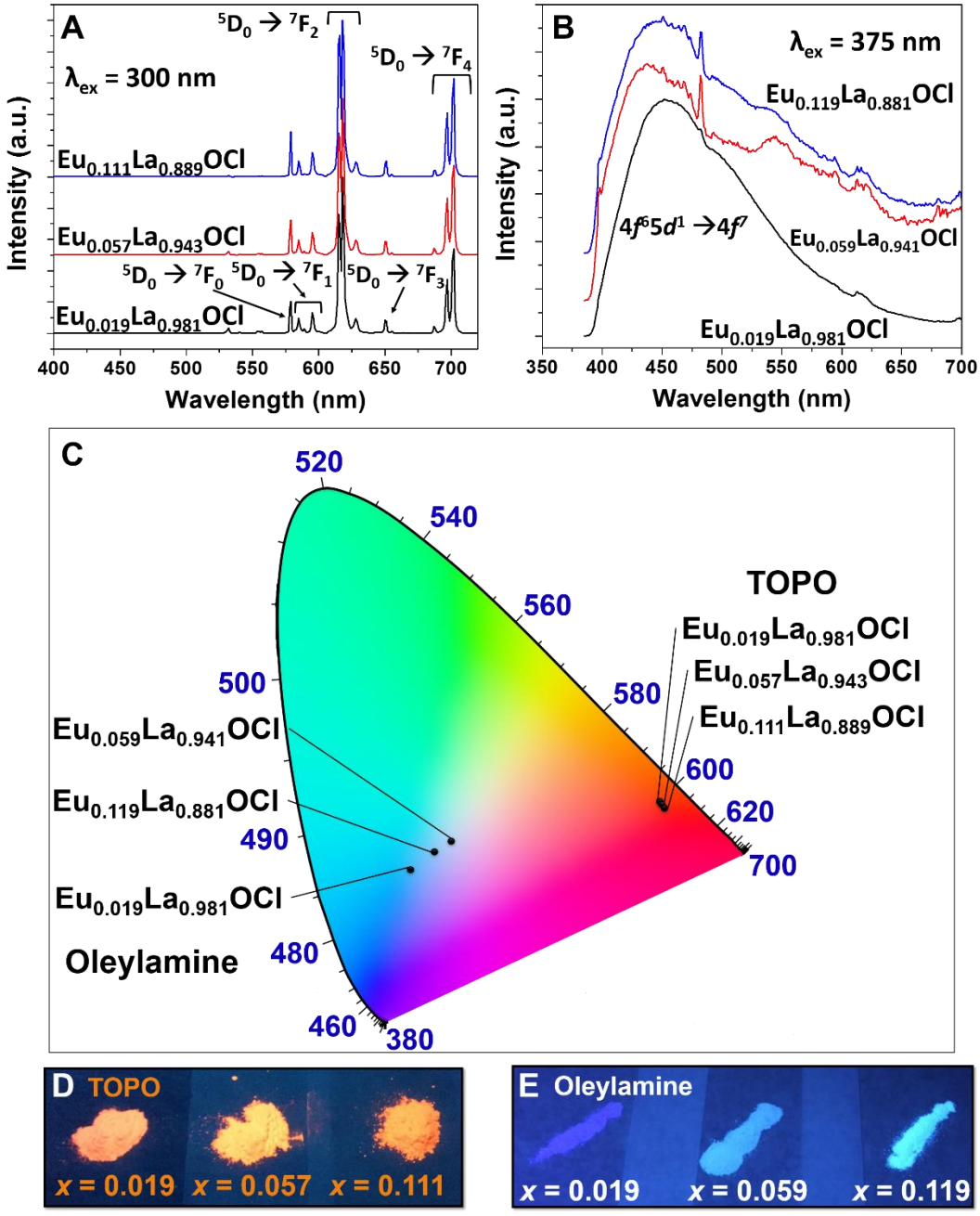

Figure V.4. Optically stimulated emission spectra measured for $Eu_xLa_{1-x}OCl$ stabilized using (A) TOPO as the passivating ligand and (B) oleylamine as the passivating ligand. The excitation wavelength used was 300 nm for the TOPO-stabilized phosphors and 375 nm for the oleylamine-stabilized phosphors. (C) CIE chromaticity diagram indicating the relative positions of the $Eu_xLa_{1-x}OCl$ phosphors. Digital photographs of (D) TOPO-stabilized (E) oleylamine-stabilized $Eu_xLa_{1-x}OCl$ phosphors with increasing Eu content upon illumination with a 254 nm UV light source.

respectively. In other words, increasing concentration of divalent europium appears to facilitate the lateral growth of the LaOCl nanocrystals without inducing a thinning of the particles. The larger ionic radii of nine-coordinate Eu^{2+} (130 pm in contrast to 121.6 pm for nine-coordinate La^{3+}) is expected to bring about an expansion of the lattice. However, in order to maintain charge balance, a vacancy must be introduced on the anion sublattice [which can be formally written as $(Eu^{2+}_{La})_x(La^{3+}_{La})_{1-x}(O^{2-}_{O})(Cl^{-}_{Cl})_{1-x}(V^{+}_{Cl})_x$ or $(Eu^{2+}_{La})_x(La^{3+}_{La})_{1-x}(O^{2-}_{O})_{1-x/2}(V^{+}_{O})_{x/2}(Cl^{-}_{Cl})$]; the combination of a larger dopant cation and a compensating anion vacancy thus results in relatively constant lattice parameters upon inclusion of divalent europium. The La—Cl bond distances are 3.15 Å for interlayer interactions and 3.20 Å for the distal La—Cl bond based on the structure depicted in Figure V.1, which are much shorter than the La—O bonds of 2.39 Å. Based on the relative bond strengths, a chloride vacancy may be easier to stabilize in this system. Indeed, the high mobility of halide ions in rare-earth oxyhalides is well documented and underpins their application as fast ion conductors at elevated temperatures.[36,37] Figure A.14 shows photoluminescence excitation spectra measured for TOPO- and oleylamine-capped $Eu_{0.019}La_{0.98}1OCl$ nanocrystals. The TOPO capped nanocrystals exhibit a broad absorption in the range between 250 and 350 nm corresponding to the $4f^6 5d^0 \rightarrow 4f^5 5d^1$ excitation of Eu^{3+} ions, whereas the oleylamine-capped nanocrystals exhibit a broad adsorption in the range between 325 and 425 nm corresponding to the $4f^7 5d^0 \rightarrow 4f^6 5d^1$ excitations of Eu^{2+} ions.[6,16–18,38,39] Figure V.4 shows digital photographs and optically stimulated photoluminescence emission spectra measured for each set of $Eu_xLa_{1-x}OCl$ nanocrystals upon excitation at $\lambda_{ex.}$ = 300 nm for TOPO-capped nanocrystals and $\lambda_{ex.}$ = 375 nm for oleylamine-capped nanocrystals, respectively, corresponding to the absorption maxima observed in Figure A.14. The emission spectra shown in Figure V.4A for the TOPO-capped solid-solution nanocrystals are characterized by sharp bands

derived from the $^5D_0 \rightarrow {}^7F_J$ (J = 4-0) relaxations of the photoexcited Eu^{3+} ion in the LaOCl framework. The $^5D_0 \rightarrow {}^7F_2$ emission at 618 nm is the most intense band resulting in a characteristic orange/red luminescence as can be seen in Figure V.4C on the Commission International de I'Eclairage (CIE) chromaticity diagram upon illumination at 300 nm. **Table V.2** lists the corresponding CIE coordinates for each of the LaOCl samples incorporating trivalent europium. In stark contrast, oleylamine-capped $Eu_xLa_{1-x}OCl$ nanocrystals are characterized by broad emission spectra extending from 400 to 500 nm derived from the $4f^6 5d^1 \rightarrow 4f^7$ transitions that encompasses many relaxations of a photoexcited Eu^{2+} ion in the LaOCl lattice; the emission band is centered at 445 nm. A substantially weaker signal corresponding to the characteristic $^5D_0 \rightarrow {}^7F_2$ radiative recombination of trivalent europium is observed at 613 nm, suggestive of trace amounts of oxidized trivalent europium. The characteristic blue luminescence of Eu^{2+} ions under 375 nm UV excitation are further depicted on the CIE chromaticity diagram in Figure V.4C. The corresponding CIE coordinates for the LaOCl samples with divalent europium are listed in Table A.6.

Comparing the standard reduction potentials with respect to NHE, E^o (La^{3+}/La^{2+}) is -3.1 V, whereas E^o (Eu^{3+}/Eu^{2+}) -0.34 V.[40,41] The latter can thus be readily reduced using a weak reducing agent. Oleylamine has been extensively used as a reducing agent in the synthesis of metal nanoparticles from metal salts.[29] For instance, Sun and co-workers have reported the synthesis of bimetallic FePt, CoPt, and NiPt nanoparticles from acetylacetonate precursors using oleylamine as a reducing agent.[42]

Oleylamine is further well known to mediate radical reactions; *N*-centered aminium as well as hydrogen radicals created from oleylamine can reduce $EuCl_3$ to $EuCl_2$ with the concomitant formation of mono-*N*-chloramines and alkylammonium salts, respectively.[43,44] Alternatively,

Table V.2. Commission International de I'Eclairage (CIE) coordinates for $Eu_xLa_{1-x}OCl$ phosphors upon 300 nm UV illumination (TOPO stabilized), 375 nm UV illumination (oleylamine stabilized), and X-ray excitation at 117.5 eV.

$Eu_{0.019}La_{0.981}$ OCl UV - TOPO	$Eu_{0.057}La_{0.943}$ OCl UV - TOPO	$Eu_{0.111}La_{0.889}$ OCl UV - TOPO	$Eu_{0.019}La_{0.981}$ OCl UV - oleylamine	$Eu_{0.059}La_{0.941}$ OCl UV - oleylamine	$Eu_{0.119}La_{0.881}$ OCl UV - oleylamine	$Eu_{0.019}La_{0.981}$ OCl XEOL - TOPO	$Eu_{0.019}La_{0.981}$ OCl XEOL - oleylamine
x = 0.646	x = 0.649	x = 0.655	x = 0.211	x = 0.281	x = 0.253	x = 0.596	x = 0.200
y = 0.353	y = 0.349	y = 0.344	y = 0.248	y = 0.292	y = 0.276	y = 0.372	y = 0.106

direct one-electron reduction of Eu^{3+} to form an oleylamine-substituted *N*-centered radical cation might be possible under the reaction conditions.[45] Further compelling evidence that the oxidation state of the incorporated europium is determined entirely by the passivating ligand and not the europium precursor used in synthesis comes from syntheses performed using $EuCl_2$ instead of $EuCl_3$ as the europium precursor. Figure A.15 shows a XRD pattern, TEM image, and photoluminescence emission spectrum for $Eu_xLa_{1-x}OCl$ nanocrystals obtained using $EuCl_2$ as the precursor and oleylamine as the capping ligand. A sheet-like or nanoplatelet morphology is obtained with the nanocrystals still crystallizing in the tetragonal PbFCl structure; the morphologies of the obtained nanocrystals are similar to that obtained using oleylamine and $EuCl_3$ (Figure V.3D—F). A broad blue emission band centered at 422 nm, characteristic of divalent europium (similar to Figure V.4B), is furthermore observed. Figure A.16 shows analogous characterization data for $Eu_xLa_{1-x}OCl$ nanocrystals obtained using $EuCl_2$ as the precursor and TOPO as the capping ligand. Again, the nanocrystals crystallize in the PbFCl structure with anisotropic broadening of the (101) and (102) reflections in the powder XRD pattern reminiscent of the TOPO synthesis described above. The photoluminescence emission spectrum (Figure A.16B) shows orange/red bands characteristic of trivalent europium transitions

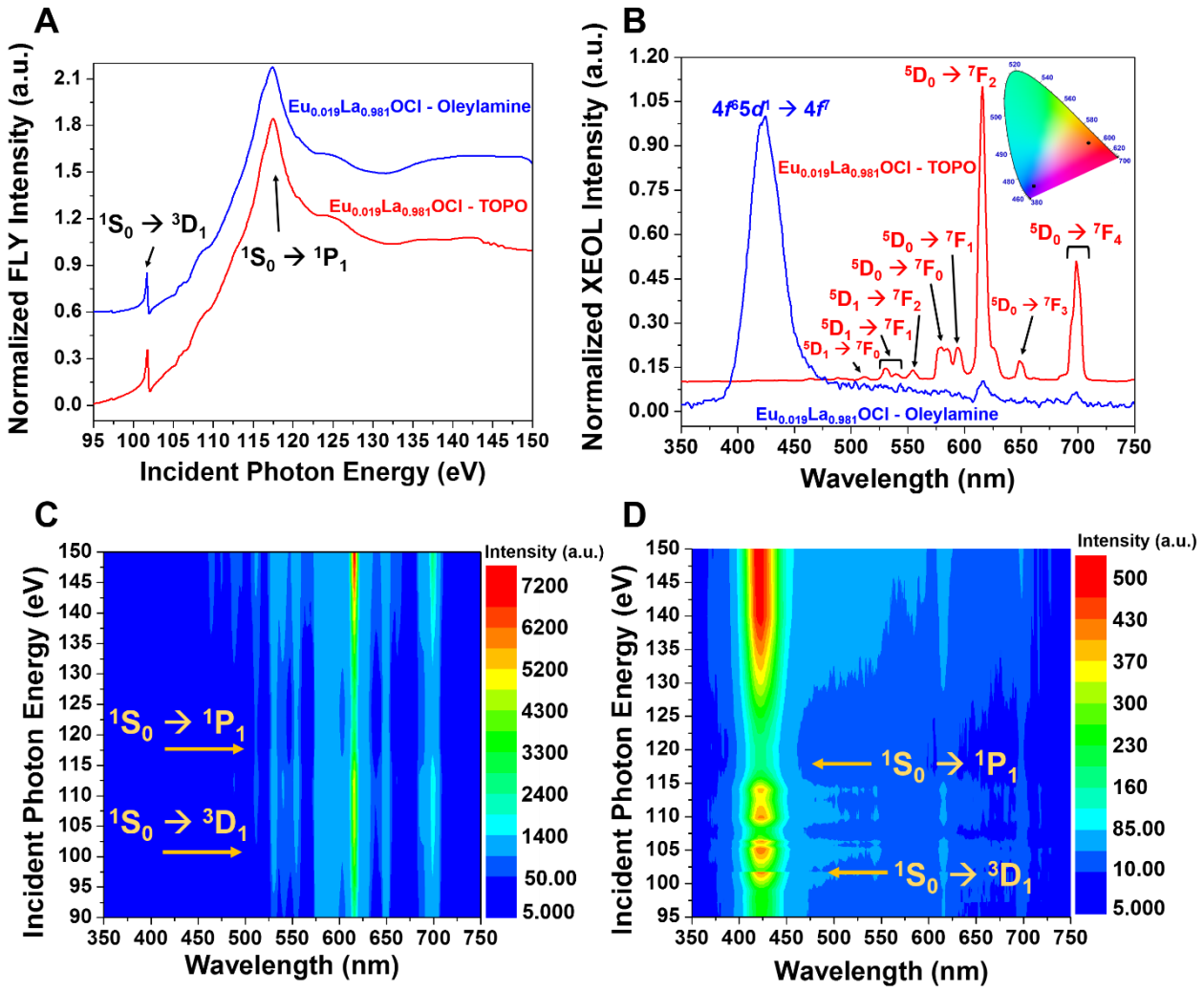

Figure V.5. (A) Normalized fluorescence yield (FLY) XANES spectra of $Eu_{0.019}La_{0.981}OCl$ stabilized with TOPO and oleylamine in red and blue, respectively, acquired at the La $N_{4,5}$-edge in the range of 95—150 eV. The specific $4d \rightarrow 4f$ transitions are delineated. A giant resonance feature centered at *ca*. 117.5 eV is observed corresponding to the $^1S_0 \rightarrow {}^1P_1$ transition. (B) Normalized XEOL spectra measured for $Eu_{0.019}La_{0.981}OCl$ stabilized with TOPO and oleylamine in red and blue, respectively, upon excitation at the center of the giant resonance at 117.5 eV. The inset depicts the CIE chromaticity diagram for the $Eu_{0.019}La_{0.981}OCl$ phosphors upon X-ray excitation. 3D plots depicting the evolution of the XEOL of $Eu_{0.019}La_{0.981}OCl$ stabilized with (C) TOPO and (D) oleylamine as a function of the excitation energy upon excitation across the La N_4-edge.

in the visible region. In other words, when $EuCl_2$ is used as the europium precursor, TOPO is able to oxidize it to trivalent europium, whereas oleylamine allows for preservation of the divalent character of the precursor. One electron reduction of phosphine oxides to the anion radical form is well established.[46] The reduction of triphenylphosphine oxide to the corresponding phosphine by metallic iron (which has a redox potential only about 100 mV lower than the Eu^{3+}/Eu^{2+} redoxcouple) has further been documented and corroborates the ability of TOPO to oxidize the divalent europium precursor.[47] In other words, both oleylamine and TOPO are redox non-innocent ligands in non-hydrolytic sol—gel condensation reactions and allow for control over the oxidation state of the dopant atom.

While optical luminescence of lanthanide phosphors results from $4f \rightarrow 5d$ excitation and subsequent relaxation, the energy transfer processes at play upon X-ray excitation are substantially different and involve $4d \rightarrow 4f$ excitation (of the host lattice) followed by thermalization of "hot" electron-hole pairs to activate luminescent centers.[19,48–51] **Figure V.5A** indicates the X-ray absorption near edge structure (XANES) spectra acquired in fluorescence yield mode for $Eu_xLa_{1-x}OCl$ nanocrystals capped with TOPO and oleylamine in the range between 95—150 eV across the La $N_{4,5}$-edge. The La^{3+}-ion has an empty 4*f* shell (and a full 4*d* subshell), which yields a singlet $^1S_0$ ground state. The XANES spectra show a distinctive $^1S_0 \rightarrow {}^3D_1$ absorption at 101.7 eV and a $^1S_0 \rightarrow {}^1P_1$ absorption centered at 117.5 eV. The high absorption cross-section of the $4d \rightarrow 4f$ excitation arises from the strong 4*d*—4*f* orbital overlap; given LS coupling selection rules, the $^1S_0 \rightarrow {}^1P_1$ transition strongly dominates the absorption spectrum and gives rise to a "giant resonance" spectral feature centered at 117.5 eV. The remarkable giant resonance feature is *ca.* 10 eV above the ionization threshold, which reflects the strong electron correlation of the 4*f* electrons localized within a narrow band (this effect is further amplified in

later lanthanides).[52–54] The pronounced enhancement of the absorption cross-section of the $^1S_0 \rightarrow {}^1P_1$ giant resonance and its broad line shape indicates a much shorter lifetime of the excitation as compared to the excitation to the triplet final state. Interestingly, the $^1S_0 \rightarrow {}^3D_1$ transition observed in the pre-edge region is forbidden by LS selection rules but is nevertheless observed as a result of strong spin—orbit coupling.[52] Because of the low concentration of Eu^{3+} and Eu^{2+} in the matrix, no discernible giant resonance feature is observed for these species.

Figure A.17 shows Eu $N_{4,5}$-edge XANES spectra acquired for $EuCl_2$ with a giant resonance centered at 141.1 eV corresponding to a $^8S_{7/2} \rightarrow {}^7D_J$ transition Figure V.5B contrasts the X-ray excited optical luminescence (XEOL) spectra of $Eu_xLa_{1-x}OCl$ nanocrystals capped with TOPO and oleylamine upon excitation at the giant resonance (117.5 eV). The TOPO-capped nanocrystals exhibit $^5D_0 \rightarrow {}^7F_J$ (red) and $^5D_1 \rightarrow {}^7F_J$ (orange) emission lines characteristic of Eu^{3+}, whereas the oleylamine-capped nanocrystals exhibit a broad $4f^65d^1 \rightarrow 4f^7$ (blue) emission characteristic of divalent Eu cations.[6,16–18,38,39] The CIE diagram in the inset of Figure V.5B compares the colors of the two samples upon X-ray excitation at the giant resonance feature centered at 117.5 eV (Table V.2 list the CIE coordinates). Figure V.5C and D display 3D contour plots of the evolution of the Eu-derived XEOL as a function of the excitation of La^{3+} cations of the $Eu_xLa_{1-x}OCl$ nanocrystals across the La $N_{4,5}$-edge.

A pronounced diminution of both Eu^{3+} (Figure V.5C) and Eu^{2+} (Figure V.5D) luminescence intensity is observed to be coincident with excitation at the giant resonance of La^{3+} cations of the host matrix. The XEOL intensity is substantially higher above and below the giant resonance. Above or below the giant resonance feature, the excitation of the La^{3+} cations creates “hot” electron—hole pairs that thermalize through multiple inelastic scattering processes transferring their energy to luminescent Eu^{3+} and Eu^{2+} centers. Subsequent radiative recombination events at

the luminescent centers yields their characteristic emission spectra. Multiple thermal electron—hole pairs are created for each "hot" electron-hole pair generated upon non-resonant X-ray excitation of a La^{3+} cation. In contrast, at the giant resonance, corresponding to a $4d^{10}4f^{0} \rightarrow 4d^{9}4f^{1}$ excitation, a singular thermal electron—hole pair is generated. Such an excitation is much less capable of exciting multiple luminescent centers.[19,51] Furthermore, resonant excitation creates a 4*d* hole that decays through a Coster-Kronig process with emission of an Auger electron.[51] Such an autoionization event is likely to be particularly pronounced for the ultra-thin nanoplatelets examined here with small escape depths. In other words, fundamentally different recombination channels are activated at the giant resonance that are inaccessible outside of the resonant excitation window.

V.5 Conclusions

In conclusion, TOPO and oleylamine are found to be redox non-innocent ligands in the non-hydrolytic sol—gel synthesis of solid-solution $Eu_xLa_{1-x}OCl$ nanocrystals. The former stabilizes trivalent europium, whereas the latter stabilizes divalent europium in the LaOCl matrix irrespective of whether $EuCl_2$ or $EuCl_3$ is used as the europium precursor. The ligands furthermore dictate the morphologies of the obtained particles; increasing incorporation of trivalent europium results in lattice expansion and dimensional confinement when TOPO is used as a ligand. In contrast, increasing incorporation of divalent europium does not bring about a substantial alteration of lattice parameters but facilitates increased lateral dimensions of the nanosheets when oleylamine is used as the ligand. Ligand control of dopant oxidation states allows for tunability of the optical and X-ray excited luminescence. The $Eu_xLa_{1-x}OCl$ nanocrystals show bright Eu-derived X-ray activated luminescence upon excitation of the La^{3+}

matrix. A pronounced modulation of XEOL intensities is observed for both divalent and trivalent Eu incorporated within LaOCl upon resonant excitation at the giant resonance of La^{3+} cations. The diminution of XEOL intensity arises from the activation of distinctive recombination channels (Auger electron ionization and relaxation of a single instead of multiple thermal electron—hole pairs) upon resonant as compared to non-resonant excitation. The synthetic strategy and mechanistic understanding of X-ray activated luminescence developed here paves the way for the design of efficient and color tunable X-ray phosphors.

V.6 References

(1) Issler, S. L.; Torardi, C. C. Solid State Chemistry and Luminescence of X-Ray Phosphors. *J. Alloys Compd.* **1995**, *229* (1), 54–65.

(2) Büchele, P.; Richter, M.; Tedde, S. F.; Matt, G. J.; Ankah, G. N.; Fischer, R.; Biele, M.; Metzger, W.; Lilliu, S.; Bikondoa, O.; Macdonald, J. E.; Brabec, C. J.; Kraus, T.; Lemmer, U.; Schmidt, O. X-Ray Imaging with Scintillator-Sensitized Hybrid Organic Photodetectors. *Nat. Photonics* **2015**, *9* (12), 843–848.

(3) Pan, W.; Wu, H.; Luo, J.; Deng, Z.; Ge, C.; Chen, C.; Jiang, X.; Yin, W.-J.; Niu, G.; Zhu, L.; Yin, L.; Zhou, Y.; Xie, Q.; Ke, X.; Sui, M.; Tang, J. $Cs_2AgBiBr_6$ Single-Crystal X-Ray Detectors with a Low Detection Limit. *Nat. Photonics* **2017**, *11* (November).

(4) Amemiya, Y.; Miyahara, J. Imaging Plate Illuminates Many Fields. *Nature* **1988**, *336* (6194), 89–90.

(5) Pokhrel, M.; Alcoutlabi, M.; Mao, Y. Optical and X-Ray Induced Luminescence from Eu^{3+} Doped $La_2Zr_2O_7$ Nanoparticles. *J. Alloys Compd.* **2017**, *693*, 719–729.

(6) Kim, D.; Jang, J.; Ahn, S. Il; Kim, S.-H.; Park, J.-C. Novel Blue-Emitting Eu^{2+}-Activated

LaOCl:Eu Materials. *J. Mater. Chem. C* **2014**, *2* (15), 2799–2805.

(7) Kawano, N.; Koshimizu, M.; Okada, G.; Fujimoto, Y.; Kawaguchi, N.; Yanagida, T.; Asai, K. Scintillating Organic-Inorganic Layered Perovskite-Type Compounds and the Gamma-Ray Detection Capabilities. *Sci. Rep.* **2017**, *7* (1), 14754.

(8) Hermus, M.; Phan, P. C.; Duke, A. C.; Brgoch, J. Tunable Optical Properties and Increased Thermal Quenching in the Blue-Emitting Phosphor Series: $Ba_2(Y_{1-x}Lu_x)_5B_5O_{17}:Ce^{3+}$(x = 0-1). *Chem. Mater.* **2017**, *29* (12), 5267–5275.

(9) George, N. C.; Brgoch, J.; Pell, A. J.; Cozzan, C.; Jaffe, A.; Dantelle, G.; Llobet, A.; Pintacuda, G.; Seshadri, R.; Chmelka, B. F. Correlating Local Compositions and Structures with the Macroscopic Optical Properties of Ce^{3+}-Doped $CaSc_2O4$, an Efficient Green-Emitting Phosphor. *Chem. Mater.* **2017**, *29* (8), 3538–3546.

(10) Boncher, W. L.; Rosa, N.; Kar, S.; Stoll, S. L. Europium Chalcogenide Nanowires by Vapor Phase Conversions. *Chem. Mater.* **2014**, *26* (10), 3144–3150.

(11) Perera, S. S.; Amarasinghe, D. K.; Dissanayake, K. T.; Rabuffetti, F. A. Average and Local Crystal Structure of β-Er:Yb:$NaYF_4$ Upconverting Nanocrystals Probed by X-Ray Total Scattering. *Chem. Mater.* **2017**, *29* (15), 6289–6297.

(12) Pokhrel, M.; Wahid, K.; Mao, Y. Systematic Studies on $RE_2Hf_2O_7$: 5% Eu^{3+} (RE = Y, La, Pr, Gd, Er, and Lu) Nanoparticles: Effects of the A-Site RE^{3+} Cation and Calcination on Structure and Photoluminescence. *J. Phys. Chem. C* **2016**, *120* (27), 14828–14839.

(13) Li, G.; Hou, Z.; Peng, C.; Wang, W.; Cheng, Z.; Li, C.; Lian, H.; Lin, J. Electrospinning Derived One-Dimensional LaOCl: Ln^{3+} (Ln = Eu/Sm, Tb, Tm) Nanofibers, Nanotubes and Microbelts with Multicolor-Tunable Emission Properties. *Adv. Funct. Mater.* **2010**, *20* (20), 3446–3456.

(14) Kong, Q.; Wang, J.; Dong, X.; Yu, W.; Liu, G. Synthesis and Luminescence Properties of LaOCl:Eu^{3+} Nanostructures via the Combination of Electrospinning with Chlorination Technique. *J. Mater. Sci. Mater. Electron.* **2013**, *24* (12), 4745–4756.

(15) Kort, K. R.; Banerjee, S. Shape-Controlled Synthesis of Well-Defined Matlockite LnOCl (Ln: La, Ce, Gd, Dy) Nanocrystals by a Novel Non-Hydrolytic Approach. *Inorg. Chem.* **2011**, *50*, 5539–5544.

(16) Lee, S.-S.; Park, H.-I.; Joh, C.-H.; Byeon, S.-H. Morphology-Dependent Photoluminescence Property of Red-Emitting LnOCl:Eu (Ln = La and Gd). *J. Solid State Chem.* **2007**, *180*, 3529–3534.

(17) Lv, L.; Wang, T.; Li, S.; Su, Y.; Wang, X. Tuning the Optical, Electronic and Luminescence Properties of LaOCl:Eu^{3+} via Structural and Lattice Strain Modulation. *CrystEngComm* **2016**, *18* (6), 907–916.

(18) Lv, L.; Zhai, H.; Liu, X.; Su, Y.; Wang, X. Structure and Optimum Luminescence for Nearly Block-Like LaOCl:Eu^{3+} Nanoparticles. *J. Nanosci. Nanotechnol.* **2016**, *16*, 3786–3790.

(19) Waetzig, G. R.; Horrocks, G. A.; Jude, J. W.; Zuin, L.; Banerjee, S. X-Ray Excited Photoluminescence near the Giant Resonance in Solid-Solution $Gd_{1-x}Tb_xOCl$ Nanocrystals and Their Retention upon Solvothermal Topotactic Transformation to $Gd_{1-x}Tb_xF_3$. *Nanoscale* **2016**, *8*, 979–986.

(20) Depner, S. W.; Kort, K. R.; Jaye, C.; Fischer, D. A.; Banerjee, S. Nonhydrolytic Synthesis and Electronic Structure of Ligand-Capped $CeO_{2-\delta}$ and CeOCl Nanocrystals. *J. Phys. Chem. C* **2009**, *113*, 14126–14134.

(21) Kort, K. R.; Banerjee, S. Oriented Electrophoretic Deposition of GdOCl Nanoplatelets. *J.*

Phys. Chem. B **2013**, *117*, 1585–1591.

(22) Terraschke, H.; Wickleder, C. UV, Blue, Green, Yellow, Red, and Small: Newest Developments on Eu^{2+}-Doped Nanophosphors. *Chem. Rev.* **2015**, *115* (20), 11352–11378.

(23) Blasse, G. On the Nature of the Eu^{2+} Luminescence. *Phys. Status Solidi B* **1973**, *131* (55), 5–8.

(24) Dorenbos, P. Energy of the First $4f^7$ --> $4f^65d$ Transition of Eu^{2+} in Inorganic Compounds. *J. Lumin.* **2003**, *104* (4), 239–260.

(25) Kort, K. R.; Banerjee, S. Ligand-Mediated Control of Dislocation Dynamics and Resulting Particle Morphology of GdOCl Nanocrystals. *Small* **2015**, *11* (3), 329–334.

(26) Hu, Y. F.; Zuin, L.; Wright, G.; Igarashi, R.; McKibben, M.; Wilson, T.; Chen, S. Y.; Johnson, T.; Maxwell, D.; Yates, B. W.; Sham, T. K.; Reininger, R. Commissioning and Performance of the Variable Line Spacing Plane Grating Monochromator Beamline at the Canadien Light Source. *Rev. Sci. Instruments* **2007**, *78*, 83109.

(27) Kasrai, M.; Yin, Z.; Bancroft, G. M.; Tan, K. H. X-Ray Fluorescence Measurments of X-Ray Absorption near Edge Strcuture at the Si, P, and S L Edges. *J. Vac. Sci. Technol. A* **1993**, *11* (5), 2694–2699.

(28) Mutin, P. H.; Vioux, A. Recent Advances in the Synthesis of Inorganic Materials via Non-Hydrolytic Condensation and Related Lowtemperature Routes. *J. Mater. Chem. A* **2013**, *1*, 11504–11512.

(29) Mourdikoudis, S.; Liz-Marzán, L. M. Oleyamine in Nanoparticle Synthesis. *Chem. Mater.* **2013**, *25*, 1465.

(30) Green, M. The Nature of Quantum Dot Capping Ligands. *J. Mater. Chem.* **2010**, *20* (28), 5797–5809.

(31) Du, Y. P.; Zhang, Y. W.; Sun, L. D.; Yan, C. H. Atomically Efficient Synthesis of Self-Assembled Monodisperse and Ultrathin Lanthanide Oxychloride Nanoplates. *J. Am. Chem. Soc.* **2009**, *131* (9), 3162–3163.

(32) Cho, J.; Jin, H.; Sellers, D.; Watson, D. F.; Son, D. H.; Banerjee, S. Influence of Ligand Shell Ordering on Dimensional Confinement of Cesium Lead Bromide ($CsPbBr_3$) Perovskite Nanoplatelets. *J. Mater. Chem. C* **2017**, *5*, 8810–8818.

(33) Puzder, A.; Williamson, A. J.; Zaitseva, N.; Galli, G.; Manna, L.; Alivisatos, A. P. The Effect of Organic Ligand Binding on the Growth of CdSe Nanoparticles Probed by Ab Initio Calculations. *Nano Lett.* **2004**, *4* (12), 2361–2365.

(34) Hamachi, L. S.; Jen-La Plante, I.; Coryell, A. C.; De Roo, J.; Owen, J. S. Kinetic Control over CdS Nanocrystal Nucleation Using a Library of Thiocarbonates, Thiocarbamates, and Thioureas. *Chem. Mater.* **2017**, *29* (20), 8711–8719.

(35) Shannon, R. D. Revised Effective Ionic Radii and Systematic Studies of Interatomic Distances in Halides and Chalcogenides. *Acta Crystallogr. Sect. A* **1976**, *A32*, 751–767.

(36) Imanaka, N.; Okamoto, K.; Adachi, G. Y. Water-Insoluble Lanthanum Oxychloride-Based Solid Electrolytes with Ultra-High Chloride Ion Conductivity. *Angew. Chemie - Int. Ed.* **2002**, *41*, 3890–3892.

(37) Imanaka, N.; Kato, Y. A New Type of Bromide Anion Conducting Solid. *Chem. Commun.* **2003**, No. 11, 1270–1271.

(38) Reisfeld, R.; Glasner, A. Absorption and Fluorescence Spectra of Eu^{2+} in Alkali Halide Crystals. *J. Opt. Soc. Am.* **1964**, *54* (3), 331–333.

(39) Kim, D.; Park, S.; Kim, S.; Kang, S. G.; Park, J. C. Blue-Emitting Eu^{2+}-Activated LaOX (X = Cl, Br, and I) Materials: Crystal Field Effect. *Inorg. Chem.* **2014**, *53* (22), 11966–

11973.

(40) Bochkarev, M. N. Molecular Compounds Of “new” divalent Lanthanides. *Coord. Chem. Rev.* **2004**, *248*, 835–851.

(41) Nugent, L. J.; Baybarz, R. D.; Burnett, J. L.; Ryan, J. L. Electron-Transfer and F-D Absorption Bands of Some Lanthanide and Actinide Complexes and the Standard (II-III) Oxidation Potential for Each Member of the Lanthanide and Actinide Series. *J. Phys. Chem.* **1973**, *77* (12), 1528–1539.

(42) Yu, Y.; Yang, W.; Sun, X.; Zhu, W.; Li, X. Z.; Sellmyer, D. J.; Sun, S. Monodisperse MPt (M = Fe, Co, Ni, Cu, Zn) Nanoparticles Prepared from a Facile Oleylamine Reduction of Metal Salts. *Nano Lett.* **2014**, *14* (5), 2778–2782.

(43) Kisner, A. Ultrathin Gold Nanowires – Chemistry, Electrical Characterization and Application to Sense Cellular Biology, Peter Grünberg Institute / Institute of Complex Systems, **2012**.

(44) Li, Q.; Rong, J.; Wang, S.; Zhou, S.; Zhang, L.; Zhu, X.; Wang, F.; Yang, S.; Wei, Y. Redox Chemistry between europium(III) Amide and Pyrrolyl-Functionalized Secondary Amines. Synthesis and Structural Characterization of Lithium and Novel Lanthanide Complexes Incorporating Functionalized Pyrrolyl Ligands. *Organometallics* **2011**, *30* (5), 992–1001.

(45) Hioe, J.; Šakić, D.; Vrček, V.; Zipse, H. The Stability of Nitrogen-Centered Radicals. *Org. Biomol. Chem.* **2015**, *13* (1), 157–169.

(46) Santhanam, K. S. V.; Bard, A. J. Electrochemistry of Organophosphorus Compounds. II. Electroreduction of Triphenylphosphine and Triphenylphosphine Oxide. *J. Am. Chem. Soc.* **1968**, *90* (5), 1118–1122.

(47) Young, D. A.; Brannock, K. C. Reduction of Triphenylphosphine Oxide with Iron to Triphenylphosphine. 3,780,111, **1973**.

(48) Dehmer, J. L.; Starace, A. F.; Fano, U.; Sugar, J.; Cooper, J. W. Raising of Discrete Levels into the Far Continuum*. *Phys. Rev. Lett.* **1971**, *26* (25), 1521–1525.

(49) Rezende, M. V. dos S.; Montes, P. J. R.; Andrade, A. B.; Macedo, Z. S.; Valerio, M. E. G. Mechanism of X-Ray Excited Optical Luminescence (XEOL) in Eu-Doped $BaAl_2O_4$ Nanopowders. *Phisycal Chem. Chem. Phisycs* **2016**, *18*, 17646.

(50) Sugar, J. Potential-Barrier Effects in Photoabsorption. II. Interpretation of Photoabsorption Resonances in Lanthanide Metals at the 4*d*-Electron Threshold. *Phys. Rev. B* **1972**, *5* (5), 1785–1792.

(51) Klaassen, D. B. M.; van Leuken, C. M. G.; Maessen, K. M. H. Giant Resonances in Luminescence Soft X-Ray Excitation Spectra of Phosphors. *Phys. Rev. B* **1987**, *36* (8), 4407–4412.

(52) Bonnelle, C.; Spector, N. *High Energy Spectroscopy and Resonance Effects*; Springer Netherlands: Dordrecht, **2015**.

(53) Moewes, A.; Winarski, R. P.; Ederer, D. L.; Grush, M. M.; Callcott, T. A. Study of 4*f* Inner Shell Excitations in Gd and Tb Using Resonant Inelastic Soft X-Ray Scattering. *J. Electron Spectrscopy Relat. Phenom.* **1999**, *101–103*, 617–622.

(54) Lenth, W.; Lutz, F.; Barth, J.; Kalkoffen, G.; Kunz, C. Giant Resonance Enhancement of the 4f, 5p, and 5s States in the Photoemission Spectra of Rare-Earth Compounds. *Phys. Rev. Lett.* **1978**, *41* (17), 1185–1188.

CHAPTER VI

IN A DIFFERENT LIGHT: DECIPHERING OPTICAL AND X-RAY SENSITIZATION MECHANISMS IN AN EXPANDED PALETTE OF LAOCL PHOSPHORS

VI.1 Overview

The conversion and numerical amplification of X-ray photons to visible light is at the heart of numerous technological applications spanning the range from X-ray detectors and scintillators to radiographic medical imaging devices. The need for increased sensitivity and spatial resolution to reduce radiation exposure and provide better differentiation of specimens presenting an X-ray contrast has been a strong driving force in the search for novel X-ray phosphors. However, the current palette of X-ray phosphors is rather sparse. The development of color tunable phosphors necessitates the incorporation of multiple dopants, which in turn interact through complex sensitization mechanisms that are poorly understood for high-energy excitation. In this chapter, we describe the stabilization of multiply doped LaOCl nanocrystals incorporating Tb^{3+} cations in conjunction with either divalent or trivalent europium ions, yielding phosphors emitting in the blue—green and green—red regions of the electromagnetic spectrum, respectively The choice of the coordinating ligand (tri-*n*-octylphosphine *versus* oleylamine) dictates the oxidation state of the incorporated Eu-ions. Pronounced differences are observed in sensitization mechanisms upon optical and X-ray excitation thereby considerably modifying the perceived color of the X-ray phosphors from those stimulated by ultraviolet illumination. Upon visible light illumination, strong $Tb^{3+} \rightarrow Eu^{3+}$ sensitization is observed for LaOCl nanocrystals incorporating trivalent europium ions; however, upon X-ray excitation, this sensitization pathway is instead supplanted by independent $La^{3+} \rightarrow Eu^{3+}$ and $La^{3+} \rightarrow Tb^{3+}$ sensitization routes.

In contrast, strong $Eu^{2+} \rightarrow Tb^{3+}$ sensitization is observed for LaOCl nanocrystals incorporating divalent europium ions upon both optical and X-ray excitation ($La^{3+} \rightarrow Eu^{2+} \rightarrow Tb^{3+}$ and $La^{3+} \rightarrow Tb^{3+}$ pathways are also observed upon X-ray excitation). The increased efficacy of the $Eu^{2+} \rightarrow Tb^{3+}$ as compared to $Eu^{3+} \rightarrow Tb^{3+}$ sensitization pathway derives from the parity allowed nature and orders of magnitude higher absorption cross-section for the excitation of the divalent Eu-ion. A strong suppression of luminescence intensity is observed upon excitation at the giant resonance absorption for all of the observed emission bands and corresponds to a change in mechanism from the creation of multiple thermal electron—hole pairs to a non-radiative Coster—Kronig process dominated by Auger photoionization.

VI.2 Introduction

Advances in miniaturization, resolving power, and response times of displays and optoelectronic components have been driven largely by the ability to scale active elements to increasingly smaller dimensions and the large scale integration of miniaturized components.[1] In the specific case of radiation detectors, scintillators, and medical imaging devices, the active element amplifies incident X-ray photons to produce a multitude of visible photons.[2–6] The imperative for effective amplification is readily understood considering that the higher the amplification, the more sensitive the detector, and lower the X-ray dose that needs to be used for radiographic imaging. Scaling the crystallite size within phosphor films is furthermore a critical imperative since the spatial resolution is directly correlated to the grain size.[7] Unlike in the case of optically stimulated phosphors where a substantial corpus of work has become available (driven by a strong worldwide push to adopt solid-state lighting as an energy efficient alternative to incandescent and fluorescent lamps), much less is known about the fundamental activation

channels, sensitization mechanisms, and recombination pathways operational upon high-energy (VUV and X-ray) excitation of luminescent centers. As a result, the current palette of X-ray phosphors is rather limited in its coverage of the visible spectrum. Color tunability typically necessitates the incorporation of multiple luminescent centers within the host matrix, which is non-trivial given the manifestation of wavelength-dependent sensitization mechanisms.[8–10] Rare-earth oxyhalides crystallized in the matlockite PbFCl structure have emerged as potential candidates for X-ray image converter devices as a result of their high sensitivity and ability to downconvert X-rays to visible photons with high amplification.[11–14] However, sensitization mechanisms remain to be elucidated and the color tunability of X-ray phosphors is constrained by the limited synthetic control established thus far over inclusion of multiple dopants within such lattices. In this chapter, we demonstrate broad color tunability of X-ray-stimulated optical luminescence based on the synthesis of multiply doped $La_{1-x-y}Tb_xEu_yOCl$ nanocrystals (with controlled incorporation of either divalent or trivalent Eu-ions) using a solution-phase non-hydrolytic sol—gel condensation route. The distinct sensitization mechanisms upon X-ray ($La^{3+} \rightarrow Tb^{3+}$, $La^{3+} \rightarrow Eu^{3+}$, and $Eu^{2+} \rightarrow Tb^{3+}$) and optical ($Eu^{2+} \rightarrow Tb^{3+}$ and $Tb^{3+} \rightarrow Eu^{3+}$) excitation are contrasted using photoluminescence emission and X-ray excited optical luminescence (XEOL) measurements.

In the case of lanthanide cations doped within a host matrix, the observed luminescence arises from electronic transitions between narrow 4*f* states. These transitions are symmetry forbidden. As a result, the absorption cross sections are low and the excited states are relatively long lived. Energy transfer can occur between closely proximate luminescent centers and indeed the extent of energy transfer strongly determines the perceived color of the phosphor. Upon optical excitation, Tb^{3+} can effectively enhance the luminescence of Eu^{3+} luminescent centers.[15–

[17] However, the sensitization of Tb^{3+} luminescence upon Eu^{2+} activation remains less studied given difficulties with stabilizing divalent europium in oxide lattices.[12] The sensitization of both dopant types upon X-ray excitation of the host lattice is almost entirely unexplored. In this chapter we demonstrate a facile synthetic route for the preparation of ligand-passivated solid-solution LaOCl nanocrystals incorporating Eu^{3+}/Eu^{2+} and Tb^{3+}-cations. Broad tunability of coloration spanning the range from red to green and green to blue regions of the electromagnetic spectrum is achieved depending on the inclusion of trivalent or divalent europium, respectively, in conjunction with trivalent terbium. Optical and X-ray excitation present a study in contrasts with the operation of sequential energy transfer cascades in the former and thermalization of high energy electron—hole pairs in the latter. A pronounced modulation of the luminescence intensity is observed near the giant resonance absorption of the LaOCl host matrix owing to a change in the recombination mechanism from thermalization of high-energy electron—hole pairs to Auger ionization and relaxation of a single electron—hole pair.

VI.3 Experimental

VI.3.1 Synthesis

$TbCl_3$, $EuCl_3$, $LaCl_3$, $La(O^iPr)_3$, and tri-*n*-octylphosphine oxide (TOPO, 90%) were purchased from Strem Chemicals and used as received. $EuCl_2$ and oleylamine were purchased from Sigma Aldrich and used as received. In a typical synthesis of LaOCl nanocrystals, 2 mmol of $LaCl_3$ and 2 mmol of $La(O^iPr)$ were weighed into a three-neck round bottom flask with 25 mmol of a stabilizing ligand, either TOPO or oleylamine, within an argon-filled glovebox. The solid-solution nanocrystals were prepared by substitution of $LaCl_3$ by the desired molar equivalent of Tb^{3+} and Eu^{3+} (or Eu^{2+}) ions using $TbCl_3$, $EuCl_3$, and $EuCl_2$ as the dopant

precursors. The reaction vessel was then heated to 340°C and stirred in an argon atmosphere under standard Schlenk conditions. After reaction for 2 h, the mixture was rapidly cooled to 70°C, followed by the addition of acetone (in the case of TOPO) or hexanes (in the case of oleylamine) to flocculate the ligand-passivated solid-solution nanocrystals. The nanocrystals were recovered by centrifugation at 12,000 rpm for 20 min and were subsequently redispersed in hexanes and recovered by centrifugation at 1,500 rpm for 5 min. Finally, the decanted dispersion was redispersed in acetone (TOPO) or hexanes (oleylamine) and the nanocrystals were recovered by centrifugation at 12,000 rpm; the resulting nanocrystals were dried in air and collected for further analysis. Nanocrystals were stored in argon-filled sealed glass vials wrapped in Parafilm that were then put into an evacuated food saver bag and heat-sealed for transportation to the synchrotron.

VI.3.2 Structural and Morphological Characterization

The solid-solution nanocrystals were examined by powder X-ray diffraction (XRD) using a Bruker-AXS D8 Advance Bragg-Brentano diffractometer with a Cu Kα source ($\lambda = 1.5418$ Å) to enable phase identification. The particle morphology was evaluated by transmission electron microscopy (TEM) using a FEI Technai G2 F20 ST instrument operated at an accelerating voltage of 200 kV. Sample preparation for TEM evaluation involved preparation of a dispersion in 2-propanol and drop casting onto a 400-mesh carbon-coated Cu grid. The stoichiometry of the solid-solution nanocrystals was determined by inductively coupled plasma-mass spectrometry (ICP-MS) using a Perkin Elmer DRCII instrument. Samples were prepared for ICP-MS analysis by digesting the nanocrystals using an aqueous solution of 15.8 M HNO_3.

VI.3.3 Measurement of Optical Properties

Photoluminescence emission and excitation spectra were acquired using a Horiba PTI QuantaMaster 40 spectrofluorometer. The photoluminescence emission of Tb^{3+} and Eu^{3+} luminescent centers was measured in the range of 400—720 nm upon excitation at 248 and 300 nm, respectively; likewise, the emission spectra of Eu^{2+} luminescent centers was measured in the range of 400—720 nm upon excitation at 354 nm. Photoluminescence excitation spectra for Tb^{3+} luminescent centers were acquired in the range of 200—520 nm at an emission wavelength of 543 nm (corresponding to the $^5D_4 \rightarrow {}^7F_5$ transition); corresponding excitation spectra were acquired for Eu^{3+} species in the range of 200—600 nm at an emission wavelength of 618 nm (corresponding to the $^5D_0 \rightarrow {}^7F_2$ transition) and for Eu^{2+} species in the range of 200—380 nm at an emission wavelength of 404 nm (corresponding to the $4f^6 5d^1 \rightarrow 4f^7$ transition). For the photoluminescence measurements, the nanocrystals were spread onto a solid sample holder and held in place by a thin layer of AP 101 vacuum grease from Apiezon. The solid sample holder is a 10x10 mm aluminum block cut at 20 degrees to reduce speculation reflectance into the detector.

XEOL and La $N_{4,5}$ X-ray absorption near-edge structure (XANES) spectra were acquired at the Variable Line Spacing-Plane Grating Monochromator (VLS-PGM) beamline of the Canadian Light Source located at the University of Saskatchewan in Saskatoon (with an energy resolution, $E/\Delta E > 10{,}000$ in the relevant energy range).[18] The nanocrystal powders were deposited on a carbon tape and studied at room temperature. The total fluorescence yield (FLY) and XEOL data were acquired concurrently for each sample. XANES spectra were acquired using VLS-PGM's high-energy grating by scanning the energy of the incident X-rays in the range between 90 and 170 eV in steps of 0.1 eV. The pressure within the sample chamber was

maintained lower than 1×10^{-8} Torr. The FLY signal was recorded using a microchannel plate detector.[19] The XANES spectra have been normalized to the intensity of the photon beam as measured by the drain current at a Ni mesh with a transmission of 90% placed upstream of the sample. XEOL data were collected using an Ocean Optics QE65000 monochromator with a fiber-optic feed-through over a working range of 200–1000 nm.

VI.4 Results and Discussion

Designing an effective phosphor exhibiting bright luminescence requires careful consideration of the crystal structure to tune interactions between luminescent centers and the host lattice as well as to suppress non-radiative recombination pathways.[20,21] A particularly useful host crystal structure that exhibits a low-phonon cutoff energy and limits cross-relaxation mechanisms is the tetragonal matlockite PbFCl structure (space group *P*4/*nmm)*.[22–24] In this article, we examine LaOCl, which adopts the PbFCl structure (as depicted in the inset of Fig. S1), as a host lattice for multiple luminescent centers. In this structure, infinite sheets of $(LaO)_n^{n+}$ and Cl^- ions are alternated along the crystallographic *c* direction.[22–26] The trivalent lanthanum cations have a local coordination environment described by C_{4v} symmetry wherein each La-ion resides in a monocapped square antiprism defined by four oxygen atoms in an underlying plane and five chloride ions in the layers above. The fifth chloride ion is derived from the next-to-nearest anionic sheet, which thus establishes 3D connectivity across the lattice. In addition to the desired luminescent attributes mentioned above for these phosphors, they also exhibit high chemical stability and are thermally robust.[27]

In Chapters IV and V, we reported the solution-phase synthesis of ligand-passivated nanocrystals of Tb-incorporated GdOCl and Eu-incorporated LaOCl (either divalent or trivalent

Eu, tunable by choice of coordinating ligand) with well-defined morphologies based on the condensation of rare earth alkoxides and rare earth halides in the presence of various coordinating solvents.[23,24] As such, this synthetic route holds promise for allowing for elaboration to a much broader palette of colors based on the preparation of multiply doped phosphors. The controllable incorporation of trivalent Tb-ions in conjunction with either divalent or trivalent Eu-ions is demonstrated here and is used here to contrast sensitization mechanisms manifested upon optical and X-ray excitation in multiply doped LaOCl. As noted in previous work and Chapters IV and V, the oxychloride framework is formed as a result of the elimination of isopropyl chloride upon the condensation of lanthanum isopropoxide with lanthanum chloride; the added coordinating ligands, oleylamine and TOPO, constrain crystal growth to nanometer-sized dimensions.[22–26]

Figure A.18 shows a powder XRD pattern acquired for undoped LaOCl prepared using TOPO as the ligand; the pattern can be indexed to the matlockite PbFCl structure (PDF # 88-0064, inset to Figure A.18). The intense reflection at $2\theta = 31°$ is indexed to diffraction from the (110) planes. The inset of Figure A.18 shows a TEM image of an individual LaOCl nanocrystal indicating a disk-like appearance; the particles have an average diameter of *ca*. 60 nm. The "self-purification" of dopant atoms, corresponding to a phenomenon wherein dopant atoms sought to be substitutionally doped within a lattice instead diffuse to the surface and are eliminated from a growing particle, makes the incorporation of dopants rather challenging at nanoscale dimensions.[28,29] However, this challenge can be substantially mitigated if the intended dopant atoms are close in size to the atoms of the host lattice.[23,30] The ionic radius of La^{3+} is estimated to be 121.6 pm; the ionic radii of Tb^{3+} (109.5 pm), Eu^{3+} (112.0 pm), and Eu^{2+} (130.0 pm) are within 11% of this value, allowing for considerable miscibility.[31] **Figure VI.1** plots XRD patterns

acquired for solid-solution Tb-incorporated LaOCl nanocrystals; Tb^{3+} ions exhibit complete miscibility in the LaOCl lattice up to a concentration of 17.9 at.% (as determined from ICP-MS measurements); however, at a Tb^{3+} concentration of 23.2 at.%, segregation of Tb^{3+} into a TbOCl phase crystallized in the tetragonal structure (PDF 48-1648) is observed, as indicated by the asterisked reflection at $2\theta = 32°$ (Figure VI.1). The Tb concentrations measured by ICP-MS are in general slightly lower than the intended concentration added to the reaction mixture. Figure VI.1B shows a low-magnification TEM image of a LaOCl nanocrystal with 12.8 at.% Tb incorporation; the nanocrystals exhibit the same quasi-spherical appearance as undoped LaOCl nanocrystals in Figure A.18. A similar evaluation of Eu^{3+} miscibility in LaOCl was presented in Chapter V, suggesting a solubility limit of 15.0 at.% for this dopant beyond which the intended dopant segregates in the form of Eu_2O_3.[24] Determining the limits of miscibility of Tb^{3+} and Eu^{3+} ions in the LaOCl lattices provides guidance for the design of co-doping schemes.

Figure A.19A shows a photoluminescence excitation spectrum measured for $La_{0.911}Tb_{0.089}OCl$ nanocrystals at $\lambda_{em} = 544$ nm; a broad absorption feature is observed in the range between 210 and 280 nm corresponding to the $4f^8 5d^0 \rightarrow 4f^7 5d^1$ excitation of Tb^{3+} ions.[32–35] Figure A.19B shows the emission spectrum obtained at $\lambda_{ex} = 248$ nm, which corresponds to the absorption maximum; sharp bands derived from the $^5D_{3\text{-}4} \rightarrow {}^7F_J$ ($J = 6$—0) relaxations of the photoexcited Tb^{3+}-ion in the LaOCl lattice dominate the spectrum; the assignment of spectral features to specific transitions is noted in the figure. The $^5D_4 \rightarrow {}^7F_5$ emission at 544 nm is the most intense band giving rise to the characteristic green luminescence of these materials seen in the digital photograph of Figure A.20A. The variation of the normalized luminescence intensity of the $^5D_4 \rightarrow {}^7F_5$ emission as a function of measured Tb concentration is also shown in Figure A.20; the intensity initially increases with Tb^{3+} incorporation and is maximum for

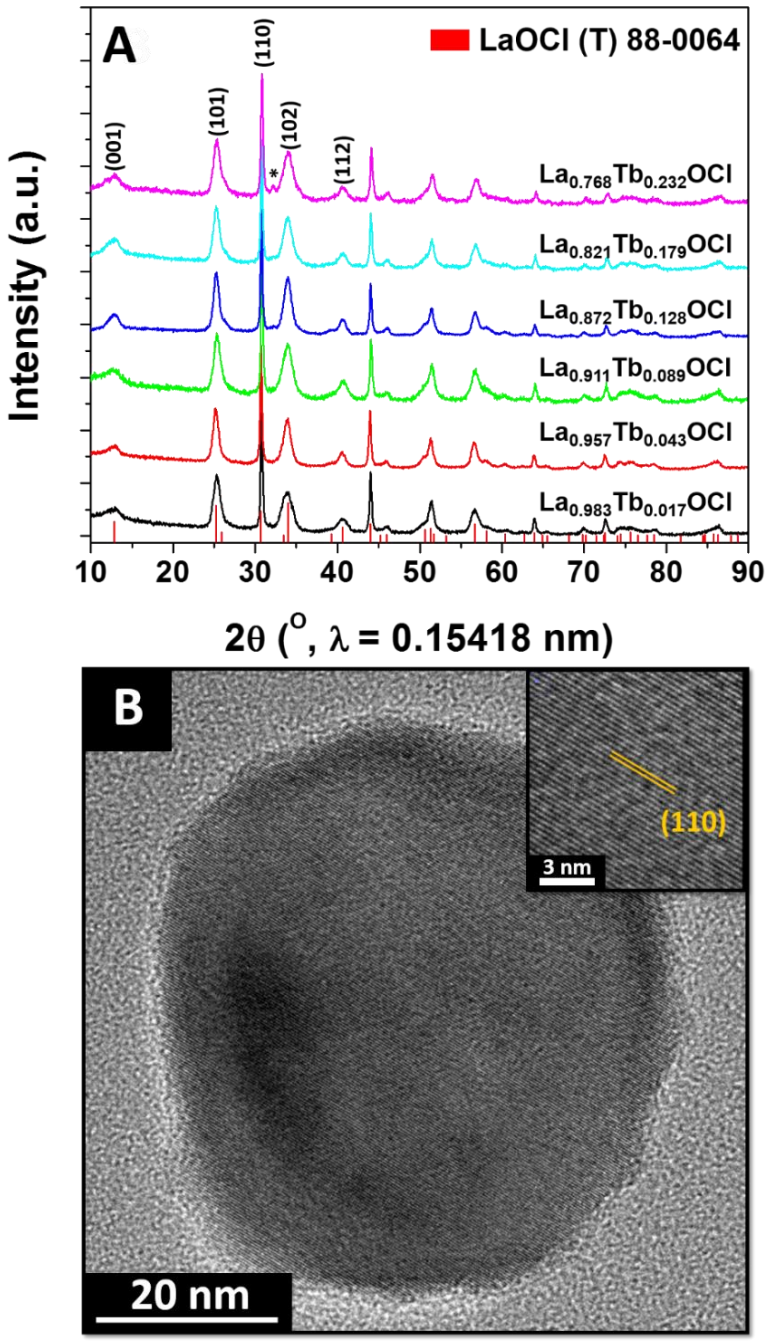

Figure VI.1. (A) Powder XRD patterns acquired for solid-solution $La_{1-x}Tb_xOCl$ nanocrystals where x = 0.017, 0.043, 0.089, 0.128, 0.179, and 0.232 grown using TOPO as a ligand. The vertical red bars denote positions and relative intensities from JCPDS # 88-0064 for tetragonal LaOCl (Space Group: *P4/nmm*). The asterisked reflection for the x = 0.232 sample can be indexed to the (110) reflection of TbOCl. (B) Low-magnification transmission electron microscopy image of a $La_{0.872}Tb_{0.128}OCl$ nanocrystal. The inset indicates the separation between the (110) lattice planes of tetragonal LaOCl.

$La_{0.911}Tb_{0.089}OCl$. The decrease in photoluminescence emission intensity for higher concentrations of Tb^{3+} is a result of concentration quenching, as also observed in Chapter IV for Tb-doped GdOCl nanocrystals where the maximum photoluminescence intensity has been observed for a Tb^{3+} concentration of 8.4 at.% in GdOCl.[23] Multipolar interactions, reabsorption of photons emitted by luminescent sites, and activation of additional non-radiative recombination channels contribute to the observed concentration quenching.[23,32]

There is a considerable literature on the co-doping of host lattices with Tb^{3+} and Eu^{3+} as a donor−acceptor pair; optically excited Tb^{3+} serves as a donor chromophore, whereas Eu^{3+} acts as an acceptor chromophore, thereby facilitating phonon-mediated energy transfer between closely spaced atoms within a co-doped lattice through dipole—dipole and dipole-quadrupole coupling.[36–38] The relative concentration of the acceptor, Eu^{3+}, determines the extent to which Tb^{3+} luminescence is observed and allows for considerable tunability between the red and green regions of the electromagnetic spectrum.[15,34,39] In order to prepare LaOCl nanocrystals incorporating both Tb^{3+} and Eu^{3+} ions, the $LaCl_3$ precursor has been substituted with desired molar amounts of $TbCl_3$ and $EuCl_3$. TOPO is used as a ligand to retain the trivalent oxidation state of europium (since as shown in Chapter V, a reductive ligand such as oleylamine reduces trivalent europium to divalent europium),[24] In order to obtain color tunability, guided by the results shown in Figure VI.1 and Figure A.20B, the dopant concentrations have been kept well below the range where concentration quenching or phase segregation are manifested. The following ratios of atomic percentages of Tb^{3+} and Eu^{3+} in LaOCl have been prepared: 1:2, 1:1, 2:1, 4:1, and 5:1. **Figure VI.2** presents powder XRD patterns acquired for these solid-solutions; the atomic percentages of Tb and Eu have been determined by ICP-MS measurements. In general, the concentrations of Tb and Eu incorporated within the solid-solution nanocrystals are

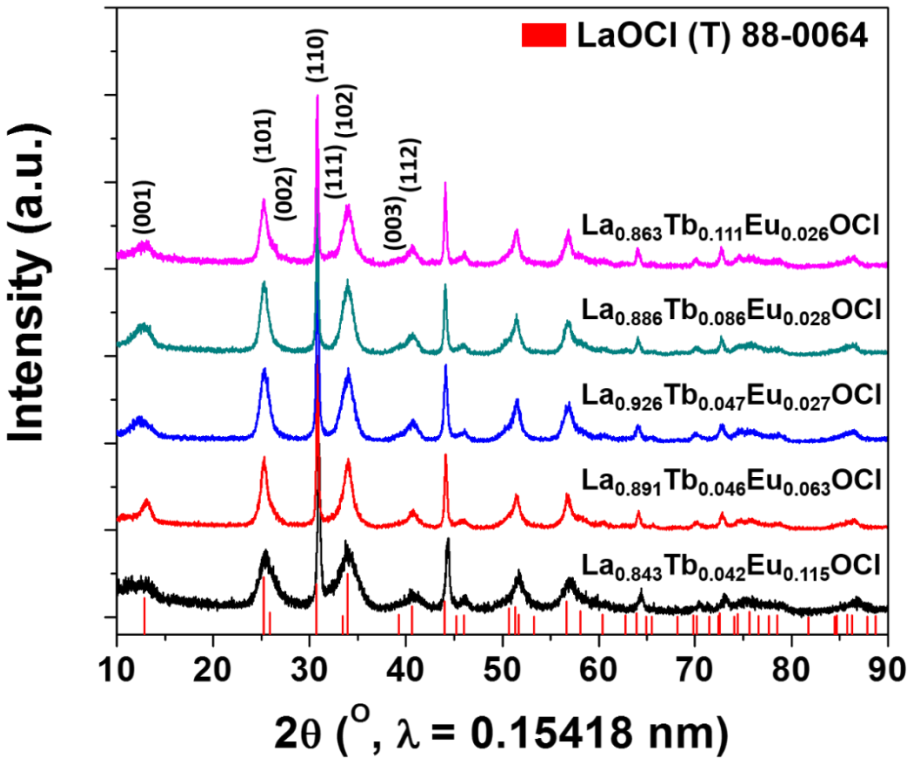

Figure VI.2. (A) Powder XRD patterns acquired for solid-solution $La_{1-x-y}Tb_xEu_yOCl$ nanocrystals capped with TOPO. The vertical red bars denote positions and relative intensities expected from JCPDS # 88-0064 for tetragonal LaOCl (space group: *P4/nmm*).

significantly lower than the concentration of the precursors in the reaction mixture. The powder XRD patterns have been indexed to PDF 88-0064, indicating retention of the tetragonal PbFCl structure of LaOCl at these concentrations. The $La_{0.843}Tb_{0.042}Eu_{0.115}OCl$ sample shows considerable anisotropic broadening of the XRD reflections at $2\theta = 25°$ and 34°, indexed to the (101) and (102) lattice planes, respectively, which is indicative of growth confinement along the crystallographic *c* direction.[24,25] Such a pronounced growth constraint, resulting in stabilization of thinner nanoplatelets, has been observed previously upon incorporation of trivalent europium and has been attributed to the smaller Eu^{3+} cation being relatively weakly bonded to the Cl^- in the next-to-nearest Cl^- sheet, which thus reduces the 3D connectivity of the structure.[24]

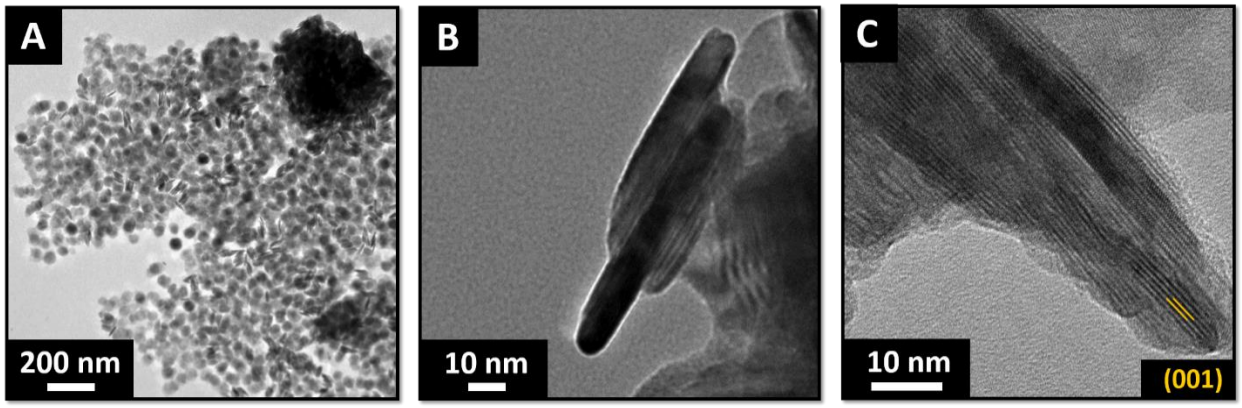

Figure VI.3. Low-magnification transmission electron microscopy images of $La_{1-x-y}Tb_xEu_yOCl$ nanocrystals grown using TOPO as a ligand: A, B) $x = 0.047$ and $y = 0.027$ at different magnifications and C) $x = 0.042$ and $y = 0.115$. The crystallites exhibit a platelet-like morphology; a discernible thinning of the platelets is observed with increasing Eu concentration. The lattice planes observed in (C) have been indexed to the separation between the (001) planes of LaOCl.

Alternatively, the reduced dimensions may result from the lower reactivity of the $EuCl_3$ precursor.[30]

Figure VI.3A shows a low-magnification TEM image of $La_{0.926}Tb_{0.047}Eu_{0.027}OCl$ nanocrystals. The thickness of the nanodisks is deduced to be 10.1 nm ± 1.3 nm, as more clearly discernible in Figure VI.3B. However, with increasing Eu concentration, as also suggested by the increased Scherrer broadening of the (101) and (102) reflections in Figure VI.2, a thinning of the nanoplatelets is observed for the $La_{0.843}Tb_{0.042}Eu_{0.115}OCl$ nanocrystals in Figure VI.3B. Based on cross-sectional images, a thickness of 5.2 ± 0.5 nm is deduced for these samples with higher Eu^{3+} incorporation.

Figure A.21 shows the photoluminescence excitation spectra measured for co-doped $La_{0.926}Tb_{0.047}Eu_{0.027}OCl$ nanocrystals at Eu^{3+} and Tb^{3+} emission maxima of λ_{em} = 618 and 543 nm, respectively. The Eu^{3+} excitation spectrum is characterized by a broad absorption feature in

the range between 250 and 350 nm which can be attributed to a Eu^{3+}-O^{2-} charge transfer band arising from the transition of an electron from 2*p* states centered on the oxide ion to the empty 4*f* orbitals of Eu^{3+}.[40–43] The Tb^{3+} excitation spectrum shows an absorption maximum with a local maximum at 248 nm, which is similar in appearance to the absorption maximum observed for $La_{0.911}Tb_{0.089}OCl$ nanocrystals in Figure A.19. An additional band is observed with a maximum around 300 nm indicating that the Tb^{3+}-O^{2-} and Eu^{3+}-O^{2-} charge transfer bands are somewhat overlapped.

Figure VI.4 contrasts emission spectra of solid-solution $La_{1-x-y}Tb_xEu_yOCl$ phosphors measured upon excitation at λ_{ex} = 248 nm and 300 nm corresponding to the maxima of the Tb^{3+}-O^{2-} and Eu^{3+}-O^{2-} charge transfer bands, respectively, as observed in the photoluminescence excitation spectra of Figure A.21. In Figure VI.4A, the excitation energy is sufficient to directly excite both the Tb^{3+} and Eu^{3+} luminescent centers. The relative ratios of the peak intensities of the $^5D_4 \rightarrow {}^7F_5$ (Tb^{3+}) and $^5D_0 \rightarrow {}^7F_2$ (Eu^{3+}) emission bands centered at 544 and 618 nm, respectively, provide insight into the sensitization and recombination mechanisms. Pronounced red ($^5D_0 \rightarrow {}^7F_2$, Eu^{3+}) emission is observed for the $La_{0.926}Tb_{0.047}Eu_{0.027}OCl$, $La_{0.891}Tb_{0.046}Eu_{0.063}OCl$, and $La_{0.843}Tb_{0.042}Eu_{0.115}OCl$ nanocrystals, whereas the green ($^5D_4 \rightarrow {}^7F_5$, Tb^{3+}) emission is relatively more intense for the $La_{0.863}Tb_{0.111}Eu_{0.026}OCl$ and $La_{0.886}Tb_{0.086}Eu_{0.028}OCl$ nanocrystals. In other words, the Tb-dopants have to be present in substantial excess for the green emission band to be more intense suggesting that the Tb^{3+} emission is substantially quenched as a result of energy transfer and efficacious sensitization of the Eu^{3+} luminescent centers (as understood based on the Dieke diagram plotted in **Figure VI.5**).[15,36,38,39] Indeed, contrasting the relative intensities of the $^5D_0 \rightarrow {}^7F_J$ (J = 0—4) emission bands of the Eu^{3+} luminescent center, the J = 3 and J = 4 emission bands are strongly suppressed

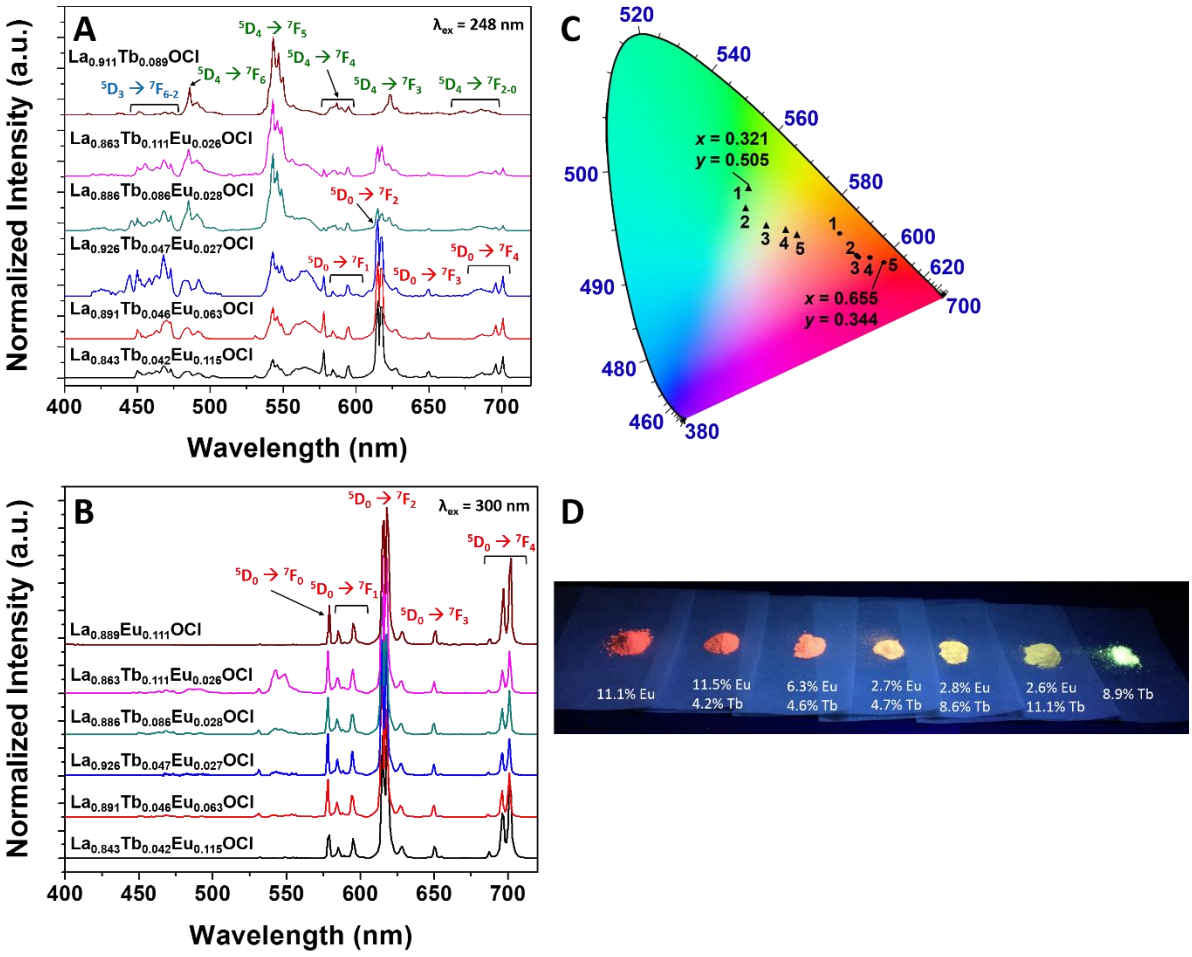

Figure VI.4. Optically stimulated emission spectra measured for solid-solution $La_{1-x-y}Tb_xEu_yOCl$ nanocrystals prepared using TOPO as the passivating ligand. The excitation wavelength used is A) 248 nm and B) 300 nm corresponding to maxima in photoluminescence excitation spectra for Tb^{3+} and Eu^{3+} luminescent centers, respectively. C) CIE chromaticity diagram indicating the relative coloration of the $La_{1-x-y}Tb_xEu_yOCl$ phosphors where 1 = $La_{0.863}Tb_{0.111}Eu_{0.026}OCl$; 2 = $La_{0.886}Tb_{0.086}Eu_{0.028}OCl$; 3 = $La_{0.926}Tb_{0.047}Eu_{0.027}OCl$; 4 = $La_{0.891}Tb_{0.046}Eu_{0.063}OCl$; and 5 = $La_{0.843}Tb_{0.042}Eu_{0.115}OCl$. The emissions depicted in (A) and (B) are represented as triangles and circles, respectively. D) Digital photograph of TOPO-passivated solid-solution $La_{1-x-y}Tb_xEu_yOCl$ phosphors upon illumination with a 254 nm UV light source.

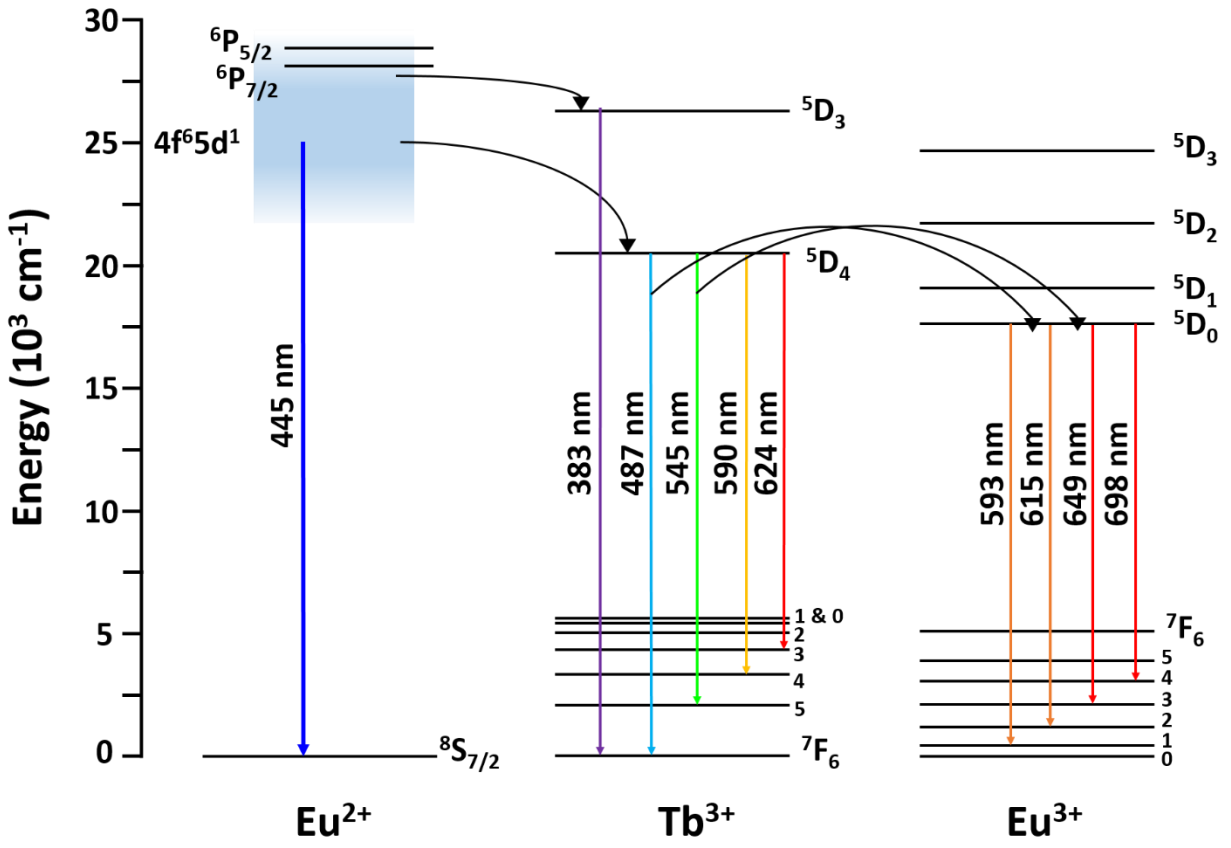

Figure VI.5. Schematic diagram of energy transfer, $Eu^{2+} \rightarrow Tb^{3+}$ and $Tb^{3+} \rightarrow Eu^{3+}$, in $La_{1-x-y}Tb_xEu_yOCl$ nanocrystals with TOPO and oleylamine as the stabilizing ligands respectively. The shaded blue region in Eu^{2+} represents the parity-allowed $4f^65d^1 \rightarrow 4f^7$ transitions indicating the origin of the broad luminescence.

with respect to the J = 0, 1, 2 bands in the co-doped samples with increasing concentration of Tb^{3+}. Contrasting the $La_{0.843}Tb_{0.042}Eu_{0.115}OCl$ and $La_{0.863}Tb_{0.111}Eu_{0.026}OCl$ samples, the relative ratio of the $^5D_0 \rightarrow {}^7F_2$ to $^5D_0 \rightarrow {}^7F_4$ intensities changes from 3.2:1 to 4.0:1. This increase in intensity reflects the relatively better dipolar coupling and stronger sensitization of the $^5D_0 \rightarrow {}^7F_2$ transition by the Tb^{3+}-centers. A broad palette of phosphors is thus accessible upon modifying the relative concentrations of Tb^{3+} and Eu^{3+} centers, as observed in the Commission International

de I'Eclairage (CIE) chromaticity plot of Figure VI.4C and the digital photograph acquired under 254 nm illumination in Figure VI.4D.

When the solid-solution phosphors are excited at λ_{ex} = 300 nm (Figure VI.4B), it is readily apparent the Eu^{3+} emission peaks dominate the spectra for all of the $La_{1-x-y}Tb_xEu_yOCl$ compositions even at higher Tb^{3+} concentrations reflecting the low absorption cross-section for the direct excitation of Tb^{3+} at this wavelength (Figure A.19). However, the influence of Tb-incorporation is again evident in comparing the relative intensities of the $^5D_0 \rightarrow {}^7F_2$ and $^5D_0 \rightarrow {}^7F_4$ emission bands, which monotonically increases with increasing Tb-concentration. Contrasting the $La_{0.843}Tb_{0.042}Eu_{0.115}OCl$ and $La_{0.863}Tb_{0.111}Eu_{0.026}OCl$ samples, the relative ratio of the $^5D_0 \rightarrow {}^7F_2$ to $^5D_0 \rightarrow {}^7F_4$ intensities changes from 1.7:1 to 4.5:1. The CIE coordinates plotted in Figure VI.4 indicate the stronger red luminescence of these phosphors upon 300 nm excitation.

The enhanced luminescence of Eu^{3+} in the presence of Tb^{3+} is explicable in the Dieke diagram picture based on energy transfer from the latter to the former as illustrated in Figure VI.5.[36–38,44] However, in stark contrast, fundamental understanding of activation channels, recombination pathways, and sensitization mechanisms upon high-energy excitation has not thus far been elucidated in this system. VUV and soft X-ray excitation near the elemental edges of the host lattice gives rise to high-energy electron—hole pairs that can thermalize to activate luminescent centers, which then decay through a variety of radiative and non-radiative recombination pathways.[23,45–47] **Figure VI.6** shows La $N_{4,5}$ ($4d \rightarrow 4f$) XANES spectra acquired in FLY mode for solid-solution $La_{0.889}Eu_{0.111}OCl$, $La_{1-x-y}Tb_xEu_yOCl$, and $La_{0.911}Tb_{0.089}OCl$ phosphors in the range between 95—150 eV. La^{3+}-ions have empty 5*d* and 4*f* orbitals (along with a full 4*d* subshell), thereby yielding a singlet $^1S_0$ ground state. The observed features in the

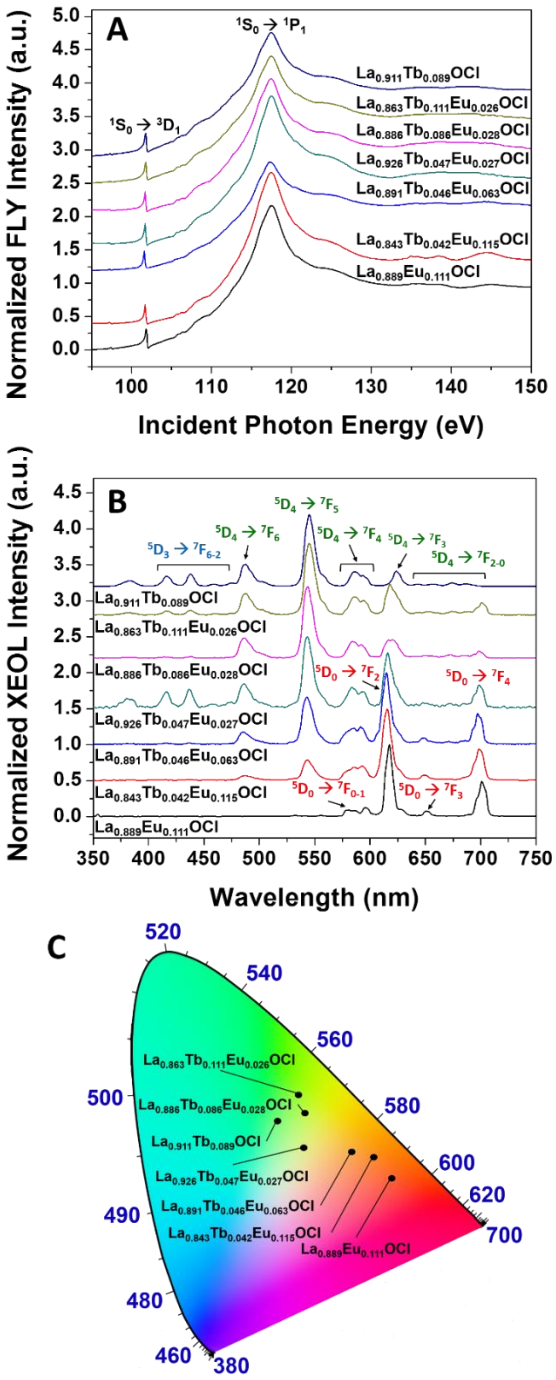

Figure VI.6. (A) Normalized La $N_{4,5}$-edge FLY XANES spectra of solid-solution $La_{0.889}Eu_{0.111}OCl$, $La_{1-x-y}Tb_xEu_yOCl$, and $La_{0.911}Tb_{0.089}OCl$ nanocrystals stabilized with TOPO as a ligand. The transitions to singlet and triplet final states are delineated. (B) Normalized XEOL spectra measured $La_{0.889}Eu_{0.111}OCl$, $La_{1-x-y}Tb_xEu_yOCl$, and $La_{0.911}Tb_{0.089}OCl$ nanocrystals upon excitation at the giant resonance absorption at 117.5 eV. (C) CIE chromaticity diagram for the $La_{0.889}Eu_{0.111}OCl$, $La_{1-x-y}Tb_xEu_yOCl$, and $La_{0.911}Tb_{0.089}OCl$ phosphors upon X-ray excitation.

XANES spectra can be assigned to ($4d \rightarrow 4f$) transitions from $^1S_0$ to a triplet $^3D_1$ state at 101.7 eV (formally forbidden, but allowed due to spin-orbit coupling) and to a singlet $^1P_1$ state at 117.5 eV (allowed by LS selection rules). In light of the strong overlap between 4*d*- and 4*f*-derived states, an intense, broad, and asymmetric giant resonance feature is observed centered at *ca*. 117.5 eV (this feature is about 10 eV above the ionization threshold, reflecting strong electron correlation in these systems).[35] The broad lineshape of this absorption feature is indicative of a short lifetime.[48] Given the relatively low concentrations of Eu^{3+} and Tb^{3+}, absorption features corresponding to the giant resonances of the luminescent centers are not observed in the XANES spectra.

Figure VI.6B depicts XEOL spectra measured for the solid-solution $La_{0.889}Eu_{0.111}OCl$, $La_{1-x-y}Tb_xEu_yOCl$, and $La_{0.911}Tb_{0.089}OCl$ phosphors upon excitation at the giant resonance (117.5 eV). The high-energy electron—hole pairs thermalize and in the process activate the luminescent centers resulting in visible light emission. Similar to the optically excited photoluminescence spectra, distinctive bands corresponding to Eu^{3+} $^5D_0 \rightarrow {}^7F_J$ and Tb^{3+} $^5D_3 \rightarrow {}^7F_J$ and $^5D_4 \rightarrow {}^7F_J$ transitions are observed albeit with several key distinctions. In all of the samples, the relative intensity of the Tb^{3+} emission bands to the Eu^{3+} emission bands is substantially increased as compared to the optically excited photoluminescence spectra in Figure VI.4A. For instance, comparing the XEOL and optically excited spectra for $La_{0.926}Tb_{0.047}Eu_{0.027}OCl$ (Figure A.22), the Tb^{3+} blue—green emission is much more pronounced than the Eu^{3+} emission in the XEOL spectrum, whereas the reverse is true in the optically excited spectrum. In other words, $La^{3+} \rightarrow Tb^{3+} \rightarrow Eu^{3+}$ sensitization is less effective as compared to direct $Tb^{3+} \rightarrow Eu^{3+}$ sensitization. It appears that the host La^{3+} cations directly and independently sensitize both the Eu^{3+} and Tb^{3+} luminescent centers. Indeed, the suppression of the $^5D_0 \rightarrow {}^7F_4$ bands at the expense of the $^5D_0 \rightarrow$

$^7F_2$ bands as a result of Tb^{3+} sensitization noted above is almost entirely eliminated in the XEOL spectra further suggesting direct $La^{3+} \rightarrow Eu^{3+}$ activation.

Figure VI.7 displays 3D contour plots mapping the intensity of XEOL features (corresponding to the relaxation of the incorporated Eu^{3+} or Tb^{3+} ions) as a function of the incident photon energy across the La $N_{4,5}$-edge (corresponding to excitation of La^{3+} ions of the host lattice). The plot thus depicts the efficacy of sensitization of the luminescent centers upon $4d \rightarrow 4f$ excitation of La^{3+} cations. Comparing the plots for the different compositions demonstrates the relative intensification of the blue—green Tb^{3+} emissions at the expense of red Eu^{3+} emissions with increasing Tb incorporation. For all the solid-solution $La_{1-x-y}Tb_xEu_yOCl$ nanocrystals, it is apparent that the luminescence intensity at the giant resonance (117.5 eV excitation) is diminished with respect to higher and lower energies. The substantially diminished intensity is intriguing and is a result of the activation of distinctive non-radiative recombination channels upon photoexcitation at the giant resonance.[23,49] At higher and lower energies, thermalization of high-energy electron—hole pairs results in activation of multiple Tb^{3+} and Eu^{3+} luminescent centers and thereby each X-ray photon yields scores of visible photons. In contrast, excitation at the giant resonance creates a 4*d* hole that decays through non-radiative Auger ionization and furthermore yields just a single thermal electron—hole pair.[23,24,49] For thin LaOCl nanoplatelets (Figure VI.3B and C), it is reasonable to expect that the ionized Auger electrons can be readily emitted from the surface.

While Figure VI.6C suggests considerable tunability of the perceptible color of X-ray phosphors as a function of the relative ratios of incorporated Tb^{3+} and Eu^{3+} cations, the X-ray excited luminescence can further be tuned to access an entirely different region of the electromagnetic spectrum through incorporation of divalent instead of trivalent europium cations

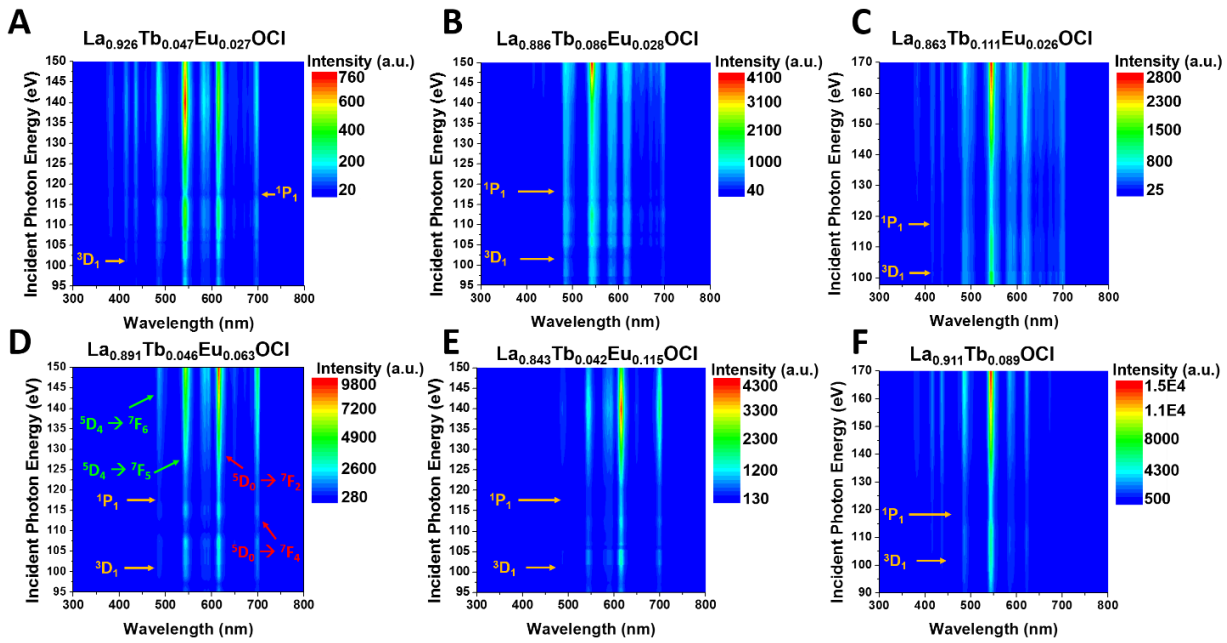

Figure VI.7. 3D plots depicting the evolution of the XEOL intensity of solid-solution $La_{1-x-y}Tb_xEu_yOCl$ and $La_{0.911}Tb_{0.089}OCl$ nanocrystals (stabilized using TOPO as a ligand) as a function of the incident photon energy upon excitation across the La $N_{4,5}$-edge.

given the characteristic blue luminescence of the former.[12,50,51] In Chapter V, we demonstrated the stabilization of divalent europium in the LaOCl lattice, which is accomplished either by reducing a trivalent europium precursor *in situ* during the reaction using oleylamine as a redox non-innocent ligand or by using $EuCl_2$ as the halide precursor again with oleylamine as the capping ligand.[24] In order to prepare LaOCl nanocrystals incorporating Tb^{3+} and Eu^{2+} ions, the $LaCl_3$ precursor has this time been substituted with desired molar amounts of $TbCl_3$ and $EuCl_2$ using oleylamine as the ligand and coordinating solvent. **Figure VI.8** depicts indexed powder XRD patterns acquired for solid-solution $La_{1-x-y}Tb_xEu_yOCl$ nanocrystals capped with oleylamine. The PbFCl structure is observed to be preserved across this range of Eu^{2+} and Tb^{3+} concentrations. The Tb- and Eu atomic percentages have been determined using ICP-MS

analysis. In general, the concentration added to the reaction mixture is slightly lower than the intended concentration as determined by ICP-MS. **Figure VI.9** shows TEM images of the obtained nanocrystals suggesting a nanosheet morphology with rectangular cross-sections; average edge dimensions of 59 ± 13 nm, 79 ± 9.0 nm, and 106 ± 13 nm have been deduced for solid-solution nanocrystals of $La_{0.938}Tb_{0.015}Eu_{0.047}OCl$, $La_{0.893}Tb_{0.048}Eu_{0.059}OCl$, and $La_{0.874}Tb_{0.024}Eu_{0.102}OCl$ respectively. Increasing the concentration of dopant atoms leads to increased lateral growth of the nanosheets; indeed, larger particle sizes have been previously observed with increasing incorporation of divalent Eu in LaOCl and can be attributed to the greater reactivity of the divalent precursor.[24] The incorporation of divalent europium results in the likely creation of a chloride vacancy to maintain charge balance, which further facilitates accommodation of the larger divalent Eu^{2+}-ion (130.0 pm as compared to the 121.6 pm ionic radius of trivalent lanthanum in a nine-coordinated geometry).[24,31]

Figure A.23 shows photoluminescence excitation spectra measured for oleylamine-capped $La_{1-x-y}Tb_xEu_yOCl$ nanocrystals at an emission wavelength of 544 nm, which again corresponds to the $4f^8 5d^0 \rightarrow 4f^7 5d^1$ excitation of Tb^{3+} ions, and 404 nm which is within the blue region of the electromagnetic spectrum where a broad emission band corresponding to the radiative $4f^6 5d^1 \rightarrow 4f^7$ transitions of divalent Eu^{2+} ions in the LaOCl lattice is observed.[24] Two broad features are noticeable in the Tb^{3+} photoluminescence excitation spectra spanning 220–280 nm and 290–330 nm with excitation maxima at 248 nm and 311 nm respectively, whereas the Eu^{2+} photoluminescence excitation spectra has a broad absorption feature from 320-380 nm with an excitation maxima at 354 nm. The bands centered at 248 and 354 nm correspond to the $4f^8 5d^0 \rightarrow 4f^7 5d^1$ excitation of Tb^{3+} and the $4f^7 5d^0 \rightarrow 4f^6 5d^1$ excitation of Eu^{2+} ions, respectively.[12,51,52] Figure A.24 shows emission spectra acquired upon excitation at each of these wavelengths for

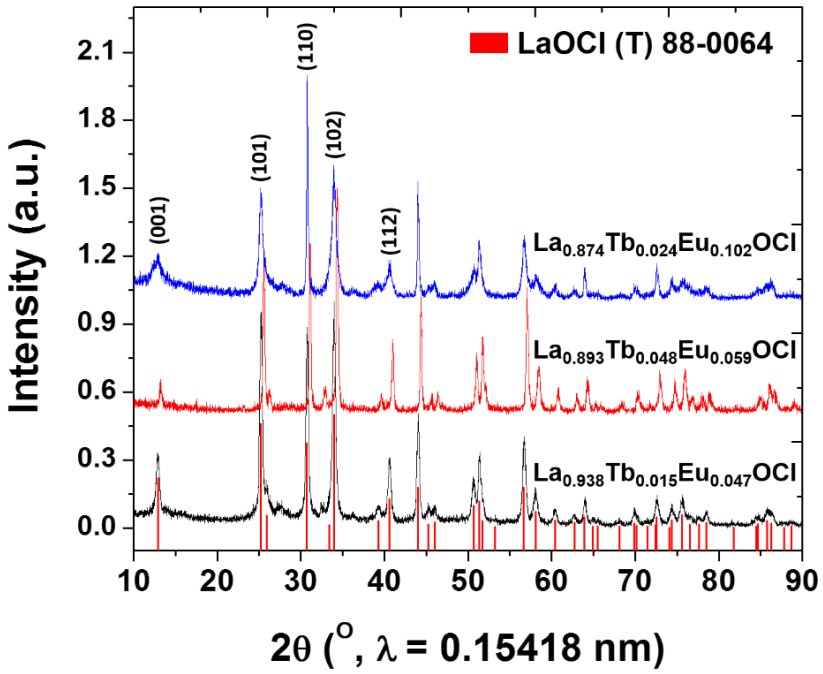

Figure VI.8. Powder XRD patterns acquired for solid-solution $La_{1-x-y}Tb_xEu_yOCl$ nanocrystals capped with oleylamine (thereby stabilizing divalent europium). The vertical red bars denote positions and relative intensities from JCPDS # 88-0064 for tetragonal LaOCl (Space Group: *P4/nmm*).

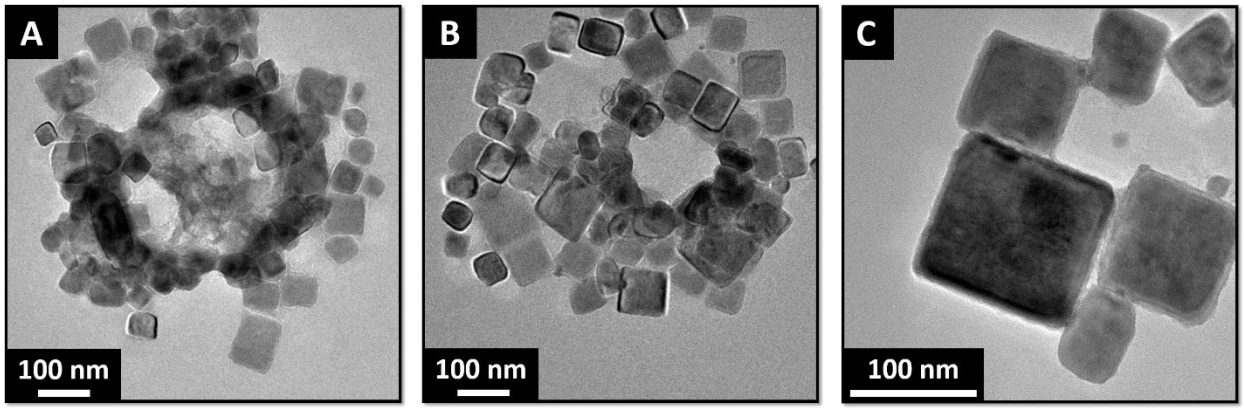

Figure VI.9. Low-magnification transmission electron microscopy images of $La_{1-x-y}Tb_xEu_yOCl$ nanocrystals grown using oleylamine as a ligand where A) $x = 0.015$ and $y = 0.047$; B) $x = 0.048$ and $y = 0.059$; and C) $x = 0.024$ and $y = 0.102$.

the $La_{1-x-y}Tb_xEu_yOCl$ nanocrystals. At 248 nm excitation, there is sufficient energy to directly excite both the Tb^{3+} and Eu^{2+} luminescent centers. The emission spectra exhibit characteristic $^5D_3 \rightarrow {}^7F_J$ (J = 6—2) and $^5D_4 \rightarrow {}^7F_J$ (J = 6—4) relaxations of Tb^{3+} superimposed on a broad blue emission band. With increasing incorporation of Tb^{3+}-ions, the broad blue emission is quenched and the corresponding CIE chromaticity diagram in Figure A.24D indicates a greener coloration. Indeed, the strong quenching of the blue emission and pronounced green coloration is suggestive of efficacious $Eu^{2+} \rightarrow Tb^{3+}$ sensitization. Upon photoexcitation at 354 nm, coincident with the Eu^{2+} absorption, Figure A.24C depicts a broad $4f^65d^1 \rightarrow 4f^7$ blue emission characteristic of divalent europium with only a minor contribution from the $^5D_4 \rightarrow {}^7F_J$ (J = 6—4) radiative transitions of Tb^{3+} ions. The corresponding chromaticity plot in Figure A.24F depicts a pronounced blue coloration for all of the samples at this excitation wavelength. Figure A.24B shows emission spectra acquired upon excitation at 311 nm, at the low energy tail of the Tb^{3+}-absorption band, which thereby also allows for excitation of a fraction of the Tb^{3+} centers as well as the Eu^{2+} luminescent centers. Characteristic blue emission bands derived from $4f^65d^1 \rightarrow 4f^7$ relaxations of divalent europium and green emission bands derived from $^5D_4 \rightarrow {}^7F_J$ (J = 6—4) radiative relaxations of Tb^{3+}-ions can be distinguished.

Figure VI.10 presents XANES and XEOL spectra measured for the oleylamine-capped $La_{1-x-y}Tb_xEu_yOCl$ nanocrystals. In Figure VI.10A, the XANES spectra show element-specific ($4d \rightarrow 4f$) forbidden $^1S_0 \rightarrow {}^3D_1$ and allowed $^1S_0 \rightarrow {}^3P_1$ absorptions characteristic of trivalent lanthanum at 101.7 eV and 117.5 eV, respectively, similar to spectra observed in Figure VI.6A for TOPO-capped nanocrystals.[48,53,54] The XEOL spectra acquired using X-ray excitation at the center of the giant resonance (at 117.5 eV) are plotted in Figure VI.10B; spectra acquired for the multiply doped solid-solution nanocrystals are contrasted with spectra measured for

$La_{0.941}Eu_{0.059}OCl$ and $La_{0.911}Tb_{0.089}OCl$ nanocrystals under the same conditions. Intriguingly, the characteristic $^5D_4 \rightarrow {}^7F_J$ green emission and $^5D_3 \rightarrow {}^7F_J$ blue emission bands of Tb^{3+} are dominant for all of the multiply doped samples, even for samples where the ratio of divalent europium atoms to trivalent terbium atoms approaches 4:1. The broad $4f^6 5d^1 \rightarrow 4f^7$ blue emission characteristic of divalent europium, observed as an intense band for the $La_{0.941}Eu_{0.059}OCl$ sample, has only a minor contribution to the XEOL spectra acquired for the multiply doped samples. Indeed, this observation suggests a highly efficient energy transfer mechanism from $Eu^{2+} \rightarrow Tb^{3+}$. Based on a comparison of emission intensities, the blue $^5D_3 \rightarrow {}^7F_J$ relaxations of Tb^{3+} are enhanced in relative intensity as compared to the green $^5D_4 \rightarrow {}^7F_J$ relaxations of Tb^{3+} for samples with lower Tb^{3+}:Eu^{2+} ratios, as also observed in the CIE diagram depicted in Figure VI.10C. In other words, incorporation of a greater abundance of divalent europium cations facilitates increased sensitization through energy transfer to the $^5D_3$ state. In contrast, the

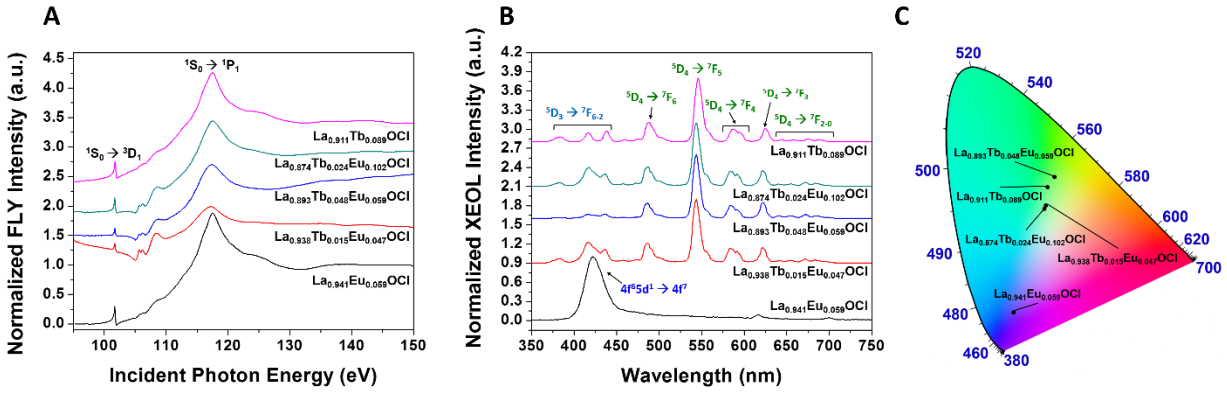

Figure VI.10. (A) Normalized FLY XANES spectra of $La_{1-x}Eu_xOCl$, $La_{1-x-y}Tb_xEu_yOCl$, and $La_{1-x-y}Tb_xEu_yOCl$ nanocrystals stabilized with oleylamine and acquired at the La $N_{4,5}$-edge in the range of 95—150 eV. The specific $4d \rightarrow 4f$ transitions are delineated. A giant resonance feature centered at *ca*. 117.5 eV is observed corresponding to the $^1S_0 \rightarrow {}^1P_1$ transition. (B) Normalized XEOL spectra measured for $La_{0.941}Eu_{0.059}OCl$, $La_{1-x-y}Tb_xEu_yOCl$, and $La_{0.911}Tb_{0.089}OCl$ upon excitation at the center of the giant resonance at 117.5 eV. (C) CIE chromaticity diagram for the $La_{1-x-y}Tb_xEu_yOCl$ phosphors upon X-ray excitation.

$La_{0.893}Tb_{0.048}Eu_{0.059}OCl$ sample shows a more pronounced green luminescence, which is ascribed to the relatively reduced extent of sensitization at this composition, which thereby suppresses population of $^5D_3$ states, yielding phosphors with a much greener appearance. Such an observation of efficacious $Eu^{2+} \rightarrow Tb^{3+}$ sensitization can be rationalized based on the Dieke diagram depicted in Figure VI.5. Upon X-ray excitation, the high-energy electron—hole pairs thermalize to create multiple thermal electron—hole pairs; the excited trivalent La-ions sensitize the luminescent dopant centers. However, excitations of divalent europium atoms decay rapidly through efficient non-radiative energy transfer processes that result in the excitation of Tb^{3+} cations. Comparing these observations to Figure VI.6, the $Eu^{2+} \rightarrow Tb^{3+}$ energy transfer process is thus observed to be substantially more efficient as compared to $Tb^{3+} \rightarrow Eu^{3+}$ sensitization (which is almost entirely eliminated upon high energy excitation). This substantial difference can be rationalized considering that the $4f^6 5d^1 \rightarrow 4f^7$ transition in Eu^{2+} is electric-dipole allowed and has a several orders of magnitude stronger absorption cross-section as compared to the forbidden $4f \rightarrow 4f$ electronic transitions within the $4f^n$ configurations of Tb^{3+}.[34] A greater absorption cross-section implies a higher population of excited atoms, which in turn are proportionately better able to transfer energy to adjacent Tb^{3+} cations, thereby populating the $^5D_3$ and $^5D_4$ energy levels of Tb^{3+} in $La_{1-x-y}Tb_xEu_yOCl$ nanocrystals.

Figure VI.11 depicts 3D contour plots mapping the intensity of XEOL bands (corresponding to the relaxation of the incorporated Eu^{3+} or Tb^{3+} ions) as a function of the incident photon energy across the La $N_{4,5}$-edge. A pronounced diminution of intensity is again observed at the giant resonance and can be similarly attributed to non-radiative Auger photoionization processes and the creation of a single electron—hole pair from the $4d^{10}4f^0 \rightarrow$

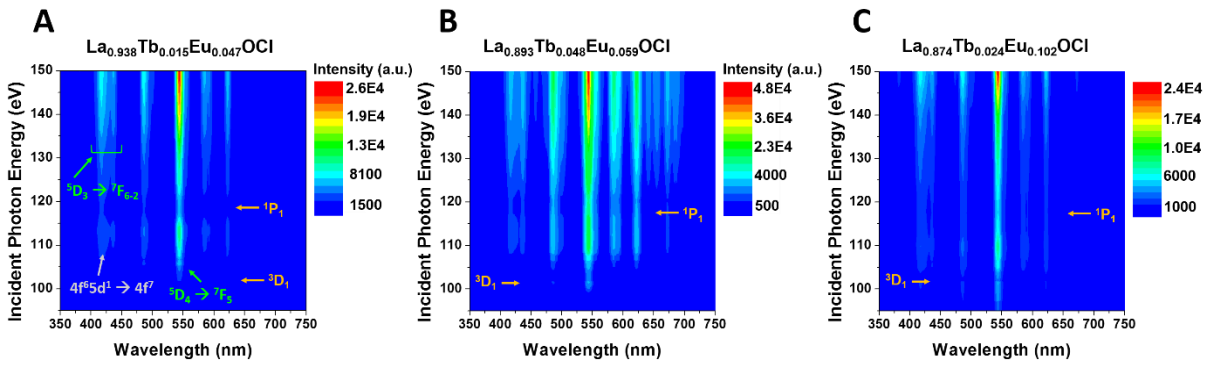

Figure VI.11. 3D plots depicting the evolution of the XEOL of solid-solution $La_{1-x-y}Tb_xEu_yOCl$ nanocrystals (stabilized using oleylamine as a ligand) as a function of the excitation energy upon excitation across the La N_4-edge.

$4d^9 4f^1$ excitation of trivalent La-ions.[23,24,49]

VI.5 Conclusions

In conclusion, the luminescence of LaOCl nanocrystals can be tuned across the red—green and green—blue regions of the electromagnetic spectrum through substitutional incorporation of trivalent terbium ions in conjunction with trivalent and divalent europium ions, respectively, on the cation lattice. A broad palette of nanocrystalline phosphors, amenable to optical as well as X-ray excitation, have been stabilized using a solution-phase process involving condensation of a metal halide with a metal alkoxide in the presence of ligand molecules. The ligands dictate both the dimensions of the nanocrystals as well as the oxidation state of the incorporated europium; the use of TOPO as a ligand results in stabilization of trivalent europium, whereas oleylamine brings about the incorporation of divalent europium within the LaOCl lattice.

Optical stimulation and X-ray excitation have been contrasted for the solid-solution $La_{1-x-y}Tb_xEu_yOCl$ nanocrystals and suggest the manifestation of starkly different sensitization mechanisms. Direct optical excitation is a relatively low cross-section process and results in the formation of a 4*f* hole; $Tb^{3+} \rightarrow Eu^{3+}$ and $Eu^{2+} \rightarrow Tb^{3+}$ sensitization is observed upon optical excitation. In contrast, X-ray excitation leaves behind a 4*d* hole in the trivalent La^{3+}-ions of the host lattice. The hole decays through thermalization to form scores of electron—hole pairs that activate luminescent dopant atoms. Strong $La^{3+} \rightarrow Tb^{3+}$ and $La^{3+} \rightarrow Eu^{3+}$ sensitization mechanisms are operational and underpin the strong X-ray luminescence. In addition, a substantial $Eu^{2+} \rightarrow Tb^{3+}$ sensitization mechanism is observed, facilitated by the dipole-allowed absorption of divalent europium, which allows for a much higher cross-section for excitation and energy transfer. A pronounced diminution of XEOL intensity is observed upon resonant excitation within the giant resonance absorption and is attributed to the activation of distinctive non-radiative recombination channels such as Auger photo-ionization and creation of single electron—hole pairs

VI.6 References

(1) Talbot, J. B. Electrophoretic Deposition of Phosphors for Information Displays and Solid State Lighting. In *Electrophoretic Deposition of Nanomaterials*; Dickerson, J. H., Boccaccini, A. R., Eds.; Springer New York: New York, NY, **2012**; pp 267–294.

(2) Shrestha, S.; Fischer, R.; Matt, G. J.; Feldner, P.; Michel, T.; Osvet, A.; Levchuk, I.; Merle, B.; Golkar, S.; Chen, H.; Tedde, S. F.; Schmidt, O.; Hock, R.; Rührig, M.; Göken, M.; Heiss, W.; Anton, G.; Brabec, C. J. High-Performance Direct Conversion X-Ray

Detectors Based on Sintered Hybrid Lead Triiodide Perovskite Wafers. *Nat. Photonics* **2017**, *11* (7), 436–440.

(3) Wei, H.; Fang, Y.; Mulligan, P.; Chuirazzi, W.; Fang, H. H.; Wang, C.; Ecker, B. R.; Gao, Y.; Loi, M. A.; Cao, L.; Huang, J. Sensitive X-Ray Detectors Made of Methylammonium Lead Tribromide Perovskite Single Crystals. *Nat. Photonics* **2016**, *10* (5), 333–339.

(4) Büchele, P.; Richter, M.; Tedde, S. F.; Matt, G. J.; Ankah, G. N.; Fischer, R.; Biele, M.; Metzger, W.; Lilliu, S.; Bikondoa, O.; Macdonald, J. E.; Brabec, C. J.; Kraus, T.; Lemmer, U.; Schmidt, O. X-Ray Imaging with Scintillator-Sensitized Hybrid Organic Photodetectors. *Nat. Photonics* **2015**, *9* (12), 843–848.

(5) Issler, S. L.; Torardi, C. C. Solid State Chemistry and Luminescence of X-Ray Phosphors. *J. Alloys Compd.* **1995**, *229* (1), 54–65.

(6) Amemiya, Y.; Miyahara, J. Imaging Plate Illuminates Many Fields. *Nature* **1988**, *336* (6194), 89–90.

(7) Wang, C.; Cheng, R.; Liao, L.; Duan, X. High Performance Thin Film Electronics Based on Inorganic Nanostructures and Composites. *Nano Today* **2013**, *8* (5), 514–530.

(8) Jing-he, Y.; Gui-yun, Z.; Bo, W. Enhanced Luminescence of the Europium/Terbium/Thenoyltrifluoroacetone/1,10-Phenanthroline/Surfactant System, and Its Analytical Application. *Anal. Chim. Acta* **1987**, *198*, 287–292.

(9) Qin, X.; Zhang, X.; He, P.; Pang, Q.; Zhou, L.; Gong, M. Enhanced Luminescence Properties and Energy Transfer in Ce^{3+} and Tb^{3+} co-doped $NaCaBO_3$ phosphor. *Ceram. Int.* **2015**, *41* (4), 5554–5560.

(10) Li, G.; Hou, Z.; Peng, C.; Wang, W.; Cheng, Z.; Li, C.; Lian, H.; Lin, J. Electrospinning Derived One-Dimensional LaOCl: Ln^{3+} (Ln = Eu/Sm, Tb, Tm) Nanofibers, Nanotubes and Microbelts with Multicolor-Tunable Emission Properties. *Adv. Funct. Mater.* **2010**, *20* (20), 3446–3456.

(11) Dhananjaya, N.; Shivakumara, C.; Saraf, R.; Behera, S.; Nagabhushana, H. Comparative Study of Eu^{3+}-Activated LnOCl (Ln=La and Gd) Phosphors and Their Judd-Ofelt Analysis. *J. Rare Earths* **2015**, *33* (9), 946–953.

(12) Kim, D.; Jang, J.; Ahn, S. Il; Kim, S.-H.; Park, J.-C. Novel Blue-Emitting Eu^{2+}-Activated LaOCl:Eu Materials. *J. Mater. Chem. C* **2014**, *2* (15), 2799.

(13) Li, G.; Li, C.; Zhang, C.; Cheng, Z.; Quan, Z.; Peng, C.; Lin, J. Tm^{3+} And/or Dy^{3+} Doped LaOCl Nanocrystalline Phosphors for Field Emission Displays. *J. Mater. Chem.* **2009**, *19* (47), 8936–8943.

(14) Xia, Z.; Li, J.; Luo, Y.; Liao, L. Comparative Investigation of Green and Red Upconversion Luminescence in Er^{3+} Doped and Yb^{3+}/Er^{3+} Codoped LaOCl. *J. Am. Ceram. Soc.* **2012**, *95* (10), 3229–3234.

(15) Jiang, T.; Yu, X.; Xu, X.; Yu, H.; Zhou, D.; Qiu, J. Realization of Tunable Emission via Efficient Tb^{3+}-Eu^{3+} Energy Transfer in $K_3Gd(PO_4)_2$ for UV-Excited White Light-Emitting-Diodes. *Opt. Mater. (Amst).* **2014**, *36* (3), 611–615.

(16) Xia, Z.; Zhuang, J.; Meijerink, A.; Jing, X. Host Composition Dependent Tunable Multicolor Emission in the Single-Phase $Ba_2(Ln_{1-z}Tb_z)(BO_3)_2Cl$:Eu Phosphors. *Dalt. Trans.* **2013**, *42* (18), 6327–6336.

(17) Zhou, J.; Xia, Z. Multi-Color Emission Evolution and Energy Transfer Behavior of $La_3GaGe_5O_{16}$:Tb^{3+}, Eu^{3+} Phosphors. *J. Mater. Chem. C* **2014**, *2* (34), 6978–6984.

(18) Hu, Y. F.; Zuin, L.; Wright, G.; Igarashi, R.; McKibben, M.; Wilson, T.; Chen, S. Y.; Johnson, T.; Maxwell, D.; Yates, B. W.; Sham, T. K.; Reininger, R. Commissioning and Performance of the Variable Line Spacing Plane Grating Monochromator Beamline at the Canadien Light Source. *Rev. Sci. Intruments* **2007**, *78*, 83109.

(19) Kasrai, M.; Yin, Z.; Bancroft, G. M.; Tan, K. H. X-Ray Fluorescence Measurments of X-Ray Absorption near Edge Strcuture at the Si, P, and S L Edges. *J. Vac. Sci. Technol. A* **1993**, *11* (5), 2694–2699.

(20) Hermus, M.; Brgoch, J. Phosphors by Design: Approaches Toward the Development of Advanced Luminescent Materials. *Electrochem. Soc. Interface* **2015**, *24* (4 (Winter)), 55–59.

(21) George, N. C.; Brgoch, J.; Pell, A. J.; Cozzan, C.; Jaffe, A.; Dantelle, G.; Llobet, A.; Pintacuda, G.; Seshadri, R.; Chmelka, B. F. Correlating Local Compositions and Structures with the Macroscopic Optical Properties of Ce^{3+}-Doped $CaSc_2O_4$, an Efficient Green-Emitting Phosphor. *Chem. Mater.* **2017**, *29* (8), 3538–3546.

(22) Kort, K. R.; Banerjee, S. Shape-Controlled Synthesis of Well-Defined Matlockite LnOCl (Ln: La, Ce, Gd, Dy) Nanocrystals by a Novel Non-Hydrolytic Approach. *Inorg. Chem.* **2011**, *50*, 5539–5544.

(23) Waetzig, G. R.; Horrocks, G. A.; Jude, J. W.; Zuin, L.; Banerjee, S. X-Ray Excited Photoluminescence near the Giant Resonance in Solid-Solution $Gd_{1-x}Tb_xOCl$ Nanocrystals and Their Retention upon Solvothermal Topotactic Transformation to $Gd_{1-x}Tb_xF_3$. *Nanoscale* **2016**, *8* (2), 979–986.

(24) Waetzig, G. R.; Horrocks, G. A.; Jude, J. W.; Villalpando, G. V.; Zuin, L.; Banerjee, S. Ligand-Mediated Control of Dopant Oxidation State and X-Ray Excited Optical Luminescence in Eu-Doped LaOCl. *under review.* **2018**.

(25) Kort, K. R.; Banerjee, S. Ligand-Mediated Control of Dislocation Dynamics and Resulting Particle Morphology of GdOCl Nanocrystals. *Small* **2015**, *11* (3), 329–334.

(26) Kort, K. R.; Banerjee, S. Oriented Electrophoretic Deposition of GdOCl Nanoplatelets. *J. Phys. Chem. B* **2013**, *117*, 1585–1591.

(27) Imanaka, N.; Okamoto, K.; Adachi, G. Y. Water-Insoluble Lanthanum Oxychloride-Based Solid Electrolytes with Ultra-High Chloride Ion Conductivity. *Angew. Chemie - Int. Ed.* **2002**, *41* (20), 3890–3892.

(28) Dalpian, G. M.; Chelikowsky, J. R. Self-Purification in Semiconductor Nanocrystals. *Phys. Rev. Lett.* **2006**, *96* (22), 1–4.

(29) Nag, A.; Chakraborty, S.; Sarma, D. D. To Dope Mn^{2+} in a Semiconducting Nanocrystal. *J. Am. Chem. Soc.* **2008**, *130* (32), 10605–10611.

(30) Waetzig, G. R.; Depner, S. W.; Asayesh-Ardakani, H.; Cultrara, N. D.; Shahbazian-Yassar, R.; Banerjee, S. Stabilizing Metastable Tetragonal HfO_2 Using a Non-Hydrolytic Solution-Phase Route: Ligand Exchange as a Means of Controlling Particle Size. *Chem. Sci.* **2016**, *7* (8), 4930–4939.

(31) Shannon, R. D. Revised Effective Ionic Radii and Systematic Studies of Interatomic Distances in Halides and Chalcogenides. *Acta Crystallogr. Sect. A* **1976**, *A32*, 751–767.

(32) Kong, Q.; Wang, J.; Dong, X.; Yu, W.; Liu, G. Synthesis and Luminescence Properties of Terbium-Doped Lanthanum Oxychloride Nanostructures. *J. Nanosci. Nanotechnol.* **2015**, *15*, 4304–4315.

(33) Heigl, F.; Jürgensen, A.; Zhou, X. T.; Hu, Y. F.; Zuin, L.; Sham, T. K. Communication: X-Ray Excited Optical Luminescence from TbCl3 at the Giant Resonance of Terbium. *J. Chem. Phys.* **2013**, *138* (6), 061104.

(34) Xia, Z.; Zhuang, J.; Liu, H.; Liao, L. Photoluminescence Properties and Energy Transfer of $Ba_2Lu(BO_3)_2Cl:Eu^{2+}/Eu^{3+},Tb^{3+}$ Phosphors. *J. Phys. D. Appl. Phys.* **2012**, *45* (1), 15302.

(35) Mohapatra, S.; Adhikari, S.; Riju, H.; Maji, T. K. Terbium(III), europium(III), and Mixed terbium(III)-europium(III) Mucicate Frameworks: Hydrophilicity and Stoichiometry-Dependent Color Tunability. *Inorg. Chem.* **2012**, *51* (9), 4891–4893.

(36) Rodrigues, M. O.; Dutra, J. D. L.; Nunes, L. A. O.; De Sá, G. F.; De Azevedo, W. M.; Silva, P.; Paz, F. A. A.; Freire, R. O.; Júnior, S. A. $Tb^{3+} \rightarrow Eu^{3+}$ Energy Transfer in Mixed-Lanthanide-Organic Frameworks. *J. Phys. Chem. C* **2012**, *116* (37), 19951–19957.

(37) Khan, W. U.; Li, J.; Li, X.; Wu, Q.; Yan, J.; Xu, Y.; Xie, F.; Shi, J.; Wu, M. Efficient Energy Transfer and Luminescence Properties of $Ca_3Y(GaO)_3(BO_3)_4:Tb^{3+}, Eu^{3+}$ as a Green-to-Red Colour Tunable Phosphor under near-UV Excitation. *Dalt. Trans.* **2017**, *46* (6), 1885–1891.

(38) Zhang, X.; Zhou, L.; Pang, Q.; Shi, J.; Gong, M. Tunable Luminescence and $Ce^{3+} \rightarrow Tb^{3+} \rightarrow Eu^{3+}$ Energy Transfer of Broadband-Excited and Narrow Line Red Emitting $Y_2SiO_5:Ce^{3+}, Tb^{3+}, Eu^{3+}$ Phosphor. *J. Phys. Chem. C* **2014**, *118* (14), 7591–7598.

(39) Li, Q.; Li, T.; Wu, J. Luminescence of europium(III) and terbium(III) Complexes Incorporated in Poly(vinyl Pyrrolidone) Matrix. *J. Phys. Chem. B* **2001**, *105* (49), 12293–12296.

(40) Holsa, J. Anti-Stokes Luminescence of Europium(III)-Doped Lanthanum Oxychloride. *Chem. Phys. Lett.* **1984**, *112* (3), 246–248.

(41) Choubey, A.; Som, S.; Biswas, M.; Sharma, S. K. Characterization of Optical Transitions of Eu^{3+} in Lanthanum Oxychloride Nanophosphor. *J. Rare Earths* **2011**, *29* (4), 345–348.

(42) Binnemans, K. Interpretation of europium(III) Spectra. *Coord. Chem. Rev.* **2015**, *295*, 1–45.

(43) Blasse, G.; Bril, A. Fluorescence of Eu^{3+}-Activated Lanthanide Oxyhalides LnOX. *J. Chem. Phys.* **1967**, *46* (7), 2579–2582.

(44) Dieke, G. H. *Spectra and Energy Levels of Rare Earth Ions in Crystals*; Interscience, **1968**.

(45) Dehmer, J. L.; Starace, A. F.; Fano, U.; Sugar, J.; Cooper, J. W. Raising of Discrete Levels into the Far Continuum. *Phys. Rev. Lett.* **1971**, *26* (25), 1521–1525.

(46) Rezende, M. V. dos S.; Montes, P. J. R.; Andrade, A. B.; Macedo, Z. S.; Valerio, M. E. G. Mechanism of X-Ray Excited Optical Luminescence (XEOL) in Eu-Doped BaAl2O4 Nanopowders. *Physical Chem. Chem. Physics* **2016**, *18*, 17646.

(47) Sugar, J. Potential-Barrier Effects in Photoabsorption. II. Interpretation of Photoabsorption Resonances in Lanthanide Metals at the 4d-Electron Threshold. *Phys. Rev. B* **1972**, *5* (5), 1785–1792.

(48) Bonnelle, C.; Spector, N. *High Energy Spectroscopy and Resonance Effects*; Springer Netherlands: Dordrecht, **2015**.

(49) Klaassen, D. B. M.; van Leuken, C. M. G.; Maessen, K. M. H. Giant Resonances in Luminescence Soft X-Ray Excitation Spectra of Phosphors. *Phys. Rev. B* **1987**, *36* (8), 4407–4412.

(50) Wan, J.; Liu, Q.; Liu, G.; Zhou, Z.; Ni, J.; Xie, R. A Novel Synthesis of Green Apatite-Type $Y_5(SiO_4)_3N:Eu^{2+}$ Phosphor via SiC-Assisted Sol-Gel Route. *J. Am. Ceram. Soc.* **2016**, *99* (3), 748–751.

(51) Rajamohan Reddy, K.; Annapurna, K.; Buddhudu, S. Fluorescence Spectra of $BaFCl:Eu^{2+}$ Powder Phosphors. *Mater. Lett.* **1996**, *29* (4–6), 29–30.

(52) Reisfeld, R.; Glasner, A. Absorption and Fluorescence Spectra of Eu^{2+} in Alkali Halide Crystals. *J. Opt. Soc. Am.* **1964**, *54* (3), 331–333.

(53) Moewes, A.; Winarski, R. P.; Ederer, D. L.; Grush, M. M.; Callcott, T. A. Study of 4f Inner Shell Excitations in Gd and Tb Using Resonant Inelastic Soft X-Ray Scattering. *J. Electron Spectrscopy Relat. Phenom.* **1999**, *101–103*, 617–622.

(54) Lenth, W.; Lutz, F.; Barth, J.; Kalkoffen, G.; Kunz, C. Giant Resonance Enhancement of the 4f, 5p, and 5s States in the Photoemission Spectra of Rare-Earth Compounds. *Phys. Rev. Lett.* **1978**, *41* (17), 1185–1188.

CHAPTER VII

SUMMARY AND OUTLOOK

VII.1 Summary and Outlook

In this dissertation, the development of a versatile sol—gel condensation process for defining oxo and oxychloride linkages starting from molecular precursors has been explored. Precise compositional, structural, and dimensional control of solid-solution oxide and oxychloride nanocrystals has been established by matching the reactivity of precursors and the selection of passivating ligands. The salient research accomplishments discussed in this dissertation include (i) accessing the metastable high-dielectric-constant tetragonal phase of HfO_2, stable only above 1720°C in the bulk, through dimensional confinement below a size of ca. 3.8 nm; (ii) constituting siloxane frameworks utilizing muskeg fibers as templates to obtain load-bearing composites in order to facilitate the construction of roads and drill pads in the marshy soil of the Alberta Oil Sands; (iii) stabilization of solid-solution rare-earth oxychloride nanocrystals crystallized in the PbFCl crystal structure with full tunability of optically stimulated and X-ray excited optical luminescence across the visible region of the electromagnetic spectrum.

Chapter II explored the stabilization of the technologically important metastable tetragonal polymorph of HfO_2 by retarding the kinetics of condensation by cross-coupling with Ce- and La-precursors. This approach allowed for precise control of the size of the nanocrystals in the range of 3—10 nm; the tetragonal phase was observed to be stabilized below a critical size of 3.6—3.8 nm. At these dimensions, the surface energy terms outweigh the bulk free energy differential, allowing for stabilization of the tetragonal phase under conditions of constrained

equilibrium. Future work will focus on stabilization of the cubic phase of HfO_2 as well as dielectric measurements of composite thin films incorporating HfO_2 nanocrystals.

Chapter III employed a similar, but hydrolytic, condensation reaction to achieve the geopolymerization of silicate matrices within muskeg soil, thereby forming a cross-linked continuous siloxane network that links together muskeg fibers within a dense nanocomposite. Additional cross-linking modes were realized within the composite by the incorporation of wood fibers and hydroxyethylcellulose, thereby yielding a load-bearing and low-subsidence composite for the construction of oil well pads and roads in the marshy sub-Arctic regions of Canada. The composites could be dissolved through a leaching process involving addition of a strong base and gypsum, thereby providing a means to restore the habitat to natural conditions, as specified by environmental regulatory agencies charged with stewardship of natural resources in Alberta. Future work will focus on pilot-scale trials to explore the viability of this approach.

Chapter IV further extends the versatility of the non-hydrolytic sol—gel cross-coupling route by incorporating luminescent Tb^{3+} cations into a GdOCl host matrix. Further demonstration of the synthetic capabilities of metastable polymorphs was shown wherein $Gd_{1-x}Tb_xOCl$ nanocrystals were topotactically transformed via solvothermal treatment with XeF_2 to metastable hexagonal $Gd_{1-x}Tb_xF_3$. The X-ray activation pathways were then examined in these materials wherein the stimulated emission arises from the formation of a 4*d* hole in the host matrix followed by thermalization of "hot" electron-hole pairs to activate the Tb^{3+} luminescent centers. The recombination mechanism was also deduced wherein resonant excitation generates a singular electron—hole pair that decays through a Coster-Kronig Auger electron ionization process. The intensity of the luminescence at the giant resonance is significantly diminished due to the singular electron—hole pair and its non-radiative decay, whereas outside the giant

resonance, the thermalization of "hot" electron-hole pairs generates multiple electron—hole pairs that activate the luminescent Tb^{3+} centers.

Chapter V demonstrated additional control of the non-hydrolytic sol—gel technique by utilizing TOPO and oleylamine as redox non-innocent ligands to control the oxidation state of europium dopants, and thus the resulting optical and X-ray-excited luminescence of solid-solution $La_{1-x}Eu_xOCl$ nanocrystals. TOPO stabilizes the trivalent oxidation state whereas oleylamine stabilizes the divalent oxidation state of europium. Incorporation of larger concentrations of dopants further allows for tunability of nanocrystal morphologies. The incorporation of Eu^{3+} results in a thinning of the observed nanoplatelets, whereas the incorporation of Eu^{2+} appears to facilitate increased lateral growth without substantially altering the vertical dimensions. The changes in particle size result from modulation of 3D connectivity of the PbFCl-structured lattices as a result of variations in the ionic radii of the host and dopant atoms. The X-ray activation pathways and recombination channels for the $La_{1-x}Eu_xOCl$ nanocrystals are assigned similarly to the $Gd_{1-x}Tb_xOCl$ case in Chapter IV wherein resonant excitation at the giant resonance of the La^{3+} results in a singular electron—hole pair that decays through Auger ionization, thereby significantly diminishing the intensity of europium luminescence, whereas non-resonant excitation outside the giant resonance creates multiple electron—hole pairs that activate the Eu^{3+} and Eu^{2+} luminescent centers yielding bright red and blue emission bands, respectively.

Chapter VI combines the synthetic techniques and lessons learned from Chapters IV and V by incorporating variable concentrations of multiple luminescent centers of Tb^{3+} and Eu^{3+} with the stabilizing ligand TOPO in a LaOCl host matrix as well as a combination of Tb^{3+} and Eu^{2+} with the stabilizing ligand oleylamine in a LaOCl host matrix to stabilize phosphors spanning the

entire visible range of the electromagnetic spectrum. The optical and X-ray excitation and sensitization pathways have been contrasted. Direct optical excitation results in the formation of a 4*f* hole and facilitates $Tb^{3+} \rightarrow Eu^{3+}$ and $Eu^{2+} \rightarrow Tb^{3+}$ sensitization, whereas X-ray excitation results in the formation of a 4*d* hole and facilitates $La^{3+} \rightarrow Tb^{3+}$ and $La^{3+} \rightarrow Eu^{3+}$ sensitization for the TOPO-stabilized nanocrystals and $La^{3+} \rightarrow Eu^{2+} \rightarrow Tb^{3+}$ sensitization for the oleylamine-stabilized nanocrystals. Now that full tunability of color across the visible range of the electromagnetic spectrum has been demonstrated, future work will focus on the incorporation of the nanocrystals within ordered thin films. In addition, incorporation of trivalent erbium will be explored to facilitate upconversion of NIR illumination to visible light. Finally, rare-earth oxybromide and oxyiodide nanocrystals will be explored as templates for topochemical modification to stabilize metastable lanthanide phosphides, nitrides, and chalcogenides.

APPENDIX A

SUPPLEMENTARY FIGURES AND TABLES

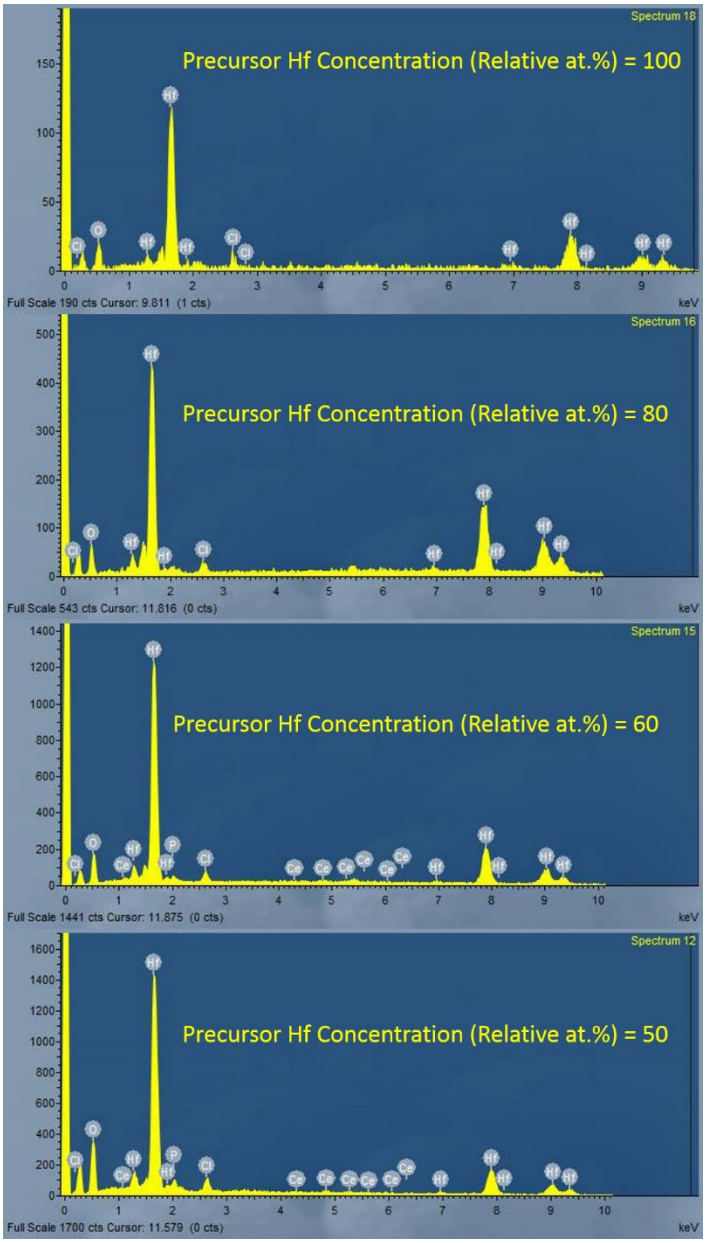

Figure A.1. Energy dispersive X-ray spectroscopy (EDX) of pristine HfO_2 and selected $Hf_{1-x}Ce_xO_2$ nanocrystals. The detected concentrations of hafnium and cerium are listed in Table A.2.

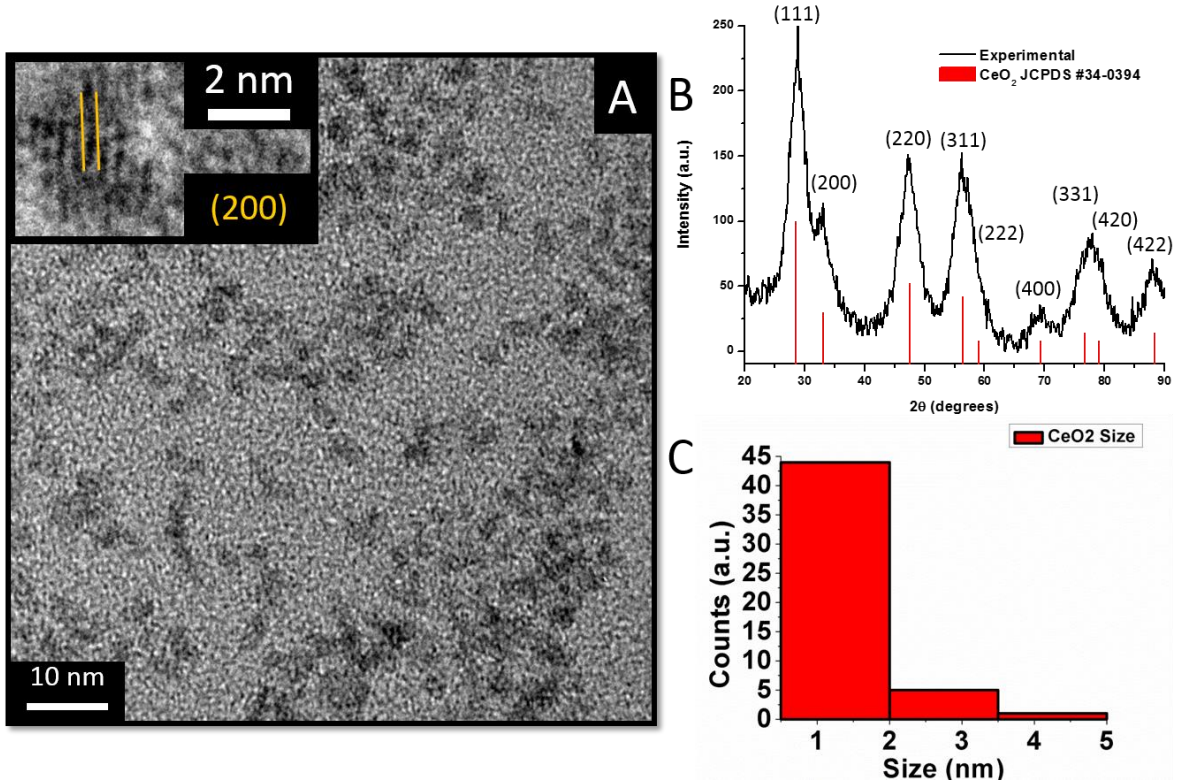

Figure A.2. (A) Low-magnification transmission electron microscopy image of CeO_2 nanocrystals. The inset shows a HRTEM image indicating the separation between the (200) lattice planes of the cubic phase. (B) X-ray diffraction pattern of CeO_2 nanocrystals synthesized using 2 mmol of $CeCl_3$ and 2 mmol of $Ce(O^tBu)_4$. Reflections of cubic CeO_2 are indicated in red (JCPDS # 34-0394). (C) Size distribution histogram indicating the size of the CeO_2 nanoparticles to be *ca*. 1.5 ± 0.5 nm.

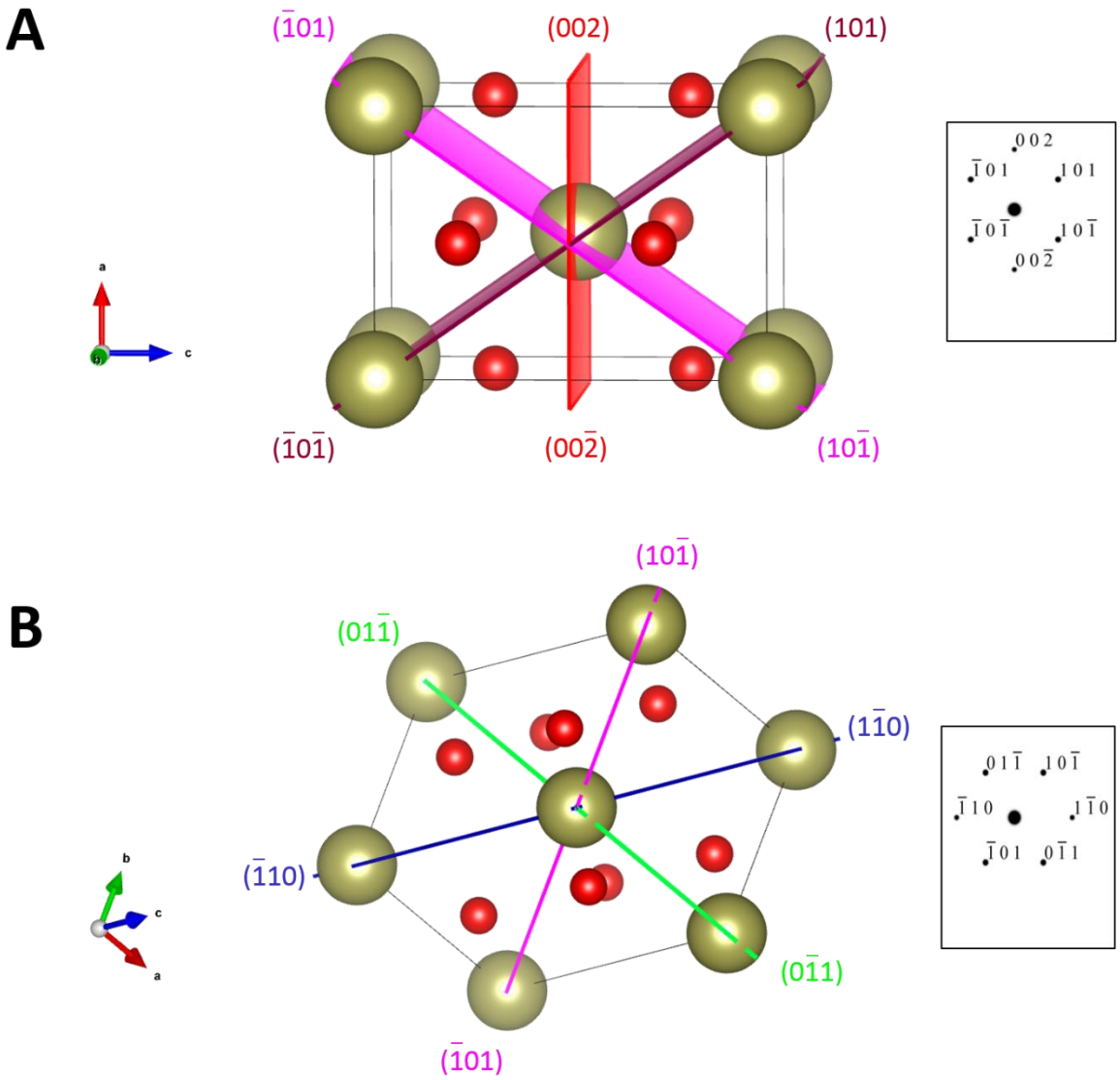

Figure A.3. (A) HfO_2 tetragonal unit cell depicting the corresponding lattice planes from Figure II.4D. (B) HfO2 tetragonal unit cell depicting the corresponding lattice planes from Figure II.4H. The unit cells were constructed using the lattice parameters given in Ref. 40 of Chapter II.

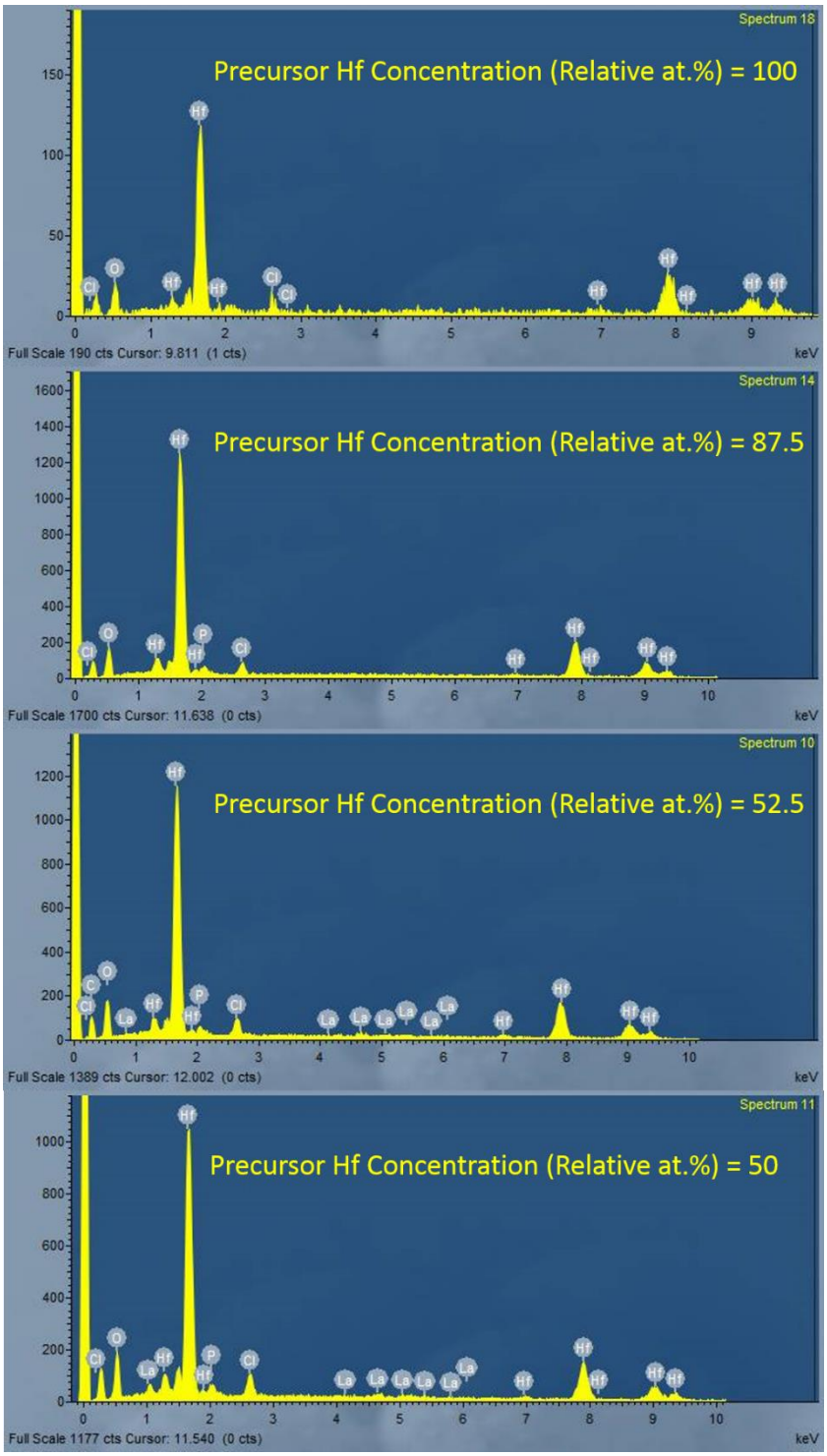

Figure A.4. Energy dispersive X-ray spectroscopy (EDX) of pristine HfO2 and selected $Hf_{1-x}La_xO2$ nanocrystals. The detected concentrations of hafnium and lanthanum are listed in Table A.3.

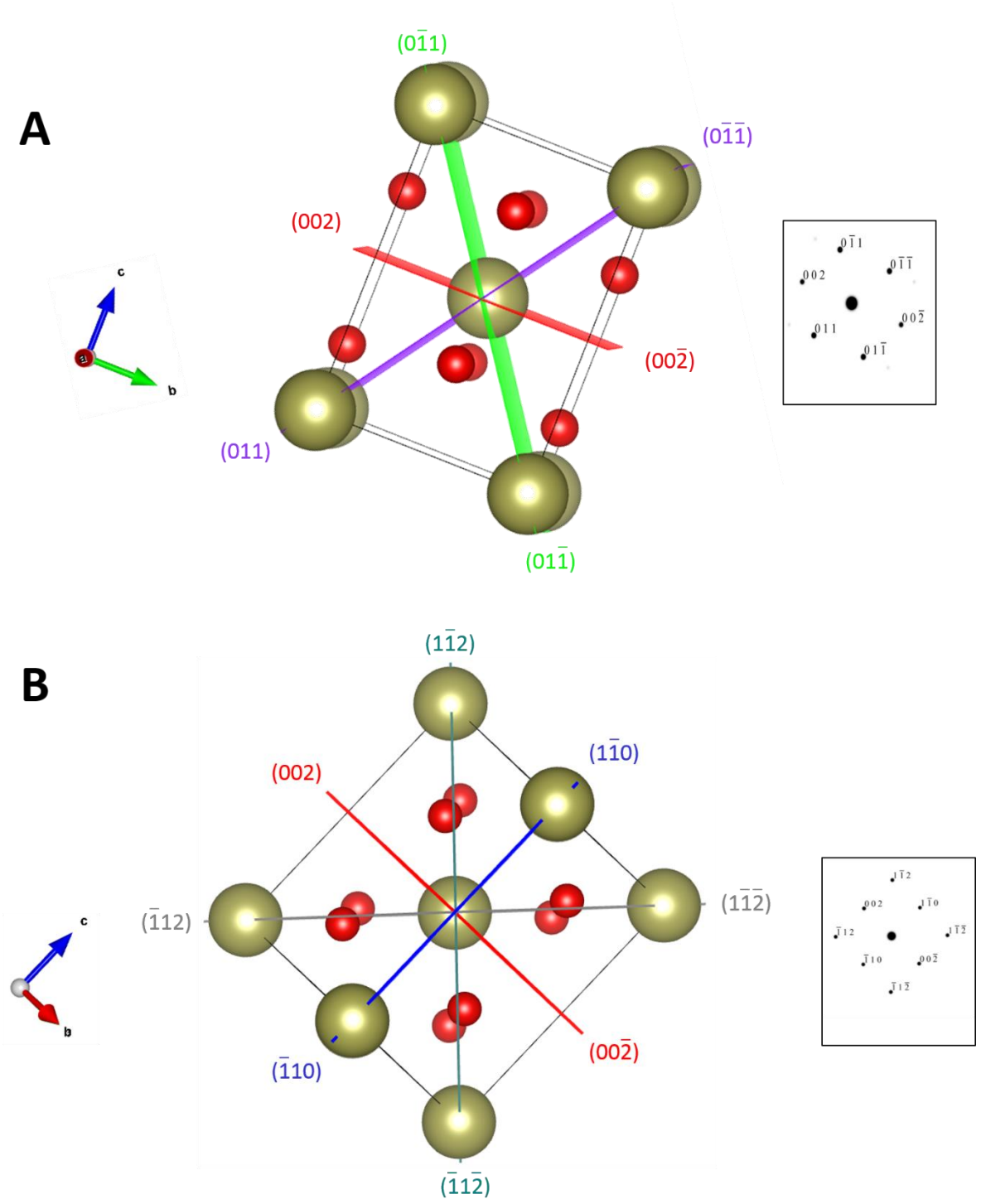

Figure A.5. (A) HfO_2 tetragonal unit cell depicting the corresponding lattice planes from Figure II.7D. (B) HfO_2 tetragonal unit cell depicting the corresponding lattice planes from Figure II.7H. The unit cells are constructed using lattice parameters given in Ref. 40 of Chapter II.

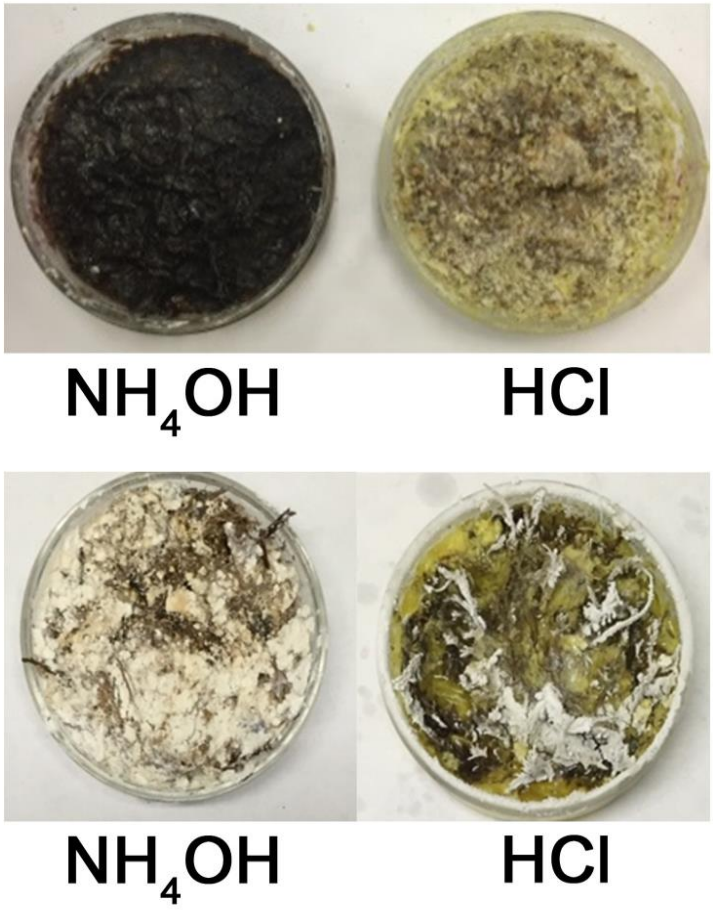

Figure A.6. Modified Muskeg at Different pH Conditions. Digital photographs of modified muskeg prepared using Na_2SiO_3 (top) or TEOS (bottom) with either NH_4OH (left) or HCl (right) as the catalyst. No mulch or hydroxyethylcellulose were used to prepare these samples. All samples depicted were prepared within a glass mold with a diameter of 6 cm.

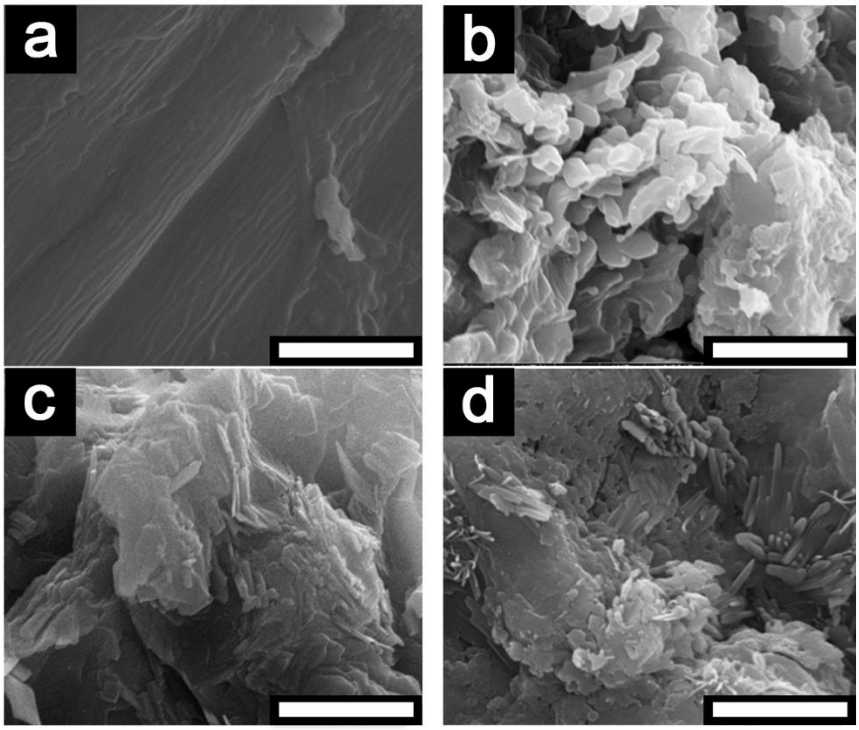

Figure A.7. Electron Microscopy Characterization of Modified Muskeg. Magnified SEM images of (a) unmodified muskeg, (b—d) modified muskeg with different ratios of Na_2SiO_3 and mulch; (b) 20 mL and 10 g, respectively; (c) 30 mL and 15 g, respectively; and (d) 30 mL and 5 g, respectively. The amount of NH_4OH and hydroxyethylcellulose were held constant for each modified muskeg specimen at 10 mL and 2 g, respectively. Scale bar = 4 μm.

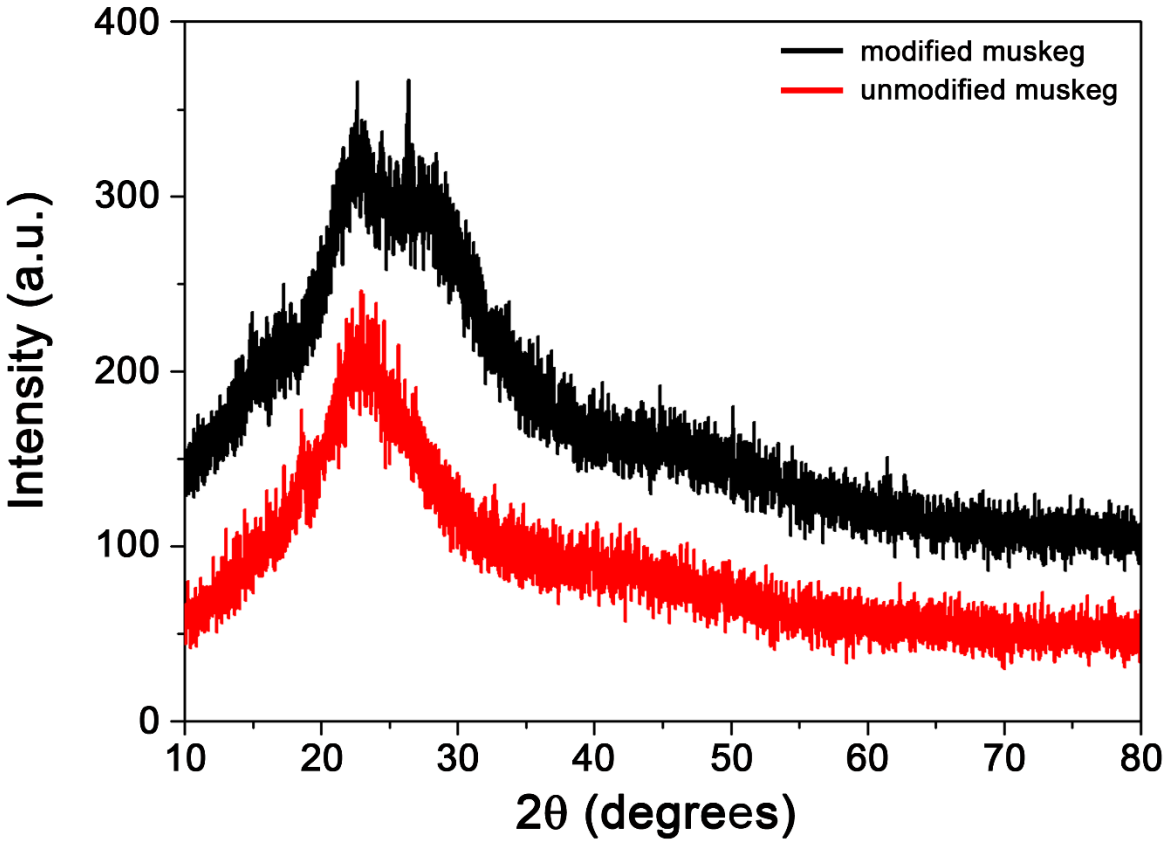

Figure A.8. X-ray Diffraction (XRD) Patterns of Modified Muskeg. Powder XRD pattern of unmodified muskeg (red) and modified muskeg (black) prepared using 20 mL Na_2SiO_3, 10 g mulch, 10 mL NH_4OH, and 2 g hydroxyethylcellulose. No evidence for crystalline species is discernible in the XRD patterns.

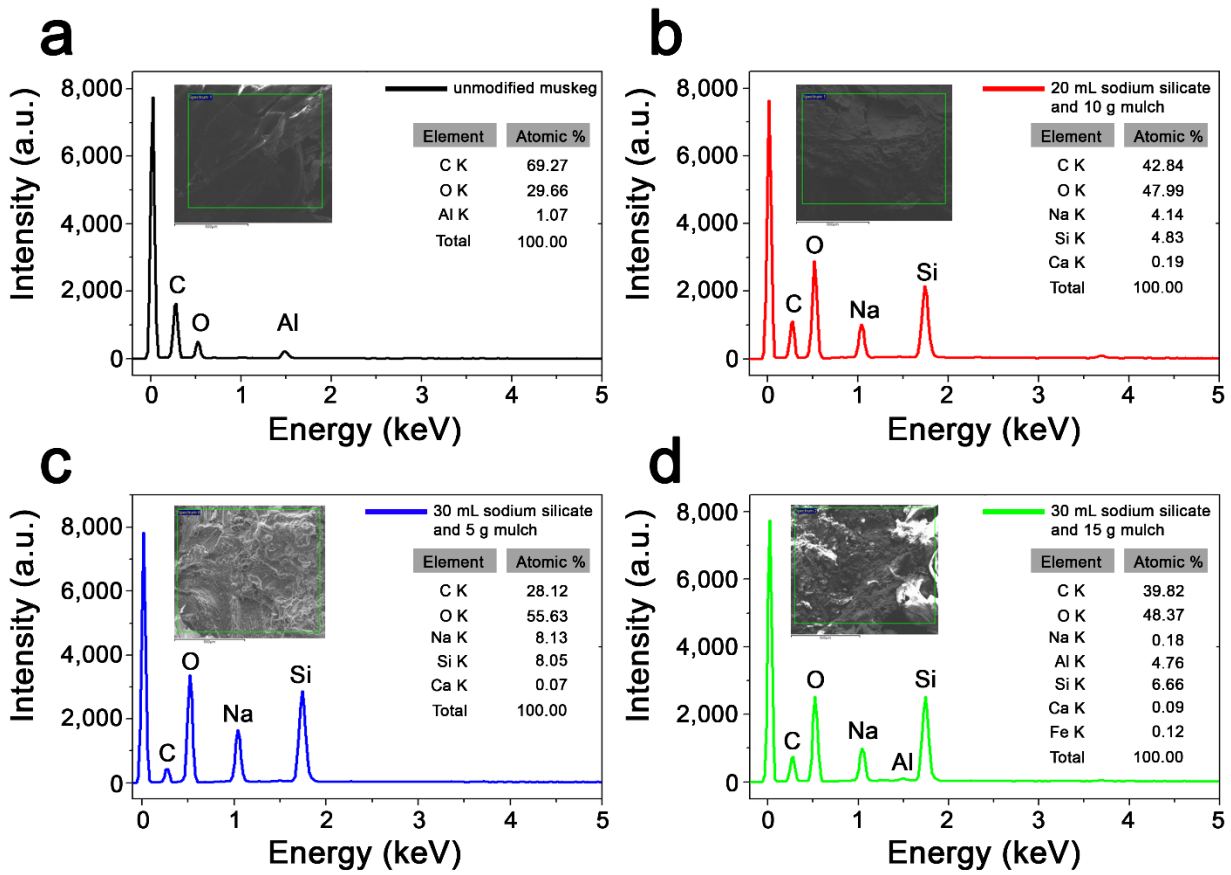

Figure A.9. Elemental Analysis of Muskeg Composites. EDS spectra of (a) unmodified and (b—d) modified muskeg with different added ratios of Na_2SiO_3 and mulch; (b) 20 mL and 10 g, respectively; (c) 30 mL and 5 g, respectively; and (d) 30 mL and 15 g, respectively. The insets illustrate SEM images of the areas examined by EDS. The amounts of NH_4OH and hydroxyethylcellulose were held constant for each modified muskeg specimen at 10 mL and 2 g, respectively.

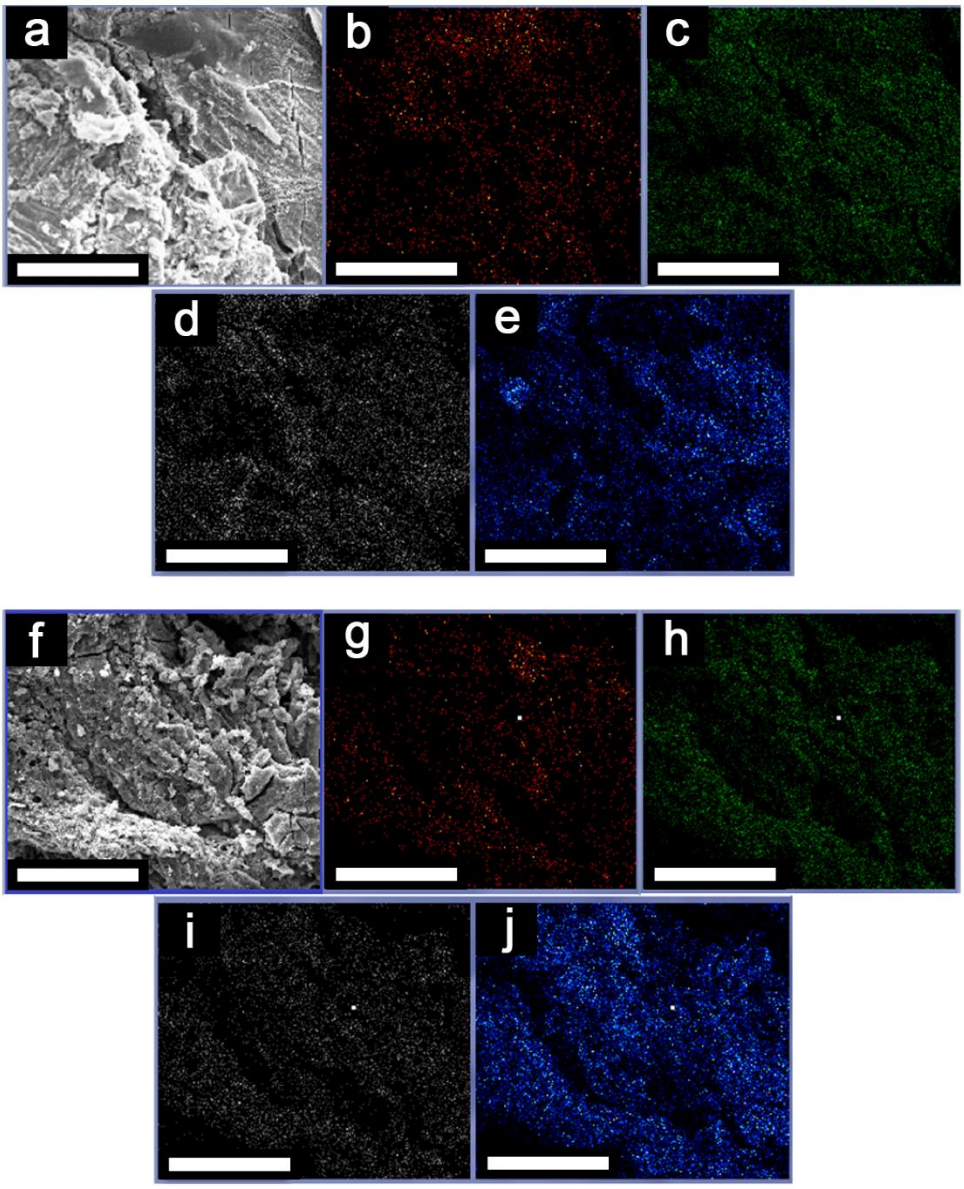

Figure A.10. Homogeneous Distribution of Components in Modified Muskeg Composites EDS color mapping of modified muskeg using (a—e) 20 mL Na_2SiO_3 and 10 g mulch and (f—j) 30 mL Na_2SiO_3 and 5 g mulch; (a,f) SEM images, (b, g) C K (red), (c,h) O K (green), (d, i) Na K (grey), (e,j) and Si K (blue). The amount of NH_4OH and hydroxyethylcellulose were held constant for each specimen at 10 mL and 2 g, respectively. Scale bar = 10 μm.

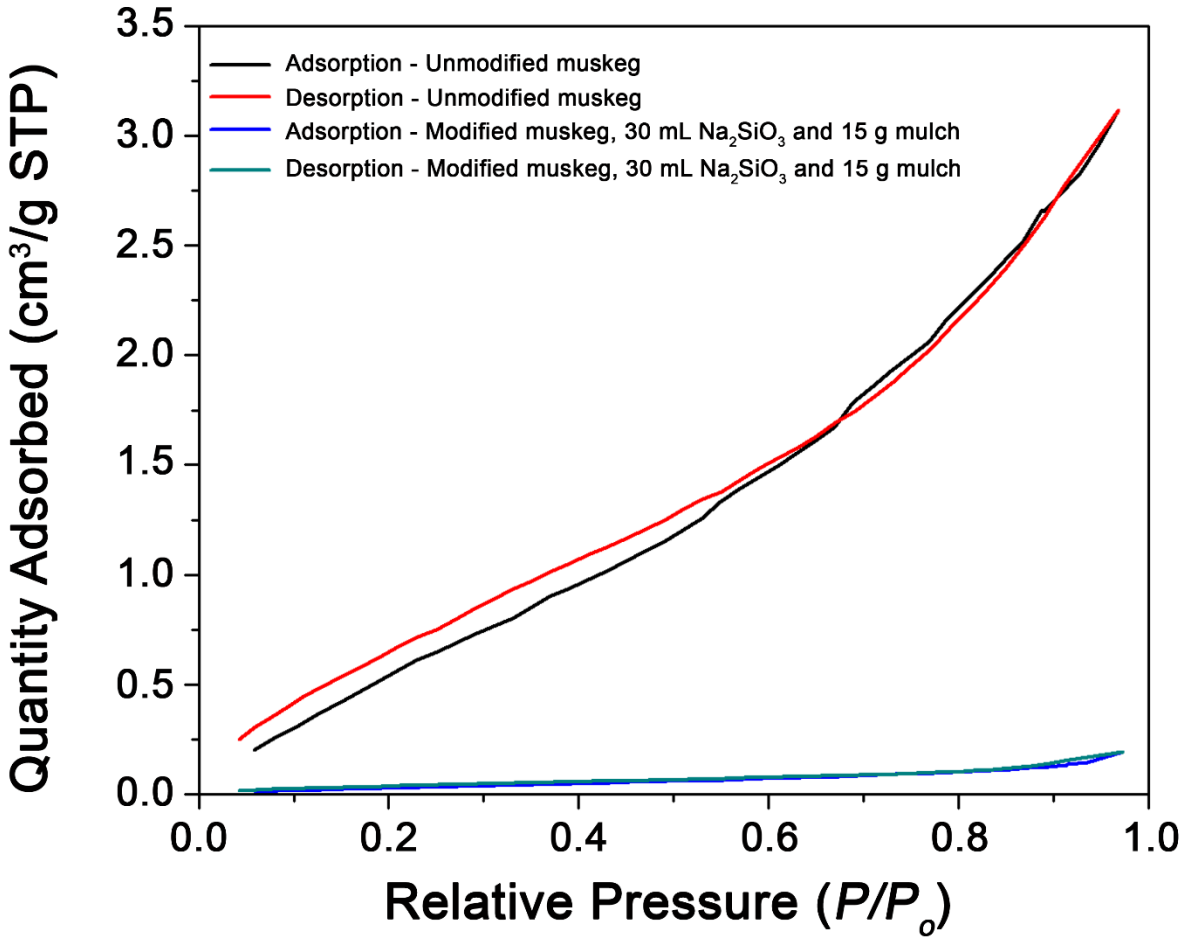

Figure A.11. Porosity Measurements of Muskeg Composites. Nitrogen adsorption/desorption plots measured for unmodified muskeg and modified muskeg laden with 30 mL Na_2SiO_3, 15 g mulch, 10 mL NH_4OH, and 2 g hydroxyethylcellulose.

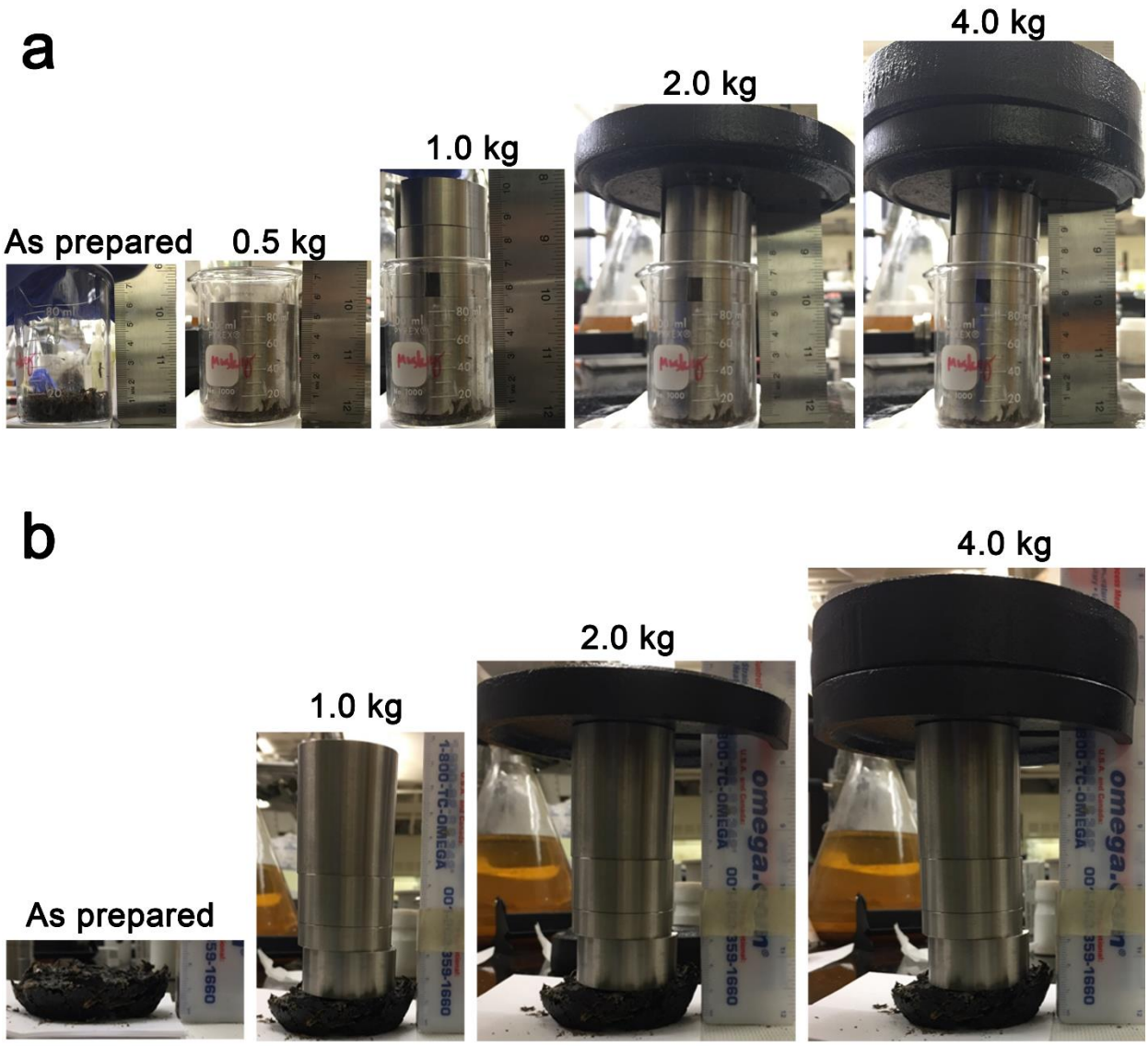

Figure A.12. Compressibility of Modified Muskeg Composites. Digital photographs of compressibility test for (a) unmodified muskeg (top) and (b) modified muskeg (bottom) as a function of weight placed on top of muskeg samples. The specific modified muskeg sample depicted here corresponds to 20 mL Na_2SiO_3, 10 g mulch, 10 mL of NH_4OH, and 2 g of hydroxyethylcellulose. See also Video A.2 that illustrates the contrast in compressibility for modified and unmodified muskeg.

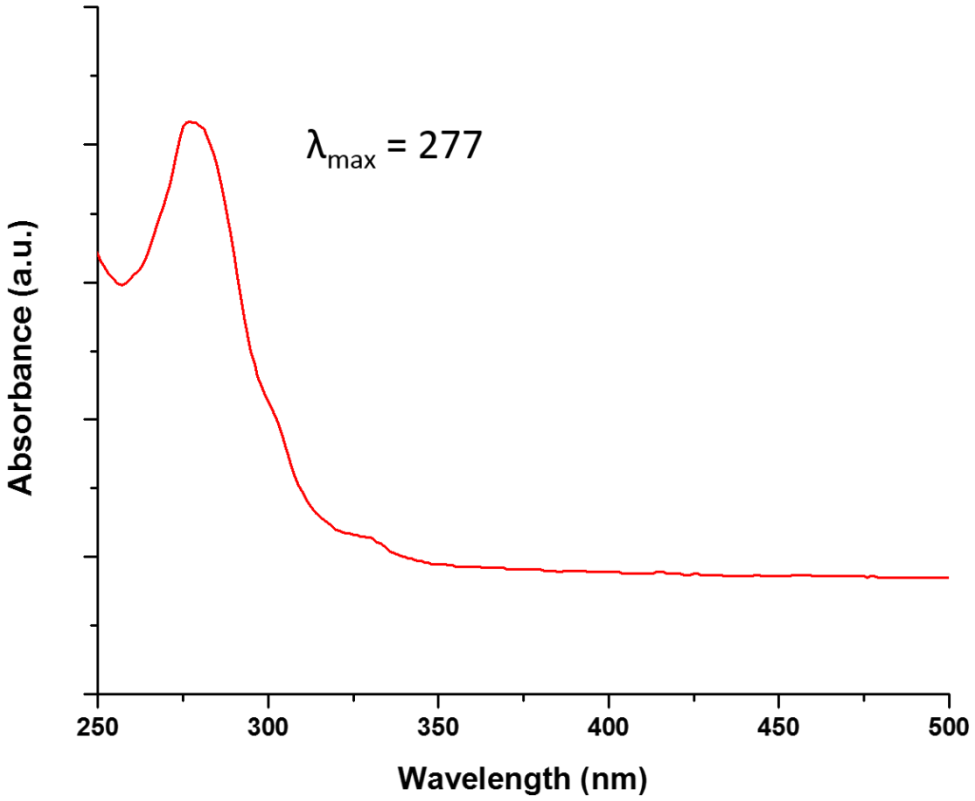

Figure A.13. Optical absorption spectrum of $Gd_{0.985}Tb_{0.015}OCl$ nanocrystals dispersed in hexanes.

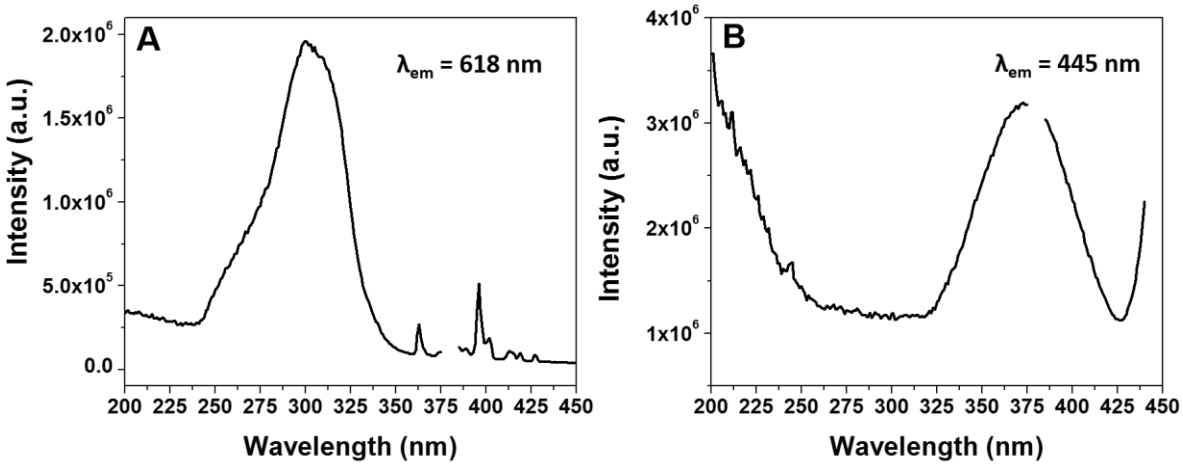

Figure A.14. Photoluminescence excitation spectra of $Eu_{0.019}La_{0.981}OCl$ nanocrystals capped with (A) TOPO and (B) oleylamine. The emission wavelength used was (A) 618 nm and (B) 445 nm.

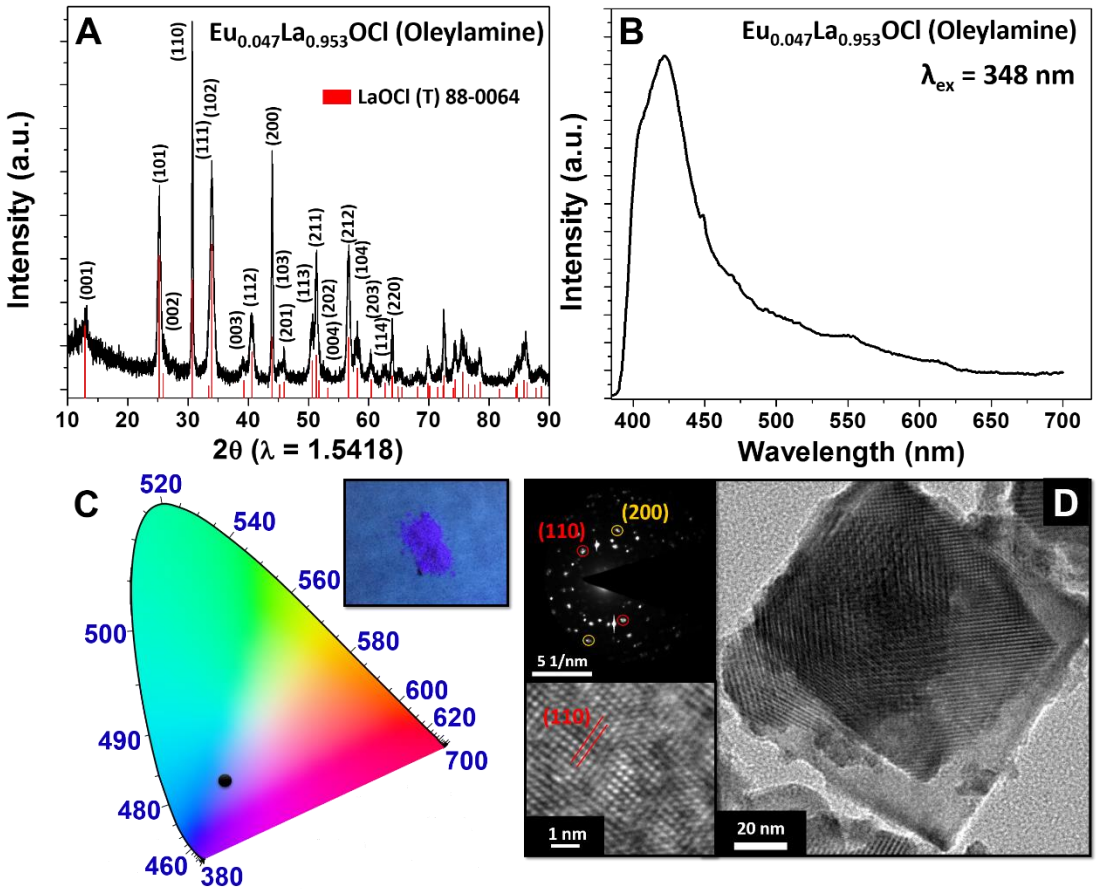

Figure A.15. (A) X-ray diffraction pattern of $Eu_{0.047}La_{0.953}OCl$ nanocrystals capped with oleylamine prepared using $EuCl_2$ as the halide precursor. (B) Photoluminescence emission spectra of $Eu_{0.047}La_{0.953}OCl$ nanocrystals acquired using an excitation wavelength of 348 nm. (C) Corresponding CIE chromaticity diagram depicting the blue luminescence of the sample and the inset depicting a digital photograph of the $Eu_{0.047}La_{0.953}OCl$ phosphor upon illumination with a 254 nm UV light source. (D) High-resolution TEM image of $Eu_{0.047}La_{0.953}OCl$ nanocrystals. The bottom inset shows a lattice-resolved HRTEM image and indicates the separation between the (110) lattice planes of tetragonal LaOCl viewed along the basal planes of the nanoplatelets. The top inset shows an indexed selected area electron diffraction pattern corresponding to the bottom inset.

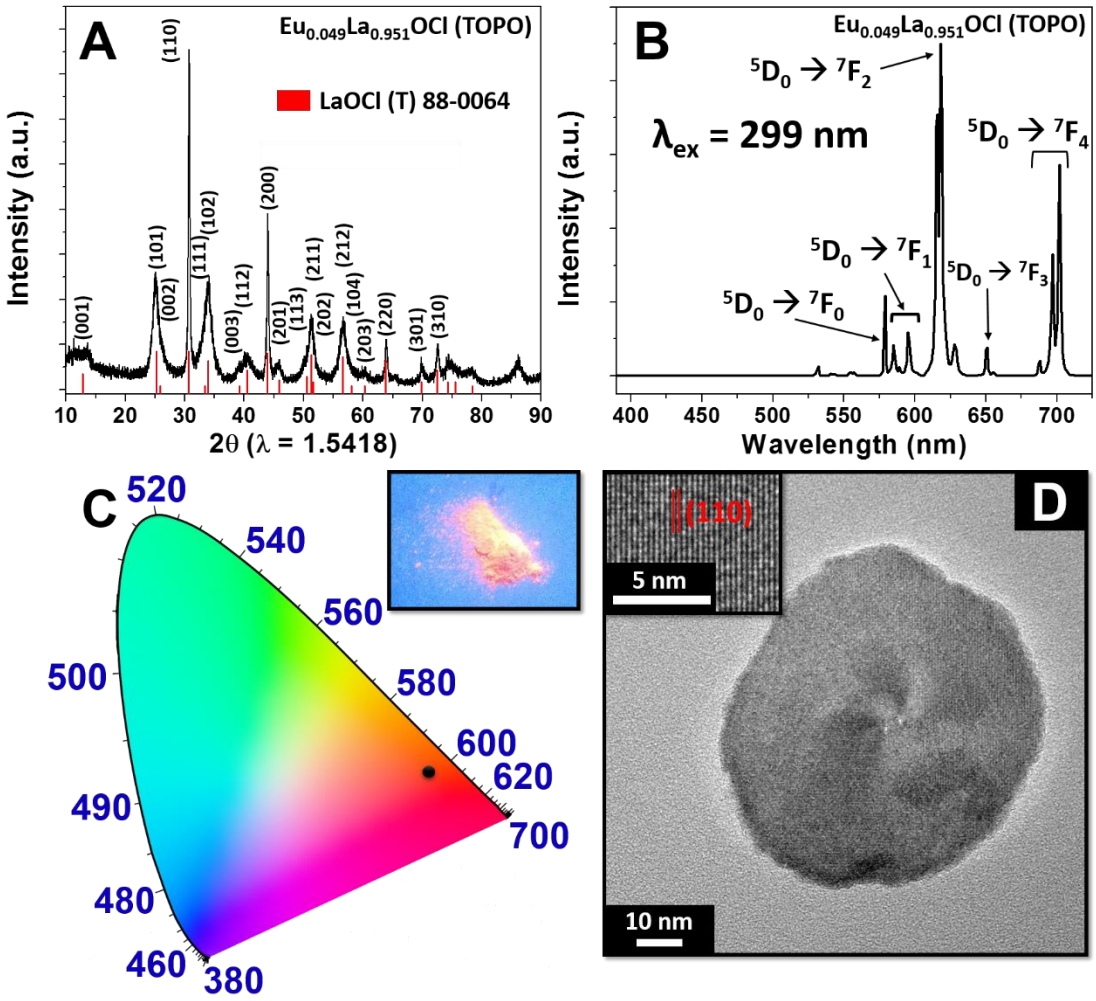

Figure A.16. (A) X-ray diffraction pattern of $Eu_{0.049}La_{0.951}OCl$ nanocrystals capped with TOPO prepared using $EuCl_2$ as halide precursor. (B) Photoluminescence emission spectra of $Eu_{0.049}La_{0.951}OCl$ nanocrystals acquired using an excitation wavelength of 299 nm. The corresponding CIE chromaticity diagram is depicted in (C). The inset in (C) depicts a digital photograph of the $Eu_{0.049}La_{0.951}OCl$ phosphor upon illumination with a 254 nm UV light source. (D) High-resolution transmission electron microscopy images of the same $Eu_{0.049}La_{0.951}OCl$ nanocrystals. The inset indicates the separation between the (110) lattice planes of tetragonal LaOCl.

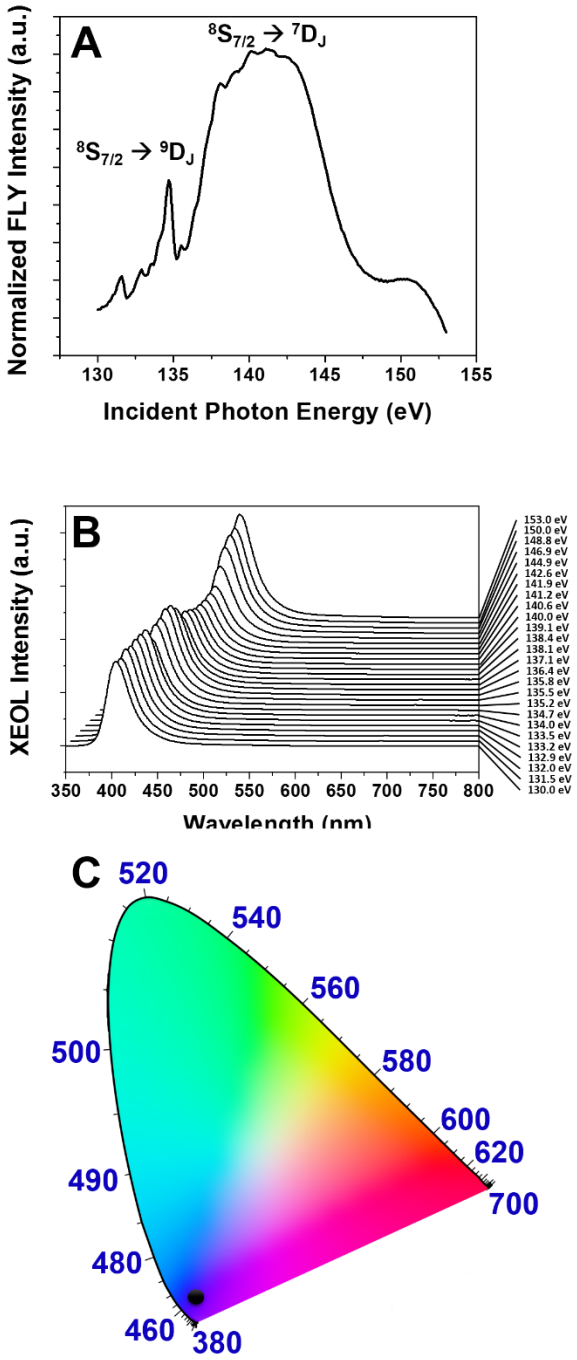

Figure A.17. (A) XANES spectrum of $EuCl_2$ acquired at the Eu $N_{4,5}$-edge. (B) Stacked XEOL spectra measured for $EuCl_2$ with the corresponding CIE chromaticity diagram depicted in (C). Each spectrum in (B) was acquired at specific excitation energies upon excitation across the Eu $N_{4,5}$-edge.

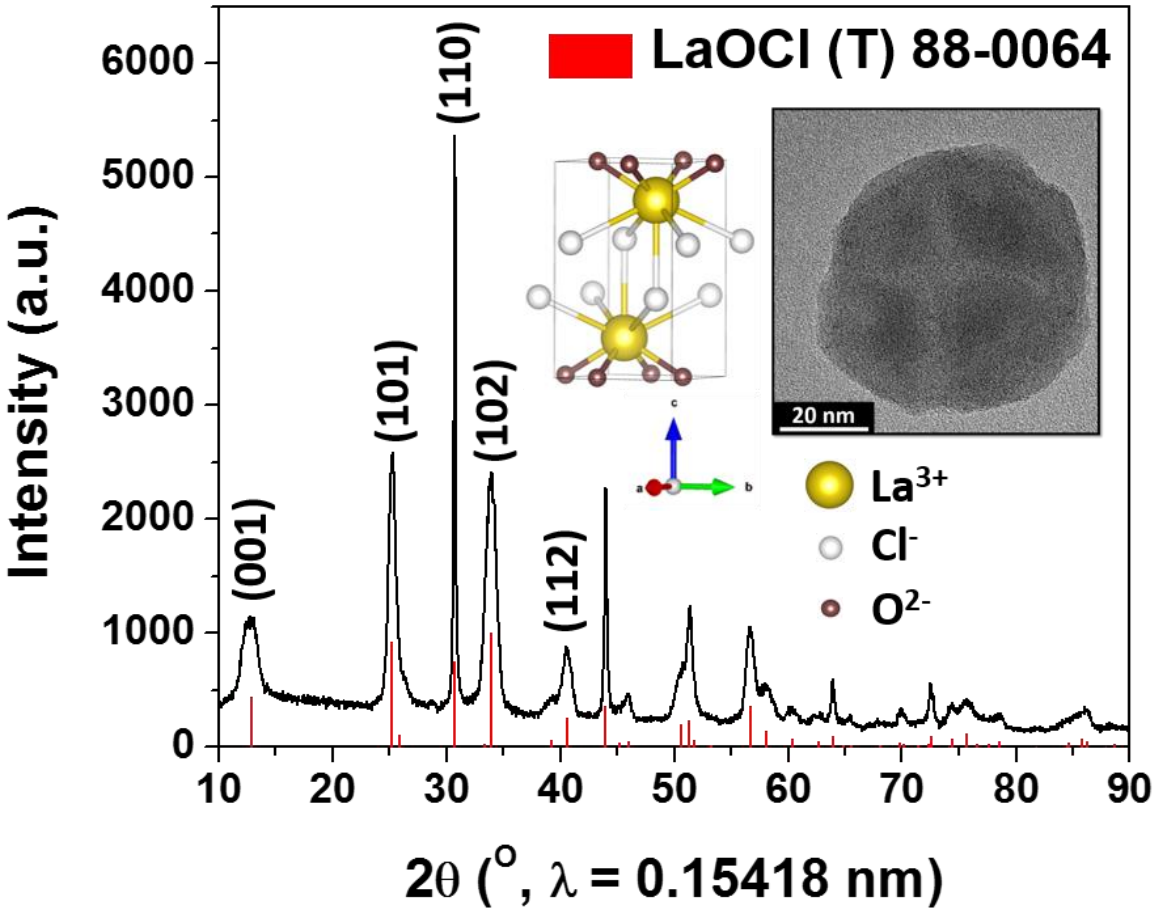

Figure A.18. (A) Powder XRD pattern of LaOCl nanoplatelets prepared using TOPO as the stabilizing ligand. The vertical red bars denote positions and relative intensities for tetragonal LaOCl (space group: *P4/nmm*, JCPDS # 88-0064). The top inset depicts the crystal structure of tetragonal LaOCl. The top right inset depicts a low-magnification transmission electron microscopy image of an individual LaOCl nanoplatelet.

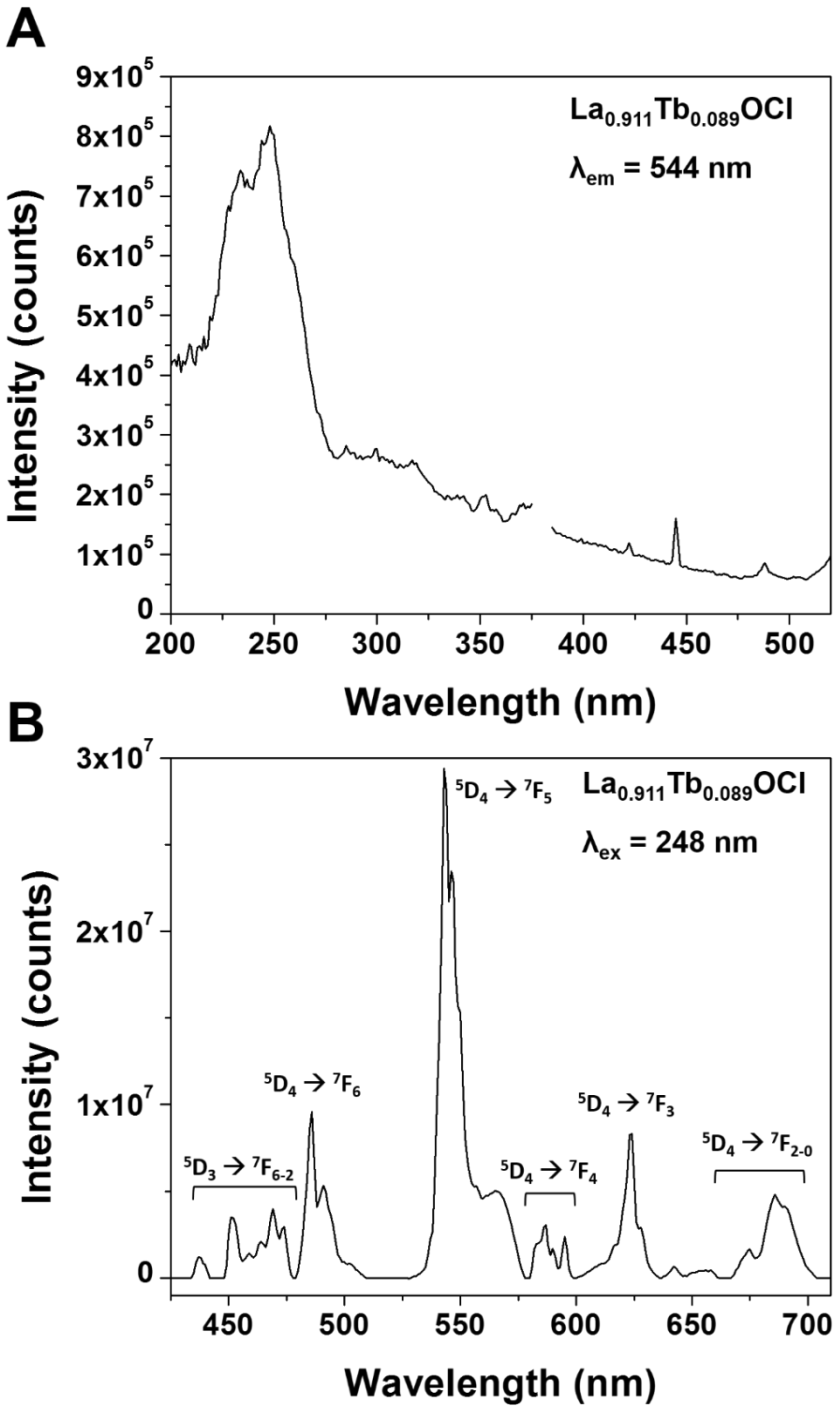

Figure A.19. (A) Photoluminescence excitation spectrum of $La_{0.911}Tb_{0.089}OCl$ nanocrystals capped with TOPO. The excitation spectrum has been acquired at an emission wavelength of 544 nm corresponding to the intense $^5D_4 \rightarrow {}^7F_5$ band. (B) Photoluminescence emission spectrum of the same $La_{0.911}Tb_{0.089}OCl$ nanocrystals acquired at an excitation wavelength of 248 nm.

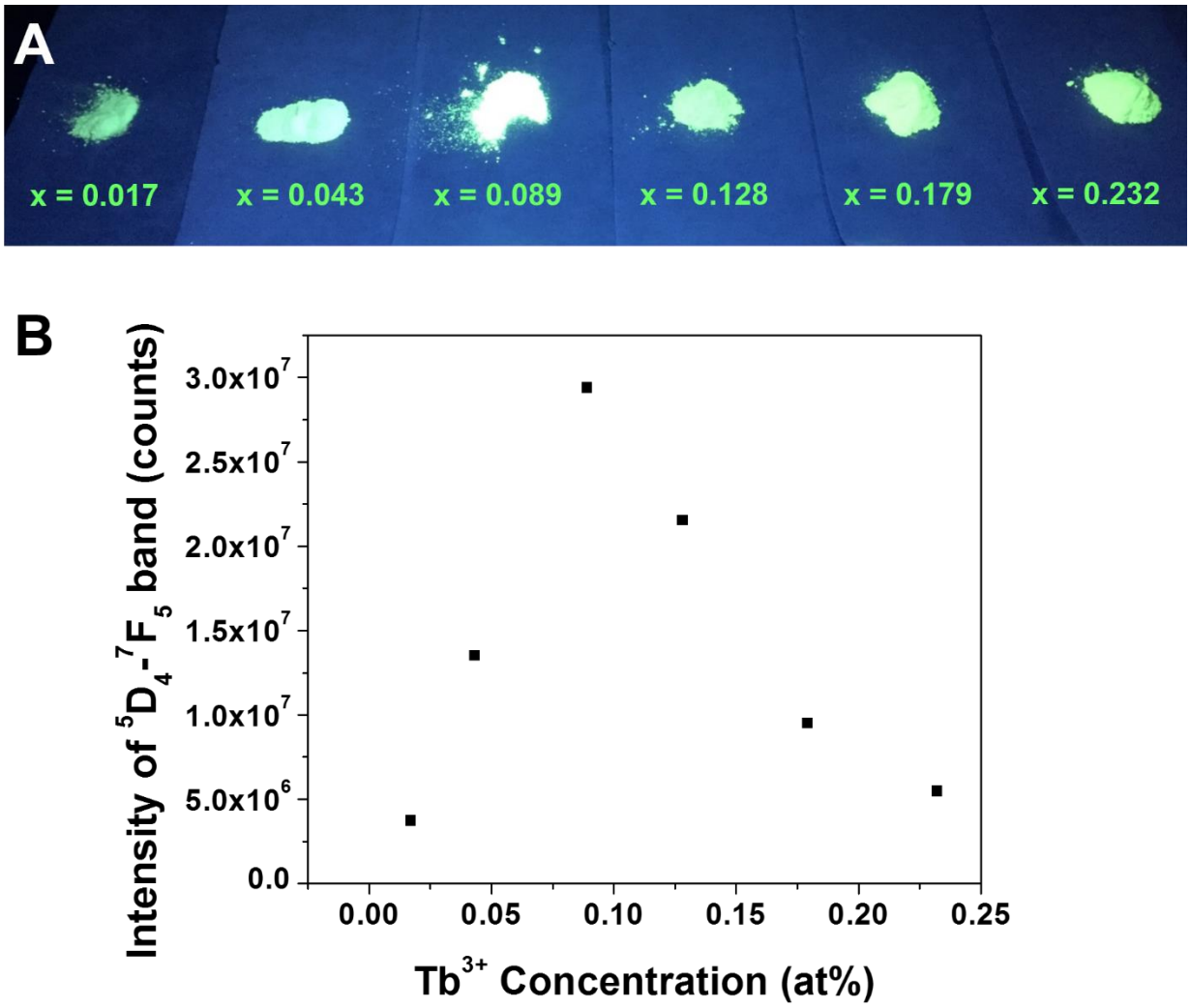

Figure A.20. (A) Digital photographs of TOPO-passivated $La_{1-x}Tb_xOCl$ nanoplatelets with increasing Tb content upon illumination with a 254 nm UV light source. (B) Evolution of the normalized intensity of the $^5D_4 \rightarrow {}^7F_5$ emission as a function of the Tb^{3+} concentration for $La_{1-x}Tb_xOCl$ nanocrystals (in the Tb^{3+} range of $0.1 \leq x \leq 0.24$ at.%).

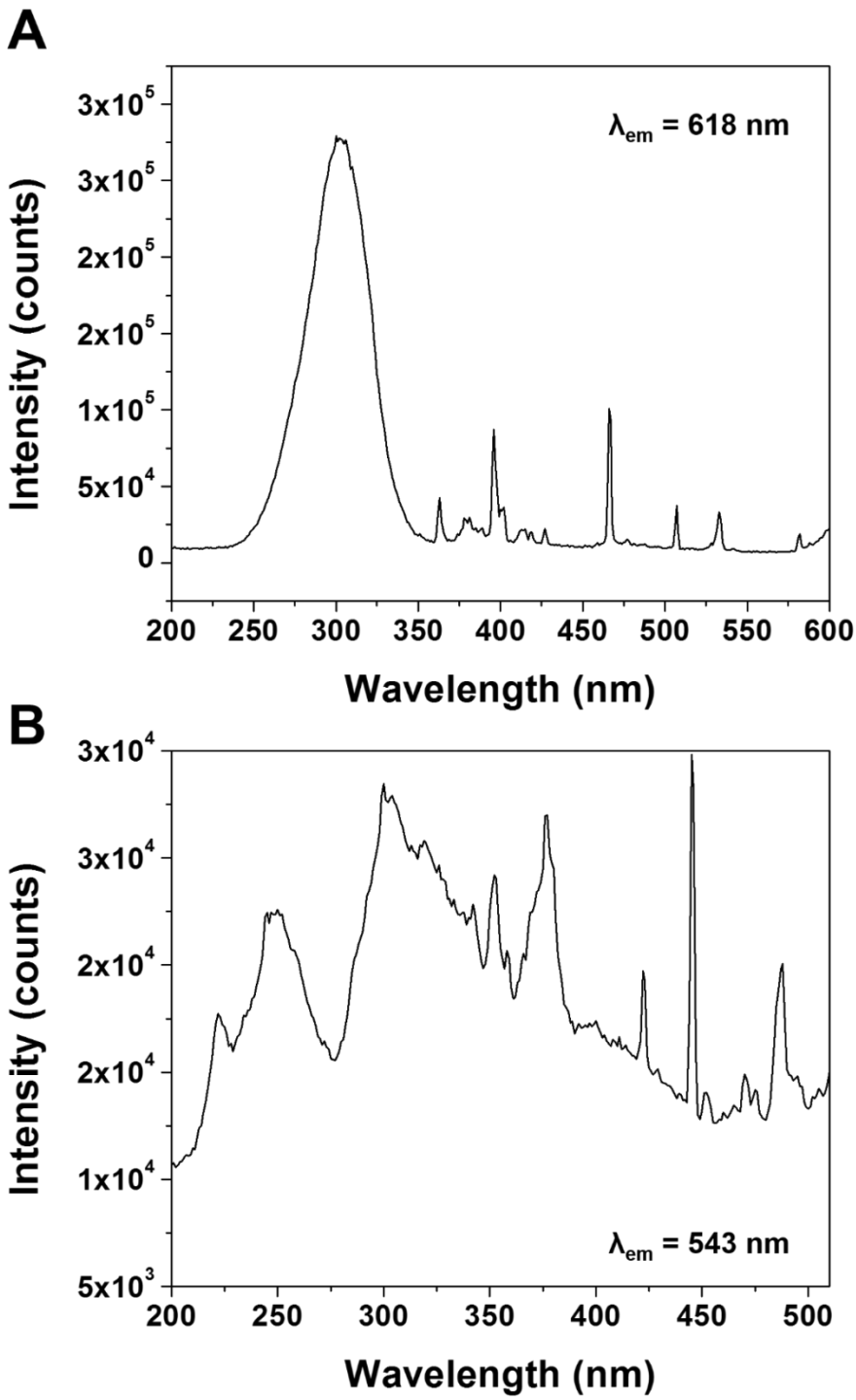

Figure A.21. Photoluminescence excitation spectra of $La_{0.926}Tb_{0.047}Eu_{0.027}OCl$ nanocrystals capped with TOPO. The emission wavelengths used are A) 618 nm and B) 543 nm corresponding to the $^5D_0 \rightarrow {}^7F_2$ transition of Eu^{3+} and the $^5D_4 \rightarrow {}^7F_5$ transition of Tb^{3+}, respectively.

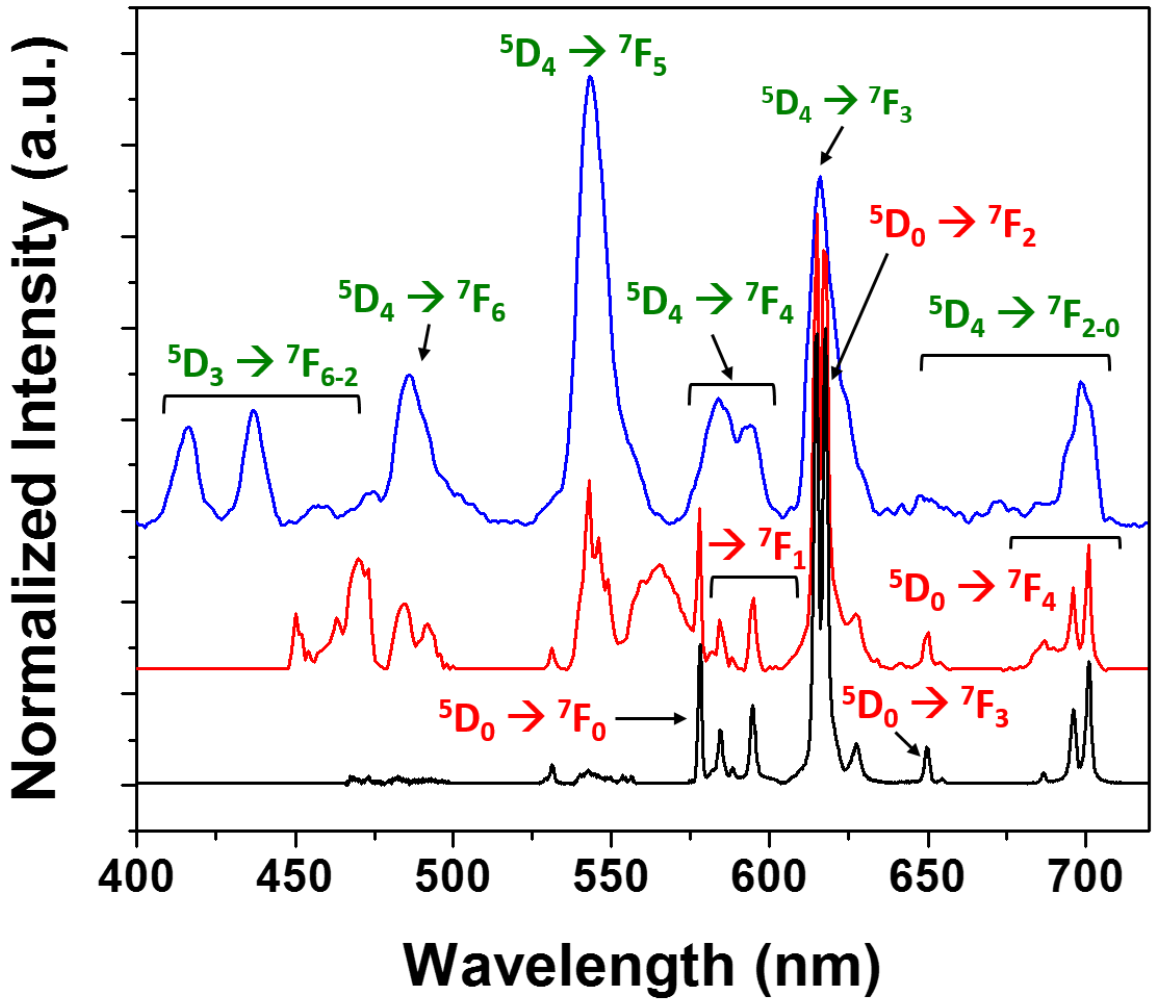

Figure A.22. Contrasting the photoluminescence emission spectra (black and red, acquired at 300 and 248 nm excitation, respectively) and XEO/.L spectrum (blue) of $La_{0.926}Tb_{0.047}Eu_{0.027}OCl$ nanocrystals capped with TOPO. The XEOL spectrum has been acquired at the giant resonance absorption of 117.5 eV. The intensity of each spectrum has been normalized to the emission peak at 618 nm.

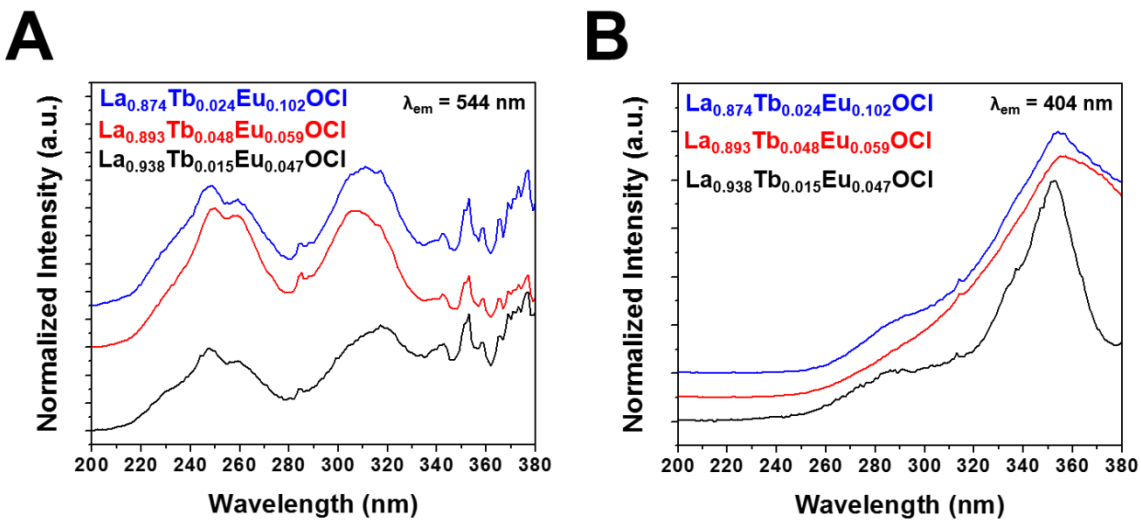

Figure A.23. Photoluminescence excitation spectra of $La_{1-x-y}Tb_xEu_yOCl$ nanocrystals capped with oleylamine. The excitation spectrum acquired in A) was at an emission wavelength of 544 nm whereas the excitation spectrum acquired in B) was at an emission wavelength of 404 nm corresponding to the the $4f^8 5d^0 \rightarrow 4f^7 5d^1$ excitation of Tb^{3+} ions and the intense $4f^6 5d^1 \rightarrow 4f^7$ emission band of Eu^{2+} ions respectively. The intensity of the spectrums in A) have been normalized to the excitation peak at 248 nm while the intensity of the spectrums in B) have been normalized to the excitation maximum at 354 nm.

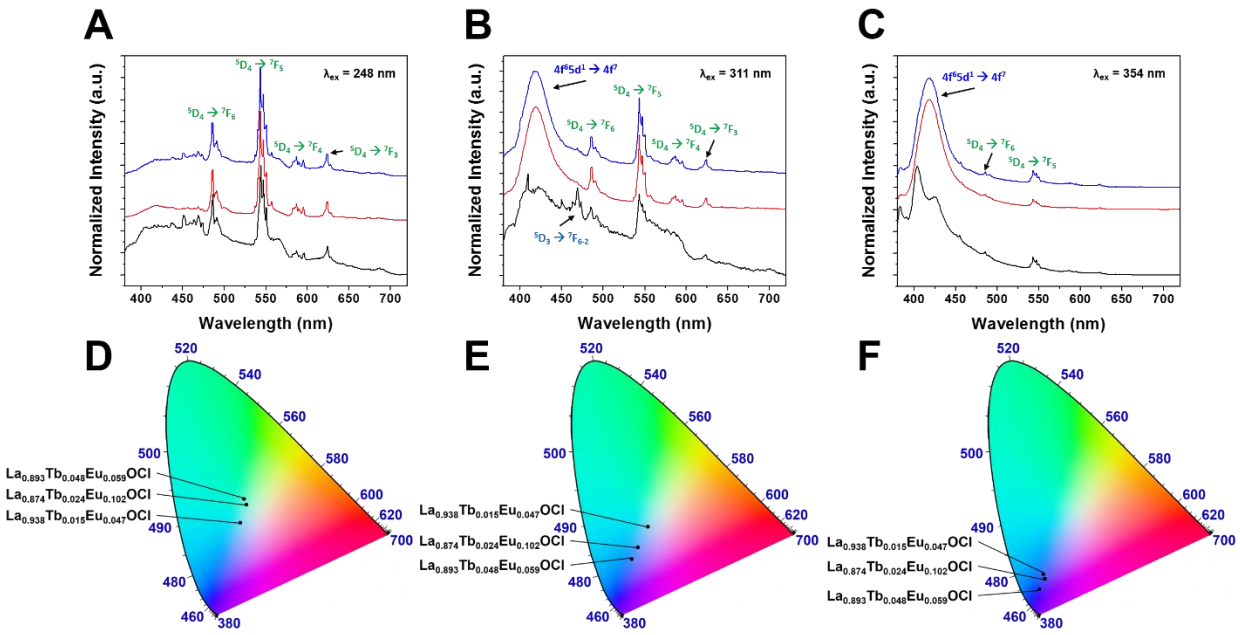

Figure A.24. Photoluminescence emission spectra of $La_{1-x-y}Tb_xEu_yOCl$ nanocrystals prepared using oleylamine as the stabilizing ligand. The spectra have been acquired at excitation wavelengths of A) 248 nm, B) 311 nm, and C) 354 nm corresponding to the excitation maxima observed in Figure A.23. D-F) CIE chromaticity diagrams for $La_{1-x-y}Tb_xEu_yOCl$ nanocrystals corresponding to (A-C), respectively.

Precursor Hf Concentration (Relative at.%)	Detected Hf Concentration by EDX (Relative at. %)	Detected Ce Concentration by EDX (Relative at. %)
100	100	0
80	100	Not Detected
60	99.75	0.25
50	96.13	3.87

Table A.1. Detected concentrations of hafnium and cerium by EDX analysis based on integration of the data shown in Figure A.1.

HfO_2 (Monoclinic) – JCPDS # 78-0050				
atom	*x*	*y*	*z*	occupancy
Hf1	0.2755(2)	0.0397(1)	0.2080(2)	1.0
O1	0.0739(20)	0.3318(17)	0.3466(17)	1.0
O2	0.4489(20)	0.7582(16)	0.4800(22)	1.0
Space Group = $P2_1/c$, a = 5.1170(1), b = 5.1754(2), c = 5.2915(2) α, γ = 90, β= 99.216(2)				
HfO_2 (Tetragonal) – From Ref. 40				
atom	*x*	*y*	*Z*	occupancy
Hf1	0.0	0.0	0.0	1.0
Hf2	0.5	0.5	0.5	1.0
O1	0.5	0.0	0.21282	1.0
O2	0.5	0.0	-0.28718	1.0
O3	0.0	0.5	0.28718	1.0
O4	0.0	0.5	-0.21282	1.0
Space Group = $P4_2/nmc$, a, b = 3.560000, c = 5.110000, α, β, γ = 90				

Table A.2. Unit cell parameters for the monoclinic and tetragonal phases of HfO_2.

Precursor Hf Concentration (Relative at.%)	Detected Hf Concentration by EDX (Relative at. %)	Detected La Concentration by EDX (Relative at. %)
100	100	0
87.5	100	Not Detected
52.5	96.81	3.19
50	95.99	4.01

Table A.3. Detected concentrations of hafnium and lanthanum by EDX analysis integrated from the spectra depicted in Figure A.4.

Condition	pH
Na_2SiO_3 + HCl	0.37
TEOS + HCl	2.13
Muskeg alone	6.82
TEOS + NH_4OH	8.40
Na_2SiO_3 + NH_4OH	10.94

Table A.4. pH values measured for reaction mixtures when different catalysts are used to constitute the silica framework.

Intended Tb^{3+} Dopant Concentration in $Gd_{1-x}Tb_xOCl$	x = 0.020	x = 0.050	x = 0.100	x = 0.150	x = 0.200	x = 0.250	x = 0.300
Actual Tb^{3+} Dopant Concentration in $Gd_{1-x}Tb_xOCl$	x = 0.018	x = 0.042	x = 0.084	x = 0.131	x = 0.171	x = 0.216	x = 0.234

Table A.5. The top row shows the intended Tb^{3+} dopant concentration for $Gd_{1-x}Tb_xOCl$, whereas the bottom row shows the actual dopant concentration as determined by inductively coupled plasma mass spectrometry.

$Eu_{0.047}La_{0.953}OCl$ UV - oleylamine	$Eu_{0.049}La_{0.951}OCl$ UV - TOPO	$EuCl_2$ XEOL
x = 0.223	x = 0.649	x = 0.172
y = 0.192	y = 0.351	y = 0.053

Table A.6. Commission International de I'Eclairage (CIE) coordinates for $Eu_xLa_{1-x}OCl$ phosphors prepared with $EuCl_2$ precursor upon 348 nm and 299 nm UV illumination and $EuCl_2$ upon excitation at 141.2 eV.